Plasma Processes in Pulsar Environments

by

Craig Ronald Stark, MSci.

Thesis
submitted to the
University of Glasgow
for the degree of
Ph.D.

Astronomy and Astrophysics Group
Department of Physics and Astronomy
University of Glasgow
Glasgow, G12 8QQ.

Submitted
July 2008

"The scientist is not a person who gives the right answers, he's one who asks the right questions."
– Claude Lévi-Strauss

"Back off, man. I'm a scientist."
– Dr. Peter Venkman

Contents

Abstract

The aim of this thesis is to study coherent plasma effects and collective plasma processes in pulsar environments. Pulsars are one of the most enigmatic objects in the universe. Formed in supernova explosions, pulsars are rapidly rotating neutron stars identified by their periodically pulsed electromagnetic emission. The source of the radiation is believed to be associated with the electron-positron (pair) plasma populating the pulsar magnetosphere. The theory of pulsar radiation is still in its infancy and there is lack of understanding about the energetic processes involved.

The initial aim of this thesis is to study a possible emission mechanism in which electrostatic oscillations are coupled to propagating electromagnetic waves by a magnetic field inhomogeneity, thus creating a source of radiation in the pulsar magnetosphere. The full nonlinear equations in cylindrical geometry for a streaming cold pair plasma are solved numerically, together with Maxwell's equations, using a Finite-Difference Time Domain method. Electrostatic oscillations are induced in a streaming plasma in the presence of a non-uniform magnetic field, and the resulting electromagnetic waves are modelled self-consistently. Also presented is the linear perturbation analysis of these model equations perturbed from a dynamical equilibrium in order to probe the fundamental modes present in the system. These simulations successfully exhibit the coupling mechanism and the nonlinear interaction between electromagnetic waves and independent plasma oscillations, confirming the importance of coherent plasma effects and collective plasma processes in the pulsar magnetosphere.

The observed electromagnetic signature is characterised by the nature of the emission mechanism and possibly by the menagerie of dust it encounters as it propagates through the surrounding supernova remnant. Supernova remnants are composed of multi-species electron-ion dusty plasmas. Conventional modelling of dust growth in this environment is based upon coagulation and nucleation of gas phase material. The second aim of this thesis is to study a possible spheroidal dust growth mechanism via plasma deposition. Dust grains immersed in a plasma acquire a net negative charge forming a plasma sheath. Ions are accelerated from the bulk plasma into the sheath and are deposited on the surface of the grain altering its shape and size. Grains with an elliptical geometry have a non-radial electric field and further anisotropic growth occurs if the deposited ions are non-inertial. In reality the extent of such growth depends upon the initial kinetic energy of the ions and the magnitude of the electric field in the sheath. Laplace's equation for the electric field for a range grain eccentricities is numerically solved using a bespoke finite difference method, the dynamics of the ions in the sheath are solved, showing how elliptical growth is related to the initial eccentricity and size of the seed relative to the sheath length.

Acknowledgments

I would like to take this opportunity to thank those who made this all possible.

First and foremost I would like to thank my supervisor Declan, without his help and pearls of wisdom this thesis would not have been possible. His knowledge of plasma physics is second to none and I can only aspire to such enlightenment. For originally getting me hooked on pulsars I thank my second supervisor John, his guidance and discussions were insightful. I would also like to thank António, my unofficial supervisor, his enthusiasm for pulsars is contagious. His help has been invaluable and it is much appreciated. Thanks to Luís for all the help and support, for proof reading my thesis and for looking after my textbooks. Can I have them back now please.

I would like to thank the Astronomy and Astrophysics group and all the staff at Glasgow for their help and for giving me the opportunity to work on such a great project. Due to my fear of the machines and their impending apocalyptic rise to power I would like to thank Iain Sim, Graeme Stewart and Norman Gray for all their computer related heroics. My inability to fill out forms correctly and my impatience with all things bureaucratic was remedied by the delightful Daphne!

To the plasma boys, my office mates Craig and Hugh, I am thankful for the welcome light relief they provided. Craig – thanks for being instrumental in conspiring to annoy Hugh. Hugh – I'm sorry about sabotaging your keyboard, the opportunity was too good to miss! Thanks also for all the pointers and for tolerating my incompetent programming. Twas a pleasure gentlemen.

I would also like to thank all my friends both old and new. In particular my old high school friends Vikki, David, Scott and Alan; My undergraduate comrades Andy, Robert, Iain, Gordon, Jen and Jennifer; and of course the astro amigos – you know who you are!

My long suffering parents, the smartest people I know, thank you for the years of support. I would never have embarked on such an escapade, nor finished it if it wasn't for you. A big special thank you to my family: the Starks, the Somers, the Taylors, the Witheys, the Troianos and the Gunnings. You all helped in ways you probably didn't even realise.

To Debbie, her sure and steadfast faith in me was an inspiration. Despite the miles between us, you are my anchor – thank you for putting up with the thesis blues.

And finally to the two people that first turned my attention to physics. I of course refer to the legendary Mr Weir and Mr MacDonald, the champions of physics at Cumbernauld High School.

Conveniently, the author reserves the right to thank anyone whom he may have inadvertently forgotten.

Declaration

This thesis is my own composition except where indicated in the text and the work presented herein has not been submitted for any other qualification from any other institution.

List of Figures

List of Tables

Chapter 1

Introduction

Forty one years ago, at the Mullard Radio Astronomy Observatory, an unusual rapidly pulsating radio source was observed. Discovered by Jocelyn Bell and Antony Hewish, the signal was initially dismissed to be sporadic radio interference, but its persistent occurrence established that the radiation was emanating from an astrophysical object within the immediate galaxy. Extraordinarily, the observed signal consisted of a series of short pulses each lasting ~ 0.3 seconds and repeating every ~ 1.337 seconds with unearthly accuracy [1]. It was not long until similar phenomena were being observed across the celestial sphere [2]. Yet, mystery surrounded the origin of such an astronomical spectacle.

Initial speculation suggested the radiation was associated with the oscillating modes of white dwarf or neutron stars [1; 2]. In his seminal paper in 1968, Thomas Gold argued that this scenario was unlikely. He contended that the lowest oscillating mode must have a period which is of the same order as the period of fastest rotation, without centrifugal break-up. For white dwarfs the fundamental period is not small enough to account for the observed sub-pulse structure, whereas for neutron stars the fundamental period is too small. Gold suggested that pulsars, rapidly rotating neutron stars, were the origin of the pulsating radio source [3]. See Fig. 1.1.

Pulsars are rapidly rotating neutron stars characterised by ultra strong magnetic fields, $B \sim 10^8 - 10^{11}$ T, and broadband, periodic, pulsed electromagnetic emission. The observed pulses are the result of directional beams, that originate from the magnetic polar caps, rotating like a lighthouse beacon (Fig. 1.2). The source of the radiation mechanism remains unknown, but it is believed that the electron-positron (pair) plasma constituting the pulsars magnetosphere is the main protagonist.

This brief introduction gives a basic overview of pulsars and their environments, paying particular attention to the pair magnetospheric plasma and the electron-ion plasma present in the surrounding supernova remnant. It begins with a discussion concerning the creation and formation of pulsars and their associated remnants, continuing with a description of the basic observational properties of pulsars. The chapter then proceeds with an overview of the main contenders for the pulsar radio emission mechanism and concludes with a discussion regarding the effect of remnant dust on pulsar radiation.

Figure 1.1: One of the most famous pulsars is the Crab pulsar. The image includes the supernova remnant, showing the X-ray (blue) and optical (red) emission. Image created by NASA and ESA.

Pulsars and their environments

Pulsars are forged in spectacular Type II supernova explosions following the catastrophic gravitational core collapse of a massive star $> 8M_{\odot}$ [4].

It all begins, ironically, with the death of a star. After a star has depleted all the hydrogen in its core, fusion processes cease and the core contracts under the relentless force of gravity. As it contracts, the temperature and density increase until conditions become favourable for the fusion of heavier elements. In this eventuality, the generated thermodynamic pressure momentarily halts the collapse of the star. Successively heavier elements can be fused in the core until iron is reached: iron fusion processes are endothermic and so require energy to fuse, as result all fusion processes stop. With no energy source to balance gravity, the density of the stellar core increases until the onset of electron degeneracy pressure. This quantum mechanical effect is a consequence of the Pauli exclusion principle which forbids two fermions occupying the same quantum state at the same time. From the Heisenberg uncertainty relation, $\Delta x \Delta p \geq \hbar/2$, it is evident that for an object subject to ever increasing pressure, the uncertainty in the electrons position becomes smaller and so the uncertainty in momentum becomes larger. Therefore, regardless of the thermodynamic temperature of the system, the electrons must have a finite momentum contributing to the pressure. If the electron degeneracy pressure is able to balance gravity a white dwarf star is formed. White dwarfs typically have a mass $\sim 0.5 - 1.0M_{\odot}$, a radius $\sim 0.008 - 0.02R_{\odot}$ and a core density $\sim 10^{11}$ kgm^{-3} [4; 5].

Low-mass stars $\sim 0.5 - 0.8M_{\odot}$ cannot burn elements heavier than helium, resulting in a carbon-oxygen rich white dwarf. Stellar masses of order $\sim 8M_{\odot}$ to $\sim 60 - 100M_{\odot}$ can fuse carbon producing oxygen, neon and magnesium. Stars with $\sim 9 - 10M_{\odot}$ are able to fuse these resulting elements, producing silicon, sulphur, calcium and argon. These elements can continue to fuse forming iron and its associated isotopes. At this stage the stellar interior has an 'onion-skin' structure where the iron or oxygen-neon-magnesium rich core

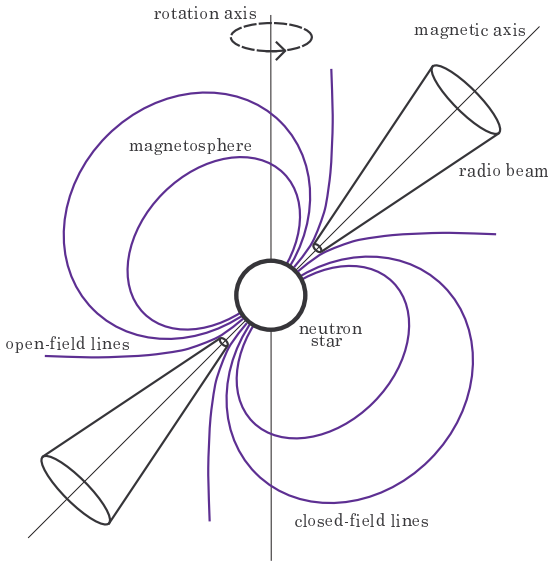

Figure 1.2: Diagram illustrating the currently accepted pulsar model. Pulsars are rapidly rotating neutron stars characterised by ultra strong magnetic fields, $B \sim 10^8 - 10^{11}$ T, and broadband, periodic, pulsed electromagnetic emission. The observed pulses are the result of directional beams, that originate from the magnetic polar caps, rotating like a lighthouse beacon. The light cylinder defines a surface around a pulsar where a point in strict corotation would move at the speed of light. Magnetic field lines that close within the light cylinder are called closed-field lines and those who do not are termed open-field lines.

is surrounded by concentric shells composed of successively lower atomic number, exempli gratia Fe→Si→O→He→H. This of course is a simplification, in reality these shells are composed of a mixture of elements and isotopes [5].

If the mass of the progenitor star is $\sim 8M_\odot$ to $\sim 60 - 100M_\odot$, or equivalently the mass of the white dwarf is greater than the Chandrasekhar Mass $\mathcal{M}_{ch} \sim 1.4M_\odot$, electron degeneracy pressure cannot stop the gravitational collapse. As the star collapses further, the Fermi energy of the electron's increases until it is energetically favourable for them to combine with protons producing neutrons and electron neutrinos via inverse beta decay, $p^+ + e^- \rightarrow n^0 + \nu_e$. If the neutron degeneracy pressure is able to counteract the gravitational collapse of the core a neutron star is formed. Neutron stars have a mass $\sim 10^{30}$ kg or $\sim 1.5M_\odot$ confined within a radius 10^4 m or $\sim 10^{-5}R_\odot$ and a core density $\sim 10^{17}$ kgm^{-3}. The Tolman-Oppenheimer-Volkoff upper mass limit, $\mathcal{M}_{tov}$, is the largest neutron star mass obtainable. Stellar objects with a mass $> \mathcal{M}_{tov}$ collapse indefinitely and are doomed to evolve into Black Holes [4; 5].

As the collapse is halted by degeneracy pressure the core rebounds, generating a massive shock wave. The core of the star implodes in spectacular fashion, collapsing at velocities $\sim 0.25c$ and achieving phenomenal densities [5]. The shock propagates radially outward through the infalling inner-mantle layers of the progenitor star. At this stage the outer-mantle layers of the star are oblivious to the surprise boiling below.

The violent collapse of the star releases a mammoth amount of energy $\sim 10^{46}$ J. Roughly 1% of the energy budget is partitioned into the kinetic energy of the resulting supernova ejecta; 1% manifests itself as electromagnetic radiation, with 0.01% being emitted in the visible spectrum [4]. The majority of the energy is transmitted as neutrinos, formed from the dissipation of the stars thermal energy. The densities and temperatures reached during the core collapse create an abundance of neutrino-antineutrino pairs of all flavours. The shock propagates radially outward through the infalling inner-mantle layers of the star disassociating the heavy nuclei into its constituent nucleons. Due to these dissipative processes the shock stalls after $\sim 10 - 20$ ms at a radius $\sim 100 - 200$ km.

Although the precise physical mechanism of a Type II supernovae is unknown, it is speculated that the neutrinos are the main protagonists in reviving the wilting shock. Upon creation the neutrinos are trapped within the collapsed star and must diffuse through the interior to escape. The effective cross-sectional area for neutrino-baryon collisions is $\sigma \approx 10^{-44}$ m^{-2}, which translates to a mean free path $l = (\sigma n)^{-1} \approx 0.1$ m, where the baryon number density, n, is taken to be comparable to the density of the neutron star [4]. For a typical neutron star radius $\sim 10^4$ m, this implies approximately 10^5 collisions occur per neutrino as it travels from the centre of the compact object to its surface. The escaping flux of neutrinos heats the material within the stalled shock reviving it, igniting a colossal supernovae explosion[5].

The outer-mantle layers of the progenitor star are driven out by the supernova explosion and are ejected at $\sim 10^4$ km s^{-1} into the interstellar medium. This expanding shell of stellar material forms a supernova remnant, populating the interstellar environment with heavy elements. Temperatures in the remnant can become significant that fusion processes can synthesize the existing elements into heavier nuclei. Large quantities of radioactive isotopes such as ^{56}Ni, ^{57}Ni and ^{41}Ti are formed in this way. As a result the remnant is composed of a hot multi-species, electron-ion plasma the composition of which is dependent upon the elemental composition of the stellar atmosphere that went before it. The remnant gradually cools and slowly diffuses into the surrounding interstellar medium. Fig. 1.3 illustrates the

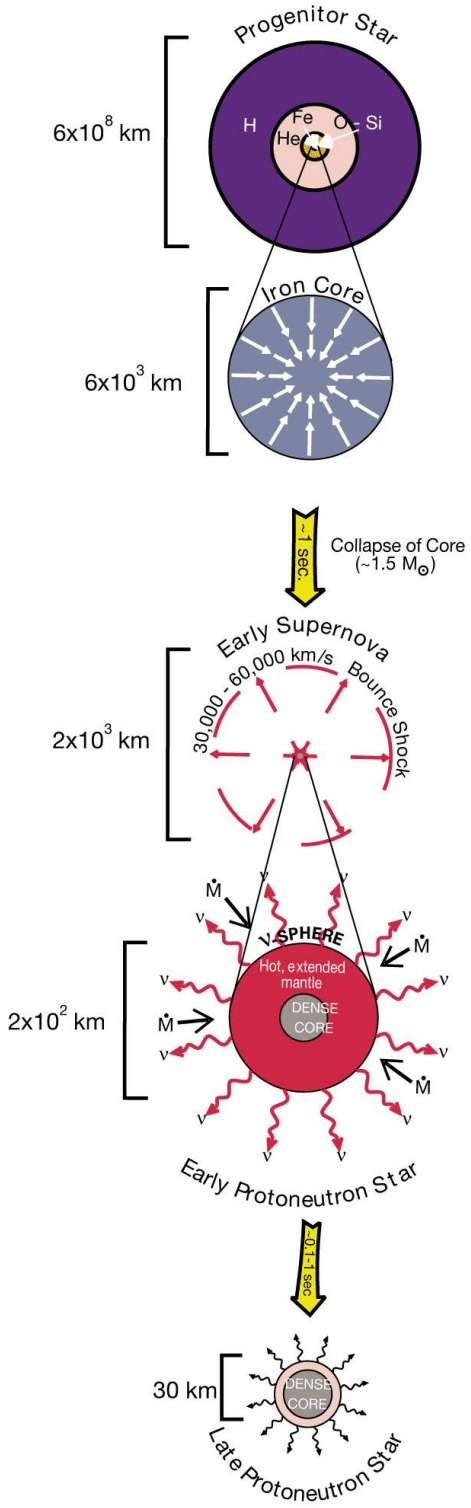

Figure 1.3: Diagram shows the main stages of evolution in the gravitational collapse of a stellar core once all the its hydrogen has been depleted. Reprinted by permission from Macmillan Publishers Ltd: Nature (http://www.nature.com) [5], copyright 2006.

main stages in the gravitational collapse of a stellar core [5].

The origin of the pulsars rapid rotation and the ultra strong magnetic field permeating its structure is inherently related to the gravitational collapse of the progenitor star. Most main sequence stars are observed to possess a magnetic field, presumably generated by the motion of conducting material in its interior, exempli gratia $B_{\odot} \sim 10^{-2}$ T. With the death of the star and the onset of its gravitational collapse, the evolution of the magnetic field relies solely on the conservation of magnetic flux. Therefore, if the progenitor star has a radius 10^9 m and a surface magnetic flux density $B \sim 10^2$ T, the newborn neutron star of radius 10^4 m would possess a surface magnetic flux density $\sim 10^8$ T.

The rapid rotation of the pulsar results from the conservation of angular momentum during the collapse. A star with an initial period comparable to that of the Sun ($P_{\odot} \sim$ 27 days $\sim 10^6$ secs) becomes approximately 0.1 secs. The maximum theoretical spin rate of any object held together by gravity, such as a neutron star, before centrifugal break-up is ~ 0.1 ms [6]. In the rotating neutron star model the magnetic field is misaligned with the rotation axis, resulting in the release of the pulsars rotational energy through the induced electromagnetic radiation due to rotation. The generated low frequency electromagnetic wave is the primary cause of energy loss from the rotating neutron star - note that this electromagnetic radiation is not the observed radio signals. The loss of rotational kinetic energy yields a slowdown in pulsar rotation hence an increase in the pulse period. Typically for normal pulsars the rate of change of the period, $\dot{P}$, is of the order $\sim 10^{-15}$s/s [7]. It is expected that young, newly born pulsars have rapid rotation with short pulse periods that increase with time as the pulsar ages [8; 9].

In 1974 across the gulf of space, as the heavens were being watched keenly and closely for more pulsars, the first pulsar with a binary companion was discovered. Initially believed to be a single pulsar, periodic variations in the observed pulsation period were attributed to Doppler shifts resulting from the orbital motion of the pulsar around an unseen neutron star. Discovered by Joseph Taylor and Russell Hulse at the Arecibo Observatory, it opened an observational window on the gravitational interactions between two compact objects [10]. The existence of the binary pulsar raised new pertinent questions regarding the origin and evolution of pulsars, suggesting that only half of the story had been revealed. This was further amplified with the discovery of a millisecond pulsar, with a period of 1.558 ms, in 1982 and the discovery of a double pulsar binary system in 2004 [11]. The lack of any supernova debris and no observable rapid period decay via gravitational radiation, imply that despite its large rotational energy millisecond pulsars are not young [12].

It is suspected that millisecond pulsars originate from binary pulsar systems. Consider an initial binary system consisting of a primary and a less massive secondary star, Fig. 1.4. The primary star will evolve off the main sequence first, forming a neutron star and possibly a pulsar as previously described. If the supernova explosion disrupts the binary system, a solitary young pulsar and a runaway main sequence star are produced. In both scenarios the pulsars energy output will diminish with time. If the secondary star in a surviving binary system is massive enough to evolve into its giant phase, its outer layers will expand and may cross its Roche lobe resulting in mass transfer with the pulsar via a keplerian accretion disk. This mass transfer will increase the angular momentum of the pulsar, increasing its rotation rate at the expense of the orbital angular momentum of the binary system. The pulsar is resurrected and is termed as recycled. The infall of matter from the accretion disk to the pulsar emits energy in the X-ray waveband, the system is an X-ray binary system. In low-mass X-ray binaries, the pulsar will accrete matter from

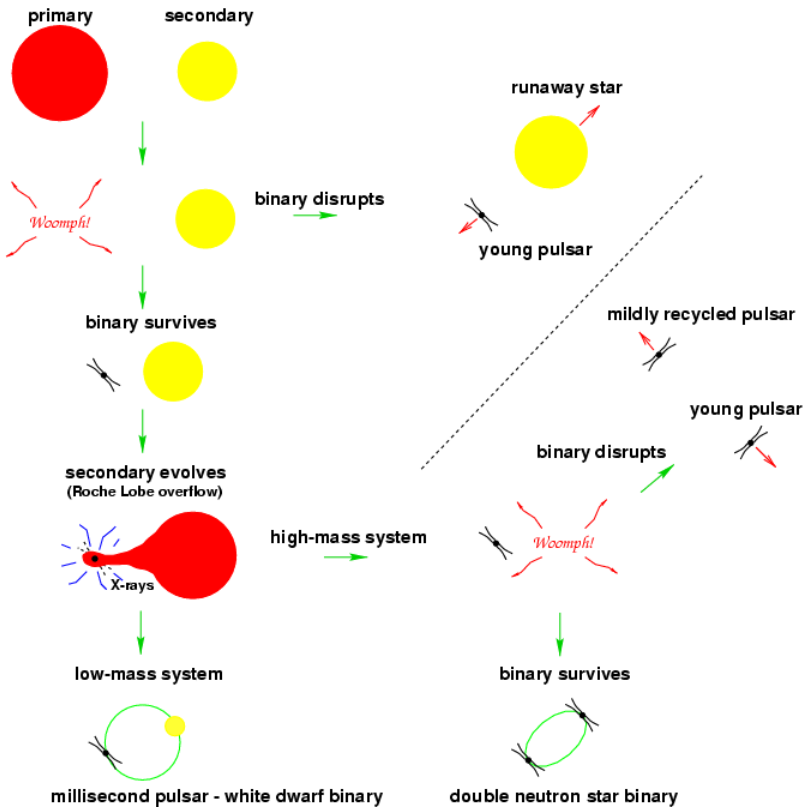

Figure 1.4: Depiction of the evolutionary scenarios from a binary star system to the formation of binary pulsar systems and millisecond pulsars. If the system survives the evolution of the primary star into a pulsar a binary pulsar system is formed, otherwise a solitary pulsar results. For those systems that remain bounded the secondary star may evolve into its giant phase allowing mass transfer with the pulsar. Due to the exchange of angular momentum the pulsars rotation rate increases. In the case of a low-mass binary, the pulsar is spun up to millisecond periods and its companion evolves into a white dwarf. In the case of a high-mass binary, the secondary star is of sufficient mass to form a second neutron star or pulsar. A double pulsar binary system is formed if the system is not disrupted [14].

its companion spinning it up to periods of the order of a millisecond. The companion star subsequently sheds its outer layers forming a white dwarf in a binary system with a millisecond pulsar. In high-mass X-ray binaries, the companion star is of sufficient mass that it can form a second neutron star via a Type II supernovae. In this eventuality if the binary system is not disrupted a double neutron star, or pulsar, binary system is born. If the system is disrupted a solitary young pulsar and a solitary mildly recycled pulsar are born. 'Mildly' implying that not enough mass was accreted to increase its angular momentum significantly to give a considerably small rotation period [13; 14].

Observational Properties of Pulsars

Approximately $\sim$ 1700 radio pulsars have been discovered so far, with this number increasing all the time [14]. The most rapidly rotating pulsar observed has a pulse pe-

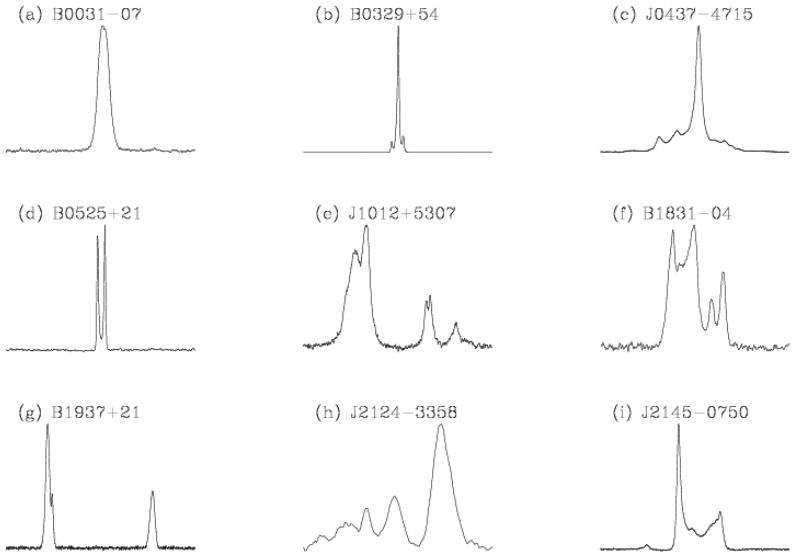

Figure 1.5: Collection of integrated pulsar profiles from a range of pulsars. Each profile is a plot of intensity versus time representing 360° of rotational phase (also known as the pulse longitude). Pulse (a) displays a stereotypical gaussian shape profile; (b)-(i) exhibit sub-pulses that compose the general profile shape; (g) shows an example of an interpulse.[14]

riod 1.39 ms [15] which is approximately 10^3 orders of magnitude faster than the longest recorded pulse period of 8.5 s [16]. Pulsars are observed as very weak radio sources, so weak in fact that individual pulses can be lost amongst spurious background noise upon detection - observed flux densities are typically of the order $\sim 1\mu$Jy -1 Jy [7]. For the majority of pulsars observed above 100 MHz, the average flux density spectra can be approximated by a simple power-law where $S(\nu) \propto \nu^{\alpha}$ where ν is the observing frequency and α is the spectral index such that $0 \gtrsim \alpha \gtrsim -4$. The spectral behaviour of some pulsars are described better by a two-component power law but in general all pulsars, including millisecond pulsars, appear to exhibit similar power-law spectra [7; 17].

Due to the weak nature of the observed radiation, integrated pulse profiles are generated from the coherent superposition of hundreds or thousands of individual pulses, Fig. 1.5. These profiles characterise the geometry of the beamed emission. The angular extent of the profiles is typically $\sim 20°$ of the pulse longitude, in some cases the profile can extend to 360°. A variety of complex structure is observed in the profiles such as the Gaussian shaped sub-pulses that compose the overall integrated pulse profile. Some integrated pulse profiles contain secondary pulses separated from the main pulse by about 180° - these are interpulses. If the main pulse is attributed to beamed radiation from the magnetic pole of the pulsar, the interpulse is explained in terms of radiation emitted from the opposite pole [7]. The individual and integrated pulses are generally strongly polarised. The emission is predominately linearly polarised but there can be a considerable component of circularly polarised radiation. It is not always clear if the complex polarisation signatures are an effect inherent in the emission mechanism or from the propagation of the radiation through the magnetosphere. These polarisation characteristics appear to be fairly invariant over the whole range of observed periods and radio-frequencies [17; 18].

The observed individual pulses constituting the integrated pulse profile exhibit a rich and complex structure observable on a range of timescales from microseconds, known as

microstructure, to even nanoseconds. This implies that the plasma structures responsible for the radiation must be smaller than one metre in size [19]. Giant pulses are short timescale sporadic outbursts that have flux densities exceeding 1000 times that of an individual pulse. Giant pulses for the Crab pulsar have been observed to occur on micro- and nano-timescales, with brightness temperatures[1] $T_B \geq 5 \times 10^{37}$ K and are detected over a wide radio frequency range [19]. Only 11 pulsars are observed to share this phenomena [20].

Individual pulses are generally composed of multiple sub-pulses, that appear to drift across the main pulse window at a fixed rate [21]. If the pulse period is P_1, P_2 is the spacing between sub-pulses within a single pulse and P_3 is the drift periodicity, the drift rate is P_2/P_3. A number of different drift modes can be present simultaneously in a single pulsar with characteristic drift rates. Typically observed drift rates are roughly a few degrees of pulse longitude per pulse period - a drift mode would therefore complete a full drift period of a 10° pulse profile in $\sim 10P_1$. Sub-pulses are a broadband phenomena and are interpreted to be beams of radiation from discrete plasma sources within the main beam of radiation itself [18].

Pulse nulling occurs when emission from a pulsar abruptly and randomly stops or 'switches off' for a number of pulse periods [22]. Typically nulls occur for two or three pulses in succession separated by intervals of order 100 pulses [22]. The time duration of the nulls is different depending on the pulsar being observed and can be quite long, lasting for intervals from minutes to hours with some pulsars emission being dominated by nulling. Nulling occurs simultaneously at all radio-frequencies and can be interpreted as the pulsar emission mechanism switching on and off. Interestingly this phenomena is absent in millisecond pulsars and it has been suggested that nulling is the pulsar emission mechanism wavering as it grows old. [7] An associated phenomena is mode changing and occurs when the pulsar emission mechanism appears to switch between two or more modes of emission, manifesting itself as two distinct integrated pulse profiles [23]. The pulsar is assumed to favour one state (the normal mode) prevailing most of the time and then abruptly changes to a second state (the abnormal mode) the remainder of the time. If drifting sub-pulses are present, their drift rate can be observed to change during the mode transition [7].

In recent years, due to new advances in observing techniques, new breeds of pulsars exhibiting unusual emission properties have been discovered. Periodically active pulsars appear to be normal radio pulsars on timescales of about $5-10$ days, but then switch off in less than 10 seconds being undetectable for $25-35$ days. The pulsars emission mechanism appears to quasi-periodically switch off! Intriguingly the pulsar rotation period slows down much faster when it is on. The origin of such behaviour is unclear and it seems plausible to assume that it is related to a global failure of charged particle currents in the pulsar magnetosphere. [24] Rotating Radio Transients, or RRATs, are another population of pulsars that are similar in nature to periodically active pulsars. RRATs are characterised by single, solitary bursts of radio emission sustained for timescales of $2-30$ ms and are separated by time intervals of 4 minutes to 3 hours. RRATs have observed pulse periods of $0.4-7$ seconds and flux densities of about $0.1-3.6$ Jy, making them very bright radio sources [25].

[1] Brightness temperature is the temperature at which a blackbody emitter would have to be at to duplicate the observed intensity at a specific frequency.

Pulsar radio emission mechanisms

After forty years of study the pulsar emission mechanism still eludes researchers; the theory of pulsar radiation is still in its infancy and there is lack of understanding about the energetic processes involved. The recent observations of Rotating Radio Transients [25], periodically active pulsars [24] and pulsar binary systems [11] show there is a wealth of emission phenomena. A theory of pulsars must explain all observed phenomena: the periodic, radiation and beaming mechanisms. The periodic mechanism is widely accepted to be provided by the rotating neutron star model. To this date there is still no widely accepted consensus on the radiation and beaming mechanisms.

The key to understanding the complex emission mechanism is an explicit understanding of the pulsar magnetosphere. Consider the pulsar as a conducting sphere that, when non-rotating, has a dipolar magnetic field. As a result of rotation each free charge in the stellar interior experiences the force $q(\mathbf{\Omega} \times \mathbf{r}) \times \mathbf{B}/c$, where $\mathbf{\Omega}$ is the angular velocity of the pulsar. In response the charge within the pulsar redistributes itself, establishing an electric field in order to gain equilibrium and a force free system. The induced surface charges on the stellar surface constitute an external electric field which, at the surface of the pulsar exceeds that of gravity resulting in copious amounts of electrons being stripped from the pulsar and occupying the magnetosphere. It is assumed that the liberated charged particles are accelerated in the external electric field, emitting photons as they go. If the photons acquire the appropriate energy and interact with the magnetic field they produce an electron-positron pair. These produced pairs go on to produce more pairs and a cascade effect is initiated that populates the magnetosphere with a pair plasma. This plasma redistributes itself in order to produce a force-free scenario and experience the same $\mathbf{E} \times \mathbf{B}$ as in the interior of the pulsar, forcing the pair plasma to co-rotate with the pulsar. Co-rotation can only be sustained up to a certain radius from the star where the plasma speed reaches the speed of light, this defines an imaginary boundary known as the light cylinder. The light cylinder defines closed-field lines and open-field lines as the magnetic field lines that close and don't close within the light cylinder respectively. The open field lines define a region above the magnetic poles known as the polar cap, Fig. 1.2. The pair plasma that resides within the magnetosphere is the source of the broadband electromagnetic radiation observed from the pulsar [7; 26].

The distinguishing feature between incoherent and coherent emission mechanisms is the brightness temperature of the source. For incoherent emission, where the particles comprising the source emit out of phase with each other, the brightness temperature is $T_B \lesssim 10^{12}$ K. For a pulsar with a flux density ~ 1 Jy, at a distance of 1 kpc and size of 10 km, the brightness temperature is $\sim 10^{30}$ K. The very high brightness temperatures, $T_B \sim 10^{25} - 10^{30}$ K, of pulsar radio emission implies that a coherent emission mechanism must be at work, that is, a large number of particles emitting in phase [27].

The mechanism, as well as successfully describing the observed brightness temperatures, must also satisfactorily encompass the high degree of polarisation and the broadband nature of the emission. Existing candidates for the pulsar coherent emission mechanism are referred to as antenna mechanisms, relativistic plasma emission and maser mechanisms.

Antenna mechanisms involve the emission of radiation by a population of particles, all radiating in phase. A family of N particles, each of charge q, that are confined to a volume of dimension less than the emitted wavelength, will act like a particle of charge Nq and all radiate in phase. As a result the radiated power of the source will be greater than that

from an individually emitting particle by a factor N^2. The favoured antenna mechanism in the pulsar context is curvature emission, despite it being a relatively inefficient emission process. Curvature radiation is the radiation emitted by a charge particle when it moves along a curved magnetic field line. If the magnetic field is sufficiently strong the particle will be unable to move perpendicular to the field, as a result if the magnetic field line curves the particle will be accelerated and hence radiate electromagnetically. Curvature radiation is insensitive to the mass and charge of the particle and radiates at a specific frequency. It is regarded as a natural and unavoidable emission process in pulsar magnetospheres [7] [27].

Komesaroff was one of the first to discuss the concept of curvature radiation in the context of pulsar emission. He built a pulsar emission model assuming that groups of charged particles are accelerated along the open field lines at the magnetic pole, radiating by the curvature mechanism [28]. The main issue with coherent curvature radiation is finding a reasonable mechanism that creates and sustains the required particle bunches for the timescale required [7]. Particle bunching can occur in the magnetosphere if a two-stream instability is present, propagating along a curved field line [29]. The unstable electrostatic oscillations bunch the plasma particles together, yielding a source of coherent emission [30]. Additionally, the presence of charged solitons in electron-ion plasmas [31] hints at the possibility of such a feature being sustainable in magnetospheric pair or pair-ion plasma, yielding a suitable bunching mechanism [32]. However it is argued that the radiation back-reaction tends to disperse the particle bunch that created it acting against the coherent process [27].

Relativistic plasma emission is the generation of electromagnetic radiation near the local plasma frequency or its harmonics. It operates in two distinct phases: the generation of Langmuir waves, or Alfvén-type waves, through some form of plasma instability (generally a streaming instability); a nonlinear process that converts the wave energy into a desirable propagating electromagnetic mode that escapes the pulsar magnetosphere. A Langmuir wave is a propagating electrostatic plasma oscillation: these waves cannot escape the plasma region since they are not electromagnetic in nature and require a plasma to sustain them. To produce escaping radiation a process must exist that converts the mode into a propagating electromagnetic Ordinary or Extraordinary mode [27].

Within the pulsar context a pair plasma above the polar caps is considered to be relativistic and streaming. The plasma particles are assumed to radiate all their energy perpendicular to the ambient magnetic field so that the plasma is one-dimensional. This type of plasma is referred to as a pulsar plasma. At high frequencies two modes are present that are analogous to the ordinary (O) and extraordinary (X) modes in magnetoionic theory. In the low frequency regime ($\omega < \omega_c$) the parallel propagating wave modes are analogous to the transverse Alfvén and the Langmuir modes. The dispersion curves describing these two modes intersect at what is referred to as the cross-over frequency. The significance of this cross-over is clear when considering oblique propagation with respect to the ambient magnetic field - the two modes reconnect and the Langmuir mode evolves into the O-mode to form the Langmuir-Ordinary (L-O) mode. Escaping radiation must be in one of the high frequency modes: the X, O or L-O mode. If the resonant condition for the beam instability coincides with this cross-over point energy from the Langmuir mode can be partially partitioned into the L-O mode. This is linear wave conversion, for instance the unstable evolution of a two-stream instability in the linear regime can induce an electric field perpendicular to the ambient magnetic field, perturbing an escaping transverse Alfvén wave [33]. Alternatively nonlinear processes could be utilised [34].

No consensus has been reached as to the favoured nonlinear process that produce an escapable mode. Relevant processes include three-wave interactions, scattering processes, parametric and modulational instabilities [35]. The induced scattering of Langmuir waves by the electrons and positrons constituting the main plasma flow can transfer energy from the Langmuir mode to an escapable transverse electromagnetic mode [36].

Maser emission mechanisms involve negative absorption. A maser is a low frequency equivalent of the Laser and operates under the same principles. In a bound-state system, such as an atom, stimulated emission occurs when an incident photon encounters an excited atom forcing it to emit another photon with the same frequency, direction of propagation, phase and polarisation as the incident photon. In a plasma, maser emission can occur under a variety of conditions where there are a continuum of states. The particle distribution, $f(\gamma)$, in the plasma must have an inverted population for the process to be a maser - this condition is $\partial f/\partial\gamma > 0$. A number of maser mechanisms have been proposed such as maser curvature emission, free electron maser emission and curvature-drift instability driven emission [27].

Maser curvature emission is founded upon the curvature drift experienced by charged particles in a curved magnetic field configuration [37]. The combined acceleration of a distribution of particles undergoing this process produces an electromagnetic signal. The Free electron maser emission is a form of linear acceleration emission where an electric field parallel to the ambient magnetic field accelerates charge particles allowing them to radiate electromagnetic emission. However this emission requires that the parallel electric field varies in space and time. The outstanding issue with this mechanism is how the accelerating electric field is generated [27].

Cosmic dust

Dust is ubiquitous in the universe. The growth of dust grains precedes that of stellar, planetary, cometary and asteroid formation. It exists in a variety of environments such as young protoplanetary disks, the outflow of red giant stars, the atmospheres of asymptotic giant branch stars, nova ejecta [38; 39], circumstellar envelopes, brown dwarf atmospheres and circumstellar dust shells of luminous post-main sequence stars where the temperature can be low enough ($T \sim 10^2$ K) to allow the growth of dust seeds via nucleation and condensation [40]. These astrophysical environments act as dust factories populating the interstellar medium with dust composed of silicates, carbonaceous material, silicon carbide (SiC) and carbonates [41]. See Fig. 1.6 for images of interstellar dust grains.

Supernova remnants are potentially a major source of interstellar dust in the Universe [43; 42]. The high abundance of heavy elements and the high density of the remnant appear to make the environment favourable for dust formation via various chemical and physical mechanisms. Recent observations of Cassiopeia A have revealed that the excess sub-millimetre radiation of the remnant can be explained by the large radiative efficiency of conducting metallic dust needles. With an expected total mass of 10^{-4} to $10^{-3} M_{\odot}$, the presence of the needles opens a further diagnostic window on the environment via polarimetric studies of the polarization from the dust [44].

The existence of dust in supernova remnants and interstellar space affects the propagation of electromagnetic radiation in terms of extinction and scattering, this is evident

Figure 1.6: Images of dust grains found in meteorites. The top dust grain is composed of silicon carbide (SiC) and the bottom is composed of graphite. Images obtained using scanning electron microscopy.[42]

from the average interstellar extinction curve [41]. Davis and Greenstein [45] first proposed that the observed polarization of electromagnetic radiation from stars was the result of anisotropic extinction by aligned spheroidal grains in the interstellar medium. These grains collectively align themselves with the background galactic magnetic field via paramagnetic relaxation of the thermally rotating grains. However this mechanism assumes an abundance of paramagnetic material that is too large compared to the actual interstellar abundance. Grain alignment via a diamagnetic process removes this limitation [46]. Alternatively if you have a non-axisymmetric rotating charged grain in a magnetic field a magnetically induced torque realigns the grain [47].

Within the context of a pulsar at the centre of a dust laden supernova remnant the electromagnetic emission from the pulsar must traverse through a dusty plasma. Depending on the shape, size and composition of the grains grown in the remnant, the radiation will be absorbed and preferentially polarised altering the characteristics of the electromagnetic radiation. The true interpretation and nature of the pulsar radiation field can only be made if the effect of the dust is explicitly known. This can be done if the nature of the dust and the processes involved in its formation and growth are well understood. The most pertinent aspect of dust is its formation and growth, it precedes all subsequent studies and explicit knowledge of the mechanisms and processes involved in dust growth is paramount in a holistic understanding. With such information polarimetric studies of the radiation could infer properties of the environment in which the pulsar resides opening a useful diagnostic window. The effects of spheroidal dust grains on electromagnetic radiation is an active field of study. Most modelling operates using the Discrete Dipole Approximation (DDA) method, where the dust is modelled to be composed of an array of small polarisable elements that mimic the dielectric properties of a specifically composed and shaped grain [48]. The resulting polarisation, extinction and scattering of silicate and graphite [49], porous [50] and composite grains [51; 52; 53] has been studied in an attempt to reproduce the interstellar extinction curve. This has raised many questions about suitable dust forming mechanisms that produce the observed quantities of dust.

The modelling of dust growth in this environment predominately follows that of nucle-

ation and accretion in the gas. Todini and Ferrara consider the nucleation of dust grains in ejecta formed from heavy elements in the helium remains of the progenitor star [54]. Their calculations focus on the formation of the solid compounds Al_2O_3, Fe_3O_4, $MgSiO_3$, Mg_2Si_4 and amorphous carbon. Deneault [55] recently suggested a kinetic model for the growth of carbon grains in the ejecta. They suggest that in a cooling, expanding supernova shell, oxygen and carbon rich regions are the most probable for dust formation. The radioactive decay of certain radioactive elements, such as ^{56}Co, can suppress the creation of CO molecules encouraging C to condense into solids. A kinetic chemistry model is proposed, including the relevant reaction pathways to produce linear chains of atoms subsequently growing to larger grains via isomerisation.

Supernova events are associated with the creation of a series of shocks that propagate through the ejecta. Recent investigations have tried to ascertain the balance of dust creation and destruction in the ejecta related to the presence of reverse shocks [56; 57]. By considering the dynamics of a dust test particle, and its destruction via sputtering and collisions, it is expected that grains with a length scale $\lesssim 0.05\mu$m are destroyed by sputtering in the post-shock flow while those $\sim 0.05 - 0.2\mu$m are trapped in the shock. Larger grains are injected into the interstellar medium [57]. The fraction of dust that survives the passage of the shock ranges between $2\% - 20\%$, which is dependent on the density of the interstellar medium [56]. These models assume that the ejecta is in the gas phase, this may not always be the case since the material could be fully or partially ionised.

Dust growth in plasmas

Dust, in its many facets, has become synonymous with plasma physics and has forged a vibrant field - dusty (complex) plasmas. Dust appears in many disparate contexts within plasma physics such as in laboratory processing plasmas, fusion plasmas and in astrophysical plasmas. Typical values for the electron number density and temperature in processing plasmas, tokamaks and interstellar molecular clouds are: $n_e \sim 10^{15}$ m^{-3}, $T_e \sim 2$ eV; $n_e \sim 10^{20}$ m^{-3}, $T_e \sim 10^4$ eV; and $n_e \sim 10^3$ m^{-3}, $T_e \sim 10^{-3}$ eV respectively [58]. Despite the contrast in the spatial and temporal scales between these diverse contexts, there exists a strong correspondence in the fundamental physical processes involved.

The majority of what is known about the formation of dust is based on laboratory experiments involving the growth of dust in silane (SiH_4), hydrocarbon or noble gas diluted silane reactive plasmas, where Argon and Helium are predominately used. The original emphasis of these investigations pivoted around the removal of undesirable dust grown in processing plasmas. Dust growth in reactive plasmas is initiated by species dependent chemical processes. Explicit knowledge and understanding of the processes leading to dust growth in most plasmas is unknown. In some, such as in capacitive high frequency silane plasmas dust formation has been well studied. Note that the SiH_4 molecule has a similar structure to that of GeH_4 and CH_4 and hence many chemical reactions are similar [59]. It has been argued that dust growth in these laboratory plasmas occurs in four distinct phases: proto-particle formation via plasma chemistry; subsequent growth via homogeneous and heterogeneous nucleation up to a critical dust density, n_{crit}; a rapid agglomeration (coagulation and flocculation) phase; and then a steady growth phase via plasma deposition processes resulting in macroparticles ~ 10 nm [60]. Although stipulated within the context of laboratory based silane plasmas it is expected to be largely invariant with the fine details, such as specific chemical reactions, being variant.

In low-pressure plasmas, experimental investigations on the formation and behaviour of dust have been dominated by the research groups led by Y. Watanabe at the Kyushu Electric College, Japan; Ch. Hollenstein at the Centre de Recherches en Physique des Plasmas, Switzerland; and A. Bouchoule at the Laboratorie GREMI, France [59]. Apart from minor discrepancies regarding the size and density of the dust in the discharges experimental results generally agree. The experiments by those implicated have been conducted using capacitive high frequency, silane discharges, with electrode diameters ranging from $10-13$ cm; electrode spacing $\sim 2.2-4.2$ cm; operated at frequencies between $\sim 6.5-30$ MHz; at pressures of the order ~ 10 Pa with the bulk gas flow of the order $\sim 0.1-10$ sccm, where the flow can be parallel and perpendicular to the electrodes [59].

In these experiments the dust grown has a size of the order $d \geq 10$ nm ($n_p \sim 10^9$ cm^{-3}) composed of two particle populations: a small group that remains constant in size, $d \sim 10$ nm, during the discharge (SS group) and a large sized group (LS) that grows with time. The dust then appears to grow through three distinct phases namely: the initial growth phase (IG), the rapid growth phase (RG) and the growth saturation phase (GS). The LS component grows through the RG phase through the coagulation of the SS component of dust. Particle growth via coagulation in the RG phase is dependent upon a number of factors including the source gas flow, the excitation frequency of the discharge and the supplied high frequency power. Periodic growth of dust following the GS phase has been observed where the dust reaches a certain size and is lost from the plasma allowing smaller particulates to grow in their place [59].

Proto-particle formation

Much is known about the growth of micrometre sized grains but comparatively little is known about the precursor dust they originate from. The main physical processes in the production of proto-dust in reactive plasmas is via homogeneous and heterogeneous nucleation. Nucleation dominates up to a critical dust number density, n_{crit}, where subsequent rapid growth by agglomeration results in macroparticles of scale ~ 10 nm. The agglomeration phase is restricted by the dust acquiring a net charge, after which accretion then becomes the dominant process forging dust grains in the micrometre size range [61].

To model these growth processes in a low-pressure silane plasma, never mind an arbitrary plasma, is a formidable task thanks to the countless number of possible chemical reactions and participating species involved. Proto-nanoparticle formation, via an initial nucleation phase, can be modelled via fluid and kinetic models where the plasma can be described by a combination of balance or rate equations and Poisson's equation describing the ions, neutrals, electrons and the electric field in the plasma [62; 63; 64]. Such modelling by De Bleecker [63] incorporates 11 possible reactions, 66 species containing up to 12 silicon atoms each, implying that the production of SiH_3^- forms the foundation for anion and hence dust formation via the silyl anion pathway ($Si_nH_{2n+1}^-$). This type of modelling is also useful in its application to other species of plasma and is not necessarily restricted to the study of processing silane plasmas. The formation of carbonaceous dust in hydrocarbon plasmas is also of interest in the astrophysical context and that of fusion plasma devices. Within this framework it is found that positive and negative ions starting from $C_2H_2^+$ and C_2H^- could be the main precursor to particulate formation [65]. Such modelling techniques can also be used to reveal a great deal about dust growth in plasmas beyond nanoparticle formation via agglomeration, describing the sub-millimetre particles $\sim 10-100$ nm and

their influence on the plasma [66].

In other types of plasma growth mechanisms are not well known, it is speculated that generally homogeneous nucleation dominates but heterogeneous processes could still be significant. It is hard to determine experimentally if homogeneous or heterogeneous processes dominate in the formation of dust precursors. In unreactive plasmas it is suspected that heterogeneous growth dominates and is characterised by a greater distribution of grain sizes. Silicon nitride particulate formation in SiH_4/NH_3 RF plasmas occurs via ion-molecule reactions resulting in mantle growth [61].

Post proto-particle formation

After the initial phase of proto-dust growth up to n_{crit}, agglomeration becomes the dominant mechanism. Modelling of neutral agglomeration provides reasonably good agreement with experiments but deviations occur due to the particles acquiring a significant net charge. If the dust density exceeds that of the negative ion density the charging on the dust becomes significant to counteract agglomeration [61]. The rapid growth of dust via agglomeration as modelled by Kim and Kim incorporates the influence of particulate charging, nucleation and transport [67]. After the agglomeration phase the resulting particle size 10 nm -1μm that are predominately negatively charged [61].

Watanabe [59] have proposed a model of particle growth that explains the experimental results to date for the RG and GS phases. The model assumes that during the RG phase the dust grows from $\sim 1-10$ nm and is predominately electrically neutral with a small population harboring a small net positive or negative charge. Neutral particles in the vicinity of the plasma sheath become ionised due to collisions from high energy electrons accelerated in the sheath. This process leaves a population of positively charged particles with a density greater than that of the ions in the bulk plasma. The rapid growth phase then commences with the coagulation of positive and negatively charged particulates $\sim 1-10$ nm. The grown particles acquire a net negative charge from the bulk plasma, accelerating their growth as they can now coagulate more readily with positively charged dust. Dust growth in this way ceases when all the particulates have acquired a negative charge. The plasma has now entered the gas saturation phase where a plasma sheath is now formed around the dust grains and subsequent growth is dominated by deposition of ions, mono-radicals and smaller particulates.

In this latter stage the dust grows by influxes of radicals, molecular clusters and positive ions. The dust particles are of a sufficient size, $\sim$ μm, that they can sustain a net negative charge on their surfaces resulting in the formation of a plasma sheath around the particle. Ions from the bulk plasma are then accelerated into the plasma sheath and ultimately deposited on the surface of the dust grain, forming a thin layer of material. In low-pressure laboratory conditions ultrathin films have been deposited on the surfaces of nanoparticles via plasma polymerisation [68]. Electron microscopy reveals that a thin film ~ 2 nm is uniformly deposited on the particulates surface. Other laboratory experiments with a size distribution of dust seeds reveal that the deposited film thickness is not necessarily uniform over the grain surface and is proportional to the deposition time. Smaller grains tend to yield non-uniform surface deposition producing spheroidal dust [69; 70]. The complex physiochemical phenomena instigated can be explained by complex kinetic models to predict the fluxes of particles at the surface of the dust grain and hence the deposition

rate. This could be achieved in principal for an arbitrary species plasma, such as a silane-hydrogen plasma, given detailed knowledge of the principle reactions involved. For a methane-hydrogen plasma, CH_4/H_2, the deposition rate of amorphous carbon at the dust surface is calculated to be $\sim 0.69 - 1.12$ nm/min, in agreement with what is observed experimentally [71].

Outline of thesis

This thesis is concerned with plasma processes in pulsar environments. So far this introductory chapter has briefly outlined pulsars and their environments, in particular it has drawn attention to the pair plasma magnetosphere, the associated electromagnetic emission and its interaction with the dust grown in the surrounding supernova remnant. The work detailed here extends upon these concepts and is composed of two distinct components: nonlinear mode coupling in pair plasmas and elliptical growth of dust grains in electron-ion plasmas.

Chapter 2 introduces the concept of an electron-positron (pair) plasma, setting the scene for future discussions regarding the proposed mode coupling mechanism. It begins by constructing a mathematical model that describes the pair plasma as a cold two-fluid plasma and its evolution under the influence of electromagnetic fields via Maxwell's equations. Using this set of differential equations the linear wave modes in a homogeneous pair plasma are subsequently derived, giving a flavour of the types of modes that can be sustained by the plasma. Taking a step away from the linear regime the nonlinear evolution of electrostatic plasma oscillations is then discussed, showing the inevitable density instability associated with them. The chapter concludes by looking at the proposed coupling between the plasma oscillation and an electromagnetic mode in the linear regime. In this linear approximation the background magnetic field is inhomogeneous and the equilibrium plasma is uniform. This mode coupling produces a natural and unavoidable source of radiation in the pulsar magnetosphere.

With the basic mathematical groundwork set in place, chapters 3, 4 and 5 focus on the fundamental nature of the mode coupling. This work extends upon the linear consideration by self-consistently dealing with the equilibrium configuration which, due to the inhomogeneous magnetic field, must be non-uniform and dynamical. Chapter 3 details the linear analysis performed to identify the required modes needed for the mode coupling, namely the electrostatic mode and the electromagnetic mode. This linear perturbation analysis also offers guidance on modal stability and provides an insight on what to expect in future numerical simulations.

The ultimate goal is to perform a full nonlinear numerical simulation of the model set of equations describing the mode coupling mechanism. Chapter 4 assesses the appropriate numerical technique that suits the problem best. In chapter 5 the mode coupling is numerically simulated and the nonlinear nature of the interaction is exhibited.

With the successful simulation of the nonlinear mode coupling in the pair plasma, the generated electromagnetic radiation propagates through the magnetosphere and escapes to be ultimately detected by the observer. The radiation must traverse the supernova remnant and the interstellar medium that are both populated with dust. As described previously the presence of dust affects the nature of the electromagnetic radiation and its effect can only be entirely understood if the nature of the dust grown in the remnant

is known. A model of elongated dust growth in an electron-ion plasma is described and numerically verified in chapter 6. This plasma process provides a alternative process for the production of spheroidal dust grains in astrophysical plasmas such as those found in supernova remnants.

Finally, chapter 7 briefly summarises the work in this thesis and suggests potential extensions to the models presented here.

Chapter 2

Pair plasma primer

2.1 Introduction

Pair plasmas are composed of two constituent species both having identical mass and opposite charge: electron-positron plasmas fall into this category. This is in contrast to conventional electron-ion plasmas where the ions are much heavier than the electrons. In wave propagation terms generally only one species dominates the plasma dynamics depending on the frequency regime of interest: electron motion is important at high frequencies and ion motion is significant at low frequencies. If the dynamics of both the electrons and ions is considered one species dominates the response of the plasma and the other contributes secondary effects only.

When dealing with high frequency phenomenon the ions generally constitute an immobile background and the dynamics of the electrons dominates due to their swifter response to imposed electromagnetic fields. In the cold plasma context perturbing the electron charge density induces electrostatic oscillations at the electron plasma frequency. The infinitely massive, static, neutralising ion background regulates the dynamics of the electrons ensuring the evolution of the plasma does not become unstable. Pair plasmas do not possess this regulating ion background so the evolution of electrostatic oscillations is fundamentally different. The equal mobility of the species and the plasmas inherent natural symmetry make the pair plasma dynamics fundamentally nonlinear.

Pair plasmas have gained considerable attention over the recent years due to their existence in a number of astrophysical environments such as pulsar magnetospheres, active galactic nuclei, microquasars and gamma-ray bursters. The various wave modes that exist in a pair plasma when the background is homogeneous has been extensively covered in the cold plasma regime [72]. Generation of magnetic fluctuations by field-aligned flows in plasmas [73] shows a new range of instabilities relevant to strongly flowing constant-density plasmas; further instability studies in homogeneous pair plasmas have been undertaken by Marklund [74], relevant to bursty systems; under certain simplifying conditions, pair-plasma waves can be described by the KdV equation [75]. There are also studies of the plasma electromagnetic wave coupling from actual pair production [76]. Our treatment

will deal with a cold, free-streaming (but not field-aligned) anisotropic and inhomogeneous pair plasma, using the full nonlinear equations.

This chapter is concerned with wave propagation in pair plasmas, setting the mathematical bedrock for the work described in subsequent chapters. It begins by introducing the two-fluid, cold plasma model. Within this mathematical framework, the linear wave modes in a homogeneous pair plasma are described. The chapter concludes by examining the nonlinear evolution of a pair plasma electrostatic oscillation introduces the concept of mode coupling between this mode and an electromagnetic one.

2.2 Electromagnetic wave propagation in plasmas

This section introduces the cold pair plasma model and derives the associated dielectric tensor, revealing the linear wave modes present in a homogeneous pair plasma. The derivations presented here follow that of Stewart 1993 [72].

2.2.1 The effective dielectric tensor

By definition a plasma is a state of matter with a sufficiently high free charge density that its dynamics is dominated by electromagnetic forces. Electromagnetic fields permeating the plasma are determined by the ensemble motion of the charge particles yielding a self-consistent description of the plasma. As the plasma evolves through time imposed electromagnetic fields dictate the motion of the plasma and this consequently determines the resultant electromagnetic fields.

Maxwell's equations describe the temporal and spatial evolution of electromagnetic fields in a medium due to the presence and distribution of electric charge and current. In a general medium, they take the form,

$$\nabla \cdot \mathbf{D} = \rho_f \tag{2.1}$$

$$\nabla \cdot \mathbf{B} = 0 \tag{2.2}$$

$$\nabla \times \mathbf{E} = -\frac{\partial \mathbf{B}}{\partial t} \tag{2.3}$$

$$\nabla \times \mathbf{H} = \mathbf{J}_c + \frac{\partial \mathbf{D}}{\partial t} \tag{2.4}$$

where all quantities are a function of both space and time, $\mathbf{F} = \mathbf{F}(\mathbf{r}, t)$. Eq. (2.1) is Gauss' Law; Eq. (2.2) is Gauss' Law for magnetism; Eq. (2.3) is Faraday's Law of induction; and Eq. (2.4) is the Ampère-Maxwell equation. The symbols take the following meaning:

1. $\mathbf{D}$ is the electric flux density, it characterises the electric field due to the free electric charge density, ρ_f, of the material.

2. $\mathbf{E}$ is the electric field intensity characterising the electric field in a material due to the present free and bound charges, $\rho = \rho_f + \rho_b$. It is related to the electric flux density via the relation $\mathbf{D} = \epsilon_0 \mathbf{E} + \mathbf{P} = \boldsymbol{\epsilon} \cdot \mathbf{E}$, where ϵ_0 is the permittivity of free space; $\mathbf{P}$ is the electric polarisation; and $\boldsymbol{\epsilon}$ is the dielectric permittivity tensor. The polarisation quantifies the effect of applied electric fields in dielectric materials and is related to

the bound charge density, ρ_b. Therefore, the dielectric permittivity tensor describes the response of the medium to electric fields and vice versa.

3. $\mathbf{H}$ is the magnetic field intensity, characterising the magnetic field due the conduction current density, $\mathbf{J}_c$, and the displacement current density, $\partial\mathbf{D}/\partial t$, present in the medium. Time-varying electric fields act as sources of magnetic field represented by the displacement current density.

4. $\mathbf{B}$ is the magnetic flux density. This quantity describes the magnetic field strength in the medium due to the presence of the conduction, displacement and magnetisation current densities, $\mathbf{J} = \mathbf{J}_c + \mathbf{J}_m + \partial\mathbf{D}/\partial t$. $\mathbf{B}$ and $\mathbf{H}$ are related via the relation $\mathbf{B} = \mu_0(\mathbf{H} + \mathbf{M}) = \boldsymbol{\mu} \cdot \mathbf{H}$, where μ_0 is the permeability of free space; $\mathbf{M}$ is the magnetisation; and $\boldsymbol{\mu}$ is the permeability tensor. The magnetisation quantifies the effect of applied magnetic fields in magnetic materials and is related to the fictitious magnetisation current density, $\mathbf{J}_m$.

5. $\mathbf{J}_c$ is the conduction current density. It is related to the electric field intensity, $\mathbf{E}$, via Ohm's Law $\mathbf{J}_c = \boldsymbol{\sigma} \cdot \mathbf{E}$, where $\boldsymbol{\sigma}$ is the conductivity tensor of the medium.

In general, for an anisotropic medium, the quantities $\boldsymbol{\epsilon}$, $\boldsymbol{\mu}$ and $\boldsymbol{\sigma}$ contain the physical properties of the material medium. If the medium is isotropic they become scalars. In dealing with a general medium knowledge of $\boldsymbol{\epsilon}$, $\boldsymbol{\mu}$ and $\boldsymbol{\sigma}$ will allow the solution of the wave modes present via Maxwell's equations. Dealing with a plasma in this way proves too complicated and impractical, instead one deals with Maxwell's equations for a vacuum where the physical properties of the plasma are defined through the conduction current density, $\mathbf{J}_c$, and the free charge density, ρ_f. Using $\mathbf{J}_c$ and ρ_f one can define an effective dielectric tensor that characterises the entire plasma medium.

Maxwell's equations governing electromagnetic fields in a vacuum containing free charges and currents, read as

$$\nabla \cdot \mathbf{E} = \frac{\rho}{\epsilon_0} \tag{2.5}$$

$$\nabla \cdot \mathbf{B} = 0 \tag{2.6}$$

$$\nabla \times \mathbf{E} = -\frac{\partial \mathbf{B}}{\partial t} \tag{2.7}$$

$$\nabla \times \mathbf{B} = \mu_0 \mathbf{J} + \epsilon_0 \mu_0 \frac{\partial \mathbf{E}}{\partial t} \tag{2.8}$$

where ρ now denotes the total charge density in the plasma; $\mathbf{J}$ is the total current density; in the vacuum $\mathbf{D} = \epsilon_0 \mathbf{E}$ and $\mathbf{H} = \mu_0 \mathbf{B}$. Perturbing these equations from a uniform and stationary equilibrium, permeated by a homogenous magnetic field, $\mathbf{B}_0$, Maxwell's equations become

$$\nabla \times \mathbf{E} = -\frac{\partial \mathbf{B}_1}{\partial t} \tag{2.9}$$

$$\nabla \times \mathbf{B}_1 = \mu_0 \mathbf{J} + \epsilon_0 \mu_0 \frac{\partial \mathbf{E}}{\partial t} \tag{2.10}$$

where $\mathbf{B}_1$ denotes the perturbed magnetic field; $\mathbf{E}$ and $\mathbf{J}$ denote the perturbed electric field and current density in the plasma. Eliminating $\mathbf{B}_1$ in Faraday's Law using Eq. (2.10) and Fourier analysing the equations by assuming that the perturbed variables vary as $\sim \exp\left[i(\mathbf{k} \cdot \mathbf{r} - \omega t)\right]$ yields

$$\mathbf{k} \times (\mathbf{k} \times \mathbf{E}) + \frac{\omega^2}{c^2} \mathbf{K} \cdot \mathbf{E} = 0 \tag{2.11}$$

where

$$\mathbf{K} = \mathbf{I} + \frac{i}{\epsilon_0 \omega}\boldsymbol{\sigma} \tag{2.12}$$

is the effective dielectric tensor of the plasma; $\mathbf{I}$ is the identity matrix; and Ohm's Law is $\mathbf{J} = \boldsymbol{\sigma} \cdot \mathbf{E}$. Defining the refractive index of the plasma as the ratio of the phase velocity of an electromagnetic disturbance in the vacuum, c, to that in the plasma medium, ω/k,

$$\mathbf{n} = \frac{\mathbf{k}c}{\omega} \tag{2.13}$$

and substituting into Eq. (2.11) gives

$$\mathbf{n} \times (\mathbf{n} \times \mathbf{E}) + \mathbf{K} \cdot \mathbf{E} = 0 \tag{2.14}$$

This is a general equation describing the response of the plasma to electromagnetic disturbances. The next step is to quantify the physical properties of the plasma encapsulated in the conductivity tensor $\boldsymbol{\sigma}$, which itself is determined by the dynamics and distribution of the plasma.

2.2.2 Cold plasma equations

In order to explicitly define $\boldsymbol{\sigma}$, the response of the plasma due to the presence of electromagnetic fields must be obtained to complete the self-consistent description of the plasma.

The ultimate mathematical model of a plasma would entail explicitly describing the individual particle dynamics under the influence of electromagnetic fields. By summing over the total number of particles in the plasma one would obtain a collective, ensemble description of the plasma. For a plasma containing N particles each is described by three position and velocity components at a time t: giving 7 coordinates in total. Considering that N will no doubt be very large for a typical plasma solving the system proves impractical. To proceed one must simplify the model by sacrificing the deterministic nature of the model for a statistical one. This mesoscopic description is termed plasma kinetic theory and presents the most comprehensive description of the plasma available. The dynamics of the plasma is now quantified through a distribution function, f, describing the particles in 6 spatial dimensions at a time t: $f = f(\mathbf{r}, \mathbf{v}, t)$. The distribution function evolves under electromagnetic fields as dictated by the non-relativistic Boltzmann Equation, the fundamental equation in kinetic theory,

$$\frac{\partial f_s}{\partial t} + \mathbf{v} \cdot \nabla f_s + \frac{q_s}{m_s}(\mathbf{E} + \mathbf{v} \times \mathbf{B}) \cdot \frac{\partial f_s}{\partial \mathbf{v}} = \left(\frac{\partial f_s}{\partial t}\right)_c \tag{2.15}$$

where s denotes the species constituting the plasma and the term of the right-hand side denotes the effect of collisions in the plasma. The Boltzmann equation is essentially the continuity equation for the quantity f in a 6 dimensional space in analogy with fluid mechanics.

The moments of the distribution function correspond to a macroscopic, fluid description of the plasma transforming the system from a 6 dimensional description plus time, to 3 dimensional description plus time. The zeroth moment yields the plasma number density

and the first moment gives the plasma bulk fluid velocity,

$$n_s(\mathbf{r},t) = \int f_s(\mathbf{r},\mathbf{v},t)\mathrm{d}\mathbf{v} \tag{2.16}$$

$$\mathbf{u}_s(\mathbf{r},t) = \frac{1}{n_s}\int \mathbf{v} f_s(\mathbf{r},\mathbf{v},t)\mathrm{d}\mathbf{v} \tag{2.17}$$

respectively. In general the average over velocity space of an arbitrary function $\phi(\mathbf{r},\mathbf{v},t)$ is defined to be

$$<\phi>(\mathbf{r},t) = \frac{1}{n_s}\int \phi(\mathbf{r},\mathbf{v},t) f(\mathbf{r},\mathbf{v},t)\mathrm{d}\mathbf{v} \tag{2.18}$$

Note that the moment equations do not form a closed set of equations since each moment involves the next highest. A closure condition is required in the form of a imposed equation of state.

Setting $(\partial f/\partial t)_c = 0$ yields the Vlasov Equation, where the plasma is considered to be collisionless. Stipulating that the plasma is in the cold limit such that electromagnetic effects dominate any thermodynamic, one can formally set the temperature of the plasma to zero. Integrating the Vlasov equation and obtaining the first two moments yields,

$$\frac{\partial n_s}{\partial t} + \nabla\cdot(n_s\mathbf{u}_s) = 0 \tag{2.19}$$

$$m_s n_s\left[\frac{\partial \mathbf{u}_s}{\partial t} + (\mathbf{u}_s\cdot\nabla)\mathbf{u}_s\right] = n_s q_s(\mathbf{E}+\mathbf{u}_s\times\mathbf{B}) \tag{2.20}$$

$$\mathbf{J} = \sum_s n_s q_s \mathbf{u}_s \tag{2.21}$$

where n_s is the species number density; and q_s is the particle charge of the species.

Eqs. (2.5-2.8) and (2.19-2.21) form a closed system of equations for the description of a cold, collisionless plasma. The system of equations consist of 17 scalar unknowns and 17 scalar equations. This is a two-fluid description where the characteristic spatial scale lengths of interest are $\gg \lambda_{mfp}$ and time scales are much greater than any kinetic collisional relaxation time. Note that in the Vlasov description there are no collisions and so the later restriction can be relaxed. Here, the mean fluid flow produced by the collective self-fields, dominates any random velocity component associated with thermal processes. Therefore pressure and collisional terms may formally be dropped. These equations are non-relativistic and are valid in the rest frame of the pair plasma. Ultimately, in the pulsar context a relativistic treatment will be desirable, but it is wise to begin from a simplified foundation upon which further layers of complexity can be added once the relevant physics has been established.

2.2.3 Conductivity tensor

In cartesian coordinates consider a homogenous magnetic field permeating the plasma directed in the $\hat{\mathbf{z}}$-direction, $\mathbf{B} = \hat{\mathbf{z}}B$. The plasma equilibrium is assumed to be uniform and stationary. Recall the cold plasma momentum equation, Eq. (2.20): linearising and Fourier analysing as before yields

$$\mathbf{u}_s = \frac{iq_s}{\omega m_s}(\mathbf{E}+\mathbf{u}_s\times\mathbf{B}_0) \tag{2.22}$$

Note that in the linear analysis there is no zero order velocity component. This vector equation can be rearranged to give the velocity components in the $\hat{\mathbf{x}}$, $\hat{\mathbf{y}}$ and $\hat{\mathbf{z}}$ directions respectively. Through Eq. (2.21) one can express these velocity components in terms of the total current density in the plasma. Using the linearised form of Eq. (2.21) gives

$$J_x = \sum_s \frac{q_s^2 n_{0,s}}{m_s}\left(\frac{i\omega E_x - \Omega_s E_y}{\omega^2 - \Omega_s^2}\right) \tag{2.23}$$

$$J_y = \sum_s \frac{q_s^2 n_{0,s}}{m_s}\left(\frac{i\omega E_y + \Omega_s E_x}{\omega^2 - \Omega_s^2}\right) \tag{2.24}$$

$$J_z = \sum_s \frac{i q_s^2 n_{0,s} E_z}{m_s \omega} \tag{2.25}$$

where $\Omega_s = q_s B_0/m_s$ is the cyclotron frequency for the species s. Ohm's Law relates the current density to the conductivity tensor which quantifies the ability of the plasma to conduct an electric current: $\mathbf{J} = \boldsymbol{\sigma} \cdot \mathbf{E}$. In this cold plasma model the conductivity tensor takes the form

$$\boldsymbol{\sigma} = \begin{bmatrix} \sum_s \frac{q_s^2 n_{0,s}}{m_s}\frac{i\omega}{\omega^2-\Omega_s^2} & -\sum_s \frac{q_s^2 n_{0,s}}{m_s}\frac{\Omega_s}{\omega^2-\Omega_s^2} & 0 \\ \sum_s \frac{q_s^2 n_{0,s}}{m_s}\frac{\Omega_s}{\omega^2-\Omega_s^2} & \sum_s \frac{q_s^2 n_{0,s}}{m_s}\frac{i\omega}{\omega^2-\Omega_s^2} & 0 \\ 0 & 0 & \sum_s \frac{n_{0,s}q_s^2}{m_s}\frac{i}{\omega} \end{bmatrix} \tag{2.26}$$

Without loss of generality, let the direction of propagation of the waves, $\mathbf{k}$, be restricted to the $x-z$ plane: $\mathbf{n} = \hat{\mathbf{x}} n \sin\theta + \hat{\mathbf{z}} n \cos\theta$. Substituting this expression for $\mathbf{n}$ into Eq. (2.14) along with the calculated conductivity tensor yields

$$\mathbf{M}\cdot\mathbf{E} = \begin{bmatrix} S - n^2\cos^2\theta & -iD & n^2\cos^2\theta\sin^2\theta \\ iD & S - n^2 & 0 \\ n^2\cos^2\theta\sin^2\theta & 0 & P - n^2\sin^2\theta \end{bmatrix} \begin{bmatrix} E_x \\ E_y \\ E_z \end{bmatrix} = 0 \tag{2.27}$$

where

$$D = -\sum_s \frac{\omega_{p,s}^2}{\omega}\frac{\Omega_s}{\omega^2-\Omega_s^2} \tag{2.28}$$

$$P = 1 - \sum_s \frac{\omega_{p,s}^2}{\omega} \tag{2.29}$$

$$S = 1 - \sum_s \frac{\omega_{p,s}^2}{\omega^2-\Omega_s^2} \tag{2.30}$$

and $\omega_{p,s}^2 = n_{0,s}q_s^2/(\epsilon_0 m_s)$ is the plasma frequency of the species s such that $\omega_p^2 = \sum_s \omega_{p,s}^2$ is the total plasma frequency. Solutions of Eq. (2.27) exist when the determinant of $\mathbf{M}$ is zero.

2.2.4 Linear wave modes in a homogeneous pair plasma

In an electron-positron (pair) plasma $q_\pm = \pm e$ and $m_\pm = m$ therefore

$$D = 0 \tag{2.31}$$

$$P = 1 - \frac{\omega_p^2}{\omega^2} \tag{2.32}$$

$$S = 1 - \frac{\omega_p^2}{(\omega^2 - \Omega^2)} \tag{2.33}$$

where $\omega_p^2 = 2n_0e^2/(\epsilon m)$ is the total plasma frequency squared and $\Omega^2 = e^2B_0^2/m^2$ is the cyclotron frequency squared.

Parallel propagation, $\theta = 0$

For parallel propagation $\theta = 0$, hence

$$\mathbf{M} \cdot \mathbf{E} = \begin{bmatrix} S - n^2 & 0 & 0 \\ 0 & S - n^2 & 0 \\ 0 & 0 & P \end{bmatrix} \begin{bmatrix} E_x \\ E_y \\ E_z \end{bmatrix} = 0 \tag{2.34}$$

The determinant of $\mathbf{M}$ yields

$$P(S - n^2)^2 = 0 \tag{2.35}$$

This has solutions: $P = 0$, giving

$$\omega = \omega_p \tag{2.36}$$

for $E_z \neq 0$, $E_x = E_y = 0$; and $S = n^2$ giving

$$n^2 = S = 1 - \frac{\omega_p^2}{(\omega^2 - \Omega^2)} \tag{2.37}$$

for E_x, $E_y \neq 0$ and $E_z = 0$.

Eq. (2.36) is the electrostatic plasma oscillation directed along, and therefore unaffected by, the magnetic field. Using the definition of the refractive index stated earlier, one can write Eq. (2.37) as

$$k^2 = \frac{\omega^2}{c^2}\left(1 - \frac{\omega_p^2}{\omega^2 - \Omega^2}\right) \tag{2.38}$$

This solution has a resonance ($k = \infty$) at $\omega = \Omega$ where energy is absorbed by the plasma - its behaviour becomes nonlinear and hence not treatable by this linear perturbation method. At $\omega^2 = \omega_p^2 + \Omega^2$ there is also a cut-off ($k = 0$) where there is no wave propagation and an oscillation only. At high frequencies $\omega \gg \Omega$ the solution reduces to that of a transverse electromagnetic wave $\omega^2 = \omega_p^2 + k^2c^2$. At low frequencies $\omega \ll \Omega$ the dispersion relation becomes $\omega \approx v_A k$, where v_A is the Alfvén speed such that $v_A^2 = B_0^2/(\mu_0\rho_m)$ and ρ_m is the plasma mass density.

Perpendicular propagation, $\theta = \pi/2$

For perpendicular propagation $\theta = \pi/2$, hence

$$\mathbf{M} \cdot \mathbf{E} = \begin{bmatrix} S & 0 & 0 \\ 0 & S - n^2 & 0 \\ 0 & 0 & P - n^2 \end{bmatrix} \begin{bmatrix} E_x \\ E_y \\ E_z \end{bmatrix} = 0 \tag{2.39}$$

The determinant of $\mathbf{M}$ yields

$$S(S - n^2)(P - n^2) = 0 \tag{2.40}$$

This has solutions: $S = 0$, giving

$$\omega^2 = \omega_p^2 + \Omega^2 \tag{2.41}$$

for $E_x \neq 0$, $E_y = E_z = 0$; and $n^2 = P$, giving

$$\omega^2 = \omega_p^2 + k^2 c^2 \tag{2.42}$$

for $E_x = E_y = 0$ and $E_z \neq 0$; and finally $n^2 = S$, giving

$$n^2 = S = 1 - \frac{\omega_p^2}{(\omega^2 - \Omega^2)} \tag{2.43}$$

for $E_x = E_z = 0$ and $E_y \neq 0$.

Eq. (2.41) describes the plasma hybrid oscillation. In contrast to Eq. (2.36) the oscillation occurs perpendicularly to the magnetic field, altering the plasma dynamics. This can be seen by the presence of the cyclotron frequency in the dispersion relation. Eq. (2.42) is a transverse electromagnetic wave with a cut-off at $\omega = \omega_p^2$, it is called the ordinary mode since $E_z \parallel B_0$. The dispersion relation described by Eq. (2.43) is the same as Eq. (2.37) and is called the extraordinary mode since $E_y \perp B_0$. At low frequencies ($\omega \ll \Omega$) the extraordinary mode is transverse electrodynamically and mechanically longitudinal.

2.3 Nonlinear electrostatic pair plasma oscillations

Electrostatic plasma oscillations are a fundamental plasma process, defining a characteristic timescale within which a plasma can respond to imposed perturbed electric fields. It seems reasonable to first study such a fundamental process to gain insight into potential mechanisms that could lead to a source of radiation in the pulsar context. The waves outlined in the previous section were derived in a linear cold plasma model where the plasma equilibrium was uniform and was permeated by a homogeneous magnetic field. In this analysis when $\theta = 0$, $E_x = E_y = 0$ and $E_z \neq 0$, the pair plasma supported an electrostatic oscillation aligned with the background magnetic field. The oscillation occurs at the plasma frequency $\omega_p^2 = 2n_0e^2/(\epsilon_0 m)$, where it would occur ad infinitum in the absence of any dissipative processes in the plasma. The following discussion gives a brief summary of nonlinear pair plasma oscillations following the work of da Costa and Diver [77, hereafter referred to as Paper I].

Nonlinear pair plasma oscillations evolve in a much different way. To illustrate this difference consider a one dimensional plasma oscillation in a cold pair plasma. The governing equations can be cast in the form

$$\partial_t n_\pm + \partial_z(n_\pm v_\pm) = 0 \tag{2.44}$$
$$\partial_t v_\pm + v_\pm \partial_z v_\pm = \pm\frac{e}{m}E \tag{2.45}$$
$$\partial_t E = -\frac{e}{\epsilon_0}(n_+ v_+ - n_- v_-) \tag{2.46}$$
$$\partial_z E = \frac{e}{\epsilon_0}(n_+ - n_-) \tag{2.47}$$

where $\partial_{t,z}$ denote partial derivatives in time and space respectively; $n_\pm$ is the positron and electron number density; and $v_\pm$ is the positron and electron velocity in the z-direction. These equations describe an electrostatic oscillation in the z-direction, which is assumed to be aligned with the magnetic field present in the plasma as in the linear case. The equations can be cast into a form that highlights the symmetry inherent in the pair plasma, this can be done via the following relations

$$\Sigma = \frac{1}{2}(n_+ + n_-)L^3 \tag{2.48}$$
$$\Delta = \frac{1}{2}(n_+ - n_-)L^3 \tag{2.49}$$
$$\sigma = \frac{1}{2}(v_+ + v_-)T/L \tag{2.50}$$
$$\delta = \frac{1}{2}(v_+ - v_-)T/L \tag{2.51}$$
$$\rho = \frac{eT^2}{mL}E \tag{2.52}$$
$$\xi = z/L \tag{2.53}$$
$$\tau = t/T \tag{2.54}$$

where T and L are characteristic time and length scales respectively. Note that in the pulsar context a variety of characteristic length scales could be used such as the plasma skin depth, the electron gyroradius, the magnetospheric scale height and the magnetic inhomogeneity scale height. In the pair plasma work reported here and in subsequent sections a characteristic length scale will not be assigned aiding in its generality. The resulting set of differential equations governing the evolution of the cold pair plasma becomes

$$\dot{\Sigma} = -(\Sigma\sigma + \Delta\delta)' \tag{2.55}$$
$$\dot{\Delta} = -(\Sigma\delta + \Delta\sigma)' \tag{2.56}$$
$$\dot{\sigma} = -\frac{1}{2}(\sigma^2 + \delta^2)' \tag{2.57}$$
$$\dot{\delta} = -(\sigma\delta)' + \rho \tag{2.58}$$
$$\dot{\rho} = -p(\Sigma\delta + \Delta\sigma) \tag{2.59}$$
$$\rho' = p\Delta \tag{2.60}$$

where $p = 2e^2T^2/(\epsilon_0 mL^3)$. In equilibrium one shall assume that there are no electric fields and that there is no charge separation. Performing a linear perturbation analysis, where

equilibrium values of plasma variables are denoted by a subscript zero, yields

$$\dot{\Sigma} = -(\Sigma_0\sigma)' \tag{2.61}$$
$$\dot{\Delta} = -(\Sigma_0\delta)' \tag{2.62}$$
$$\dot{\sigma} = 0 \tag{2.63}$$
$$\dot{\delta} = \rho \tag{2.64}$$
$$\dot{\rho} = -p\Sigma_0\delta \tag{2.65}$$

Note that no constraint has been made upon the form of the average plasma density in equilibrium. Combining Eqs. (2.64) and (2.65) yields

$$\ddot{\rho} + \omega_p^2\rho = 0 \tag{2.66}$$

This differential equation describes simple harmonic motion of the electric field ρ in the plasma, oscillating at the plasma frequency $\omega_p^2 = p\Sigma_0$. In the linear regime when the charge density is perturbed an electrostatic plasma oscillation is induced. When the average plasma density in equilibrium is uniform, the plasma variables oscillate indefinitely. Note that a non-uniform plasma equilibrium results in unconstrained, secular growth of the density plasma variables in the linear regime (Paper I). This is can seen by taking $\rho = A\exp(i\omega_p(\xi)\tau)$ yielding $\Delta \propto \tau\omega_p'$ from Eq. (2.60) implying secular growth in the plasma density.

The numerical solution of the governing set of equations reveals the nonlinear evolution of the pair plasma during the oscillation, Figs. 2.1-2.6. A nonlinear charge density perturbation creates a decrease in the plasma density, hence the plasma frequency, at the centre of the oscillation site, Fig. 2.1. The number density becomes a function of position across the spatial extent of the oscillation, as a result the plasma oscillates over differing timescales dependent upon the local plasma frequency, Fig. 2.5. This differential response transports the plasma from slowly varying to rapidly oscillating regions. As a result density spikes are formed that cannot be resolved by the numerical mesh and the oscillation ceases, Fig. 2.6. The degree of nonlinearity is dependent upon the amplitude of the initial charge density perturbation. The greater the amplitude the greater the total energy of the oscillation; the greater the initial total energy, the greater the kinetic energy necessary to transport the plasma forming the density spikes.

In reality other physical processes come into to play that could counteract the density instability, for example if the cold plasma approximation is relaxed and thermodynamical processes are allowed. Pressure effects in the plasma would help to oppose the build up of any density spikes. In the absence of thermodynamics the pair plasma would ultimately annihilate itself creating a sea of photons, given the right conditions to allow the conservation of the appropriate quantum numbers in the interaction.

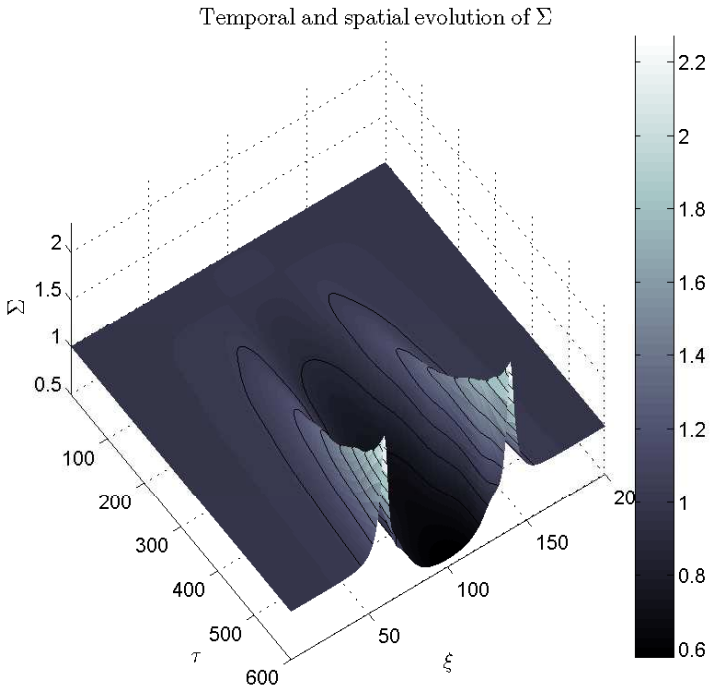

Figure 2.1: Evolution of the average dimensionless plasma number density, Σ, after an initial 10% density perturbation. The plot exhibits the characteristic deepening of the density at the centre of the oscillation site and that Σ becomes a strong function of position across the domain.

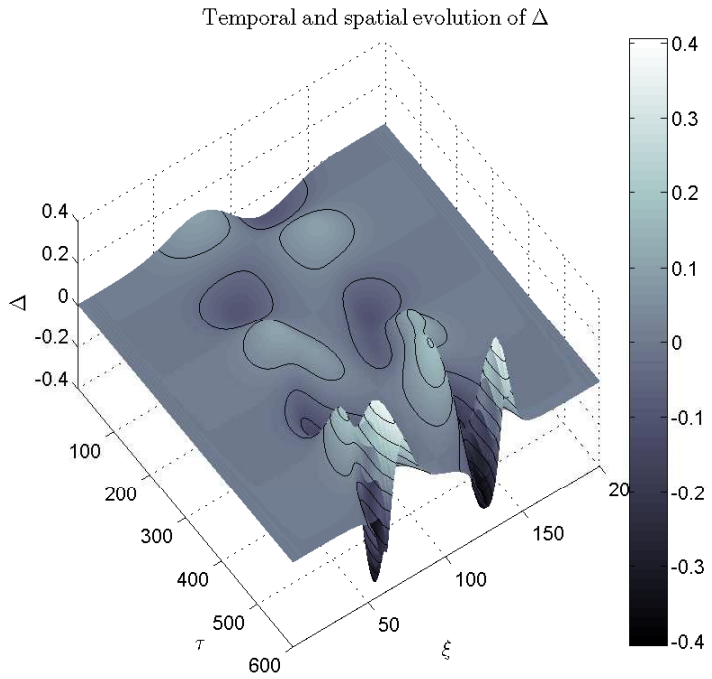

Figure 2.2: Evolution of the difference between the dimensionless e^+-e^- number densities, Δ, after an initial 10% density perturbation. Note the onset of the nonlinear behaviour of the oscillation with the charge density evolving sharp features at the edge of the oscillation site.

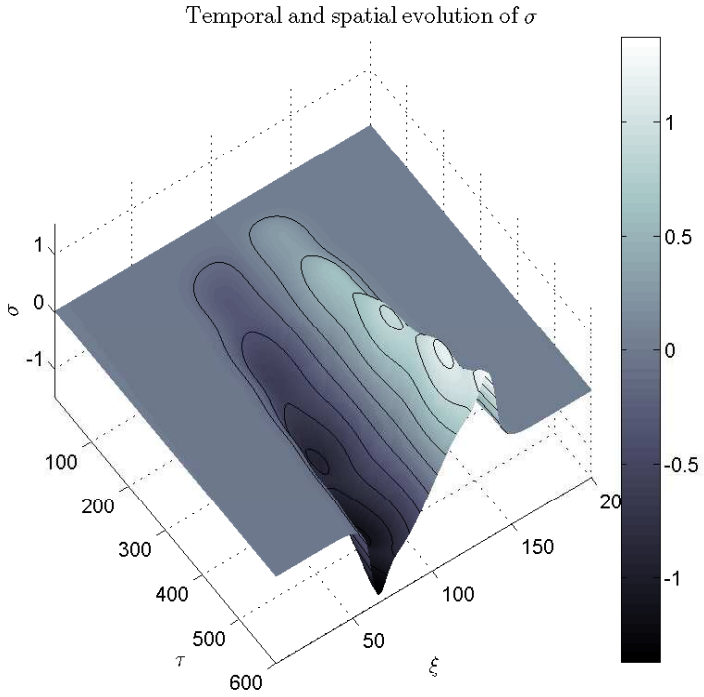

Figure 2.3: Evolution of the average dimensionless radial plasma flow, σ, after an initial 10% density perturbation. In the linear regime σ is constant in time (Eq. (2.63)), here deviations from this characterise the degree of nonlinearity in the plasma oscillation.

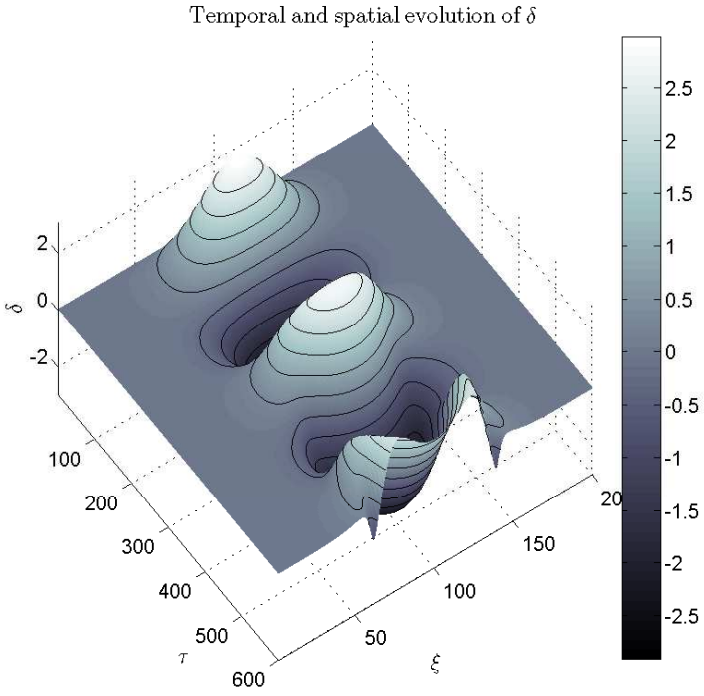

Figure 2.4: Evolution of the difference between the dimensionless e^+-e^- radial velocities, δ, after an initial 10% density perturbation.

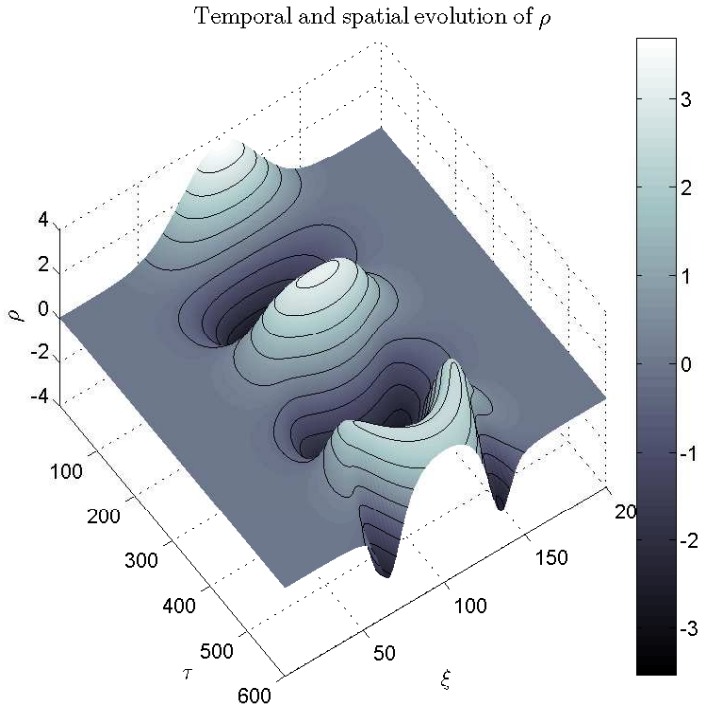

Figure 2.5: Evolution of the dimensionless radial electric field, ρ, associated with the electrostatic oscillation after an initial 10% density perturbation. The hallmark features of the nonlinear evolution of the oscillation are evident with the decrease in the plasma frequency at the centre of the oscillation site.

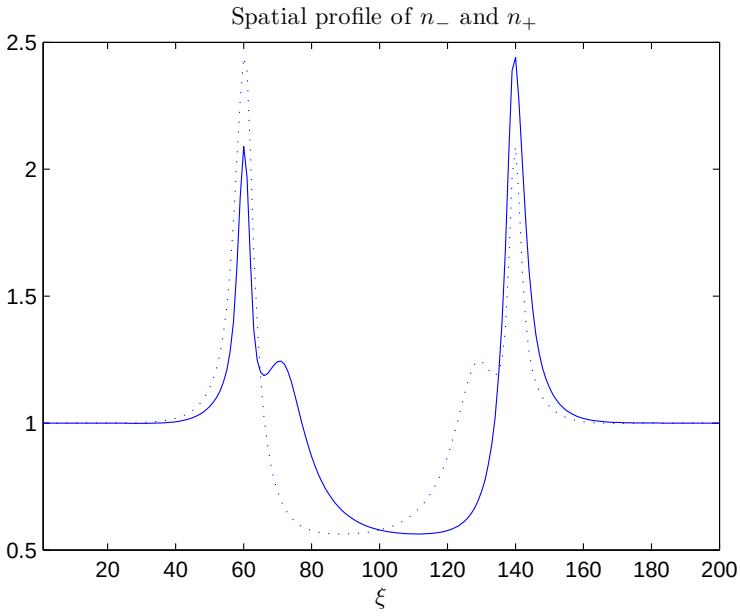

Figure 2.6: Spatial profile of the dimensionless positron number density, n_+L^3, (dotted line) and the dimensionless electron number density, n_-L^3, (unbroken line) for last time step, after an initial 10% density perturbation. The plot clearly shows the development of the density spikes caused by the nonlinear evolution of the oscillation.

2.4 Electromagnetic mode coupling

In a pair plasma permeated by an inhomogeneous magnetic field, electrostatic oscillations couple to electromagnetic modes. This is advantageous for two reasons: firstly it provides a mechanism for quenching the density instability apparent in the nonlinear pair plasma oscillation by radiating energy away from the oscillation site and limiting its nonlinear evolution. Secondly, the mode coupling produces a source of electromagnetic radiation in the pulsar magnetosphere. Simple models are favoured in nature, where elaborate ones are penalised for their relative complexity. The mode coupling described here is in keeping with this philosophy: electrostatic oscillations are a fundamental plasma process, their coupling to electromagnetic radiation unavoidable when there ambient magnetic field is inhomogeneous. The following discussion regarding the mode coupling follows the work of Diver and da Costa [78, hereafter referred to as Paper II]. The coupling mechanism is a nonlinear effect, requiring the full set of nonlinear equations to describe it. The work in paper II, reproduced below, identified the participating modes of the coupling mechanism in the linear regime. The coupling was then verified in the quasi-linear regime, via the numerical solution of the linearised equations using a nonlinear, second-order correction to accommodate the coupling mechanism.

To facilitate the mode coupling mechanism it is assumed that: the electrostatic oscillations are radial; the electromagnetic behaviour consists of an axial magnetic perturbation and an azimuthal electric field; and that all plasma variables depend only on r and t allowing the model to have an azimuthal symmetry, see Fig. 3.1. Hence with an axial magnetic field $\mathbf{B} = \hat{\mathbf{z}}B_z$; an electric field in the r-θ plane $E_{r,\theta}$; with $q_\pm = \pm e$ and $m_\pm = m$, the full nonlinear model equations for a cold non-relativistic electron-positron plasma are

$$
\begin{aligned}
r\dot{n}_+ + (rn_+u_r)' &= 0 && (2.67)\\
r\dot{n}_- + (rn_-v_r)' &= 0 && (2.68)\\
\dot{u}_r + u_r u_r' - u_\theta^2/r &= (e/m)(E_r + u_\theta B_z) && (2.69)\\
\dot{u}_\theta + u_r u_\theta' + u_r u_\theta/r &= (e/m)(E_\theta - u_r B_z) && (2.70)\\
\dot{v}_r + v_r v_r' - v_\theta^2/r &= -(e/m)(E_r + v_\theta B_z) && (2.71)\\
\dot{v}_\theta + v_r v_\theta' + v_r v_\theta/r &= -(e/m)(E_\theta - v_r B_z) && (2.72)\\
(rE_r)' &= (e/\epsilon_0)r(n_+ - n_-) && (2.73)\\
0 &= -\dot{E}_r/c^2 - \mu_0 e(n_+u_r - n_-v_r) && (2.74)\\
(rE_\theta)' &= -r\dot{B}_z && (2.75)\\
B_z' &= -\dot{E}_\theta/c^2 - \mu_0 e(n_+u_\theta - n_-v_\theta) && (2.76)
\end{aligned}
$$

where n_+, n_- are the positron and electron number densities; u, v are the positron and electron velocities. Eq. (2.73) is Poisson's equation for the electric field in the plasma; (2.75) is the single z component of the $\nabla \times \mathbf{E}$ equation describing Faraday's law of induction; and (2.74), (2.76) are the r and θ components of the $\nabla \times \mathbf{B}$ (Ampère-Maxwell) equation. Appendix A has more details regarding the derivation of these equations. Eqs. (2.73) and (2.74) describing the radial electric field are not both required, in this analysis Eq. (2.74) is used.

The linearised equations can be rewritten in a non-dimensional form as

$$\dot{\Sigma} = -\sigma' \quad (2.77)$$
$$\dot{\Delta} = -\delta' \quad (2.78)$$
$$\dot{\sigma} = p_1\zeta \quad (2.79)$$
$$\dot{\delta} = \rho + p_1\chi \quad (2.80)$$
$$\dot{\chi} = -p_1\delta \quad (2.81)$$
$$\dot{\zeta} = \theta - p_1\sigma \quad (2.82)$$
$$\dot{\rho} = -2p_2\delta \quad (2.83)$$
$$\dot{\theta} = -p_3\xi\beta' - 2p_2\zeta \quad (2.84)$$
$$\dot{\beta} = -\theta'/\xi \quad (2.85)$$

where

$$\Sigma = (n_+ + n_-)\xi/2n_0 \quad (2.86)$$
$$\Delta = (n_+ - n_-)\xi/2n_0 \quad (2.87)$$
$$\sigma = (u_r + v_r)\xi T/(2L) \quad (2.88)$$
$$\delta = (u_r - v_r)\xi T/(2L) \quad (2.89)$$
$$\chi = (u_\theta + v_\theta)\xi T/(2L) \quad (2.90)$$
$$\zeta = (u_\theta - v_\theta)\xi T/(2L) \quad (2.91)$$
$$\rho = \xi e T^2 E_r/(mL) \quad (2.92)$$
$$\theta = \xi e T^2 E_\theta/(mL) \quad (2.93)$$
$$\beta = eTB_z/m \quad (2.94)$$
$$r = L\xi \quad (2.95)$$
$$t = T\tau \quad (2.96)$$

and

$$p_1 = \omega_c T \quad (2.97)$$
$$p_2 = \omega_p^2 T^2 \quad (2.98)$$
$$p_3 = c^2T^2/L^2 \quad (2.99)$$
$$\omega_p^2 = n_0 e^2/(\epsilon_0 m) \quad (2.100)$$
$$\omega_c = eB_0/m \quad (2.101)$$

In this new notation $'$ and $\dot{}$ denote $\partial/\partial\xi$ and $\partial/\partial\tau$ respectively. L and T are characteristic length and time scales respectively, despite the same notation they do not refer to the same scale lengths defined in § 2.3. The choice of non-dimensional variables, as defined above, differ from those used in § 2.3 since it greatly simplifies the form of the linear set of governing equations in this geometry. n_0 and B_0 are the equilibrium plasma charge number density and the background equilibrium magnetic field respectively. Note that in the subsequent linear mode analysis n_0 and B_0 are assumed to be constant for simplicity.

2.4.1 Electrostatic mode

The electrostatic oscillation is characterised by a homogeneous, constant magnetic field, $\beta = \beta_0$. From the governing set of equations this requires that $\theta = 0$, $\zeta = 0$, $\sigma = 0$ and

Σ = constant. A differential expression can be obtained that describes the temporal and spatial evolution of ρ from Eq. (2.83) such that:

$$\ddot{\rho} + 2p_2\rho = -2p_1p_2\chi \tag{2.102}$$

therefore

$$\ddot{\rho} + \omega_H^2\rho = f(\xi) \tag{2.103}$$

The radial electric field associated with the electrostatic mode is described by simple harmonic motion in the linear limit. The characteristic frequency of oscillation is the plasma hybrid frequency, given by $\omega_H^2{=}2p_2 + p_1^2$ – in this context p_1 denotes the cyclotron frequency and encapsulates the influence of the background magnetic field on the plasma dynamics. In the magnetised case, perturbing the plasma density creates a time-varying restoring electric field that accelerates the species in radially opposite directions; hence $\sigma = 0$. The magnetic field permeating the plasma forces the species to participate in partial larmor orbits with the same azimuthal velocity; therefore $\zeta = 0$. In the magnetised case the electrostatic oscillation constitutes a radial expansion and contraction plus a torsional twist.

2.4.2 Electromagnetic mode

The radially propagating electromagnetic mode is characterised by $\beta = \beta(\xi, \tau)$, $\theta = \theta(\xi, \tau)$ and $\rho = 0$ requiring that $\Delta = 0$, $\chi = 0$ and $\delta = 0$, for self-consistency. Eq. (2.84) becomes

$$\ddot{\theta} = -p_3\xi\dot{\beta}' - 2p_2\dot{\zeta} \tag{2.104}$$

$$= -p_3\xi(-\theta''/\xi + \theta'/\xi^2) - 2p_2\dot{\zeta} \tag{2.105}$$

Defining the operator $\mathcal{P}$ as

$$\mathcal{P} = \ddot{\theta} - p_3\xi(\theta''/\xi - \theta'/\xi^2) \tag{2.106}$$

yields

$$P = -2p_2\dot{\zeta} \tag{2.107}$$

$$= -2p_2(\theta - p_1\sigma) \tag{2.108}$$

Hence

$$\dot{\mathcal{P}} + 2p_2\dot{\theta} = 2p_1^2p_2\zeta \tag{2.109}$$

This yields a differential expression for θ describing electric field component of the propagating electromagnetic mode,

$$\ddot{\mathcal{P}} + p_1^2\mathcal{P} + 2p_2\ddot{\theta} = 0 \tag{2.110}$$

Expanding out the differential operator and assuming $\theta(\xi, \tau) = y(\xi)\exp(-i\omega\tau)$ yields

$$(y'/\xi)' + \kappa^2 y/\xi = 0 \tag{2.111}$$

where

$$\kappa^2 = \frac{\omega^2}{p_3}\frac{(\omega^2 - 2p_2 - p_1^2)}{(\omega^2 - p_1^2)} \tag{2.112}$$

This has the general solution

$$y(\xi) = A\xi J_1(\kappa\xi) + B\xi Y_1(\kappa\xi) \tag{2.113}$$

where J_1, Y_1 are Bessel functions of the first and second kind respectively and A, B are constants. For a propagating electromagnetic mode κ has to be real yielding a cut-off frequency such that

$$\kappa^2 > 0 \Rightarrow \omega^2 > 2p_2 + p_1^2 \tag{2.114}$$

2.4.3 Numerical results

The coupling mechanism is a nonlinear effect, requiring the full set of nonlinear equations to describe it. In paper II, the coupling was numerically verified in the quasi-linear regime where the linear equations were solved using a nonlinear, second-order correction. In the simulations the background inhomogeneous magnetic is prescribed and enters the equations via p_1, the equilibrium plasma density is taken to be uniform. Perturbing the radial velocity field induces an electrostatic oscillation with $\delta \neq 0$ (Fig. 2.7), $\rho \neq 0$ (Fig. 2.8) and $\sigma = 0$. When the background magnetic field is inhomogeneous the disparate, mutually exclusive conditions for the independent electrostatic and electromagnetic modes are relaxed. The non-uniform magnetic field gradient actuates a $\mathbf{B} \times \nabla B$ drift that violates the azimuthal symmetry of the velocity fields in the plasma oscillation, therefore $\zeta \neq 0$. This time-varying azimuthal current density produces axial magnetic field fluctuations ($\beta \neq 0$) that generate a corresponding azimuthal electric field ($\theta \neq 0$), constituting a radially propagating electromagnetic mode; see Fig. 2.9 and 2.10. The $\mathbf{B} \times \nabla B$ drift does not explicitly appear in the governing equations but its effect is encapsulated within the plasma dynamics they describe. Note that the frequency of the electromagnetic disturbance is twice that of the uncoupled hybrid plasma oscillation, this will be explained in Chapter 3.

The mathematical analysis and numerical results reproduced here are conducted in the linear and quasi-linear regimes respectively, where the plasma equilibrium is uniform and the inhomogeneous magnetic field is prescribed. In reality, self-consistency requires that a plasma permeated by an inhomogeneous magnetic field must be non-uniform and dynamical. The mode coupling is a second order effect and can only be fully realised in the nonlinear regime. It is the aim of this thesis to address these pressing issues.

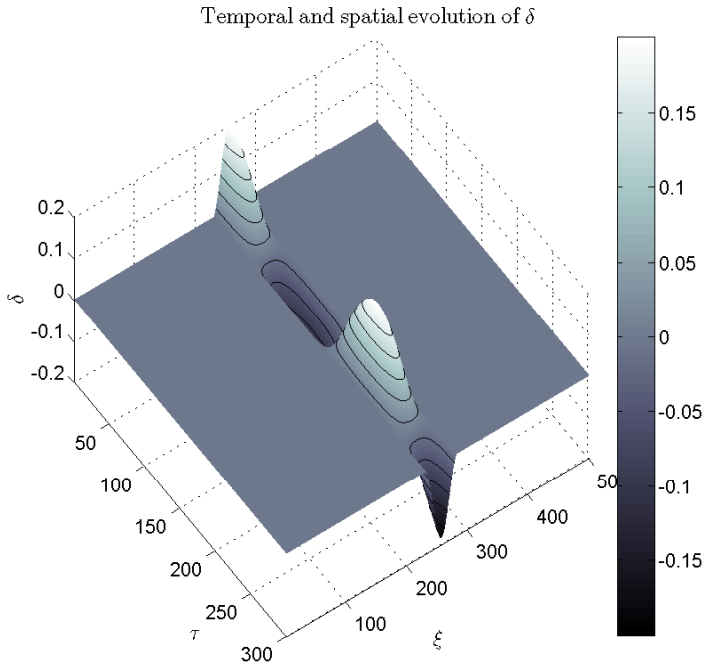

Figure 2.7: Surface plot showing the spatial and temporal evolution of the difference between the dimensionless e^+-e^- radial velocities, δ. Here the electrostatic oscillation is perturbed in the vicinity of inhomogeneous magnetic field.

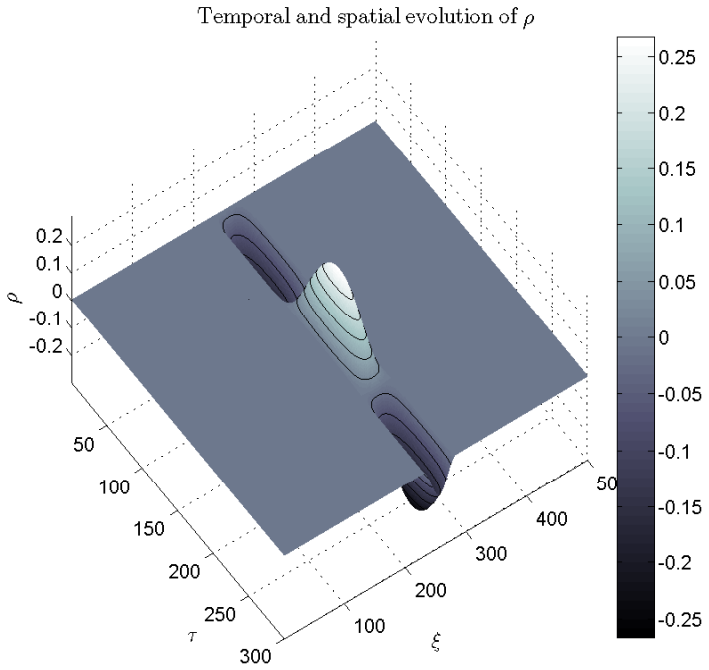

Figure 2.8: The temporal and spatial evolution of the self-consistently calculated dimensionless radial electric field, ρ, associated with the plasma oscillation in Fig. 2.7.

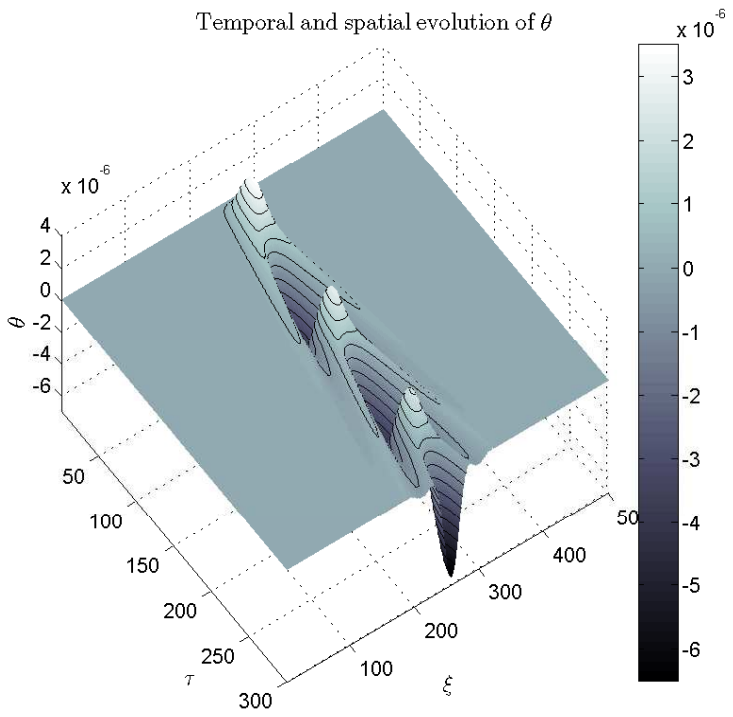

Figure 2.9: The dimensionless electric field component, θ, of the radially propagating electromagnetic wave generated from the mode coupling mechanism. The electrostatic oscillation, Figs. 2.7-2.8, couples to an electromagnetic mode when the background magnetic field is non-uniform. Note that the frequency of the electromagnetic disturbance is twice the uncoupled hybrid plasma frequency.

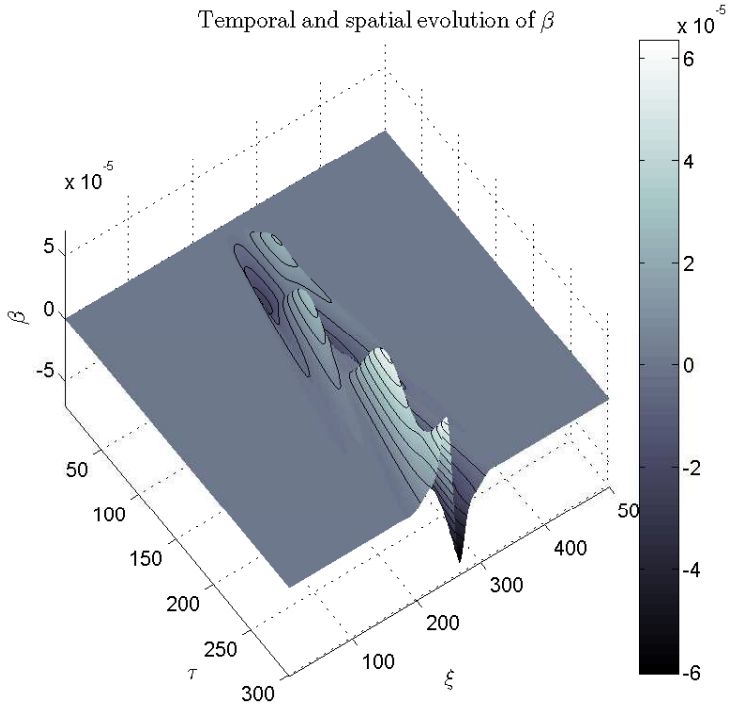

Figure 2.10: The dimensionless magnetic field component, β, of the electromagnetic mode consistent with Figs. 2.7, 2.8 and 2.9.

Chapter 3

Nonlinear mode coupling in pair plasmas: Linear analysis

3.1 Introduction

In cold non-relativistic plasma theory nonlinear electrostatic oscillations in electron-positron plasmas develop a density instability in which the density of both species grows sharply at the edges of the oscillation site (Paper I). Perturbing the electron density induces an electric field that the positrons respond to on the same timescale as the electrons. In trying to restore equilibrium to the plasma the positrons exacerbate the initial density perturbation, sewing the seeds of the instability.

Folding thermodynamics into the system provides a possible mechanism for avoiding the onset of the instability, since pressure effects would oppose the density build up. Coupling the oscillation to an electromagnetic mode via an inhomogeneous background magnetic field would provide another means to avoid the onset of the instability. This would allow energy to be radiated away from the oscillation, quenching the density instability and giving a source of radiation in the pulsar magnetosphere (Paper II). Ultimately thermodynamics will have to be incorporated into a more complete model but it would be advantageous to explore the coupling before relaxing the cold plasma approximation. Previous work has studied this mechanism in the quasi-linear regime, Paper II, in which the background magnetic field was inhomogeneous but the plasma density was uniform. A fully consistent nonlinear treatment requires that both the density and magnetic field be inhomogeneous simultaneously.

This core chapter addresses the basic mathematical formulation of the pair cold magnetoplasma in Section 3.2 and the mode coupling mechanism in Section 3.4. In Section 3.5 linear analysis of the equations perturbed from dynamical equilibrium is performed to gain an understanding of the modes present in the plasma. The work detailed in §3.3 and §3.5 has been published in a paper written by the author in the journal Astronomy and Astrophysics [79] and in the conference proceedings for the 363^{rd} WE-Heraeus Seminar on

"Neutron Stars and Pulsars" [80]. Elements of the work described in §3.4 follows that of Papers I and II, cast in new notation.

3.2 Model equations

The governing equations for a two fluid cold magnetoplasma are:

$$\frac{\partial n_s}{\partial t} + \nabla \cdot (n_s \mathbf{u}_s) = 0 \tag{3.1}$$

$$m_s n_s \left[\frac{\partial \mathbf{u}_s}{\partial t} + (\mathbf{u}_s \cdot \nabla)\mathbf{u}_s \right] = n_s q_s (\mathbf{E} + \mathbf{u}_s \times \mathbf{B}) \tag{3.2}$$

$$\mathbf{J} = \sum_s n_s q_s \mathbf{u}_s \tag{3.3}$$

$$\nabla \times \mathbf{B} = \mu_0 \mathbf{J} + \epsilon_0 \mu_0 \frac{\partial \mathbf{E}}{\partial t} \tag{3.4}$$

$$\nabla \times \mathbf{E} = -\frac{\partial \mathbf{B}}{\partial t} \tag{3.5}$$

$$\nabla \cdot \mathbf{E} = \frac{1}{\epsilon_0} \sum_s n_s q_s \tag{3.6}$$

$$\nabla \cdot \mathbf{B} = 0 \tag{3.7}$$

where s denotes the species constituting the plasma; n_s is the species number density; u_s is the species velocity; m_s is the particle mass of the species and q_s is the particle charge of the species. Eqs. (3.1) and (3.2) are the continuity and momentum equations of the plasma fluids describing the conservation of particle number and the dynamics of the fluid under the influence of electromagnetic fields respectively; Eq. (3.3) quantifies the current generated by the motion of the plasma dictated by the electromagnetic fields; Eqs. (3.4) to (3.7) are Maxwell's Equations expressing the temporal and spatial evolution of electromagnetic fields in the plasma. Maxwell's Equations along with Eq. (3.3) couple the two, otherwise non-interacting, fluids together. For details regarding these governing equations including their translation into cylindrical polar coordinates, their non-dimensional counterparts and their linearisation, please refer to Appendix A.

The model equations cast in cylindrical polar coordinates (r, θ, z) are,

$$r\dot{n}_s + (r n_s u_{s,r})' = 0 \tag{3.8}$$

$$\dot{u}_{s,r} + u_{s,r} u'_{s,r} - u^2_{s,\theta}/r = (q_s/m_s)(E_r + u_{s,\theta} B_z) \tag{3.9}$$

$$\dot{u}_{s,\theta} + u_{s,r} u'_{s,\theta} + u_{s,r} u_{s,\theta}/r = (q_s/m_s)(E_\theta - u_{s,r} B_z) \tag{3.10}$$

$$(rE_r)' = \frac{r}{\epsilon_0} \sum_s n_s q_s \tag{3.11}$$

$$0 = -\dot{E}_r/c^2 - \mu_0 \sum_s n_s q_s u_{s,r} \tag{3.12}$$

$$(rE_\theta)' = -r\dot{B}_z \tag{3.13}$$

$$B'_z = -\dot{E}_\theta/c^2 - \mu_0 \sum_s n_s q_s u_{s,\theta} \tag{3.14}$$

where $\dot{}$ denotes $\partial/\partial t$ and $'$ denotes $\partial/\partial r$. For details please refer to appendix A.

In a pair plasma permeated by a inhomogeneous magnetic field, electrostatic oscillations couple to electromagnetic modes. To facilitate the mode coupling mechanism it is assumed that: the electrostatic oscillations are radial; the electromagnetic behaviour consists of an axial magnetic perturbation and an azimuthal electric field; and that all plasma variables depend only on r and t allowing the model to have an azimuthal symmetry, Fig. 3.1. Note that the plasma is considered to be infinite in extent in the $\hat{\mathbf{z}}$ direction. Hence with an axial magnetic field $\mathbf{B} = \hat{\mathbf{z}}B_z$; an electric field in the r-θ plane $E_{r,\theta}$; with $q_\pm = \pm e$ and $m_\pm = m$, the full nonlinear model equations for a cold non-relativistic electron-positron plasma are

$$
\begin{aligned}
r\dot{n}_+ + (rn_+u_r)' &= 0 && (3.15)\\
r\dot{n}_- + (rn_-v_r)' &= 0 && (3.16)\\
\dot{u}_r + u_r u_r' - u_\theta^2/r &= (e/m)(E_r + u_\theta B_z) && (3.17)\\
\dot{u}_\theta + u_r u_\theta' + u_r u_\theta/r &= (e/m)(E_\theta - u_r B_z) && (3.18)\\
\dot{v}_r + v_r v_r' - v_\theta^2/r &= -(e/m)(E_r + v_\theta B_z) && (3.19)\\
\dot{v}_\theta + v_r v_\theta' + v_r v_\theta/r &= -(e/m)(E_\theta - v_r B_z) && (3.20)\\
(rE_r)' &= (e/\epsilon_0) r(n_+ - n_-) && (3.21)\\
0 &= -\dot{E}_r/c^2 - \mu_0 e(n_+u_r - n_-v_r) && (3.22)\\
(rE_\theta)' &= -r\dot{B}_z && (3.23)\\
B_z' &= -\dot{E}_\theta/c^2 - \mu_0 e(n_+u_\theta - n_-v_\theta) && (3.24)
\end{aligned}
$$

where n_+, n_- are the positron and electron number densities; u, v are the positron and electron velocities. Eq. (3.21) is Poisson's equation for the electric field in the plasma; (3.23) is the single z component of the $\nabla\times\mathbf{E}$ equation describing Faraday's law of induction; and (3.22), (3.24) are the r and θ components of the $\nabla \times \mathbf{B}$ (Ampère-Maxwell) equation. Appendix A has more details regarding the derivation of these equations.

The equations can be recast into a form that highlights the symmetry of the electron-positron plasma, this can be done via the following relations

$$
\begin{aligned}
\Sigma &= (n_+ + n_-)\,\xi/(2n_0) && (3.25)\\
\Delta &= (n_+ - n_-)\,\xi/(2n_0) && (3.26)\\
\sigma &= (u_r + v_r)\,/(2\omega_0 L) && (3.27)\\
\delta &= (u_r - v_r)\,/(2\omega_0 L) && (3.28)\\
\chi &= (u_\theta + v_\theta)\,/(2\omega_0 L) && (3.29)\\
\zeta &= (u_\theta - v_\theta)\,/(2\omega_0 L) && (3.30)\\
\rho &= eE_r/(m\omega_0^2 L) && (3.31)\\
\theta &= eE_\theta/(m\omega_0^2 L) && (3.32)\\
\beta_0 + \beta &= eB_z/(m\omega_0) && (3.33)\\
\xi &= r/L && (3.34)\\
\tau &= \omega_0 t && (3.35)\\
\omega_0^2 &= n_0 e^2/(\epsilon_0 m) && (3.36)
\end{aligned}
$$

where $L, 1/\omega_0$ are appropriate characteristic length, time scales and β_0, β are the equilibrium and perturbed magnetic field respectively. For details consult Appendix A. The choice of non-dimensional variables, as defined above, differ from those used in Chapter 2

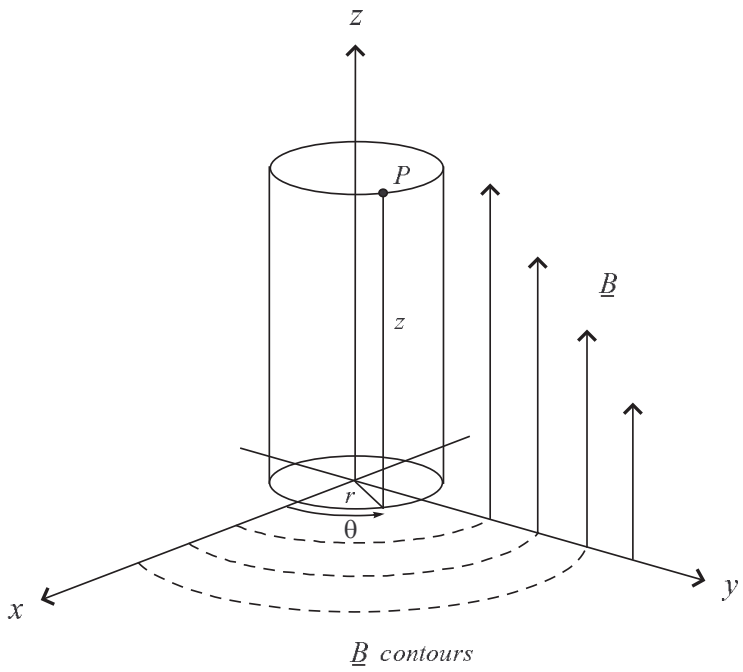

Figure 3.1: Diagram showing the geometrical construction of the model in cylindrical polar coordinates. Note that the conventional notation for cylindrical coordinates is (ρ, ϕ, z), but here the use of ρ will be reserved to denote the radial electric field so r shall be used instead.

since it greatly simplifies the form of the nonlinear set of governing equations in this geometry. Table A.1, Appendix A summarises the physical meaning of the non-dimensional plasma quantities defined here and should be referred to during the subsequent analytical and numerical analysis described in this chapter and the next.

The system of governing equations then becomes

$$\dot{\Sigma} = -\left(\Sigma\sigma + \Delta\delta\right)' \tag{3.37}$$

$$\dot{\Delta} = -\left(\Delta\sigma + \Sigma\delta\right)' \tag{3.38}$$

$$\dot{\sigma} = -\frac{1}{2}(\sigma^2 + \delta^2)' + (\chi^2 + \zeta^2)/\xi + \zeta\left(\beta_0 + \beta\right) \tag{3.39}$$

$$\dot{\delta} = -\left(\sigma\delta\right)' + 2\chi\zeta/\xi + \rho + \chi\left(\beta_0 + \beta\right) \tag{3.40}$$

$$\dot{\chi} = -\chi'\sigma - \zeta'\delta - \left(\chi\sigma + \zeta\delta\right)/\xi - \delta\left(\beta_0 + \beta\right) \tag{3.41}$$

$$\dot{\zeta} = -\sigma\zeta' - \delta\chi' - \left(\sigma\zeta + \delta\chi\right)/\xi + \theta - \sigma\left(\beta_0 + \beta\right) \tag{3.42}$$

$$(\xi\rho)' = 2\Delta \tag{3.43}$$

$$\dot{\rho} = -\frac{2}{\xi}\left(\Delta\sigma + \Sigma\delta\right) \tag{3.44}$$

$$\dot{\theta} = -p\left(\beta_0 + \beta\right)' - \frac{2}{\xi}\left(\Sigma\zeta + \Delta\chi\right) \tag{3.45}$$

$$\dot{\beta} = -\theta' - \theta/\xi \tag{3.46}$$

where $p = c^2/(\omega_0^2 L^2)$ is the dimensionless speed of light squared in the plasma. Note

Poisson's equation, Eq. (3.43), and the r component of the Ampère-Maxwell equation, Eq. (3.44), are not both required but have been included for completeness.

3.3 Dynamical equilibrium

Having an inhomogeneous magnetic field permeating the plasma requires the equilibrium to be non-uniform for the system to be self-consistent.

3.3.1 Non-uniform equilibrium

In equilibrium there is no time evolution, it will be assumed that the plasma is overall electrically neutral and that there is no electric field present. Hence $\partial/\partial\tau = 0$, and $\Delta = \rho = \theta = \beta = 0$. The system of governing equations becomes:

$$\begin{aligned}
0 &= -(\Sigma\sigma)' && (3.47)\\
0 &= -(\Sigma\delta)' && (3.48)\\
0 &= -\frac{1}{2}(\sigma^2+\delta^2)' + (\chi^2+\zeta^2)/\xi + \zeta\beta_0 && (3.49)\\
0 &= -(\sigma\delta)' + 2\chi\zeta/\xi + \chi\beta_0 && (3.50)\\
0 &= -\chi'\sigma - \zeta'\delta - (\chi\sigma+\zeta\delta)/\xi - \delta\beta_0 && (3.51)\\
0 &= -\sigma\zeta' - \delta\chi' - (\sigma\zeta+\delta\chi)/\xi - \sigma\beta_0 && (3.52)\\
0 &= -2\Sigma\delta/\xi && (3.53)\\
0 &= -p\beta_0' - 2\Sigma\zeta/\xi && (3.54)
\end{aligned}$$

The quantity $\Sigma \propto n_+ + n_-$ cannot equal zero since this would imply a negative particle number density. Self-consistency requires, in accordance with Eq. (3.53), that $\delta \propto u_r - v_r$ equals zero. This consequently satisfies Eq. (3.48) and stipulates that $\sigma \propto u_r + v_r$ cannot equal zero since $u_r = v_r$; this is consistent with Eq. (3.47). For the background magnetic field to be inhomogeneous, Eq. (3.54), the azimuthal current density must be non-zero hence $\zeta \neq 0$. This does not directly put any constraint on the behaviour of χ. However, since $\chi \propto (u_\theta + v_\theta)$ and $\zeta \propto (u_\theta - v_\theta)$, Eq. (3.50) becomes:

$$\begin{aligned}
0 &= 2\chi\zeta/\xi + \chi\beta_0 && (3.55)\\
&= 2(u_\theta^2 - v_\theta^2)/\xi + \beta_0(u_\theta + v_\theta) && (3.56)
\end{aligned}$$

This indicates that $\chi = 0$ since $u_\theta = -v_\theta$, this is consistent with Eq. (3.51). With these conditions in place the remaining equations are

$$\begin{aligned}
0 &= -(\Sigma\sigma)' && (3.57)\\
0 &= -\frac{1}{2}(\sigma^2)' + \zeta^2/\xi + \beta_0\zeta && (3.58)\\
0 &= -\sigma(\zeta' + \zeta/\xi + \beta_0) && (3.59)\\
0 &= -p\beta_0' - 2\Sigma\zeta/\xi && (3.60)
\end{aligned}$$

Since $\sigma \neq 0$ this implies that,

$$\zeta' + \zeta/\xi + \beta_0 = 0 \qquad (3.61)$$

Rearranging this expression for β_0 and substituting into Eq. (3.58) yields a relation between σ and ζ namely,

$$(\sigma^2)' + (\zeta^2)' = 0 \tag{3.62}$$

Integrating Eq. (3.57) and (3.62) with respect to ξ, the resulting equations show that the plasma is in a dynamical equilibrium described by

$$\Sigma_0 = \kappa_0/\sigma_0 \tag{3.63}$$

$$\sigma_0 = \sqrt{\kappa_1^2 - \zeta_0^2} \tag{3.64}$$

$$\zeta_0' = -\frac{\zeta_0}{\xi} - \beta_0 \tag{3.65}$$

$$\beta_0' = -\frac{2\kappa_0}{p\xi}\frac{\zeta_0}{\sqrt{\kappa_1^2 - \zeta_0^2}} \tag{3.66}$$

where 0 subscripts denote equilibrium values and κ_0, κ_1 are naturally occurring non-dimensional constants. Eq. (3.66) is obtained by substituting for Σ_0 from Eq. (3.63) and making use of Eq. (3.64). The equilibrium equations describe the self-consistent response of the plasma to a prescribed inhomogeneous background magnetic field, β_0. κ_0 via Eq. (3.63) defines the conservation of the total number density flux; κ_1 via Eq. (3.64) defines the kinetic energy conservation of the equilibrium flow and Eq. (3.65), (3.66) describe the magnetic field generation via the ζ_0, β_0 coupling. Note that this set of equations assumes $\sigma_0 \neq 0$, since the equilibrium velocity field is linked to the form of the magnetic inhomogeneity. The dynamical equilibrium situation is analogous to that of equilibrium flow in a river: the flow at any point is independent of time.

3.3.2 Uniform equilibrium

When $\zeta_0 = \sigma_0 = 0$ the system of governing equations reduce to describe a system equivalent to that in paper II. Self-consistency requires

$$0 = -(\Sigma_0\delta_0)' \tag{3.67}$$

$$0 = -\frac{1}{2}(\delta_0^2)' + \chi_0^2/\xi \tag{3.68}$$

$$0 = \chi_0\beta_0 \tag{3.69}$$

$$0 = -\delta_0\beta_0 \tag{3.70}$$

$$0 = -\delta_0(\chi_0' + \chi_0/\xi) \tag{3.71}$$

$$0 = -2\Sigma_0\delta_0/\xi \tag{3.72}$$

$$0 = -p\beta_0' \tag{3.73}$$

Again the quantity Σ_0 cannot equal zero since this would imply a negative particle number density. As a result this requires that $\delta_0 = 0$ in accordance with Eq. (3.72) and is additionally consistent with having a non-zero magnetic field, Eq. (3.70), permeating the plasma. For $\beta_0 \neq 0$ we must also have $\chi_0 = 0$ to satisfy Eq. (3.69). These conditions are in agreement with Eqs. (3.67), (3.68) and (3.71). In this regime the background plasma is uniform and therefore the equilibrium magnetic field must be constant as dictated by Eq. (3.73). Note that no constraint is placed on the behaviour of Σ_0 in this regime other than $\Sigma_0 \neq 0$.

3.3.3 Exclusive azimuthal motion

In the situation where $\sigma_0 = 0$ and $\zeta_0 \neq 0$ the equilibrium is defined by:

$$
\begin{aligned}
0 &= -(\Sigma_0\delta_0)' && (3.74)\\
0 &= -\frac{1}{2}(\delta_0^2)' + (\chi_0^2 + \zeta_0^2)/\xi + \beta_0\zeta_0 && (3.75)\\
0 &= \chi_0(2\zeta_0/\xi + \beta_0) && (3.76)\\
0 &= -\delta_0(\zeta_0' + \zeta_0/\xi + \beta_0) && (3.77)\\
0 &= -\delta_0(\chi_0' + \chi_0/\xi) && (3.78)\\
0 &= -2\Sigma_0\delta_0/\xi && (3.79)\\
0 &= -p\beta_0' - 2\Sigma_0\zeta_0/\xi && (3.80)
\end{aligned}
$$

Note that as in the $\sigma_0, \zeta_0 = 0$ regime there is no constraint on the behaviour of Σ_0 and that $\delta_0 = 0$, Eq. (3.79). Asserting that $\chi_0 = 0$ requires that $\zeta_0 = -\xi\beta_0$ from Eq. (3.75) which, coupled with the result from Eq. (3.80), describe an inhomogeneous magnetic field generated from a spatially varying azimuthal current density in the plasma,

$$
\begin{aligned}
\zeta_0 &= -\xi\beta_0 && (3.81)\\
\beta_0' &= -2\Sigma_0\zeta_0/(p\xi) && (3.82)
\end{aligned}
$$

This is consistent with Eqs. (3.74), (3.76), (3.77) and (3.78). Note that an equilibrium cannot be self-consistently constructed for the case where $\sigma_0 \neq 0$ and $\zeta_0 = 0$.

3.4 The mode coupling mechanism

To understand the coupling mechanism it is important to become familiar with the plasma dynamics involved in an electrostatic oscillation in an unmagnetised and magnetised pair plasma. Within the mathematical framework presented here, linearising the model equations will help to illustrate the dynamics of the modes when $\beta_0 = \beta = 0$ and $\beta_0 \neq 0$, $\beta = 0$.

To linearise the coupled set of equations (3.37-3.46) all variables are perturbed from an equilibrium state, $y = y_0(\xi) + y_1(\xi, \tau)$, such that the perturbation is much smaller than the equilibrium value, $|y_0| \gg |y_1|$. Nonlinear combinations of y can be linearised by disregarding powers of y_1 greater than 1. Hence:

$$
\begin{aligned}
\Sigma &= \Sigma_0 + \Sigma_1 && (3.83)\\
\sigma &= \sigma_0 + \sigma_1 && (3.84)\\
\zeta &= \zeta_0 + \zeta_1 && (3.85)
\end{aligned}
$$

where the other plasma variables have a zero valued equilibrium: $y = y_1$. Therefore the

linearised governing set of equations read:

$$\dot{\Sigma} = -(\Sigma_0\sigma + \Sigma\sigma_0)' \tag{3.86}$$
$$\dot{\Delta} = -(\sigma_0\Delta + \Sigma_0\delta)' \tag{3.87}$$
$$\dot{\sigma} = -(\sigma_0\sigma)' + 2\zeta_0\zeta/\xi + \zeta_0\beta + \zeta\beta_0 \tag{3.88}$$
$$\dot{\delta} = -(\sigma_0\delta)' + 2\zeta_0\chi/\xi + \rho + \chi\beta_0 \tag{3.89}$$
$$\dot{\chi} = -\sigma_0\chi' - \zeta_0'\delta - (\sigma_0\chi + \zeta_0\delta)/\xi - \delta\beta_0 \tag{3.90}$$
$$\dot{\zeta} = -\sigma_0\zeta' - \sigma\zeta_0' - (\sigma_0\zeta + \sigma\zeta_0)/\xi + \theta - \sigma_0\beta - \sigma\beta_0 \tag{3.91}$$
$$(\xi\rho)' = 2\Delta \tag{3.92}$$
$$\dot{\rho} = -\frac{2}{\xi}(\Delta\sigma_0 + \Sigma_0\delta) \tag{3.93}$$
$$\dot{\theta} = -p\beta' - \frac{2}{\xi}(\Sigma_0\zeta + \Sigma\zeta_0) \tag{3.94}$$
$$\dot{\beta} = -\theta' - \theta/\xi \tag{3.95}$$

Where the perturbation subscripts have been dropped. Eqs (3.43) and (3.46) linearise trivially and require no explicit exposition.

3.4.1 Electrostatic oscillations in an unmagnetised plasma

Consider an unmagnetised pair plasma with a uniform and stationary plasma equilibrium, therefore $\beta_0 = \beta = \theta = \sigma_0 = \zeta_0 = 0$. The linearised governing equations describing this plasma process are:

$$\dot{\Sigma} = -(\Sigma_0\sigma)' \tag{3.96}$$
$$\dot{\Delta} = -(\Sigma_0\delta)' \tag{3.97}$$
$$\dot{\sigma} = 0 \tag{3.98}$$
$$\dot{\delta} = \rho \tag{3.99}$$
$$\dot{\chi} = 0 \tag{3.100}$$
$$\dot{\zeta} = 0 \tag{3.101}$$
$$\dot{\rho} = -2\Sigma_0\delta/\xi \tag{3.102}$$
$$0 = -2\Sigma_0\zeta/\xi \tag{3.103}$$

In this regime the equilibrium configuration requires that $\sigma_0 = \delta_0 = \zeta_0 = 0$ so that $\Sigma_0 \neq 0$, however there is no other constraint placed upon Σ_0. Since the equilibrium plasma density cannot be equal to zero the azimuthal fluid velocity must be equal to zero for the system to be self-consistent: $\Sigma_0 \neq 0$ implies that $\zeta = 0$ from Eq. (3.103). This is consistent with Eq. (3.101). Eqs. (3.98) and (3.100) require that the average plasma fluid velocity in the radial and azimuthal directions be constant in time and functions of ξ only: $\sigma = f_1(\xi)$, $\chi = f_2(\xi)$. For simplicity one shall stipulate that $\sigma = 0$ and due to the azimuthal symmetry inherent in the model $\chi = 0$ also. Differentiating Eq. (3.102) with respect to τ yields

$$\ddot{\rho} = -2\Sigma_0\dot{\delta}/\xi \tag{3.104}$$

Substituting from Eq. (3.99) gives the differential equation,

$$\ddot{\rho} + \omega_p^2\rho = 0 \tag{3.105}$$

where $\omega_p^2 = 2\Sigma_0/\xi$. This differential equation for ρ describes simple harmonic equation, the characteristic frequency of which is ω_p representing the plasma frequency. When the plasma charge density is perturbed, the plasma collectively responds to the resulting radial electric field, trying to restore equilibrium. The electric field accelerates the electrons and positrons in opposite directions. The particles overshoot their initial positions, due to their acquired kinetic energy, generating a new charge imbalance. Without any dissipating mechanisms this process occurs ad infinitum.

Using the dimensionalised form of the governing equations the plasma frequency is given by $\omega_p^2 = 2n_0e^2/(\epsilon_0 m)$, n_0 being the equilibrium number density (Paper I). The notable difference with the above analysis is the $1/\xi$ dependence. Recall Eq. (3.25):

$$\frac{\Sigma_0}{\xi} = \frac{(n_+ + n_-)_0}{2n_0} \tag{3.106}$$

The Paper I result where $(n_+ + n_-)_0 =$ constant is recovered by setting $\Sigma_0/\xi =$ constant, which is fully consistent with the plasma equilibrium.

3.4.2 Electrostatic oscillations in a homogeneous magnetic field

Now consider a homogeneous background magnetic field with a uniform plasma equilibrium. Returning to the full linearised equations and prescribing $\beta = \theta = \sigma_0 = \zeta_0 = 0$ yields,

$$\dot{\Sigma} = -\Sigma_0\sigma' \tag{3.107}$$
$$\dot{\Delta} = -\Sigma_0\delta' \tag{3.108}$$
$$\dot{\sigma} = \beta_0\zeta \tag{3.109}$$
$$\dot{\delta} = \rho + \beta_0\chi \tag{3.110}$$
$$\dot{\chi} = -\beta_0\delta \tag{3.111}$$
$$\dot{\zeta} = -\beta_0\sigma \tag{3.112}$$
$$\dot{\rho} = -2\Sigma_0\delta/\xi \tag{3.113}$$
$$0 = -2\Sigma_0\zeta/\xi \tag{3.114}$$

For this regime the equilibrium configuration is as described in § 3.3.2. As in the unmagnetised case Eq. (3.114) requires that $\zeta = 0$. This requires that $\sigma = 0$ from Eq. (3.112) for a non-zero magnetic field. This is consistent with Eq. (3.109) and implies that $\Sigma_0 = f_3(\xi)$ via Eq. (3.107). Differentiating Eq. (3.113) with respect to τ and substituting from Eq. (3.110) gives

$$\ddot{\rho} + 2\Sigma_0\rho/\xi = -2\Sigma_0\beta_0\chi/\xi \tag{3.115}$$

Differentiating this expression with respect to τ, substituting from Eqs. (3.111) and (3.113) and integrating with respect to time yields

$$\ddot{\rho} + \omega_H^2\rho = f_4(\xi) \tag{3.116}$$

where $\omega_H^2 = 2\Sigma_0/\xi + \beta_0^2$ is the hybrid frequency. The β_0^2 term represents the cyclotron frequency in the plasma. Following the same argument stated in the unmagnetised case one can recover the Paper II result by choosing $\Sigma_0/\xi =$ constant, which is consistent with the equilibrium configuration as elucidated in § 3.3.2.

Now, when the plasma charge density is perturbed, as the electric field accelerates the electrons and positrons in radially opposite directions the magnetic field causes the particles to participate in partial Larmor orbits with the same azimuthal velocity, Fig. 3.2(a). The electrostatic oscillation now constitutes a radial expansion and contraction, due to the electric field, plus a torsional twist thanks to the presence of the magnetic field, Fig. 3.3.

3.4.3 Electromagnetic mode in a uniform plasma permeated by a homogeneous magnetic field

When the magnetic field is homogeneous, the background equilibrium is uniform and stationary the radially propagating electromagnetic mode is described by,

$$\dot{\Sigma} = -\Sigma_0 \sigma' \tag{3.117}$$
$$\dot{\sigma} = \beta_0 \zeta \tag{3.118}$$
$$\dot{\zeta} = -\beta_0 \sigma + \theta \tag{3.119}$$
$$\dot{\theta} = -p\beta' - 2\Sigma_0 \zeta/\xi \tag{3.120}$$
$$\dot{\beta} = -\theta' - \theta/\xi \tag{3.121}$$

where no constraint is made upon the behaviour of Δ, δ, χ or ρ. Differentiating Eq. (3.120) with respect to τ yields

$$\ddot{\theta} = -p\dot{\beta}' - 2\Sigma_0 \dot{\zeta}/\xi \tag{3.122}$$
$$= p(\theta'' + \theta'/\xi - \theta/\xi^2) - 2\Sigma_0 \dot{\zeta}/\xi \tag{3.123}$$

Defining the operator $\mathcal{P}$ as

$$\mathcal{P} = \ddot{\theta} - p(\theta'' + \theta'/\xi - \theta/\xi^2) \tag{3.124}$$
$$= -2\Sigma_0 \dot{\zeta}/\xi \tag{3.125}$$
$$= -2\Sigma_0(-\beta_0 \sigma + \theta)/\xi \tag{3.126}$$

Therefore one can now write

$$\dot{\mathcal{P}} + 2\Sigma_0 \dot{\theta}/\xi = 2\Sigma_0 \beta_0 \dot{\sigma}/\xi \tag{3.127}$$
$$= 2\Sigma_0 \beta_0^2 \zeta/\xi \tag{3.128}$$

Differentiating this expression once again with respect to τ and using the definition of $\mathcal{P}$ one obtains a differential equation describing the electric field component, θ, of the electromagnetic wave

$$\ddot{\mathcal{P}} + \beta_0^2 \mathcal{P} + 2\Sigma_0 \ddot{\theta}/\xi = 0 \tag{3.129}$$

Expanding out the differential operator and assuming $\theta(\xi, \tau) = y(\xi) \exp(-i\omega\tau)$ yields

$$\left[\frac{(\xi y)'}{\xi}\right]' + \kappa^2 y = 0 \tag{3.130}$$

where

$$\kappa^2 = \frac{\omega^2}{p} \frac{(\omega^2 - 2\Sigma_0/\xi - \beta_0^2)}{(\omega^2 - \beta_0^2)} \tag{3.131}$$

Solving for the remaining plasma variables σ, ζ and β yield similar differential equations.

As described in § 3.3.2 the self-consistently calculated equilibrium does not place any constraint on the form of Σ_0. Recalling Eq. (3.106), it is clear that one can recover the Paper II result for the electromagnetic solution by self-consistently setting $\Sigma_0/\xi = \text{constant}$. In this case Eq. 3.130 has solution

$$y(\xi) = AJ_1(\kappa\xi) + BY_1(\kappa\xi) \tag{3.132}$$

This solution has the same form as Eq. (2.113) when the differing non-dimensionalised forms of the azimuthal electric field, Eq. (2.93) and Eq. (3.32), are taken into account.

3.4.4 Mode coupling via an inhomogeneous magnetic field

A radially propagating electromagnetic wave exists that requires $\Sigma \neq 0$, $\sigma \neq 0$, $\zeta \neq 0$, $\theta \neq 0$, $\beta \neq 0$ and puts no constraint on the behaviour of Δ, δ, χ or ρ. The electrostatic mode requires that $\Sigma \neq 0$, $\Delta \neq 0$, $\delta \neq 0$, $\chi \neq 0$, $\rho \neq 0$, $\sigma = 0$, $\zeta = 0$, $\theta = 0$ and $\beta = 0$. When the magnetic field is inhomogeneous these conditions are relaxed facilitating the mode coupling and resolving the disparate conditions between the electrostatic and electromagnetic modes.

When the plasma charge density is perturbed, introducing an inhomogeneous magnetic field induces a charge-dependent $\mathbf{B} \times \nabla B$ drift breaking the azimuthal symmetry in the velocity field, $\chi = 0$. This actuates a net current density in the azimuthal motion of the plasma during the oscillation: $\zeta \neq 0$, Fig. 3.2(b):

$$\mathbf{v}_{\nabla B} = \frac{m v_\perp^2}{2 q_s B} \frac{\mathbf{B} \times \nabla B}{B^2} \tag{3.133}$$

where: m is the electron/positron mass; q_s is the charge of the species and $v_\perp$ is the particles speed in the plane perpendicular to the direction of the magnetic field. Eq. 3.133 describes the dynamics of a single particle, in this fluid context it is used to illustrate the collective response of the plasma. If the radial velocity of the oscillation is assumed to oscillate sinusoidally, $v_\perp \propto \sin(\omega_H \tau)$, then the drift velocity due to the inhomogeneous magnetic field varies as $v_{\nabla B} \propto v_\perp^2 \propto \sin(\omega_H \tau) = \frac{1}{2}(1 - \cos(2\omega_H \tau))$. Therefore, during the plasma oscillation the drift velocity, $\boldsymbol{v}_{\nabla B}$, and the azimuthal current density, ζ, vary periodically with a frequency $2\omega_H$, where ω_H is the hybrid frequency when the magnetic field is homogeneous. The alternating current density ($\zeta \neq 0$) triggers axial magnetic field fluctuations ($\beta \neq 0$) and an accompanying time varying azimuthal electric field ($\theta \neq 0$) that constitute a plasma electromagnetic wave that propagates radially away from the oscillation site. Hence an electrostatic oscillation in the presence of a non-uniform magnetic field couples to a propagating electromagnetic wave with frequency $2\omega_H$.

3.5 Linear analysis

The nonlinear system of equations (3.37-3.46) does not have a closed form analytical solution and must be solved numerically. Insight into the possible dynamical responses of the magnetised pair plasma can be obtained via linear perturbation analysis.

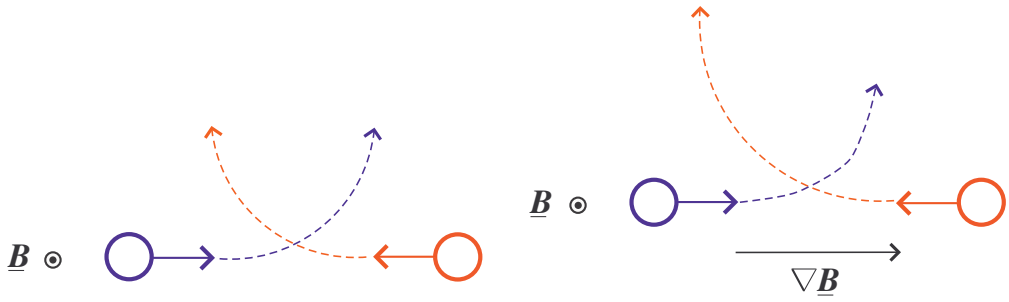

(a) Homogeneous magnetic field **(b)** Inhomogeneous magnetic field

Figure 3.2: A diagram illustrating the particle dynamics and trajectories during an electrostatic oscillation when the background magnetic field is (a) homogeneous and (b) inhomogeneous. The colour blue denotes electrons and red denotes the positrons. The picture illustrates azimuthal current density due to the charge dependent $\mathbf{B} \times \nabla B$ drift that the plasma experiences when the magnetic field is inhomogeneous. Note that in the case illustrated in (b) due to the inhomogeneous field the curvature of the trajectory will vary as $r \propto B^{-1}$.

Differentiating Eq. (3.65) with respect to ξ and replacing β_0' with Eq. (3.66) yields

$$\left[\frac{(\xi\zeta_0)'}{\xi}\right]' - \frac{2\kappa_0}{p\xi}\frac{\zeta_0}{\sqrt{\kappa_1^2 - \zeta_0^2}} = 0 \tag{3.134}$$

This defines the equilibrium of the system. Defining $\zeta_0 = \kappa_1\hat{\zeta}_0$ and substituting into Eq. (3.134) gives

$$\left[\frac{(\xi\hat{\zeta}_0)'}{\xi}\right]' - \frac{\kappa_2}{\xi}\frac{\hat{\zeta}_0}{\sqrt{1 - \hat{\zeta}_0^2}} = 0 \tag{3.135}$$

where $\kappa_2 = 2\kappa_0/(\kappa_1 p)$. According to Eq. (3.66): $\beta_0' \to 0$ when $\zeta_0 \to 0$. In the limit where $\hat{\zeta}_0$ is very small:

$$\left[\frac{(\xi\hat{\zeta}_0)'}{\xi}\right]' - \frac{\kappa_2\hat{\zeta}_0}{\xi} = 0 \tag{3.136}$$

This has solution

$$\hat{\zeta}_0 \sim K_2(2\sqrt{\kappa_2\xi}) \tag{3.137}$$

where K_2 is a modified Bessel function of the second kind. This shows that as ξ becomes large, $\hat{\zeta}_0$ and hence ζ_0 decreases in size and hence the magnitude of the magnetic field inhomogeneity β_0'. When ξ is large $\zeta_0 \ll \sigma_0$ and $\beta_0' \to 0$ allowing one to approximate $\beta_0 \approx$ constant. In this regime $\sigma_0 \to \kappa_1$, Eq. (3.64), since the radial motion of the plasma dominates the azimuthal flow and, concurrent with Eq. (3.63), implies that $\Sigma_0 \approx$ constant. To be consistent with Eq. (3.65) requires that for the scale length, R, of interest $\zeta_0' R \approx \beta_0 R \ll \kappa_1$ so that the rate of change of ζ_0 over R is very small.

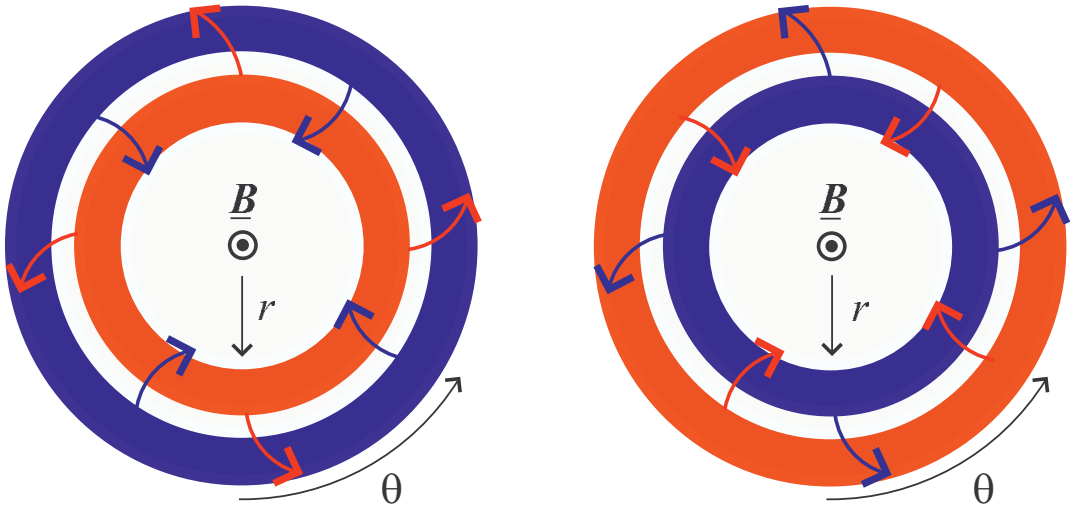

Figure 3.3: A diagram illustrating the motion of the pair plasma when the plasma charge density has been perturbed in the presence of a homogeneous magnetic field resulting in a hybrid plasma oscillation. The colour blue (red) represents a region with a net number of e^-'s (e^+'s). The diagram shows the system in the r-θ plane and exhibits the azimuthal symmetry of the problem. The arrows indicate the motion of the plasma during the plasma oscillation. The two diagrams illustrate the plasma at two separate times during a plasma oscillation. The time interval between the left and right diagrams is half a plasma period. Note that the gap between the two concentric annuli of charge is nonphysical and is included only for illustrative clarity.

Linearising the governing equations, Eqs. (3.37)-(3.46), yields

$$\dot{\Sigma} = -(\Sigma_0\sigma + \Sigma\sigma_0)' \tag{3.138}$$
$$\dot{\Delta} = -(\sigma_0\Delta + \Sigma_0\delta)' \tag{3.139}$$
$$\dot{\sigma} = -(\sigma_0\sigma)' + 2\zeta_0\zeta/\xi + \zeta_0\beta + \zeta\beta_0 \tag{3.140}$$
$$\dot{\delta} = -(\sigma_0\delta)' + 2\zeta_0\chi/\xi + \rho + \chi\beta_0 \tag{3.141}$$
$$\dot{\chi} = -\sigma_0\chi' - \zeta_0'\delta - (\sigma_0\chi + \zeta_0\delta)/\xi - \delta\beta_0 \tag{3.142}$$
$$\dot{\zeta} = -\sigma_0\zeta' - \sigma\zeta_0' - (\sigma_0\zeta + \sigma\zeta_0)/\xi + \theta - \sigma_0\beta - \sigma\beta_0 \tag{3.143}$$
$$\dot{\rho} = -\frac{2}{\xi}(\Delta\sigma_0 + \Sigma_0\delta) \tag{3.144}$$
$$\dot{\theta} = -p\beta' - \frac{2}{\xi}(\Sigma_0\zeta + \Sigma\zeta_0) \tag{3.145}$$
$$\dot{\beta} = -\theta' - \theta/\xi \tag{3.146}$$

For details refer to Appendix A. For large values of ξ the linearised equations become,

$$\begin{aligned}
\dot{\Sigma} &= -\left(\Sigma_0\sigma + \Sigma\sigma_0\right)' && (3.147)\\
\dot{\Delta} &= -\left(\sigma_0\Delta + \delta\Sigma_0\right)' && (3.148)\\
\dot{\sigma} &= -\sigma_0\sigma' + \beta_0\zeta && (3.149)\\
\dot{\delta} &= -\sigma_0\delta' + \rho + \beta_0\chi && (3.150)\\
\dot{\chi} &= -\sigma_0\chi' - \sigma_0\chi/\xi - \delta\beta_0 && (3.151)\\
\dot{\zeta} &= -\sigma_0\zeta' - \sigma_0\zeta/\xi - \sigma_0\beta - \beta_0\sigma + \theta && (3.152)\\
\dot{\rho} &= -\frac{2}{\xi}\left(\Delta\sigma_0 + \Sigma_0\delta\right) && (3.153)\\
\dot{\theta} &= -p\beta' - 2\Sigma_0\zeta/\xi && (3.154)\\
\dot{\beta} &= -\theta' - \theta/\xi && (3.155)
\end{aligned}$$

Upon inspection of the linearised governing equations it is evident that they can be split into two independent, self-consistent sets namely Eq. (3.148), (3.150), (3.151), (3.153) forming one set and Eq. (3.147), (3.149), (3.152), (3.154) and (3.155) forming the other. This simplification was exploited to obtain the following solutions.

3.5.1 Electrostatic mode

Non-zero streaming

The electrostatic solution is characterised by $\beta = 0$, $\theta = 0$ and $\zeta = 0$. Substituting these conditions into the governing equations yields,

$$\begin{aligned}
\dot{\Sigma} &= -(\Sigma_0\sigma + \sigma_0\Sigma)' && (3.156)\\
\dot{\Delta} &= -(\sigma_0\Delta + \delta\Sigma_0)' && (3.157)\\
\dot{\sigma} &= -\sigma_0\sigma' && (3.158)\\
\dot{\delta} &= -\sigma_0\delta' + \rho + \beta_0\chi && (3.159)\\
\dot{\chi} &= -\sigma_0\chi' - \sigma_0\chi/\xi - \beta_0\delta && (3.160)\\
0 &= -\beta_0\sigma && (3.161)\\
\dot{\rho} &= -2(\Delta\sigma_0 + \Sigma_0\delta)/\xi && (3.162)
\end{aligned}$$

Eq. (3.161) asserts that $\sigma = 0$, consistent with Eq. (3.158) and implies that

$$\dot{\Sigma} = -\sigma_0\Sigma' \qquad (3.163)$$

This has solution $\Sigma(\xi,\tau) = f(\tau - \xi/\sigma_0)$ where f is an arbitrary function. Rearranging Eq. (3.162) [Eq. (3.159)] for Δ [χ] and substituting into Eq. (3.157) [Eq. (3.160)] produces two differential equations both involving δ and ρ:

$$\begin{aligned}
\ddot{\delta} + 2\sigma_0\dot{\delta}' + \sigma_0^2\delta'' + \sigma_0\dot{\delta}/\xi + \sigma_0^2\delta'/\xi + \beta_0^2\delta &= \dot{\rho} + \sigma_0\rho' + \sigma_0\rho/\xi && (3.164)\\
-2\Sigma_0\delta/\xi + 2\sigma_0 C_1(\xi)/\xi &= \dot{\rho} + \sigma_0\rho' + \sigma_0\rho/\xi && (3.165)
\end{aligned}$$

where C_1 is an arbitrary function of ξ. Substituting one differential expression into the other to eliminate terms involving ρ yields the partial differential equation

$$\ddot{\delta} + 2\sigma_0\dot{\delta}' + \sigma_0^2\delta'' + \sigma_0\dot{\delta}/\xi + \sigma_0^2\delta'/\xi + (\beta_0^2 + 2\Sigma_0/\xi)\delta - 2\sigma_0 C_1(\xi)/\xi = 0 \qquad (3.166)$$

Using Eq. (3.43) as well as (3.162) in the derivation implies that $C_1 = 0 \; \forall \; \xi$. Setting $\delta(\xi, \tau) = y(\xi) \exp(-i\omega\tau)$ yields

$$\sigma_0^2 y'' + (\sigma_0^2/\xi - 2i\omega\sigma_0)y' + (\beta_0^2 + 2\Sigma_0/\xi - \omega^2 - i\omega\sigma_0/\xi)y = 0 \tag{3.167}$$

For the particular case in which the plasma density varies inversely with ξ so that $\Sigma_0 =$ constant, we can write the full solution to Eq. (3.167) as:

$$\begin{aligned} &y(\xi) = \xi^{-1/2} e^{-i\omega\xi/\sigma_0} \times \\ &\left[C_2 M\left(-\frac{i\Sigma_0}{\sigma_0\beta_0}, 0, \frac{2i\beta_0\xi}{\sigma_0} \right) + C_3 W\left(-\frac{i\Sigma_0}{\sigma_0\beta_0}, 0, \frac{2i\beta_0\xi}{\sigma_0} \right) \right] \end{aligned} \tag{3.168}$$

where M, W are Whittaker functions of the first and second kind respectively and C_2, C_3 are constants. Note that once again we assume $\sigma_0 \neq 0$ for Eq. (3.168) to be valid. M and W are related to the confluent hypergeometric functions $\mathcal{M}$ and $\mathcal{U}$ as follows [81]

$$M(\kappa, \mu, z) = e^{-z/2} z^{1/2+\mu} \mathcal{M}(1/2 + \mu - \kappa, 1 + 2\mu, z) \tag{3.169}$$

$$W(\kappa, \mu, z) = e^{-z/2} z^{1/2+\mu} \mathcal{U}(1/2 + \mu - \kappa, 1 + 2\mu, z) \tag{3.170}$$

The asymptotic expansions of $\mathcal{M}$ and $\mathcal{U}$ take the form:

$$\begin{aligned} \mathcal{M}(a, b, z) &= \frac{\Gamma(b)}{\Gamma(b-a)} e^{i\pi a} z^{-a} \left\{ \sum_{n=0}^{R-1} \frac{(a)_n (1 + a - b)_n}{n!} (-z)^{-n} \right\} \\ &+ \frac{\Gamma(b)}{\Gamma(a)} e^z z^{a-b} \left\{ \sum_{n=0}^{S-1} \frac{(b-a)_n (1-a)_n}{n!} z^{-n} \right\} \end{aligned} \tag{3.171}$$

$$\mathcal{U}(a, b, z) = z^{-a} \left\{ \sum_{n=0}^{S-1} \frac{(a)_n (1 + a - b)_n}{n!} (-z)^{-n} \right\} \tag{3.172}$$

For large $|z|$ with a and b fixed and including only the first term in the series the expansions take the form

$$\mathcal{M} = \frac{\Gamma(b)}{\Gamma(b-a)} e^{i\pi a} z^{-a} + \frac{\Gamma(b)}{\Gamma(a)} e^z z^{a-b} \tag{3.173}$$

$$\mathcal{U} = z^{-a} \tag{3.174}$$

Note that Pochhammer's Symbol $(z)_0 = 0$ [81]. Rewriting the solution in terms of the confluent hypergeometric functions and using the asymptotic expansions of $\mathcal{U}$ and $\mathcal{M}$ the solution of Eq. (3.166) yields

$$\delta(\xi, \tau) = y(\xi) \exp(-i\omega\tau) \tag{3.175}$$

$$\begin{aligned} &\sim C_4 \xi^{-1/2} \exp\left[i\omega(\xi/\sigma_0 - \tau) - i\beta_0\xi/\sigma_0 - \varphi_1 \right] \\ &+ C_5 \xi^{-1/2} \exp\left[i\omega(\xi/\sigma_0 - \tau) + i\beta_0\xi/\sigma_0 + \varphi_1 \right] \end{aligned} \tag{3.176}$$

where C_4, C_5 are complex coefficients and φ_1 is a phase term such that $|\varphi_1| \lesssim \Sigma_0 \ln\xi/(\sigma_0\beta_0)$. In the dynamical equilibrium the electrostatic oscillation is being convected at the plasma flow speed σ_0. The $\pm i\beta_0\xi/\sigma_0$ term describes the upstream and downstream movement of the plasma due to particle gyrations around the magnetic field, this effect decreases with increasing σ_0. Note the asymptotic expansion method elucidated here will be used in subsequent sections in this linear analysis.

To summarise the conditions required for the electrostatic mode are: $\beta = \beta_0$, $\theta = 0$, $\zeta = 0$, $\sigma = 0$, $\Delta \neq 0$, $\delta \neq 0$, $\chi \neq 0$ and $\rho \neq 0$.

Zero streaming

In the regime where $\sigma_0 = 0$ the differential equation (3.166) should reduce to the equivalent expression in paper II. In Paper II the linear analysis described the modes in the plasma when the background plasma was uniform and stationary. Setting $\sigma_0 = 0$ the expression becomes,

$$\ddot{\delta} + (\beta_0^2 + 2\Sigma_0/\xi)\delta = 0 \tag{3.177}$$

where the term in the brackets takes the role of the plasma hybrid frequency with the notable exception of the $1/\xi$ dependence. Since $\sigma_0 = 0$ here, there is no information governing the spatial dependence of the equilibrium density, see §3.3.3. In Paper II the background density $n_0 =$ constant is recovered by setting $\Sigma_0/\xi =$ constant [78], using the definition of ξ in Eq. (3.25). This means that the term in parenthesis in Eq. (3.177) is the square of the constant hybrid frequency ω_H, as before.

3.5.2 Electromagnetic mode

General considerations

The equations governing the decoupled electromagnetic response of the plasma are

$$\dot{\Sigma} = -(\Sigma_0\sigma + \Sigma\sigma_0)' \tag{3.178}$$
$$\dot{\sigma} = -\sigma_0\sigma' + \beta_0\zeta \tag{3.179}$$
$$\dot{\zeta} = -\sigma_0\zeta' - \sigma_0\zeta/\xi - \sigma_0\beta - \beta_0\sigma + \theta \tag{3.180}$$
$$\dot{\theta} = -p\beta' - 2\Sigma_0\zeta/\xi \tag{3.181}$$
$$\dot{\beta} = -\theta' - \theta/\xi \tag{3.182}$$

Note that no constraint is placed on the form of Δ, δ, χ and ρ. Differentiating Eq. (3.181) with respect to τ and eliminating $\dot{\beta}'$ using (3.182), one can define the operator $\mathcal{L}_0$ as,

$$\mathcal{L}_0(\theta) = \ddot{\theta} - p\left[\frac{(\xi\theta)'}{\xi}\right]' \tag{3.183}$$
$$= -2\Sigma_0\dot{\zeta}/\xi \tag{3.184}$$

Substituting for $\dot{\zeta}$ from Eq. (3.180) and collecting all θ terms together obtain,

$$\mathcal{L} = \frac{2\Sigma_0}{\xi}\left[\beta_0\sigma + \sigma_0(\beta + \zeta' + \zeta/\xi)\right] \tag{3.185}$$

where $\mathcal{L} = \mathcal{L}(\theta)$ is another operator such that

$$\mathcal{L} = \mathcal{L}_0 + 2\Sigma_0\theta/\xi \tag{3.186}$$
$$= \ddot{\theta} - p\left[\frac{(\xi\theta)'}{\xi}\right]' + 2\Sigma_0\theta/\xi \tag{3.187}$$

This definition of $\mathcal{L}$ allows $\dot{\zeta}$ to be expressed as:

$$\dot{\zeta} = \theta - \xi\mathcal{L}/2\Sigma_0 \tag{3.188}$$

Defining $\mathcal{K}$ as the operator $\mathcal{K} = \partial_\tau + \sigma_0\partial_\xi$ and applying to Eq. (3.185) yields,

$$\mathcal{K}(\xi\mathcal{L}) = 2\Sigma_0\beta_0\mathcal{K}(\sigma) + 2\Sigma_0\sigma_0\mathcal{K}(\beta + \zeta' + \zeta/\xi) \tag{3.189}$$

where $\mathcal{K}\sigma = \dot{\sigma} + \sigma_0\sigma' = \beta_0\zeta$. The second term in the expression can be expressed as,

$$\begin{aligned}
\mathcal{K}(\beta + \zeta' + \zeta/\xi) &= \dot{\beta} + \sigma_0\beta' + \dot{\zeta}' + \sigma_0\zeta'' + \dot{\zeta}/\xi + \sigma_0(\zeta/\xi)' && (3.190)\\
&= \dot{\beta} + \sigma_0\beta' + \dot{\zeta}/\xi + [\dot{\zeta} + \sigma_0(\zeta' + \zeta/\xi)]' && (3.191)\\
&= \dot{\beta} + \sigma_0\beta' + \dot{\zeta}/\xi + \theta' - \sigma_0\beta' - \beta_0\sigma' && (3.192)\\
&= \theta' - \beta_0\sigma' + \dot{\beta} + \dot{\zeta}/\xi && (3.193)
\end{aligned}$$

where we have substituted from Eq. (3.180). Therefore,

$$\mathcal{K}(\xi\mathcal{L}) = 2\Sigma_0\beta_0^2\zeta + 2\Sigma_0\sigma_0(\theta' - \beta_0\sigma' + \dot{\beta} + \dot{\zeta}/\xi) \tag{3.194}$$

Collecting terms that can be expressed directly in terms of θ on the left hand side gives,

$$\mathcal{K}(\xi\mathcal{L}) - \mathcal{H} = 2\Sigma_0\beta_0(\beta_0\zeta - \sigma_0\sigma') \tag{3.195}$$

where $\mathcal{H} = 2\Sigma_0\sigma_0(\theta' + \dot{\beta} + \dot{\zeta}/\xi)$. Focussing on $\mathcal{H}$ and substituting from equations (3.182) and (3.188) yields

$$\begin{aligned}
\mathcal{H} &= 2\Sigma_0\sigma_0(\theta' + \dot{\beta} + \dot{\zeta}/\xi) && (3.196)\\
&= 2\Sigma_0\sigma_0[\theta' - (\xi\theta)'/\xi - (\mathcal{L} - 2\Sigma_0\theta/\xi)/(2\Sigma_0)] && (3.197)\\
&= -\sigma_0\mathcal{L} && (3.198)
\end{aligned}$$

hence,

$$\mathcal{K}(\xi\mathcal{L}) + \sigma_0\mathcal{L} = 2\Sigma_0\beta_0(\beta_0\zeta - \sigma_0\sigma') \tag{3.199}$$

Applying the operator $\mathcal{K}$ to Eq. (3.199) and using equation (3.179) give,

$$\begin{aligned}
\mathcal{K}[\mathcal{K}(\xi\mathcal{L})] + \sigma_0\mathcal{K}(\mathcal{L}) &= 2\Sigma_0\beta_0^2\mathcal{K}(\zeta) - 2\Sigma_0\sigma_0\beta_0\mathcal{K}(\sigma') && (3.200)\\
&= 2\Sigma_0\beta_0[\beta_0(\dot{\zeta} + \sigma_0\zeta') - \sigma_0(\dot{\sigma}' + \sigma_0\sigma'')] && (3.201)\\
&= 2\Sigma_0\beta_0[\beta_0(\dot{\zeta} + \sigma_0\zeta') - \sigma_0\beta_0\zeta'] && (3.202)\\
&= 2\Sigma_0\beta_0^2\dot{\zeta} && (3.203)
\end{aligned}$$

where $\dot{\zeta}$ can be expressed in terms of $\mathcal{L}$ and θ via Eq. (3.188). Therefore,

$$\mathcal{K}[\mathcal{K}(\xi\mathcal{L}) + \sigma_0\mathcal{L}] + \beta_0^2\xi(\mathcal{L} - 2\Sigma_0\theta/\xi) = 0 \tag{3.204}$$

Expanding this expression and writing in terms of the parameter σ_0 yields,

$$\xi\ddot{\mathcal{L}} + \beta_0^2\xi(\mathcal{L} - 2\Sigma_0\theta/\xi) + \sigma_0[2\xi\dot{\mathcal{L}}' + 3\dot{\mathcal{L}}] + \sigma_0^2[\xi\mathcal{L}'' + 3\mathcal{L}'] = 0 \tag{3.205}$$

Writing in operator notation gives rise to

$$\mathcal{D}_0(\theta) + \sigma_0\mathcal{D}_1(\theta) + \sigma_0^2\mathcal{D}_2(\theta) = 0 \tag{3.206}$$

where

$$\begin{aligned}
\mathcal{D}_0(\theta) &= \xi\ddot{\mathcal{L}} + \beta_0^2\xi(\mathcal{L} - 2\Sigma_0\theta/\xi) && (3.207)\\
\mathcal{D}_1(\theta) &= 2\xi\dot{\mathcal{L}}' + 3\dot{\mathcal{L}} && (3.208)\\
\mathcal{D}_2(\theta) &= \xi\mathcal{L}'' + 3\mathcal{L}' && (3.209)
\end{aligned}$$

An exact solution can not be obtained for Eq. (3.205) and so an approximate solution must be pursued. Using a regular perturbation method and expressing the solution in terms of a power series in σ_0 gives

$$\theta(\xi, \tau; \sigma_0) = g(\xi, \tau) + \sigma_0 h(\xi, \tau) + \sigma_0^2 l(\xi, \tau) \tag{3.210}$$

where σ_0 is a small parameter [82]. g, h and l are solutions to $\mathcal{D}_0(g) = 0$, $\mathcal{D}_1(h) = 0$ and $\mathcal{D}_2(l) = 0$ respectively.

Zero streaming

Initially including only the zeroth order term in the expansion of the solution, $\theta = g(\xi, \tau)$, Eq. (3.206) yields

$$\mathcal{D}_0(g) = 0 \tag{3.211}$$

hence

$$\mathcal{D}(g) = \ddot{\mathcal{L}} + \beta_0^2(\mathcal{L} - 2\Sigma_0 g/\xi) = 0 \tag{3.212}$$

where $\mathcal{D}$ is an operator. Assuming $g(\xi, \tau) = y(\xi)\exp(-i\omega\tau)$

$$\begin{aligned} \mathcal{D}(y) &= \ddot{\mathcal{L}} + \beta_0^2(\mathcal{L} - 2\Sigma_0 y/\xi) && (3.213)\\ &= (\beta_0^2 - \omega^2)\mathcal{L} - 2\beta_0^2\Sigma_0 y/\xi && (3.214)\end{aligned}$$

The operator $\mathcal{L}$ becomes

$$\mathcal{L} = -\omega^2 y - p\left[\frac{(\xi y)'}{\xi}\right]' + 2\Sigma_0 y/\xi \tag{3.215}$$

Substituting this expression for $\mathcal{L}$ into Eq. (3.214) obtains,

$$\mathcal{D}(y) = \left[\frac{(\xi y)'}{\xi}\right]' + \frac{\omega^2(\omega^2 - 2\Sigma_0/\xi - \beta_0^2)}{p(\omega^2 - \beta_0^2)} y = 0 \tag{3.216}$$

This has solution of the form,

$$\begin{aligned} y(\xi) &= \frac{C_6}{\sqrt{\xi}} M\left(\frac{i\omega\Sigma_0}{\sqrt{p}(\omega^2 - \beta_0^2)}, 1, \frac{2i\omega\xi}{\sqrt{p}}\right)\\ &+ \frac{C_7}{\sqrt{\xi}} W\left(\frac{i\omega\Sigma_0}{\sqrt{p}(\omega^2 - \beta_0^2)}, 1, \frac{2i\omega\xi}{\sqrt{p}}\right) \end{aligned} \tag{3.217}$$

where M, W are Whittaker functions of the first and second kind respectively and C_6, C_7 are constants. Hence for large values of ξ, following §3.5.1, the asymptotic expansion of the solution takes the form

$$\begin{aligned} g(\xi, \tau) &= y(\xi)\exp(-i\omega\tau)\\ &\sim \frac{C_8}{\sqrt{\xi}} \exp\left[-i\omega\left(\xi + \sqrt{p}\tau\right)/\sqrt{p} + \varphi_2\right]\\ &+ \frac{C_9}{\sqrt{\xi}} \exp\left[i\omega\left(\xi - \sqrt{p}\tau\right)/\sqrt{p} - \varphi_2\right] \end{aligned} \tag{3.218}$$

where C_8, C_9 are complex coefficients and φ_2 is a phase term such that $|\varphi_2| \lesssim \omega\Sigma_0 \ln(\xi)/(\sqrt{p}(\omega^2 - \beta_0^2))$. The phase velocity of the wave is $\sqrt{p}$, the dimensionless speed of light in the plasma.

Taking only zeroth order terms corresponds to the regime where $\sigma_0 = 0$ and the above differential equation (3.216) should reduce to equivalent expression in Paper II. Following the same argument described in §3.5.1 we recover the Paper II result [78],

$$y(\xi) = C_{10} J_1(\kappa\xi) + C_{11} Y_1(\kappa\xi) \tag{3.219}$$

where

$$\kappa^2 = \frac{\omega^2(\omega^2 - 2\nu_0 - \beta_0^2)}{p(\omega^2 - \beta_0^2)} \tag{3.220}$$

J_1, Y_1 are Bessel functions of the 1^{st} and 2^{nd} kind respectively and $\nu_0 = \Sigma_0/\xi$ =constant.

Non-zero streaming

Including first order terms of the perturbation, $\theta = g(\xi,\tau) + \sigma_0 h(\xi,\tau)$, yields

$$\mathcal{D}_0(h) + \mathcal{D}_1(g) = 0 \tag{3.221}$$

$$\xi\ddot{\mathcal{L}}(h) + \beta_0^2\xi(\mathcal{L}(h) - 2\Sigma_0 h/\xi) + 2\xi\dot{\mathcal{L}}'(g) + 3\dot{\mathcal{L}}(g) = 0 \tag{3.222}$$

hence,

$$\mathcal{D}(h) = -2\dot{\mathcal{L}}' - 3\dot{\mathcal{L}}/\xi \tag{3.223}$$

Recalling that $g(\xi,\tau) = y(\xi)\exp(-i\omega\tau)$ and setting $h(\xi,\tau) = \tilde{y}(\xi)\exp(-i\omega\tau)$ yields

$$\mathcal{D}(\tilde{y}) = i\omega(2\mathcal{L}' + 3\mathcal{L}/\xi) \tag{3.224}$$

where, using Eq. (3.214), the operator $\mathcal{L}$ can be written as

$$\mathcal{L} = \frac{\mathcal{D}(y) + 2\beta_0^2\Sigma_0 y/\xi}{(\beta_0^2 - \omega^2)} \tag{3.225}$$

$$= \frac{2\beta_0^2\Sigma_0 y/\xi}{(\beta_0^2 - \omega^2)} \tag{3.226}$$

where $\mathcal{D}(y) = 0$ has been used. Using this expression for $\mathcal{L}$ and substituting into (3.224) gives,

$$\mathcal{D}(\tilde{y}) = \left[\frac{(\xi\tilde{y})'}{\xi}\right]' + \frac{\omega^2(\omega^2 - 2\Sigma_0/\xi - \beta_0^2)}{p(\omega^2 - \beta_0^2)}\tilde{y} \tag{3.227}$$

$$= \frac{2i\omega\beta_0^2\Sigma_0}{p(\omega^2 - \beta_0^2)^2}[2y'/\xi + y/\xi^2] = R(\xi) \tag{3.228}$$

One can now proceed in solving Eq. (3.228) by obtaining the complementary function from the homogeneous equation and the particular integral from a particular solution of the inhomogeneous equation. Solving $\mathcal{D}(\tilde{y}) = 0$ yields the solution (3.217) for $\tilde{y}$. For the particular integral we use the variation of parameters method [82],

$$\tilde{y}_{PI}(\xi) = -\tilde{y}_1(\xi)\int \frac{\tilde{y}_2(\xi)\,R(\xi)}{W(\tilde{y}_1,\tilde{y}_2)}\mathrm{d}\xi + \tilde{y}_2(\xi)\int \frac{\tilde{y}_1(\xi)\,R(\xi)}{W(\tilde{y}_1,\tilde{y}_2)}\mathrm{d}\xi \tag{3.229}$$

where $W(\tilde{y}_1,\tilde{y}_2)$ is the Wronskian

$$W(f_1(x),...,f_n(x)) = \begin{vmatrix} f_1(x) & f_2(x) & \dots & f_n(x) \\ f_1'(x) & f_2'(x) & \dots & f_n'(x) \\ . & . & . & . \\ . & . & . & . \\ . & . & . & . \\ f_1^{(n-1)}(x) & f_2^{(n-1)}(x) & \dots & f_n^{(n-1)}(x) \end{vmatrix} \tag{3.230}$$

and $\tilde{y}_1$, $\tilde{y}_2$ are the two linearly independent solutions to the homogeneous equation ($y = \tilde{y}_1 + \tilde{y}_2$) given by Eq. (3.217):

$$\tilde{y}_1 = C_6\frac{M(\kappa,\mu,\alpha z)}{\sqrt{z}} \tag{3.231}$$

$$\tilde{y}_2 = C_7\frac{W(\kappa,\mu,\alpha z)}{\sqrt{z}} \tag{3.232}$$

where $\kappa = i\omega\Sigma_0/[\sqrt{p}(\omega^2-\beta_0^2)]$, $\mu = 1$, $\alpha = 2i\omega/\sqrt{p}$ and $z = \xi$. Using this notation the Wronskian, $W(\tilde{y}_1, \tilde{y}_2)$, takes the form:

$$\begin{aligned} W(\tilde{y}_1,\tilde{y}_2) &= \tilde{y}_1'\tilde{y}_2 - \tilde{y}_2'\tilde{y}_1 && (3.233)\\ &= \frac{C_{12}}{z^2}[(1/2+\mu+\kappa)M(\kappa+1,\mu,\alpha z)W(\kappa,\mu,\alpha z) \\ &+ W(\kappa+1,\mu,\alpha z)M(\kappa,\mu,\alpha z)] && (3.234)\end{aligned}$$

where

$$\begin{aligned} \tilde{y}_1' &= \frac{\mathrm{d}}{\mathrm{d}z}\left[\frac{M(\kappa,\mu,\alpha z)}{\sqrt{z}}\right] && (3.235)\\ &= (\frac{1}{2}\alpha z-\kappa)\frac{M(\kappa,\mu,\alpha z)}{z^{3/2}} + (\frac{1}{2}+\mu+\kappa)\frac{M(\kappa+1,\mu,\alpha z)}{z^{3/2}} \\ &\quad -\frac{M(\kappa,\mu,\alpha z)}{2z^{3/2}} && (3.236)\\ \tilde{y}_2' &= \frac{\mathrm{d}}{\mathrm{d}z}\left[\frac{W(\kappa,\mu,\alpha z)}{\sqrt{z}}\right] && (3.237)\\ &= (\frac{1}{2}\alpha z-\kappa)\frac{W(\kappa,\mu,\alpha z)}{z^{3/2}} - \frac{W(\kappa+1,\mu,\alpha z)}{z^{3/2}} - \frac{W(\kappa,\mu,\alpha z)}{2z^{3/2}} && (3.238)\end{aligned}$$

The function R, using Eqs.(3.236) and (3.238), becomes

$$\begin{aligned} R &= \frac{2i\omega\beta_0^2\Sigma_0}{p(\omega^2-\beta_0^2)^2}[2(\tilde{y}_1+\tilde{y}_2)'/\xi + (\tilde{y}_1+\tilde{y}_2)/\xi^2] && (3.239)\\ &= \frac{C_{13}}{z^{5/2}}[C_6(\alpha z-2\kappa)M(\kappa,\mu,\alpha z) + C_6(1+2\mu+2\kappa)M(\kappa+1,\mu,\alpha z) \\ &+ C_7(\alpha z-2\kappa)W(\kappa,\mu,\alpha z) + 2C_7W(\kappa+1,\mu,\alpha z)] && (3.240)\end{aligned}$$

The integrals implicated in the particular integral do not have a closed form analytical solution. To progress the integrands will be asymptotically expanded and then evaluated, using the asymptotic forms of the solutions $\tilde{y}_{1,2}$ following §3.5.1:

$$\begin{aligned} M(\kappa,\mu,\alpha z) &\sim C_6\frac{\Gamma(1+2\mu)}{\Gamma(1/2+\mu-\kappa)}\alpha^{-\kappa}z^{-\kappa-1/2}e^{\alpha z/2} \\ &\quad -iC_6\frac{\Gamma(1+2\mu)}{\Gamma(1/2+\mu+\kappa)}e^{-i\pi\kappa}\alpha^{\kappa}z^{\kappa-1/2}e^{-\alpha z/2} && (3.241)\\ W(\kappa,\mu,\alpha z) &\sim C_7\alpha^{\kappa}z^{\kappa-1/2}e^{-\alpha z/2} && (3.242)\end{aligned}$$

Asymptotically expanding the Wronskian and retaining the dominant terms in the large ξ regime yields,

$$W(\tilde{y}_1,\tilde{y}_2) \sim \frac{C_{14}}{z^3} + \frac{C_{15}}{z} \sim \frac{C_{15}}{z} \qquad (3.243)$$

The integrands of the particular integral reduce to

$$\begin{aligned} I_1 &= \frac{\tilde{y}_1(z)R(z)}{W(\tilde{y}_1,\tilde{y}_2)} && (3.244)\\ &\sim a_0z^{2\kappa-1}e^{-\alpha z} + a_1z^{2\kappa-2}e^{-\alpha z} + a_2z^{-2} - a_3z^{-3} + a_4z^{-2\kappa-1}e^{\alpha z} \\ &\quad -a_5z^{2\kappa-2}e^{\alpha z} + a_6z^{-2\kappa-3}e^{\alpha z} - a_7z^{-1} && (3.245)\\ I_2 &= \frac{\tilde{y}_2(z)R(z)}{W(\tilde{y}_1,\tilde{y}_2)} && (3.246)\\ &\sim b_0z^{2\kappa-1}e^{-\alpha z} + b_1z^{-1} + b_2z^{2\kappa-2}e^{-\alpha z} - b_3z^{-2} + b_4z^{-3} && (3.247)\end{aligned}$$

where a_i and b_i are a set of complex coefficients. Evaluating the particular integral yields an expression consisting of Exponential integrals $E_n(z)$,

$$\begin{aligned}\int I_1 \mathrm{d}z &\sim -a_0 z^{2\kappa} E_{1-2\kappa}(\alpha z) - a_1 z^{2\kappa-1} E_{2-2\kappa}(\alpha z) - a_2 z^{-1} + \frac{1}{2} a_3 z^{-2} \\ &\quad -a_4 z^{-2\kappa} E_{2\kappa+1}(\alpha z) + a_5 z^{-2\kappa-1} E_{2\kappa+2}(-\alpha z) - a_6 z^{-2\kappa-2} E_{2\kappa+3}(-\alpha z) \\ &\quad -a_7 \ln z + a_8 \qquad (3.248)\\ \int I_2 \mathrm{d}z &\sim b_0 z^{2\kappa} E_{1-2\kappa}(\alpha z) + b_1 \ln(z) - b_2 z^{2\kappa-1} E_{2-2\kappa}(\alpha z) + b_3 z^{-1} \\ &\quad -\frac{1}{2} b_4 z^{-2} + b_5 \qquad (3.249)\end{aligned}$$

Writing these functions in their asymptotic form retaining the first term of the series viz

$$E_n(z) \sim \frac{e^{-z}}{z}\left\{1 - \frac{n}{z} + \frac{n(n+1)}{z^2} - ...\right\} \sim \frac{e^{-z}}{z} \qquad (3.250)$$

and evaluating the particular integral yields,

$$\begin{aligned}\tilde{y}_{PI} &\sim c_0 z^{3\kappa-3/2} e^{-3\alpha z/2} + c_1 z^{\kappa-1/2} \ln(z) e^{-\alpha z/2} + c_2 z^{3\kappa-5/2} e^{-3\alpha z/2} \\ &\quad + c_3 z^{\kappa-3/2} e^{-\alpha z/2} + c_4 z^{\kappa-5/2} e^{-\alpha z/2} + c_5 z^{\kappa-1/2} e^{-\alpha z/2} \\ &\quad + c_6 z^{-\kappa-1/2} \ln(z) e^{\alpha z/2} + c_7 z^{-\kappa-3/2} e^{\alpha z/2} + c_8 z^{-\kappa-5/2} e^{\alpha z/2} \\ &\quad + c_9 z^{\kappa-1/2} e^{\alpha z/2} + c_{10} z^{\kappa-7/5} e^{\alpha z/2} \qquad (3.251)\end{aligned}$$

where c_i is a set of complex coefficients. Recalling that $\kappa = i\omega\Sigma_0/[\sqrt{p}(\omega^2 - \beta_0^2)]$, $\mu = 1$, $\alpha = 2i\omega/\sqrt{p}$, $z = \xi$ and retaining only the dominant terms in the large ξ regime, the particular solution becomes,

$$\begin{aligned}\tilde{y}_{PI} \sim\ & C_{16}\xi^{-1/2}\exp\left[-i\omega\xi/\sqrt{p} + \varphi_2\right] \\ & + C_{17}\xi^{-1/2}\exp\left[i\omega\xi/\sqrt{p} - \varphi_2\right] \qquad (3.252)\end{aligned}$$

where C_{16}, C_{17} are complex coefficients. The non-zero streaming solution is therefore,

$$\begin{aligned}\theta(\xi,\tau) &= g(\xi,\tau) + \sigma_0 h(\xi,\tau) \qquad (3.253)\\ &\approx [(1+\sigma_0)C_8\xi^{-1/2} + \sigma_0 C_{16}\xi^{-1/2}]e^{-i\omega(\xi+\sqrt{p}\tau)/\sqrt{p}+\varphi_2} \qquad (3.254)\\ &+ [(1+\sigma_0)C_9\xi^{-1/2} + \sigma_0 C_{17}\xi^{-1/2}]e^{i\omega(\xi-\sqrt{p}\tau)/\sqrt{p}-\varphi_2} \qquad (3.255)\end{aligned}$$

In this non-relativistic treatment we must have $\sigma_0 \ll \sqrt{p}$ implying the radial plasma flow does not affect the propagation of the electromagnetic mode significantly. Hence the zeroth order solution dominates and higher order σ_0 terms are not required.

To summarise the conditions required for the electromagnetic mode are $\sigma \neq 0$, $\zeta \neq 0$, $\theta \neq 0$ and $\beta \neq 0$ where no constraints are placed on the form of Δ, δ, χ and ρ.

3.5.3 Convective mode

When both electromagnetic and electrostatic modes are suppressed the convective solution is obtained. Algebraically: $\theta = 0$, $\beta = 0$; and $\delta = 0$ respectively. This yields

$$\dot{\Sigma} = -(\Sigma_0\sigma + \Sigma\sigma_0)' \tag{3.256}$$
$$\dot{\Delta} = -\sigma_0\Delta' \tag{3.257}$$
$$\dot{\sigma} = -\sigma_0\sigma' + \beta_0\zeta \tag{3.258}$$
$$0 = \rho + \beta_0\chi \tag{3.259}$$
$$\dot{\chi} = -\sigma_0(\xi\chi)'/\xi \tag{3.260}$$
$$\dot{\zeta} = -\sigma_0(\xi\zeta)'/\xi - \beta_0\sigma \tag{3.261}$$
$$\dot{\rho} = -2\sigma_0\Delta/\xi \tag{3.262}$$
$$0 = -2\Sigma_0\zeta/\xi \tag{3.263}$$

Upon inspection of the equations it is clear that $\zeta = 0$ and $\sigma = 0$ in accordance with Eqs. (3.263), (3.258) respectively. Rearranging Eq. (3.262) for Δ and substituting into (3.257) gives a differential expression for ρ. The same result can be achieved by rearranging (3.259) for χ and substituting into (3.260). Therefore,

$$\dot{\rho} = -\sigma_0 \left(\xi\rho\right)' /\xi \tag{3.264}$$

Eqs. (3.256), (3.257), (3.260) and (3.264) have the general solution,

$$F(\xi,\tau) = f(\tau - \xi/\sigma_0) \tag{3.265}$$
$$G(\xi,\tau) = \frac{1}{\xi} f(\tau - \xi/\sigma_0) \tag{3.266}$$

where f is an arbitrary function, $F = \Delta, \Sigma$ and $G = \rho, \chi$. Here F and G are being convected at the streaming velocity of the plasma σ_0. Assuming $F, G \sim \exp(-i\omega\tau)$ gives the particular solutions $\propto \exp[-i\omega(\tau - \xi/\sigma_0)]$ describing a perturbation in the plasma variables propagating through the plasma at the streaming velocity σ_0. Note that the convective solution has no analogous phenomena in the zero streaming case.

3.6 Discussion and further developments

In cold pair plasmas electrostatic plasma oscillations can couple to a propagating electromagnetic mode when the background magnetic field is inhomogeneous. An inhomogeneous magnetic field permeating a plasma requires that the equilibrium be dynamic and non-uniform for the system to be self-consistent. In cylindrical coordinates, solving the system of governing equations for the equilibrium situation shows that the inhomogeneity of the field is coupled to the background plasma motion. The plasma requires that there exists a spatially varying azimuthal current to generate the magnetic gradients. The kinetic energy conservation of the equilibrium plasma flow demands that the radial flow be spatially dependent for consistency.

The linear analysis elucidated in this chapter has explored the possible dynamical responses of the magnetoplasma and hence the modes present in the system, albeit in an approximate regime. This offers guidance in respect of plasma stability and the behaviour

of the possible wave modes, aiding in the development of fully nonlinear numerical simulations. The perturbation analysis was conducted within the framework of a uniform, radially streaming plasma permeated by a constant magnetic field. The electrostatic mode in this regime manifests itself as a streaming electrostatic oscillation, in the context of the mode coupling mechanism this gives a moving source of radiation in the plasma rest frame. The electromagnetic solution is unaffected by the flow of the background plasma in this non-relativistic regime since the flow speed of the plasma is much smaller than the wave speed. This mode is analogous to the Extraordinary mode in the homogeneous pair plasma scenario. The convective solution presents an additional mode unique to the streaming regime, where perturbations of certain plasma variables are convected downstream. The connection with earlier work carried out on this problem, in which the background plasma was uniform and stationary, has been explicitly described. This analytical work lays good foundations upon which to build the fully nonlinear treatment.

This work could be extended to conduct a similar linear perturbation analysis in the small ξ regime. In this regime $\zeta_0 \gg \sigma_0$ such that the background plasma would have a dominant streaming motion in the azimuthal direction. As discussed in §3.3.3 the regime where $\sigma_0 \sim 0$ and $\zeta_0 \neq 0$ the equilibrium has an inhomogeneous magnetic field generated form a spatially dependent azimuthal current density. Recall that when there is exclusive azimuthal motion there is no constraint on the behaviour of Σ_0. Studying the dynamical response of the plasma in this context would uncover the effect, if any, of the equilibrium azimuthal motion on the plasma modes.

Chapter 4

FDTD versus Lax-Wendroff Method

4.1 Introduction

The system of equations, Eqs.(3.37)-(3.46), consists of a set of first-order hyperbolic partial differential equations, PDEs. They describe a cylindrical pair magnetoplasma permeated by a inhomogeneous magnetic field. When the plasma charge density is perturbed an electrostatic oscillation ensues that couples to a propagating electromagnetic wave. Chapter 3 investigated the mode coupling mechanism and characterised the participating normal modes in the linear regime. Although the linear perturbation analysis gave a flavour of the plasma dynamics involved, to explore the mode coupling fully the nonlinear set of equations must be solved numerically. This can be achieved using a number of procedures such as the finite element, spectral and finite difference methods, amongst others. Both the finite element and spectral methods expand the solution of the PDE in terms of a set of basis functions. In the finite element technique these basis functions are superimposed onto a family of elements that span the domain of interest, whereas spectral methods use a family of spectral functions. The finite element method excels at solving PDEs where the domain and the boundary conditions are irregular. In contrast spectral methods are less efficient at dealing with irregular domains and are much more accurate but can be exceedingly difficult to implement in comparison.

Previous work on the pair plasma mode coupling mechanism in the quasi-linear regime employed finite difference Lax-Wendroff, LW, algorithms. This numerical method transforms a continuous problem into a discrete one by replacing spatial and temporal derivatives with second order accuracy finite difference approximations, thus reducing the problem to an iterative algebraic exercise. The LW method is reliable, stable and accurate. However, depending on the complexity of the PDE and if the problem to be solved consists of a set of coupled PDEs, implementing LW can be very complicated. In comparison to the finite element and spectral method the LW method is relatively easy to implement and satisfactorily accurate.

Finite Difference Time Domain, FDTD, is an alternative method for solving first-order hyperbolic PDEs which is easier to implement and equally accurate. It entails recasting

the PDE as an ordinary differential equation, ODE, with respect to time by discretising the spatial domain and replacing the spatial derivatives with finite difference approximations. The ODE is then solved numerically via an ODE solver such as the Runge-Kutta or leap-frog methods. The FDTD method was first proposed by Yee in 1966 and was primarily used to solve electrodynamical problems where solutions to Maxwell's equations were required with imposed nontrivial boundary conditions [83]. The propagation of waves can be modelled given information regarding the permeability and permittivity of the background medium at each discrete grid point. In the pair plasma context the permittivity is dependent upon the dynamics and distribution of the plasma permeated by background electromagnetic fields.

In order to compare FDTD to LW both were used to solve the nonlinear wave equation (inviscid Burgers' equation) which emulates the form of many PDEs in which there is a convective term,

$$\partial_t u + u\partial_x u = 0 \tag{4.1}$$

The inviscid Burgers' equation describes a nonlinear wave propagating to the right with a speed proportional to its amplitude, u. Therefore larger wave amplitudes propagate faster than smaller components: this causes the wave to shock due to nonlinear steepening, like the phenomenon of breaker ocean waves. The relative empirical stability of the two numerical methods can be assessed by comparing how long it takes the convective instability to occur in each algorithm.

In comparison to Eq. (4.1) the linear wave equation describes a wave moving to the right at constant speed a,

$$\partial_t u + a\partial_x u = 0 \tag{4.2}$$

This chapter begins by discussing the Lax-Wendroff algorithm for the nonlinear wave equation and then proceeds by introducing the FDTD method. It concludes with the numerical simulations that compare the two algorithms and discusses their relative stability.

4.2 Lax-Wendroff Method

To obtain a finite difference solution of Eq. (4.1) the domain described by the PDE is defined in terms of a rectilinear grid, its edges parallel to the x and t axes. Defining discrete coordinates $x = mh$ and $t = nk$ such that $m \in [0, m_{max}]$, $n \in [0, n_{max}]$ an arbitrary grid point is given by the coordinate (mh, nk) where m, n are integers and h, k are the grid spacings in the x and t coordinates respectively. Writing $u(nk, mh) = u_m^n$ the finite difference formulae are obtained from the Taylor expansion of u about t in the neighbourhood of k, while holding x fixed [84],

$$u_m^{n+1} = \exp(k\partial_t)u_m^n \tag{4.3}$$

$$\approx \left(1 + k\partial_t + \frac{1}{2}k^2\partial_t^2\right)u_m^n \tag{4.4}$$

The LW method contains an inherent diffusion term, ∂_t^2, that helps dampen the instability. For the case of the linear wave equation $\partial_t u_m^n$ is replaced by $-a\partial_x u_m^n$ and $\partial_t^2 u_m^n$ by $a\partial_x^2 u_m^n$ using Eq. (4.2). Therefore,

$$u_m^{n+1} = \left(1 - ka\partial_x + \frac{1}{2}k^2a^2\partial_x^2\right)u_m^n \tag{4.5}$$

Using the finite difference approximations:

$$\partial_x u_m^n = \frac{u_{m+1}^n - u_{m-1}^n}{2h} \tag{4.6}$$

$$\partial_x^2 u_m^n = \frac{u_{m+1}^n - 2u_m^n + u_{m-1}^n}{h^2} \tag{4.7}$$

this yields the Lax-Wendroff algorithm for the linear wave equation,

$$u_m^{n+1} = (1 - p^2a^2)u_m^n - \frac{1}{2}pa(u_{m+1}^n - u_{m-1}^n) + \frac{1}{2}p^2a^2(u_{m+1}^n + u_{m-1}^n) \tag{4.8}$$

where $p = k/h$ is the mesh ratio. One of the advantages of the finite difference method is that it is very easily extended to the solution of nonlinear equations since in all but special cases many of the methods and proofs are invariant.

For the nonlinear equation, Eq. (4.1), the finite difference formulae Eq. (4.4) is used where $\partial_t u_m^n$ is replaced by $-u_m^n \partial_x u_m^n$, using Eq. (4.1), and $\partial_t^2 u_m^n$ is replaced by the following,

$$\partial_t^2 u_m^n = -\partial_t \left(u_m^n \partial_x u_m^n\right) \tag{4.9}$$

$$= -\partial_t u_m^n \partial_x u_m^n - u_m^n \partial_t \left(\partial_x u_m^n\right) \tag{4.10}$$

$$= u_m^n \left(\partial_x u_m^n\right)^2 + u_m^n \partial_x \left(u_m^n \partial_x u_m^n\right) \tag{4.11}$$

$$= 2u_m^n \left(\partial_x u_m^n\right)^2 + \left(u_m^n\right)^2 \partial_x^2 u_m^n \tag{4.12}$$

Substituting into the finite difference expression Eq. (4.4) yields

$$u_m^{n+1} = u_m^n - ku_m^n \partial_x u_m^n + k^2 u_m^n (\partial_x u_m^n)^2 + \frac{1}{2}k^2 (u_m^n)^2 \partial_x^2 u_m^n \tag{4.13}$$

The Lax-Wendroff algorithm for the nonlinear wave equation becomes,

$$u_m^{n+1} = u_m^n - \frac{1}{2}pu_m^n \left(u_{m+1}^n - u_{m+1}^n\right) + \frac{1}{4}p^2 u_m^n \left(u_{m+1}^n - u_{m-1}^n\right)^2 + \frac{1}{2}p^2 \left(u_m^n\right)^2 \left(u_{m+1}^n - 2u_m^n + u_{m-1}^n\right) \tag{4.14}$$

where the finite difference approximations Eq. (4.6) and (4.7) have been used. Numerical algorithms for solving partial differential equations are only useful if they are convergent and stable. A finite difference algorithm is deemed convergent if the difference between the theoretical solutions of the differential and difference equations at a fixed coordinate (x, t) tends to zero when the number of grid points in a fixed size numerical domain is increased: $h, k \to 0$ and $m, n \to \infty$ [84]. An algorithm is considered stable when the difference between the theoretical and numerical solution of the difference equation remains bounded as n tends to infinity. The von Neumann stability analysis for the linear wave equation algorithm, Eq. (4.8), states that the scheme is stable provided $0 < p|a| \leqslant 1$, which appropriately coincides with the Courant-Friedrichs-Lewy (C.F.L) condition for the convergence of the algorithm. This result is used as a guide for the stability and convergence of the nonlinear expression, ergo: $0 < p|u_m^n| \leqslant 1$. However, care must be taken in dealing with nonlinear terms in hyperbolic equations.

An alternative numerical algorithm is possible if the second righthand term of Eq.(4.11) is differenced directly: Substituting Eq. (4.11) into Eq.(4.4) gives,

$$u_m^{n+1} = u_m^n - ku_m^n \partial_x u_m^n + \frac{1}{2}k^2 u_m^n (\partial_x u_m^n)^2 + \frac{1}{2}k^2 u_m^n \partial_x (u_m^n \partial_x u_m^n) \tag{4.15}$$

where

$$\partial_x(u_m^n \partial_x u_m^n) = \frac{1}{2h}\partial_x[u_m^n(u_{m+1}^n - u_{m-1}^n)] \quad (4.16)$$

$$= \frac{1}{4h^2}[u_{m+1}^n(u_{m+2}^n - u_m^n) - u_{m-1}^n(n_m^n - u_{m-2}^n)] \quad (4.17)$$

This yields an alternative algorithm

$$u_m^{n+1} = u_m^n - \frac{1}{2}pu_m^n\left(u_{m+1}^n - u_{m-1}^n\right) + \frac{1}{8}p^2u_m^n\left(u_{m+1}^n - u_{m-1}^n\right)^2$$
$$+\frac{1}{8}p^2u_m^n\left[u_{m+1}^n\left(u_{m+2}^n - u_m^n\right) - u_{m-1}^n\left(u_m^n - u_{m-2}^n\right)\right] \quad (4.18)$$

Note that this version uses next nearest neighbours.

4.2.1 Conservative form

Additional finite difference algorithms can be derived by considering the conservative form of the nonlinear wave equation,

$$\partial_t u + \partial_x f = 0 \quad (4.19)$$

$$f(u,x,t) = u^2/2 \quad (4.20)$$

Conservative forms can be less prone to instability. Following the previous derivation and using Eq. (4.4), the $\partial_t^2 u_m^n$ term is replaced with:

$$\partial_t^2 u = -\partial_x(\partial_t f)$$
$$= -\partial_x(\partial_u f \partial_t u)$$
$$= \partial_x(\partial_u f \partial_x f)$$
$$= \partial_x(u\partial_x f) \quad (4.21)$$
$$= \partial_x u \partial_x f + u\partial_x^2 f \quad (4.22)$$

Substituting Eq.(4.22) into Eq. (4.4) and using $\partial_t u_m^n = -\partial_x f_m^n$ yields,

$$u_m^{n+1} = u_m^n - k\partial_x f_m^n + \frac{1}{2}k^2\partial_x u_m^n \partial_x f_m^n + \frac{1}{2}k^2 u_m^n \partial_x^2 f_m^n \quad (4.23)$$

where $f_m^n = (u_m^n)^2/2$. The Lax-Wendroff algorithm for the conservative form of the nonlinear wave equation is

$$u_m^{n+1} = u_m^n\left[1 + \frac{1}{4}p^2\left[\left(u_{m+1}^n\right)^2 + \left(u_{m-1}^n\right)^2 - 2\left(u_m^n\right)^2\right]\right]$$
$$- \frac{1}{4}p\left[\left(u_{m+1}^n\right)^2 - \left(u_{m-1}^n\right)^2\right]$$
$$+ \frac{1}{16}p^2\left(u_{m+1}^n - u_{m-1}^n\right)\left[\left(u_{m+1}^n\right)^2 - \left(u_{m-1}^n\right)^2\right] \quad (4.24)$$

Using Eq.(4.21) in Eq. (4.4) instead of Eq. (4.22) yields

$$u_m^{n+1} = u_m^n - k\partial_x f_m^n + \frac{1}{2}k^2\partial_x(u_m^n \partial_x f_m^n) \quad (4.25)$$

Differencing the derivative in the final term directly produces an alternative conservative algorithm:

$$\begin{aligned}\partial(u_m^n \partial_x f_m^n) &= \frac{1}{2h}\partial_x[u_m^n(f_{m+1}^n - f_{m-1}^n)] \\ &= \frac{1}{4h^2}[u_{m+1}^n(f_{m+2}^n - f_m^n) - u_{m-1}^n(f_m^n - f_{m-2}^n)] \end{aligned} \tag{4.26}$$

Therefore

$$\begin{aligned}u_m^{n+1} = u_m^n\left[1 - \frac{1}{16}p^2 u_m^n\left(u_{m+1}^n + u_{m-1}^n\right)\right] - \frac{1}{4}p\left[\left(u_{m+1}^n\right)^2 - \left(u_{m-1}^n\right)^2\right] \\ + \frac{1}{16}p^2\left[u_{m+1}^n\left(u_{m+2}^n\right)^2 + u_{m-1}^n\left(u_{m-2}^n\right)^2\right]\end{aligned} \tag{4.27}$$

4.3 Finite Difference Time Domain Method

The FDTD method is as follows. Using the predefined discrete coordinates $x = mh$ and writing $u(t, mh) = u_m(t) = u_m$ the spatial derivative in the nonlinear equation was replaced by the central difference formula, Eq. (4.6), yielding,

$$\partial_t u_m = -u_m \frac{(u_{m+1} - u_{m-1})}{2h} \tag{4.28}$$

This is a first order ODE with respect to time where h is the distance between successive spatial grid points. Solving using a 4th order Runge-Kutta method gives,

$$k_1 = -\frac{\triangle t}{2h} u_m (u_{m+1} - u_{m-1}) \tag{4.29}$$

$$k_2 = -\frac{\triangle t}{2h} (u_m + k_1/2)(u_{m+1} - u_{m-1}) \tag{4.30}$$

$$k_3 = -\frac{\triangle t}{2h} (u_m + k_2/2)(u_{m+1} - u_{m-1}) \tag{4.31}$$

$$k_4 = -\frac{\triangle t}{2h} (u_m + k_3)(u_{m+1} - u_{m-1}) \tag{4.32}$$

$$\triangle t = T/N \tag{4.33}$$

$$u_m^{n+1} = u_m^n + \frac{k_1}{6} + \frac{k_2}{3} + \frac{k_3}{3} + \frac{k_4}{6} \tag{4.34}$$

where $\triangle t$ is the time step, N is the number of time steps and T is the integration time such that $T = N\Delta t$. By considering the conservative form of the nonlinear wave equation, another FDTD algorithm can be derived. Substituting for the central difference formula yields,

$$\partial_t u_m = -\frac{1}{4h}\left[(u_{m+1})^2 - (u_{m-1})^2\right] \tag{4.35}$$

The corresponding Runge-Kutta algorithm is therefore,

$$k_1 = -\frac{\triangle t}{4h}\left[(u_{m+1})^2 - (u_{m-1})^2\right]$$

$$k_1 = k_2 = k_3 = k_4$$

$$u_m^{n+1} = u_m^n + k_1 \tag{4.36}$$

4.4 Numerical Simulations

To compare the FDTD and LW algorithms both were used to solve the nonlinear wave equation, the inviscid Burgers' equation,

$$\partial_t u + u\partial_x u = 0 \tag{4.37}$$

For the initial conditions the wave amplitude was perturbed from uniform equilibrium in the shape of a Gaussian waveform

$$u_m(0) = A_0 \exp\left[-\varsigma(m - m_0)^2\right] \tag{4.38}$$

$\forall\ m$, where A_0 is the amplitude of the perturbation, ς defines its width and m_0 is the centre of the computational domain (See Fig. 4.1). Each algorithm was computed for a prescribed length of time $T = n_{max}k = N\triangle t$ for the specified initial condition. So that the LW and FDTD methods could be compared the values of $p = k/h$ and $\triangle t$ had to be chosen carefully. Setting $N = n_{max}$ requires that $\triangle t = k$ implying $p = k/h = \triangle t/h$. For the simulations the boundary conditions were: $u_0(t) = u_{m_{max}}(t) = 0$ for all t.

4.5 Results and discussion

A comparison of all 6 numerical schemes represented by Eqs. (4.14), (4.18), (4.24), (4.27), (4.34) and (4.36) is shown in Figs. 4.2-4.8. The inviscid Burgers' equation describes a nonlinear wave where the speed of propagation is a function of amplitude, ultimately leading to wave steepening and shocks. As the coherent wave behaviour breaks down, for one spatial mesh point there exists two values for the wave amplitude, u, and the algorithm becomes unstable.

The difference between the stability of the algorithms is very small implying that the FDTD methods are just as stable as the LW ones. Looking at Fig. 4.2 it is noticeable that the stability of the conservative algorithms is slightly better than the non-conservative forms since they, in comparison, exhibit an advanced evolution of the convective instability at time step $n = 560$. Both versions of the conservative Lax-Wendroff algorithm, Figs. 4.7 and 4.8, appear the most stable closely followed by the conservative FDTD algorithm, Fig. 4.4. The FDTD algorithm presents the least stable, Fig. 4.3.

The LW algorithms contain an inherent diffusive term that help to dampen the instability, quenching the wave steepening for a while. In contrast, FDTD algorithms lack a diffusive term to counteract the inevitable instability and cannot resist the onset of wave steepening for as long. In spite of this the FDTD algorithms do well to sustain coherent behaviour. In principle one could add a stabilising diffusive term:

$$\partial_t u + u\partial_x u - \nu\partial_x^2 u = 0 \tag{4.39}$$

this is Burgers' equation where ν is the viscosity coefficient. If the diffusive term quenches the wave steepening a stable solitary wave structure persists.

The efficacy of a numerical algorithm depends upon a number of criteria including stability, accuracy and ease of implementation. In comparison to the LW method, FDTD is very easy to implement, particularly when a system of coupled differential equations is

considered. For a system of equations the LW algorithm can become hard to obtain as the Jacobian of the system becomes more involved. Although in this empirical stability assessment the LW method exhibits greater stability, it is marginal and cannot solely justify the choice of LW over FDTD. With this in mind it seems reasonable to opt for FDTD for the solution of the nonlinear set of equations governing the evolution of an inhomogeneous cold pair plasma.

Parameter	Value	
A_0	5.0×10^{-1}	amplitude of the perturbation
m_0	50	centre of computational domain
m_{max}	100	number of spatial points
N, n_{max}	1000	number of time steps
Δt, k	1.0×10^{-2}	temporal step size
h	0.2	spatial mesh increment
ς	5.0×10^{-3}	Gaussian coefficient
p	0.05	mesh ratio

Table 4.1: Parameters for FDTD vs LW numerical simulations.

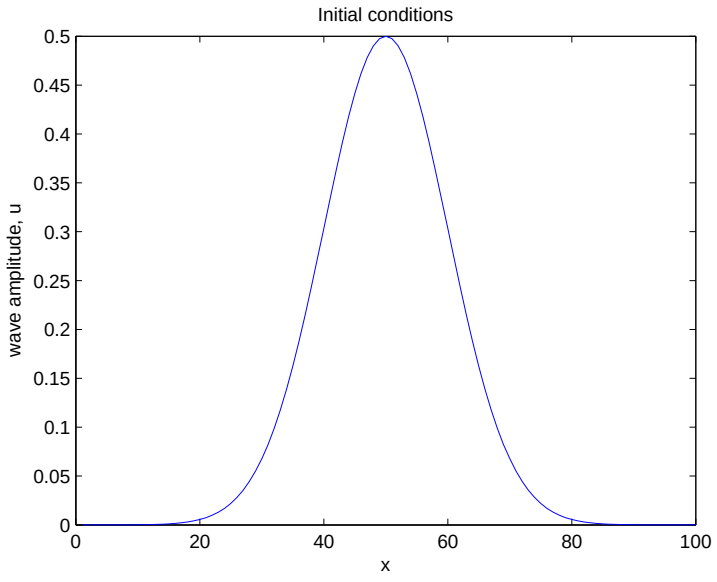

Figure 4.1: Initial perturbation for the solution of the nonlinear wave equation.

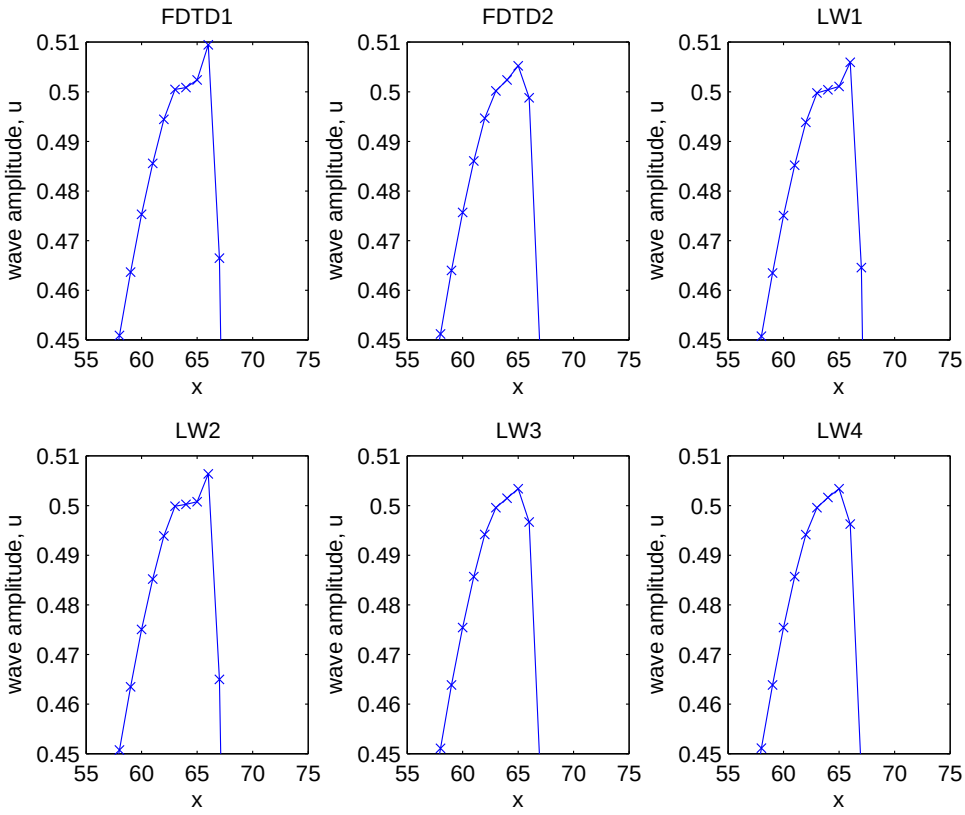

Figure 4.2: Solution of Eq. (4.1) from Eqs. (4.14), (4.18), (4.27), (4.24), (4.34), (4.36) denoted by LW1, LW2, LW3, LW4, FDTD1, FDTD2 respectively. Plots show snapshot of the spatial structure at time step $n = 560$. The spatial extent does not cover the whole numerical domain, focusing on the region of interest between $m = 55$ and $m = 75$. The plots exhibit the development of the convective instability.

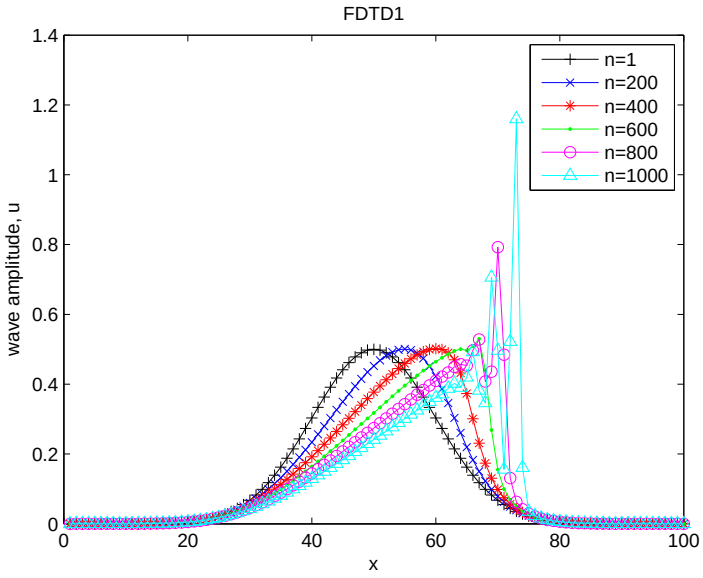

Figure 4.3: Solution of Eq. (4.1) obtained from FDTD algorithm, Eq. (4.34). Plots display spatial structure for time steps $n = 1$, 200, 400, 600, 800 and 1000 exhibiting the evolution of the convective instability.

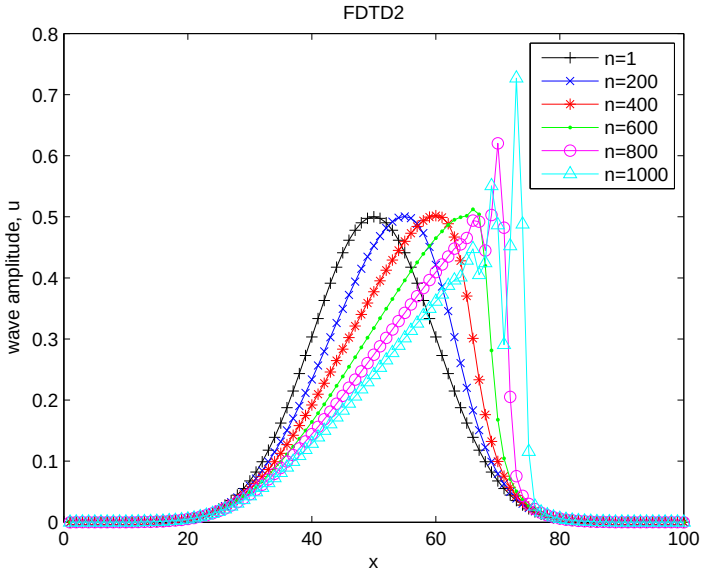

Figure 4.4: Solution of Eq. (4.1) obtained from FDTD algorithm, Eq. (4.36). Plots display spatial structure for time steps $n = 1$, 200, 400, 600, 800 and 1000 exhibiting the evolution of the convective instability.

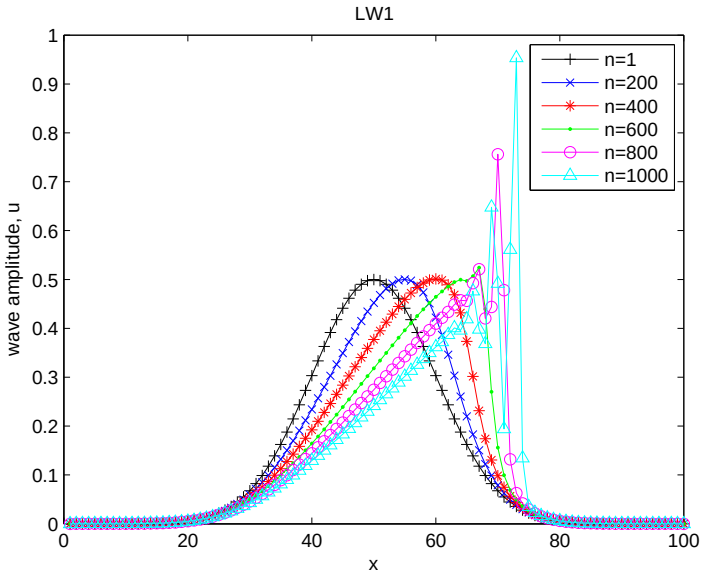

Figure 4.5: Solution of Eq. (4.1) obtained from FDTD algorithm, Eq. (4.14). Plots display spatial structure for time steps $n = 1$, 200, 400, 600, 800 and 1000 exhibiting the evolution of the convective instability.

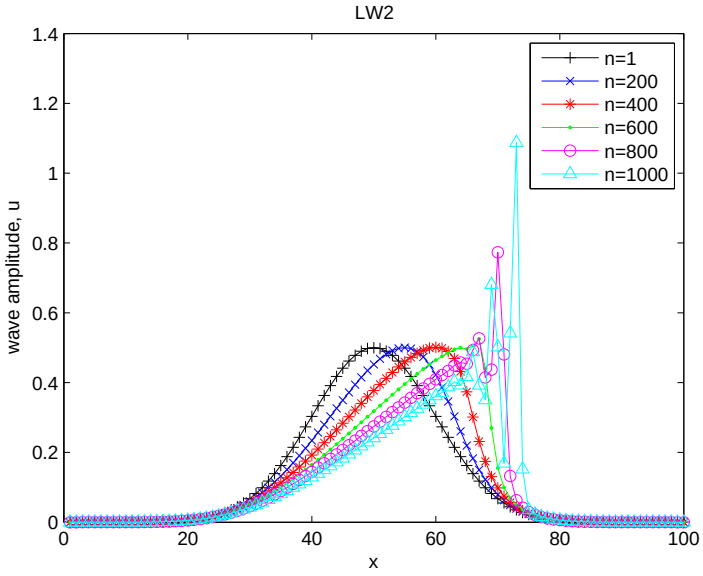

Figure 4.6: Solution of Eq. (4.1) obtained from FDTD algorithm, Eq. (4.18). Plots display spatial structure for time steps $n = 1$, 200, 400, 600, 800 and 1000 exhibiting the evolution of the convective instability.

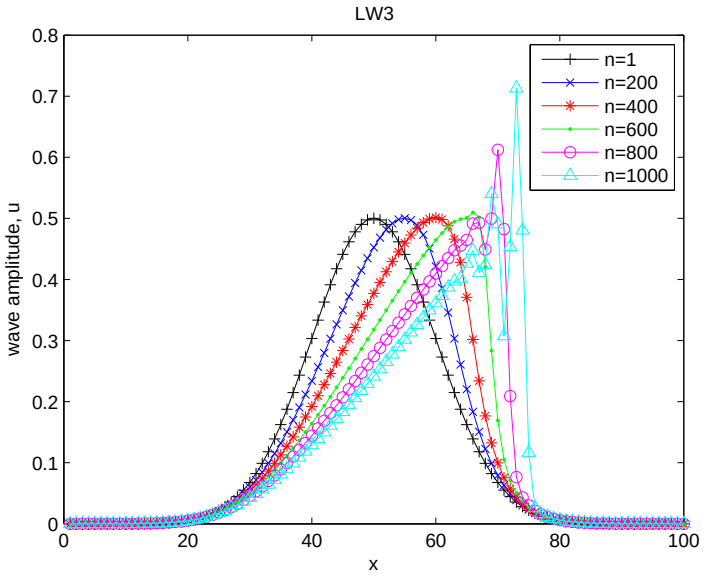

Figure 4.7: Solution of Eq. (4.1) obtained from FDTD algorithm, Eq. (4.27). Plots display spatial structure for time steps $n = 1$, 200, 400, 600, 800 and 1000 exhibiting the evolution of the convective instability.

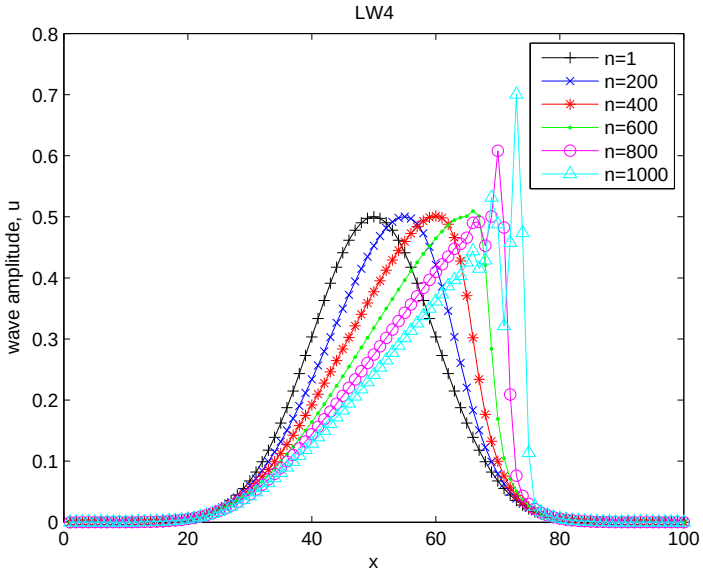

Figure 4.8: Solution of Eq. (4.1) obtained from FDTD algorithm, Eq. (4.24). Plots display spatial structure for time steps $n = 1$, 200, 400, 600, 800 and 1000 exhibiting the evolution of the convective instability.

Chapter 5

Nonlinear mode coupling in pair plasmas: Nonlinear analysis

5.1 Introduction

For a cold pair magnetoplasma in cylindrical coordinates the system of governing equations describing the mode coupling mechanism are

$$\dot{\Sigma} = -\left(\Sigma\sigma + \Delta\delta\right)' \tag{5.1}$$
$$\dot{\Delta} = -\left(\Delta\sigma + \Sigma\delta\right)' \tag{5.2}$$
$$\dot{\sigma} = -\frac{1}{2}(\sigma^2 + \delta^2)' + (\chi^2 + \zeta^2)/\xi + \zeta\left(\beta_0 + \beta\right) \tag{5.3}$$
$$\dot{\delta} = -\left(\sigma\delta\right)' + 2\chi\zeta/\xi + \rho + \chi\left(\beta_0 + \beta\right) \tag{5.4}$$
$$\dot{\chi} = -\chi'\sigma - \zeta'\delta - \left(\chi\sigma + \zeta\delta\right)/\xi - \delta\left(\beta_0 + \beta\right) \tag{5.5}$$
$$\dot{\zeta} = -\sigma\zeta' - \delta\chi' - \left(\sigma\zeta + \delta\chi\right)/\xi + \theta - \sigma\left(\beta_0 + \beta\right) \tag{5.6}$$
$$(\xi\rho)' = 2\Delta \tag{5.7}$$
$$\dot{\rho} = -\frac{2}{\xi}\left(\Delta\sigma + \Sigma\delta\right) \tag{5.8}$$
$$\dot{\theta} = -p\left(\beta_0 + \beta\right)' - \frac{2}{\xi}\left(\Sigma\zeta + \Delta\chi\right) \tag{5.9}$$
$$\dot{\beta} = -\theta' - \theta/\xi \tag{5.10}$$

where $p = c^2/(\omega_0^2 L^2)$ is the dimensionless speed of light squared in the plasma. Since the background magnetic field is inhomogeneous self-consistency demands that the plasma

equilibrium must be non-uniform and in dynamical equilibrium described by

$$\Sigma_0 = \kappa_0/\sigma_0 \tag{5.11}$$

$$\sigma_0 = \sqrt{\kappa_1^2 - \zeta_0^2} \tag{5.12}$$

$$\zeta_0' = -\frac{\zeta_0}{\xi} - \beta_0 \tag{5.13}$$

$$\beta_0' = -\frac{2\kappa_0}{p\xi}\frac{\zeta_0}{\sqrt{\kappa_1^2 - \zeta_0^2}} \tag{5.14}$$

These nonlinear systems of equations do not have a closed form analytical solution and must be solved numerically.

In the quasi-linear regime the numerical solution of these equations successfully showcased the mode coupling mechanism where the electrostatic oscillations were perturbed from a uniform plasma equilibrium. In this treatment a hybrid Law-Wendroff, Runge-Kutta algorithm was exploited, calculating the resulting electromagnetic wave fields from a prescribed magnetic field inhomogeneity. In these simulations the full nonlinear nature of the coupling mechanism could not be explored and did not calculate the equilibrium configuration self-consistently. The simulations presented here will rectify these issues.

Chapter 3 identified the modes required for the coupling mechanism in the large ξ regime where the equilibrium consisted of a constant radial flow: namely the electrostatic and electromagnetic modes. Chapter 4 investigated the efficacy of using a FDTD algorithm for the solution of the nonlinear set of equations governing the evolution of an inhomogeneous cold pair plasma. The focus of this chapter will be the nonlinear generation of electromagnetic waves by large amplitude electrostatic oscillations. It details the nonlinear numerical simulations of the mode coupling, outlining the numerical procedure utilised in Section 5.2 and discussing the subsequent simulations in Section 5.3. The numerical results presented in this chapter were obtained by the author on a code written in conjunction with A. A. da Costa. The main structure of the code was laid in place by da Costa, with the completion of the working code carried out by the author. The authors contributions include writing the equilibrium calculation algorithm, the initial condition algorithms and contributing to the FDTD algorithm.

5.2 Numerical technique

The stated sets of differential equations must be solved numerically. The inhomogeneous magnetic field permeating the pair plasma couples electrostatic oscillations to an electromagnetic mode. In order to perturb the electrostatic oscillation information is required about the form of the plasma equilibrium which can be obtained by solving Eqs. (5.11-5.14). From here the temporal and spatial evolution of the velocity and electromagnetic fields can be solved via Eqs. (5.1-5.10). This section details the numerical methods utilised to solve the self-consistent system of equations.

5.2.1 Dynamical equilibrium

Recall the system of equations describing the dynamical equilibrium of the system, namely Eq. (5.11)-(5.14). Defining

$$\zeta_0 = \kappa_1 \hat{\zeta}_0 \tag{5.15}$$
$$\beta_0 = \kappa_1 \hat{\beta}_0 \tag{5.16}$$

and substituting into (5.11)-(5.14) yields

$$\Sigma_0 = \frac{\kappa_0}{\kappa_1} \frac{1}{\sqrt{1-\hat{\zeta}_0^2}} \tag{5.17}$$
$$\sigma_0 = \kappa_1 \sqrt{1-\hat{\zeta}_0^2} \tag{5.18}$$
$$\hat{\zeta}_0' = -\frac{\hat{\zeta}_0}{\xi} - \hat{\beta}_0 \tag{5.19}$$
$$\hat{\beta}_0' = -\frac{\kappa_2}{\xi} \frac{\hat{\zeta}_0}{\sqrt{1-\hat{\zeta}_0^2}} \tag{5.20}$$

where $\kappa_2 = 2\kappa_0/p\kappa_1$ controls the strength of the magnetic inhomogeneity via Eq. (5.20). The system of equations comprise two coupled ordinary differential equations, Eq. (5.19, 5.20), the solution of which gives σ_0, Σ_0 via Eq. (5.18) and (5.17). The coupled set were numerically solved using a fourth order Runge-Kutta routine by integrating the equations from a defined starting point ξ_i (where $\hat{\zeta}_0$, $\hat{\beta}_0$ are specified) towards $\xi = 0$ for a prescribed spatial length, $\Xi \in \xi$. Note that $\Xi = m_{max}\mathrm{d}\Xi$ where m_{max} is the number of spatial grid points and $\mathrm{d}\Xi$ is the spatial step size. This defines the numerical domain within which subsequent calculations will be carried out namely, $[\xi_0, \xi_i]$ where $\xi_0 = \xi_i - \Xi$. Defining a spatial grid on this domain with discrete coordinates $\xi = \xi_0 + m\mathrm{d}\Xi$ where $m \in [0, m_{max}]$ such that $[\xi_0, \xi_i] = [\xi_0, \xi_0 + m_{max}\mathrm{d}\Xi]$

The Runge-Kutta algorithm for the solution of the coupled equilibrium equations is:

$$k_{\hat{\zeta}_0 1} = -\mathrm{d}\xi \left[-\frac{\hat{\zeta}_{0,m}}{\xi} - \hat{\beta}_{0,m} \right] \tag{5.21}$$
$$k_{\hat{\zeta}_0 2} = -\mathrm{d}\xi \left[-\frac{(\hat{\zeta}_{0,m} + k_{\hat{\zeta}_0 1}/2)}{(\xi + \mathrm{d}\xi/2)} - (\hat{\beta}_{0,m} + k_{\hat{\beta}_0 1}/2) \right] \tag{5.22}$$
$$k_{\hat{\zeta}_0 3} = -\mathrm{d}\xi \left[-\frac{(\hat{\zeta}_{0,m} + k_{\hat{\zeta}_0 2}/2)}{(\xi + \mathrm{d}\xi/2)} - (\hat{\beta}_{0,m} + k_{\hat{\beta}_0 2}/2) \right] \tag{5.23}$$
$$k_{\hat{\zeta}_0 4} = -\mathrm{d}\xi \left[-\frac{(\hat{\zeta}_{0,m} + k_{\hat{\zeta}_0 3})}{(\xi + \mathrm{d}\xi)} - (\hat{\beta}_{0,m} + k_{\hat{\beta}_0 3}) \right] \tag{5.24}$$

where the $k_{\hat{\beta}_0 i}$ parameters are given by

$$k_{\hat{\beta}_0 1} = -\mathrm{d}\xi \left[-\frac{\kappa_2}{\xi} \frac{\hat{\zeta}_{0,m}}{\sqrt{1-\hat{\zeta}_{0,m}^2}} \right] \tag{5.25}$$

$$k_{\hat{\beta}_0 2} = -\mathrm{d}\xi \left[-\frac{\kappa_2}{(\xi+\mathrm{d}\xi/2)} \frac{(\hat{\zeta}_{0,m}+k_{\hat{\zeta}_0 1}/2)}{\sqrt{1-(\hat{\zeta}_{0,m}+k_{\hat{\zeta}_0 1}/2)^2}} \right] \tag{5.26}$$

$$k_{\hat{\beta}_0 3} = -\mathrm{d}\xi \left[-\frac{\kappa_2}{(\xi+\mathrm{d}\xi/2)} \frac{(\hat{\zeta}_{0,m}+k_{\hat{\zeta}_0 2}/2)}{\sqrt{1-(\hat{\zeta}_{0,m}+k_{\hat{\zeta}_0 2}/2)^2}} \right] \tag{5.27}$$

$$k_{\hat{\beta}_0 4} = -\mathrm{d}\xi \left[-\frac{\kappa_2}{(\xi+\mathrm{d}\xi)} \frac{(\hat{\zeta}_{0,m}+k_{\hat{\zeta}_0 3})}{\sqrt{1-(\hat{\zeta}_{0,m}+k_{\hat{\zeta}_0 3})^2}} \right] \tag{5.28}$$

Therefore

$$\hat{\zeta}_{0,m+1} = \hat{\zeta}_{0,m} + \frac{k_{\hat{\zeta}_0 1}}{6} + \frac{k_{\hat{\zeta}_0 2}}{3} + \frac{k_{\hat{\zeta}_0 3}}{3} + \frac{k_{\hat{\zeta}_0 4}}{6} \tag{5.29}$$

$$\hat{\beta}_{0,m+1} = \hat{\beta}_{0,m} + \frac{k_{\hat{\beta}_0 1}}{6} + \frac{k_{\hat{\beta}_0 2}}{3} + \frac{k_{\hat{\beta}_0 3}}{3} + \frac{k_{\hat{\beta}_0 4}}{6} \tag{5.30}$$

The parameters κ_0, κ_1 and κ_2 characterise the solution and infer the value of p consistent with the system. κ_2 is a key parameter (along with Ξ, the initial values of $\hat{\beta}_0(\xi_i)$, $\hat{\zeta}_0(\xi_i)$ and ξ_i) since it defines the form of the solution while κ_0 and κ_1 merely scale it. Fig. 5.1 shows a typical example of a calculated equilibrium using the values shown in Table 5.3.

5.2.2 Non-relativistic regime

In principle the parameters κ_i can be arbitrarily chosen to characterise the system, for instance using a large value of κ_2 to obtain a large magnetic field inhomogeneity. Care has to be taken, however, since the model described here is a non-relativistic one. Recall the equation for σ,

$$\sigma = \frac{u_r + v_r}{2\omega_0 L} \tag{5.31}$$

Defining $U_r = u_r/c$ and $V_r = v_r/c$ we have

$$\sigma = \frac{\sqrt{p}}{2}(U_r + V_r) \tag{5.32}$$

In the non-relativistic limit U_r, $V_r \ll 1$, hence $U_r + V_r \ll 1$,

$$2\sigma \ll \sqrt{p} \tag{5.33}$$

Recalling $p = 2\kappa_0/(\kappa_1\kappa_2)$ and setting $\sigma = \kappa_1\hat{\sigma}$ then,

$$2\kappa_1^3\kappa_2\hat{\sigma}^2 \ll \kappa_0 \tag{5.34}$$

In the limit where $\xi \to \infty$, $\hat{\sigma} \to 1$ giving

$$2\kappa_1^3\kappa_2 \ll \kappa_0 \tag{5.35}$$

For smaller values of ξ, $\hat{\sigma} < 1$. Equation (5.35) is always true in the non-relativistic limit. Ultimately extending the model to incorporate relativistic effects will allow greater magnetic field strengths and inhomogeneities that are otherwise inaccessible. To extend the model, the problem would have to be solved using relativistic fluid dynamics.

The preceding argument ensures that the equilibrium situation is within the non-relativistic framework of the model. One must also be careful to guarantee that the perturbed fluid velocities are also non-relativistic. Following the derivation of Eq.(5.33), the non-relativistic regime also requires that

$$2\chi \ll \sqrt{p} \tag{5.36}$$

The Lorentz factor, $\gamma = [1 - (v/c)^2]^{-1/2}$, quantifies relativistic effects such that $\gamma \gg 1$ signifies a strongly relativistic regime and $\gamma \sim 1$, a non-relativistic one. In practice $v/c \lesssim 0.1$ corresponds to the non-relativistic regime. Eq. (5.35) becomes $2\kappa_1^3\kappa_2 \lesssim 0.01\kappa_0$ and Eqs. (5.33) and (5.36) yield $\sigma, \chi \lesssim 0.05\sqrt{p}$.

5.2.3 Model equations

To incorporate the effect of the non-zero equilibrium quantities, namely: Σ_0, σ_0, ζ_0 and β_0; they will be represented in Eqs. (5.1)-(5.10) resolved as $f = f_0(\xi) + f_1(\xi, \tau)$:

$$\Sigma = \Sigma_0 + \Sigma_1 \tag{5.37}$$
$$\sigma = \sigma_0 + \sigma_1 \tag{5.38}$$
$$\zeta = \zeta_0 + \zeta_1 \tag{5.39}$$

Beginning with Eq. (5.1):

$$\dot{\Sigma}_1 = -[(\Sigma_0 + \Sigma_1)(\sigma_0 + \sigma_1) + \Delta\delta]' \tag{5.40}$$
$$= -(\Sigma_0\sigma_0 + \Sigma_0\sigma_1 + \Sigma_1\sigma_0 + \Sigma_1\sigma_1 + \Delta\delta)' \tag{5.41}$$

Since $\Sigma_0\sigma_0 = \kappa_0$ its derivative equals zero leaving:

$$\dot{\Sigma}_1 = -\left[\Sigma_0\sigma_1 + \Sigma_1\left(\sigma_0 + \sigma_1\right) + \Delta\delta\right]' \tag{5.42}$$

Eq. (5.2) simply reduces to:

$$\dot{\Delta} = -\left[\Delta(\sigma_0 + \sigma_1) + \left(\Sigma_0 + \Sigma_1\right)\delta\right]' \tag{5.43}$$

Eq. (A.94) produces

$$\dot{\sigma}_1 = -\frac{1}{2}(\sigma_0^2 + 2\sigma_0\sigma_1 + \sigma_1^2 + \delta^2)' + (\chi^2 + \zeta_0^2 + 2\zeta_0\zeta_1 + \zeta_1^2)/\xi$$
$$+ (\zeta_0 + \zeta_1)(\beta_0 + \beta) \tag{5.44}$$

Recall from the equilibrium situation that $(\sigma_0^2)'/2 + \zeta_0^2/\xi + \zeta_0\beta_0 = 0$ (Eq. (3.58)) yielding

$$\dot{\sigma}_1 = -\frac{1}{2}\left[\sigma_1\left(2\sigma_0 + \sigma_1\right) + \delta^2\right]'$$
$$+ \left[\chi^2 + \zeta_1\left(2\zeta_0 + \zeta_1\right)\right]/\xi + \zeta_0\beta + \zeta_1\left(\beta_0 + \beta\right) \tag{5.45}$$
$$\tag{5.46}$$

Both Eq. (5.4) and (5.5) upon substitution trivially become:

$$\dot{\delta} = -[(\sigma_0 + \sigma_1)\delta]' + 2\chi(\zeta_0 + \zeta_1)/\xi + \rho + \xi(\beta_0 + \beta) \tag{5.47}$$

and

$$\begin{aligned} \dot{\chi} &= -\chi'(\sigma_0 + \sigma_1) - (\zeta_0 + \zeta_1)'\delta - [\chi(\sigma_0 + \sigma_1) + (\zeta_0 + \zeta_1)\delta]/\xi \\ &- \delta(\beta_0 + \beta) \end{aligned} \tag{5.48}$$

respectively. Looking at Eq. (5.6)

$$\begin{aligned} \dot{\zeta}_1 &= -(\sigma_0 + \sigma_1)(\zeta_0 + \zeta_1)' - \delta\chi' - [(\sigma_0 + \sigma_1)(\zeta_0 + \zeta_1) + \delta\chi]\xi + \theta \\ &- (\sigma_0 + \sigma_1)(\beta_0 + \beta) \end{aligned} \tag{5.49}$$

The equilibrium situation states that $\sigma_0(\zeta_0' + \zeta_0/\xi + \beta_0) = 0$ (Eq. (3.59)), ergo:

$$\begin{aligned} \dot{\zeta}_1 &= -\sigma_0\zeta_1' - \sigma_1(\zeta_0 + \zeta_1)' - \delta\chi' - [\sigma_0\zeta_1 + \sigma_1(\zeta_0 + \zeta_1) + \delta\chi]/\xi \\ &+\theta - \sigma_0\beta - \sigma_1(\beta_0 + \beta) \end{aligned} \tag{5.50}$$

The radial component of the Ampère-Maxwell equation, Eq. (A.99), yields

$$\dot{\rho} = -\frac{2}{\xi}[\Delta(\sigma_0 + \sigma_1) + (\Sigma_0 + \Sigma_1)\delta] \tag{5.51}$$

The azimuthal component of the Ampère-Maxwell equation yields

$$\dot{\theta} = -p(\beta_0 + \beta_1)' - \frac{2}{\xi}[(\Sigma_0 + \Sigma_1)(\zeta_0 + \zeta_1) + \Delta\chi] \tag{5.52}$$

$$= -p\beta' - \frac{2}{\xi}[\Sigma_0\zeta_1 + \Sigma_1(\zeta_0 + \zeta_1) + \Delta\chi] \tag{5.53}$$

noting that the equilibrium dictates that $-p\beta_0' - 2\Sigma_0\zeta_0/\xi = 0$.

Thence the governing set of equations become,

$$\dot{\Sigma}_1 = -[\Sigma_0\sigma_1 + \Sigma_1(\sigma_0 + \sigma_1) + \Delta\delta]' \tag{5.54}$$

$$\dot{\Delta} = -[\Delta(\sigma_0 + \sigma_1) + (\Sigma_0 + \Sigma_1)\delta]' \tag{5.55}$$

$$\begin{aligned} \dot{\sigma}_1 &= -\frac{1}{2}\left[\sigma_1(2\sigma_0 + \sigma_1) + \delta^2\right]' \\ &+ \left[\chi^2 + \zeta_1(2\zeta_0 + \zeta_1)\right]/\xi + \zeta_0\beta + \zeta_1(\beta_0 + \beta) \end{aligned} \tag{5.56}$$

$$\dot{\delta} = -[(\sigma_0 + \sigma_1)\delta]' + 2\chi(\zeta_0 + \zeta_1)/\xi + \rho + \chi(\beta_0 + \beta) \tag{5.57}$$

$$\begin{aligned} \dot{\chi} &= -\chi'(\sigma_0 + \sigma_1) - (\zeta_0 + \zeta_1)'\delta - [\chi(\sigma_0 + \sigma_1) + (\zeta_0 + \zeta_1)\delta]/\xi \\ &- \delta(\beta_0 + \beta_1) \end{aligned} \tag{5.58}$$

$$\begin{aligned} \dot{\zeta}_1 &= -\sigma_0\zeta_1' - \sigma_1(\zeta_0 + \zeta_1)' - \delta\chi' - [\sigma_0\zeta_1 + \sigma_1(\zeta_0 + \zeta_1) + \delta\chi]/\xi \\ &+\theta - \sigma_0\beta - \sigma_1(\beta_0 + \beta) \end{aligned} \tag{5.59}$$

$$\dot{\rho} = -\frac{2}{\xi}[\Delta(\sigma_0 + \sigma_1) + (\Sigma_0 + \Sigma_1)\delta] \tag{5.60}$$

$$\dot{\theta} = -p\beta' - \frac{2}{\xi}[\Sigma_0\zeta_1 + \Sigma_1(\zeta_0 + \zeta_1) + \Delta\chi] \tag{5.61}$$

$$\dot{\beta} = -\theta' - \theta/\xi \tag{5.62}$$

5.2.4 Finite Difference Time Domain

To solve numerically the nonlinear system of equations (5.54-5.62) a Finite Difference Time Domain (FDTD) algorithm was employed: replacing the spatial derivatives with finite difference approximations to fourth-order accuracy. Defining discrete coordinates $\xi = \xi_0 + m\mathrm{d}\Xi$ and using notation $\mathbf{\Psi}(\xi_0 + m\mathrm{d}\Xi, \tau) = \mathbf{\Psi}_m(\tau)$ we can write for a typical equation:

$$\begin{aligned} \partial_\tau \mathbf{\Psi}(\xi,\tau) &= \mathbf{Q}(\xi,\tau,\mathbf{\Psi}(\xi,\tau),\partial_\xi \mathbf{\Psi}(\xi,\tau)) \\ &= \mathbf{Q}\left(\xi_0 + m\mathrm{d}\Xi,\tau,\mathbf{\Psi}_m(\tau),\partial_\xi \mathbf{\Psi}_m(\tau)\right) \\ &= \mathbf{Q}_m(\tau,\mathbf{\Psi}_m(\tau),\partial_m \mathbf{\Psi}_m(\tau)) \\ &= \partial_\tau \mathbf{\Psi}_m(\tau) \end{aligned} \tag{5.63}$$

and

$$\partial_m \mathbf{\Psi}_m(\tau) = \frac{8(\mathbf{\Psi}_{m+1} - \mathbf{\Psi}_{m-1}) - (\mathbf{\Psi}_{m+2} - \mathbf{\Psi}_{m-2})}{12\mathrm{d}\Xi} \tag{5.64}$$

where $\mathbf{Q}$ is some function and ∂_ξ denotes the partial derivative with respect to ξ. The resulting ODEs are then solved via the fourth-order Runge-Kutta method for an integration time $T = n_{max}\mathrm{d}\tau$ where n_{max} is the number of time steps and $\mathrm{d}\tau$ is the temporal mesh increment. The 4^{th} Runge-Kutta algorithm is

$$\mathbf{k}_1 = \mathrm{d}\tau \mathbf{Q}_m(\tau,\mathbf{\Psi}_m(\tau),\partial_m\mathbf{\Psi}_m(\tau)) \tag{5.65}$$

$$\mathbf{k}_2 = \mathrm{d}\tau \mathbf{Q}_m(\tau+\mathrm{d}\tau/2,\mathbf{\Psi}_m(\tau+\mathrm{d}\tau/2)+\mathbf{k}_1/2,\partial_m[\mathbf{\Psi}_m(\tau+\mathrm{d}\tau/2)+\mathbf{k}_1/2]) \tag{5.66}$$

$$\mathbf{k}_2 = \mathrm{d}\tau \mathbf{Q}_m(\tau+\mathrm{d}\tau/2,\mathbf{\Psi}_m(\tau+\mathrm{d}\tau/2)+\mathbf{k}_2/2,\partial_m[\mathbf{\Psi}_m(\tau+\mathrm{d}\tau/2)+\mathbf{k}_2/2]) \tag{5.67}$$

$$\mathbf{k}_2 = \mathrm{d}\tau \mathbf{Q}_m(\tau+\mathrm{d}\tau,\mathbf{\Psi}_m(\tau+\mathrm{d}\tau)+\mathbf{k}_3,\partial_m[\mathbf{\Psi}_m(\tau+\mathrm{d}\tau)+\mathbf{k}_3]) \tag{5.68}$$

$$\mathbf{\Psi}_m^{n+1} = \mathbf{\Psi}_m^n + \frac{\mathbf{k}_1}{6} + \frac{\mathbf{k}_2}{3} + \frac{\mathbf{k}_3}{3} + \frac{\mathbf{k}_4}{6} \tag{5.69}$$

5.3 Numerical simulations

Using a bespoke FDTD algorithm the nonlinear set of equations, Eq. (5.1)-(5.10), can now be solved. This section will now proceed to show the nonlinear mode coupling via an inhomogeneous magnetic field and extend this concept to the interaction of radiation from multiple electrostatic oscillations.

5.3.1 Mode coupling via inhomogeneous magnetic field

Initial conditions

Once the equilibrium has been defined the plasma is driven by an initial charge density perturbation,

$$\Delta_m(\tau=0) = \begin{cases} A_0 N_0 \sin\left[\pi\dfrac{(m-m_0-\varsigma)}{\varsigma}\right]\exp\left[-\left(\lambda\dfrac{m-m_0}{\varsigma}\right)^2\right] & m \in [m_0-\varsigma, m_0-\varsigma] \\ 0 & m \notin [m_0-\varsigma, m_0+\varsigma] \end{cases} \tag{5.70}$$

where N_0 is a constant that normalises the perturbation relative to the background density at the centre of the perturbation, $\Sigma_0(m_0)$; A_0 is the amplitude of the perturbation expressed as a fraction of $\Sigma_0(m_0)$; ς is the half-width of the initial perturbation; m_0 is the centre of the perturbation and λ is a Gaussian coefficient. To avoid sharp gradients at the edges of the perturbation, the initial disturbance was multiplied by a Gaussian envelope. At $\tau = 0$ the initial conditions for the other plasma variables are: $\Sigma_1 = \sigma_1 = \delta = \chi = \zeta_1 = \theta = \beta = 0$, $\forall\ m$. The initial condition stimulates the electrostatic mode which couples to an electromagnetic mode via the background magnetic field. This perturbation creates a radially polarised electric field that will accelerate the plasma to try and restore equilibrium. Recall Poisson's equation for the electric field Eq. (3.43),

$$(\xi\rho)' = 2\Delta \tag{5.71}$$

Rearranging this one can calculate the corresponding electric field for the prescribed charge density perturbation.

$$\rho(\xi, \tau = 0) = \frac{2}{\xi}\int_{\xi_0}^{\xi_i} \Delta(\xi', \tau = 0) d\xi' \tag{5.72}$$

Thus

$$\rho_m(\tau = 0) = \begin{cases} \dfrac{2}{\xi_0 + m\mathrm{d}\Xi}\displaystyle\int_{m_0-\varsigma}^{m} \Delta_{m'}(\tau = 0)\mathrm{d}m' & m \in [m_0 - \varsigma, m_0 + \varsigma] \\ 0 & m \notin [m_0 - \varsigma, m_0 + \varsigma] \end{cases} \tag{5.73}$$

The integral is calculated numerically using a 3-point Simpson's rule. An example of the form of the initial conditions are exhibited in Fig. 5.2, where the charge density has been perturbed from the equilibrium defined in Fig. 5.1.

Boundary conditions

The generated electromagnetic radiation propagates away from the source region in radially opposite directions. The outwardly propagating component (ξ increasing) would propagate indefinitely, due to the lack of any dissipative process, encountering regions of lowering plasma density and hence plasma frequency. As a result the effect of the plasma on the electromagnetic mode would diminish. The inwardly propagating component (ξ decreasing) would encounter regions of increasing plasma density attenuating the wave until the background plasma frequency is comparable to that of the wave. This results in the wave being partially absorbed and also stimulating a new electrostatic oscillation that generates its own electromagnetic mode with a characteristic frequency dependent upon the local plasma conditions. The outwardly propagating radiation from this source travels towards the original oscillation site. Within the region between the two oscillation sites the wave solution now becomes the superposition of the two independent wave trains. There will be a finite time delay before the initial electromagnetic mode propagates to this boundary. Note that the numerical simulations are stopped before the generated waves propagate to and interact with the boundaries of the numerical domain and hence one can avoid numerically accommodating this boundary condition. The calculations discussed here employ this simplification.

Results

Solving the cold plasma fluid equations yields a continuum description incorporating the coherent motion of the pair plasma. The results in Figs. 5.4-5.13 were calculated using the equilibrium shown in Fig. 5.1 and the parameters listed in Table 5.1, showing the response of the plasma after an initial 1% initial charge density perturbation: this is in the linear regime. For the 1% charge density perturbation the equilibrium values were: $\Sigma_0 \sim 4\times10^{13}$; $\sigma_0 \sim 1\times10^{-2}$; $\zeta_0 \sim 2\times10^{-10} - 7\times10^{-6}$ and $\beta_0 \sim 5\times10^{-7} - 2\times10^{-2}$ with $|\beta_0'| \sim 1\times10^{-3} - 6\times10^{1}$. Fully nonlinear simulations are reported later in this section. The solutions illustrate the generic form of the coupling in the plasma: when the charge density of the plasma is perturbed, an electrostatic oscillation occurs in which the plasma density fluctuates, Fig. 5.3 & 5.4, under the influence of the induced radial electric field, Fig. 5.9. In the presence of an inhomogeneous background magnetic field this oscillation couples to an electromagnetic mode propagating in the radial direction with an axial magnetic field component, Fig. 5.10, and an azimuthal electric field, Fig. 5.11.

To consolidate qualitatively the mechanics of the coupling, consider an electrostatic oscillation in an unmagnetised, uniform pair plasma. The oscillation occurs at the plasma frequency $\omega_p^2 = 2\Sigma_0/\xi$ and is characterised by $\Sigma \neq 0$, $\Delta \neq 0$, $\delta \neq 0$, $\rho \neq 0$, $\sigma = 0$, $\chi = 0$, $\zeta = 0$ and $\theta = 0$. Deviations from this embody the degree of nonlinearity of the oscillation. When the background plasma is uniform, stationary and permeated by a homogeneous magnetic field, linear electrostatic oscillations are characterised by $\Delta \neq 0$, $\delta \neq 0$, $\rho \neq 0$, $\chi \neq 0$, $\sigma = 0$, $\zeta = 0$, $\beta = 0$, $\theta = 0$ and $\Sigma =$ constant, which are confined to the spatial extent of the oscillation. Within the framework of a uniform, radially streaming plasma the average radial equilibrium flow is constant, $\sigma = 0$ and $\zeta = 0$, as elucidated in § 3.5.1. In both the streaming and non-streaming contexts the radially propagating electromagnetic mode requires that $\Sigma \neq 0$, $\sigma \neq 0$, $\zeta \neq 0$, $\theta \neq 0$ and $\beta \neq 0$ and places no constraints on the form of Δ, δ, χ or ρ. In the nonlinear regime, when the magnetic field is inhomogeneous and the equilibrium is fully dynamic these conditions are relaxed facilitating in the mode coupling and resolving the disparate conditions between the electrostatic and electromagnetic modes. The inhomogeneity has the effect of breaking the azimuthal symmetry of the species fluid velocities due to the charge dependent $\mathbf{B}\times\nabla B$ drift: $\chi = 0$ (Fig. 5.7). This generates a net current density in the azimuthal direction, $\zeta \neq 0$ (Fig. 5.8), that forms the source of axial magnetic field fluctuations, β, and the oscillating azimuthal electric field, θ. As in the homogeneous case $\sigma = 0$, with deviations from this illustrating the nonlinear nature of the oscillation, Fig. 5.5, this will be discussed later.

As the generated mode propagates away from the oscillation site it will encounter regions of differing background density giving a corresponding variation in the plasma frequency, requiring a change in the wave amplitude to conserve energy. This is analogous to waves on a string with an impedance variation, but the plasma context introduces an extra feature: namely the interplay between the driving frequency of the wave and the local plasma frequency. Additionally, if an electromagnetic mode, frequency ω_{em}, traverses through a non-uniform plasma its phase speed, v_p, and wave number, k, will alter in harmony to satisfy the relation $\omega_{em} = kv_p$ in response to the varying refractive index of the anisotropic medium; $n = c/v_p = \sqrt{\varepsilon}$, where ε is the dielectric tensor of the plasma. The refractive index of the non-uniform plasma and the phase speed of propagating waves must also be tensors of the same rank.

If the frequency of the wave is very large then the effect of the plasma on the wave

propagation becomes less significant. A wave propagating towards smaller values of ξ will encounter a gradual increase in the background plasma density and will eventually be partially reflected and absorbed when the frequency of the wave, ω falls below that of the local hybrid frequency, $\omega < \omega_H(\xi)$ (Paper II). From Figs. 5.12-5.13 it is clear that the doppler shift is negligible, consistent with our earlier linear analysis.

The frequency of the propagating electromagnetic mode is twice the hybrid frequency of the uncoupled electrostatic mode. In the linear, non-streaming, uniform equilibrium case the hybrid frequency is given by,

$$\omega_H^2 = \beta_0^2 + 2\Sigma_0/\xi \tag{5.74}$$

The equilibrium configuration states that $\Sigma \propto \kappa_0\kappa_1^{-1}$ and $\beta_0 = \kappa_1\hat{\beta}_0$, thus the oscillating frequency becomes,

$$\omega_H^2 \propto \kappa_1^2 + \kappa_0\kappa_1^{-1} \tag{5.75}$$

Defining the plasma number density via κ_0 and κ_1 sets: the hybrid frequency of the plasma oscillation, ω_H; the electromagnetic mode frequency, $2\omega_H$; and for a prescribed value of κ_2 the speed of light squared in the plasma via $p = 2\kappa_0/(\kappa_1\kappa_2)$, hence setting the speed of propagation of the electromagnetic disturbance. This, along with Ξ, constrains the wavelength of the electromagnetic mode such that $\omega = kv_p$.

The relative emission efficiency of the mode coupling can be characterised by the ratio $\theta/\rho \sim 10^{-12}$. This is quite small but it is important to note that the coherent dynamical response of the electrostatic oscillation cannot propagate in the cold plasma context and hence it cannot be observed directly; only the coherent, propagating electromagnetic response can be detected. In contrast to single-particle radiation mechanisms the mode coupling here generates a collective electromagnetic mode, consistent with the background plasma conditions, from the coherent plasma motion.

Figs. 5.4-5.13 address small perturbations (1%) to the equilibrium; finite amplitude effects need larger perturbations. The nonlinearity of the mode coupling is specifically exhibited in Figs. 5.16-5.27. For these specific simulations the equilibrium, Fig. 5.14, was calculated using the parameters from Table 5.3 with an initial 70% charge density perturbation. Over the initial charge density perturbation the equilibrium values were: $\Sigma_0 \sim 4 \times 10^9$; $\sigma_0 \sim 1 \times 10^{-2}$; $\zeta_0 \sim 1 \times 10^{-6} - 5 \times 10^{-5}$ and $\beta_0 \sim 2 \times 10^{-3} - 1 \times 10^{-1}$ with $|\beta_0'| \sim 4 \times 10^2 - 2 \times 10^4$. In comparison to the simulations discussed in Figs. 5.4-5.13 the ratio $\theta/\rho \sim 10^{-6}$ is much higher. Figs. 5.24 and 5.25 clearly show the onset of the density instability consistent with Paper I and its consequent effect on the evolution of the electromagnetic wave it generates, Figs. 5.26-5.27. The nonlinear evolution of large amplitude pair plasma oscillations causes a decrease in the plasma density, and hence the local plasma frequency, at the centre of the oscillation site. With the plasma frequency being a function of position across the spatial extent of the oscillation, the ensuing phase difference results in the net motion of the plasma to regions where the plasma frequency is highest. The result is the formation of density spikes that eventually exceed the resolution of the numerical mesh of the domain. The results here display the hallmark features of the nonlinear evolution of the plasma at an early stage, but do not show the ultimate fate of the instability.

Increasing the amplitude (and therefore the energy content) of the initial density perturbation for a given background magnetic field gradient correspondingly increases the amplitude of the generated wave, and makes the wave profile more nonlinear, Fig.5.28-5.30. The extent of the nonlinear response of the plasma depends upon the electrostatic

energy of the initial charge density perturbation. The greater the energy reservoir, the greater the kinetic energy that transports the plasma to regions with a greater plasma frequency. Increasing the nonlinearity of the oscillation also affects its phase, consistent with the phase variation apparent in the nonlinear evolution of the oscillation, Paper I. The results illustrated in Fig. 5.28 were obtained, using the parameters from Table 5.5, by perturbing the plasma charge density and allowing the generated electromagnetic wave to propagate for a prescribed number of plasma oscillations. The peak-to-trough amplitude of the leading waveform propagating upstream in the radial equilibrium flow was measured, characterising the mode coupling. This is considered representative of the entire generated wave train across the numerical domain. Note that as the initial charge density perturbation is increased relative to the background plasma density the perturbed fluid velocities become relativistic. Relaxing the non-relativistic restrictions in future code developments will address this.

If the initial perturbation amplitude of the density oscillation is kept constant and the background magnetic field gradient is varied, the amplitude of the resulting EM wave increases nonlinearly as the coupling strength $\propto \mathbf{B} \times \nabla B$ is increased, Fig. 5.31. Notice that as β_0' is increased the resulting rate of increase in the EM amplitude begins to slow, hinting perhaps at a maximum fraction of the electrostatic energy that may be converted in this way.

Table 5.6 contains the parameter values for the numerical simulations conducted to obtain the results for Fig. 5.31. Following the procedure used to obtain the results plotted in Fig. 5.28, the peak-to-trough amplitude of the leading waveform propagating upstream was measured after a prescribed number of plasma oscillations. κ_2 controls the magnetic field gradient across the numerical domain. For each value of κ_2 the equilibrium equations, Eqs. (5.19-5.20), were integrated to obtain the largest domain size possible, Ξ, for prescribed values of ξ_i, m_{max}, $\hat{\zeta}_0(\xi_i)$ and $\hat{\beta}_0(\xi_i)$. Therefore varying κ_2 requires that $\mathrm{d}\Xi$ is changed in sympathy, thus altering the size of the numerical domain, Ξ, that the governing equations are solved for. To conserve the value of p so that in all scenarios the propagating waves are at the same relative position in the numerical domain after time $T = n_{max}\mathrm{d}\tau$, κ_0 and κ_1 have to be changed in sympathy. For a prescribed value of κ_1, altering κ_2 and hence Ξ, κ_0 has to be altered by an equivalent amount so that the generated electromagnetic waves can be sufficiently well resolved and do not propagate out of the numerical domain. κ_0 and κ_1 define the equilibrium plasma density and hence the number of plasma oscillations that occur in time T. Increasing (decreasing) κ_0, gives a greater (fewer) number of oscillations in time T and hence decreasing (increasing) $\mathrm{d}\tau$ by a similar amount conserves the number of oscillations in the set time.

The set of parameters κ_i determine p and hence the quantity $\omega_0 L$, where the choice of ω_0 and L define the physical system to which the results apply. For specified values of ω_0 and L one can recover the dimensional plasma variables from the non-dimensional ones via

Eqs. (3.25-3.35), ergo

$$
\begin{aligned}
n_+ &= n_0(\Sigma + \Delta)/\xi && (5.76)\\
n_- &= n_0(\Sigma - \Delta)/\xi && (5.77)\\
u_r &= \omega_0 L(\sigma + \delta) && (5.78)\\
v_r &= \omega_0 L(\sigma - \delta) && (5.79)\\
u_\theta &= \omega_0 L(\chi + \zeta) && (5.80)\\
v_\theta &= \omega_0 L(\chi - \zeta) && (5.81)\\
E_r &= m\omega_0^2 L\rho/e && (5.82)\\
E_\theta &= m\omega_0^2 L\theta/e && (5.83)\\
B_z &= m\omega_0(\beta_0 + \beta)/e && (5.84)\\
r &= \xi L && (5.85)\\
t &= \tau/\omega_0 && (5.86)
\end{aligned}
$$

For the solutions in Figs. 5.1-5.13 and using Table 5.1, $p = 2 \times 10^4$. Following Paper I and assuming that the required typical electron number densities for γ-ray radiation in the rest frame is $n_- \approx 10^{21}$ m^{-3}, then we have: u_{r0}, $v_{r0} \sim 10^4$ ms^{-1}; $u_{\theta 0}$, $v_{\theta 0} \sim 10^4$ ms^{-1}; $E_r \sim 10^9$ Vm^{-1}; $E_\theta \sim 10^{-3}$ Vm^{-1}; $B_z \sim 10^{-3}$ T, where $L \sim 10^{-2}$ m. See Table 5.2 for more values. Translated into the laboratory frame in which the pulsar rotates (i.e. the observers frame) and assuming a typical Lorentz factor $\gamma \sim 10^8$ gives $B_z \sim 10^5$ T.

Considering the solutions in Figs. 5.16-5.23, again setting $n_- \approx 10^{21}$ m^{-3} in the plasma rest frame, yields: u_{r0}, $v_{r0} \sim 10^7$ ms^{-1}; $u_{\theta 0}$, $v_{\theta 0} \sim 10^7$ ms^{-1}; $E_r \sim 10^9$ Vm^{-1}; $E_\theta \sim 10^3$ Vm^{-1}; $B_z \sim 1$ T, where $L \sim 5 \times 10^{-1}$ m. See Table 5.4 for more values.

Table 5.1: Table of parameters for numerical simulations Figs. 5.1-5.13.

Parameter	Value	
κ_0	4.0×10^{11}	a constant parameter
κ_1	1.0×10^{-2}	a constant parameter
κ_2	4.0×10^{9}	a constant parameter
$\hat{\zeta}_0(\xi_i)$	1.0×10^{-9}	initial $\hat{\zeta}_0$ value
$\hat{\beta}_0(\xi_i)$	1.0×10^{-9}	initial $\hat{\beta}_0$ value
ξ_i	500	initial ξ value
m_{max}	3001	number of spatial points
$\mathrm{d}\Xi$	2.5×10^{-6}	spatial mesh increment
A_0	0.01	perturbation amplitude, Δ/Σ_0
ς	750	half-width of initial perturbation
λ	5.0	gaussian coefficient
m_0	1750	centre of perturbation
$\mathrm{d}\tau$	1.5×10^{-8}	temporal mesh increment
n_{max}	2000	number of time steps

Table 5.2: Dimensionalised plasma parameters for linear simulations, Figs. 5.1-5.13, where $L = 0.1$, $p = 2 \times 10^4$.

Plasma variable	Approximate value
n_{-0}	2×10^{21} m^{-3}
n_{+0}	2×10^{21} m^{-3}
u_{r0}	2×10^{4} ms^{-1}
v_{r0}	2×10^{4} ms^{-1}
$u_{\theta 0}$	2×10^{4} ms^{-1}
$v_{\theta 0}$	2×10^{4} ms^{-1}
B_{z0}	3×10^{-3} T
n_{-}	1×10^{18} m^{-3}
n_{+}	1×10^{18} m^{-3}
u_r	3×10^{6} ms^{-1}
v_r	-3×10^{6} ms^{-1}
u_θ	3×10^{-6} ms^{-1}
v_θ	-3×10^{-6} ms^{-1}
E_r	1×10^{8} Vm^{-1}
E_θ	1×10^{-4} Vm^{-1}
B_z	7×10^{-13} T

Table 5.3: Table of parameters for numerical simulations Figs. 5.14-5.27

Parameter	Value	
κ_0	4.0×10^{7}	a constant parameter
κ_1	1.0×10^{-2}	a constant parameter
κ_2	2.0×10^{11}	a constant parameter
$\hat{\zeta}_0(\xi_i)$	1.0×10^{-6}	initial $\hat{\zeta}_0$ value at ξ_i
$\hat{\beta}_0(\xi_i)$	1.0×10^{-6}	initial $\hat{\beta}_0$ value at ξ_i
ξ_i	500	initial ξ value
m_{max}	3001	number of spatial points
$\mathrm{d}\Xi$	1.60075×10^{-7}	spatial mesh increment
A_0	0.7	perturbation amplitude, Δ/Σ_0
ς	400	half-width of initial perturbation
λ	5.0	gaussian coefficient
m_0	1500	centre of perturbation
$\mathrm{d}\tau$	7.5×10^{-7}	temporal mesh increment
n_{max}	2000	number of time steps

Table 5.4: Dimensionalised plasma parameters for nonlinear simulations, Figs. 5.14-5.27, where $L = 1 \times 10^1$, $p = 4 \times 10^{-4}$.

Plasma variable	Approximate value
n_{-0}	3×10^{21} m^{-3}
n_{+0}	3×10^{21} m^{-3}
u_{r0}	1×10^{7} ms^{-1}
v_{r0}	1×10^{7} ms^{-1}
$u_{\theta 0}$	1×10^{7} ms^{-1}
$v_{\theta 0}$	1×10^{7} ms^{-1}
B_{z0}	2×10^{-1} T
n_{-}	-2×10^{19} m^{-3}
n_{+}	8×10^{19} m^{-3}
u_r	7×10^{7} ms^{-1}
v_r	-7×10^{7} ms^{-1}
u_θ	1×10^{2} ms^{-1}
v_θ	-1×10^{2} ms^{-1}
E_r	2×10^{8} Vm^{-1}
E_θ	7×10^{2} Vm^{-1}
B_z	6×10^{-6} T

Table 5.5: Table of parameters for numerical simulations Figs. 5.28-5.30

Parameter	Value	
κ_0	1.0×10^{-1}	a constant parameter
κ_1	1.0×10^{-2}	a constant parameter
κ_2	1.0×10^{1}	a constant parameter
$\hat{\zeta}_0(\xi_i)$	1.0×10^{-6}	initial $\hat{\zeta}_0$ value at ξ_i
$\hat{\beta}_0(\xi_i)$	1.0×10^{-6}	initial $\hat{\beta}_0$ value at ξ_i
ξ_i	500	initial ξ value
m_{max}	3001	number of spatial points
$\mathrm{d}\Xi$	2.75×10^{-2}	spatial mesh increment
ς	1000	half-width of initial perturbation
λ	5.0	gaussian coefficient
m_0	1500	centre of perturbation
$\mathrm{d}\tau$	1.0×10^{-2}	temporal mesh increment
n_{max}	2000	number of time steps

Table 5.6: Table of parameters for numerical simulations Fig. 5.31

Parameter	Value	
$\hat{\zeta}_0(\xi_i)$	1.0×10^{-6}	initial $\hat{\zeta}_0$ value at ξ_i
$\hat{\beta}_0(\xi_i)$	1.0×10^{-6}	initial $\hat{\beta}_0$ value at ξ_i
ξ_i	500	initial ξ value
m_{max}	3001	number of spatial points
A_0	0.1	perturbation amplitude, Δ/Σ_0
ς	1000	half-width of initial perturbation
λ	5.0	gaussian coefficient
m_0	1500	centre of perturbation
n_{max}	2000	number of time steps

κ_0	κ_1	κ_2	$\mathrm{d}\Xi$	$\mathrm{d}\tau$	$\lvert\beta_0'(m_0)\rvert$
4.0×10^{7}	1.0×10^{-2}	4.0×10^{11}	1.30075×10^{-7}	5.0×10^{-7}	1.0×10^{3}
3.0×10^{7}	1.0×10^{-2}	3.0×10^{11}	1.50197×10^{-7}	5.7735×10^{-7}	7.50×10^{2}
2.0×10^{7}	1.0×10^{-2}	2.0×10^{11}	1.83954×10^{-7}	7.07×10^{-7}	5.0×10^{2}
1.0×10^{7}	1.0×10^{-2}	1.0×10^{11}	2.6015×10^{-7}	9.9×10^{-7}	2.50×10^{2}
4.0×10^{6}	1.0×10^{-2}	4.0×10^{10}	4.11333×10^{-7}	1.5811×10^{-6}	1.0×10^{2}
2.0×10^{6}	1.0×10^{-2}	2.0×10^{10}	5.81714×10^{-7}	2.23607×10^{-6}	5.0×10^{1}
4.0×10^{5}	1.0×10^{-2}	4.0×10^{9}	1.30075×10^{-6}	5.0×10^{-6}	1.0×10^{1}
4.0×10^{4}	1.0×10^{-2}	4.0×10^{8}	4.11333×10^{-6}	1.5811×10^{-5}	1.0×10^{0}
4.0×10^{3}	1.0×10^{-2}	4.0×10^{7}	1.30075×10^{-5}	5.0×10^{-5}	1.0×10^{-1}
4.0×10^{2}	1.0×10^{-2}	4.0×10^{6}	4.11333×10^{-5}	1.5811×10^{-4}	1.0×10^{-2}
4.0×10^{1}	1.0×10^{-2}	4.0×10^{5}	1.30075×10^{-4}	5.0×10^{-4}	1.0×10^{-3}

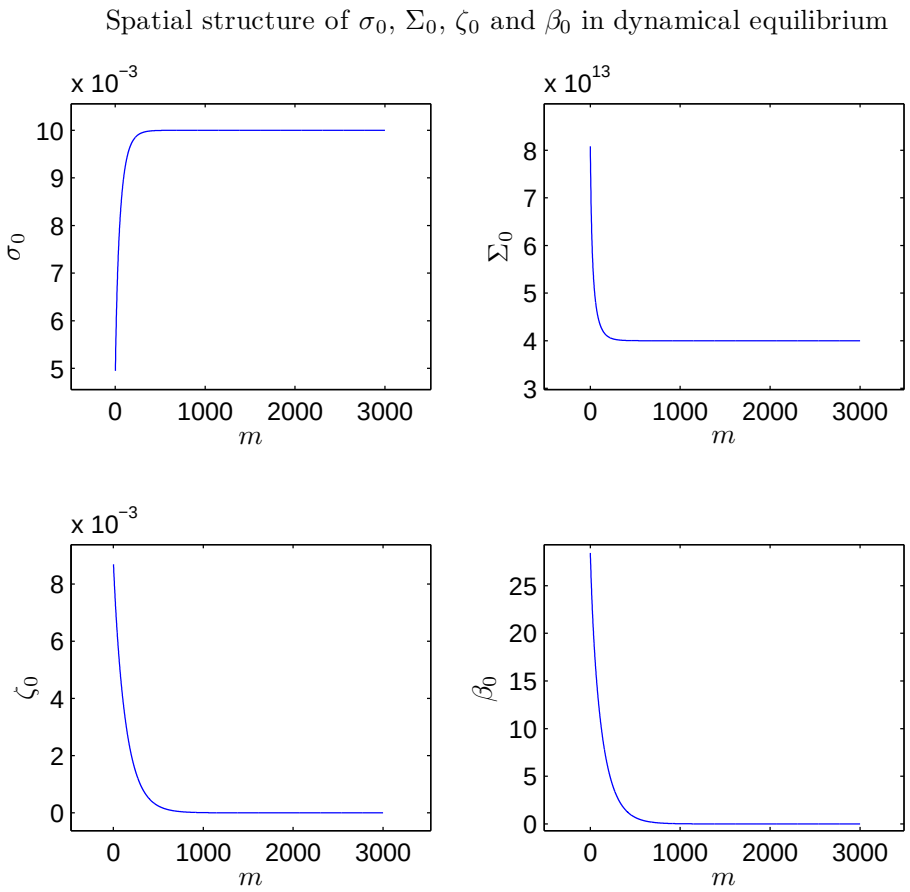

Figure 5.1: Dynamical equilibrium solutions for $\kappa_0 = 4 \times 10^{11}$, $\kappa_1 = 10^{-2}$ and $\kappa_2 = 4 \times 10^9$. Plots show behaviour as function of position for the following quantities: Top left, radial streaming speed σ_0; top right, total number density Σ_0; bottom left, differential azimuthal flow ζ_0; bottom right, magnetic field. Solutions are calculated using a bespoke Runge-Kutta routine with the parameters in Table 5.1. The equilibrium calculated here was used to produce the solutions in Figs. 5.3-5.13.

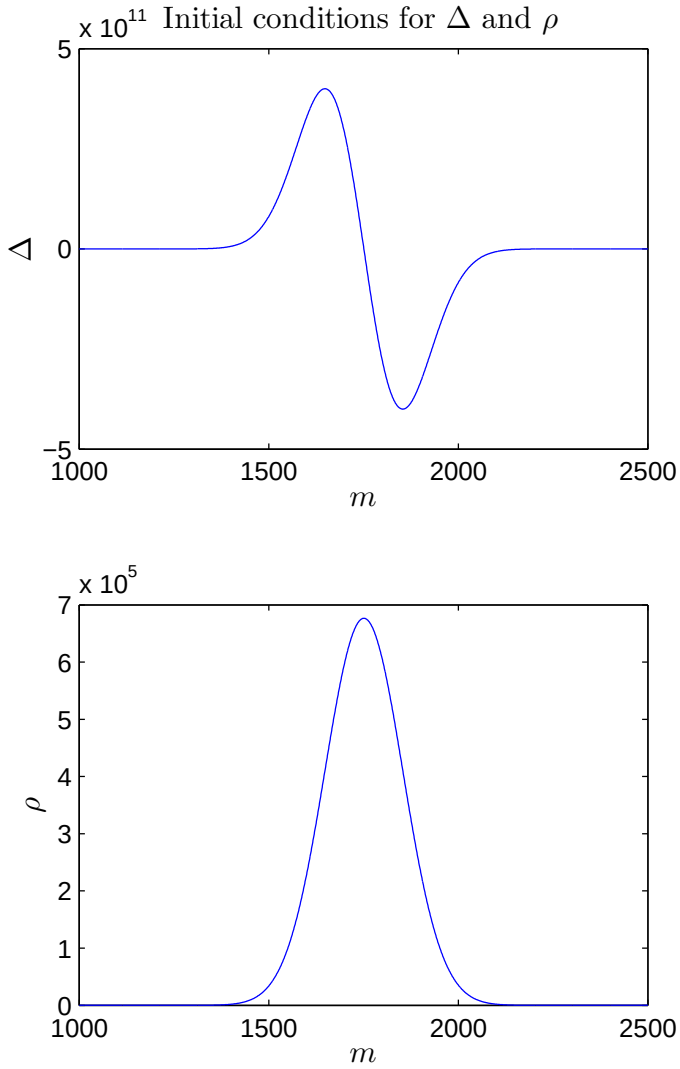

Figure 5.2: Initial conditions for mode coupling via an inhomogeneous magnetic field. Plots show an initial 1% charge density perturbation and the accompanying restoring radial electric field. The initial conditions are perturbed from an equilibrium defined using the numerical parameters in Table 5.1 and plotted in Fig. 5.1.

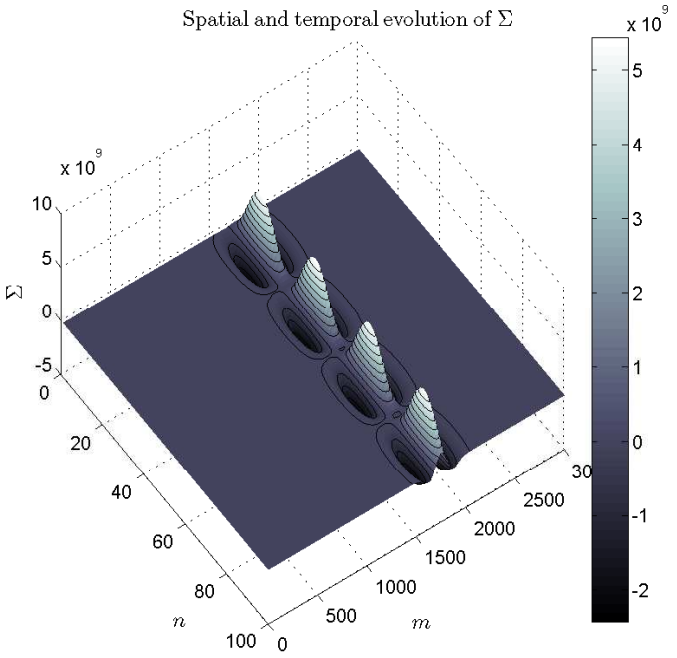

Figure 5.3: Spatial and temporal evolution of Σ, showing the average dimensionless plasma density as a function of time τ and space ξ associated with an electrostatic oscillation. This is the response after a 1% initial charge density perturbation.

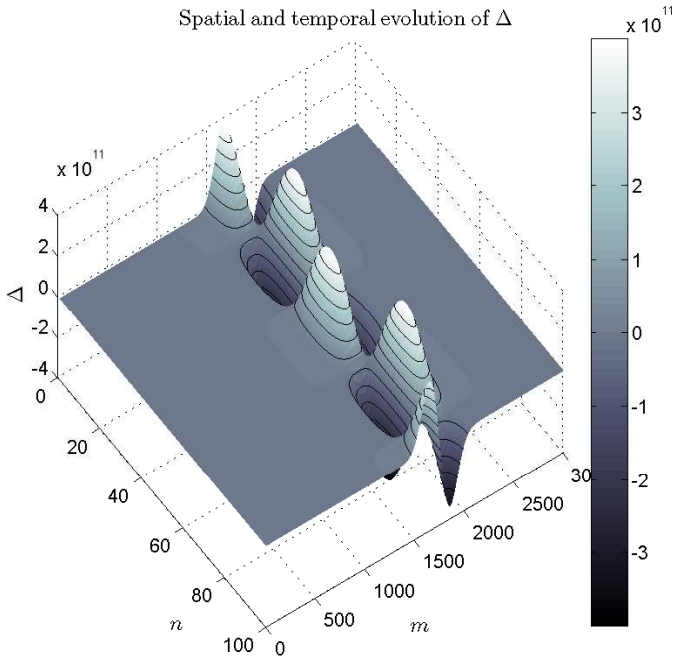

Figure 5.4: Spatial and temporal evolution of Δ, showing the difference between the dimensionless e^+-e^- plasma number density as a function of time τ and space ξ associated with an electrostatic oscillation. This is the response after a 1% initial charge density perturbation. When the charge density of the plasma is perturbed, an electrostatic oscillation occurs in which the plasma density periodically fluctuates under the influence of the induced radial electric field, Fig. 5.9

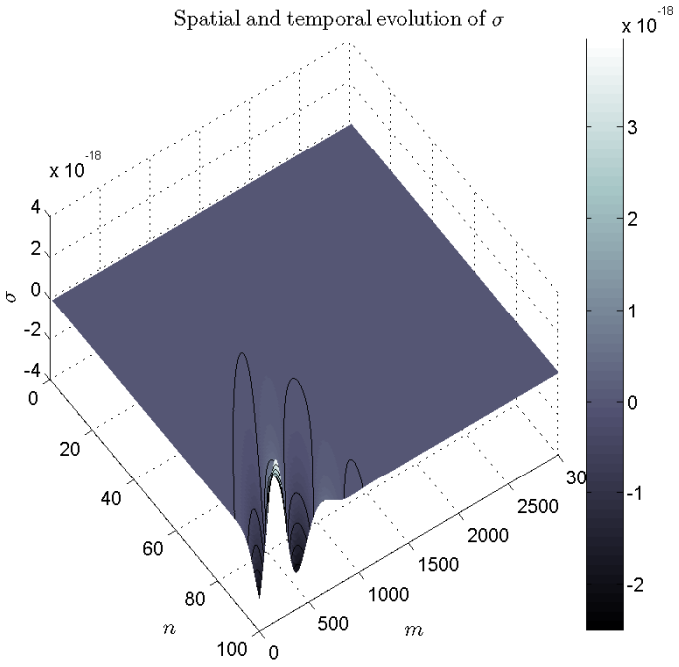

Figure 5.5: Spatial and temporal evolution of σ, showing the average dimensionless radial plasma flow as a function of time τ and space ξ associated with an electrostatic oscillation. This is the response after a 1% initial charge density perturbation. When the plasma equilibrium is stationary (or radially streaming), uniform and permeated by a homogeneous magnetic field $\sigma = 0$. Deviations from this embody the nonlinearity of the oscillation. A 1% initial perturbation is in the linear regime hence $\sigma \sim 10^{-18}$. The unusual form of this solution will be discussed later in this section.

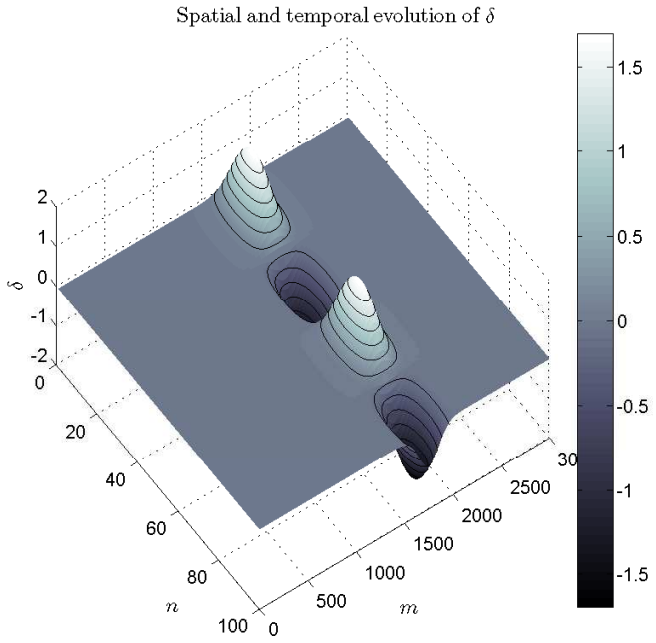

Figure 5.6: Spatial and temporal evolution of δ, showing the difference between the dimensionless e^+-e^- radial velocities as a function of time τ and space ξ associated with an electrostatic oscillation. This is the response after a 1% initial charge density perturbation. The radial electric field induced as a result of the charge density perturbation, accelerates the electron and positrons in radially opposite directions. They overshoot their original positions, due to their acquired kinetic energy, generating a new charge imbalance. The radial velocity therefore fluctuates periodically in harmony with Δ.

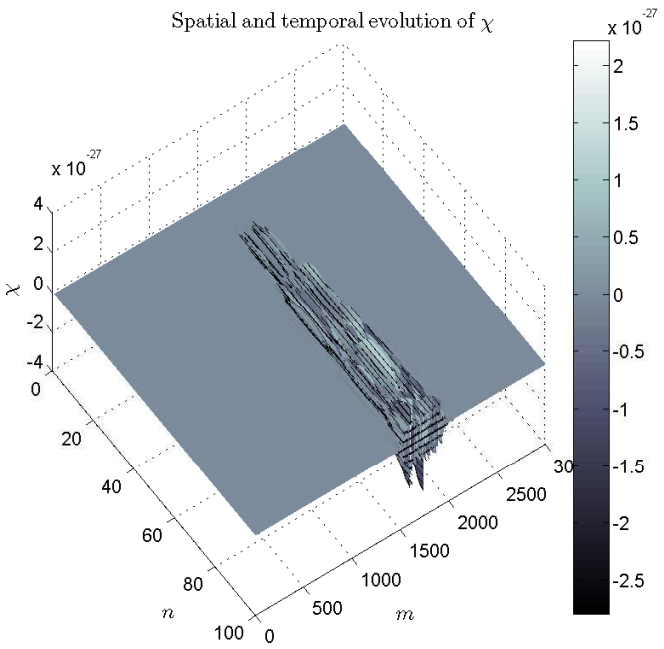

Figure 5.7: Spatial and temporal evolution of χ, showing the average dimensionless azimuthal plasma flow as a function of time τ and space ξ. This is the response after a 1% initial charge density perturbation. If the plasma equilibrium is permeated by a homogeneous magnetic field then $\chi \neq 0$. Introducing an inhomogeneous magnetic field induces a $\mathbf{B} \times \nabla B$ drift breaking the azimuthal symmetry in the velocity field hence $\chi = 0$.

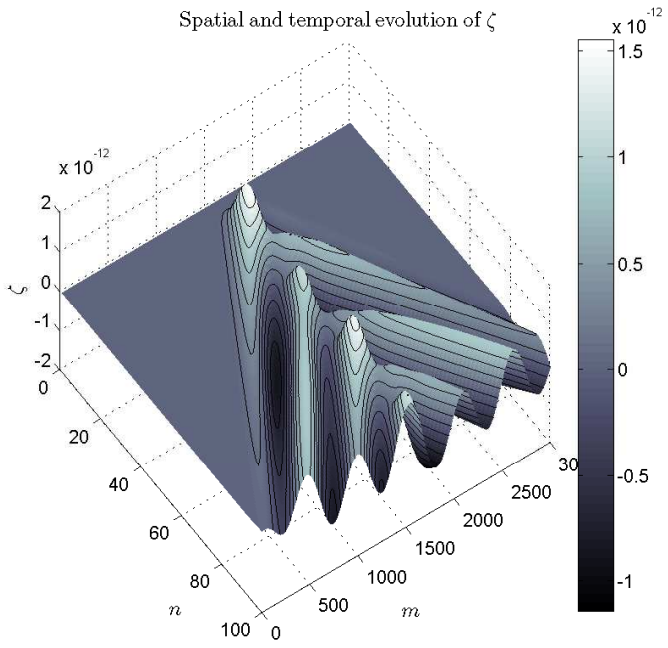

Figure 5.8: Spatial and temporal evolution of ζ, showing the difference between the dimensionless e^+-e^- azimuthal velocities as a function of time τ and space ξ. This is the response after a 1% initial charge density perturbation. The electrostatic mode when the magnetic field is homogeneous requires that $\zeta = 0$. Introducing an inhomogeneous magnetic field induces a charge dependent $\mathbf{B} \times \nabla B$ drift that breaks the azimuthal symmetry in the velocity field. This actuates a net current density in the azimuthal motion of the plasma hence $\zeta \neq 0$.

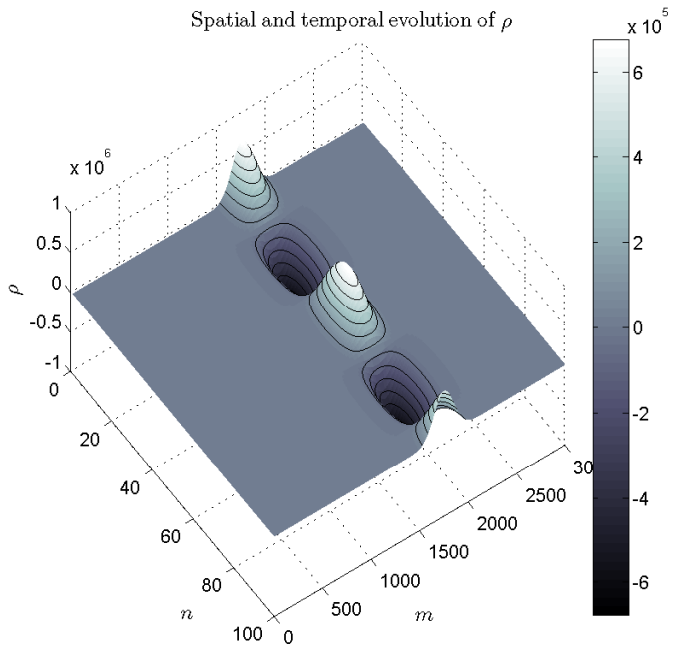

Figure 5.9: Spatial and temporal evolution of the dimensionless radial electric field, ρ, of the plasma oscillation, consistent with Fig. 5.4. When the plasma charge density is perturbed the plasma collectively responds to the resulting radial electric field trying to restore equilibrium. The accelerated particles overshoot their initial positions due to their acquired kinetic energy, generating a new charge imbalance.

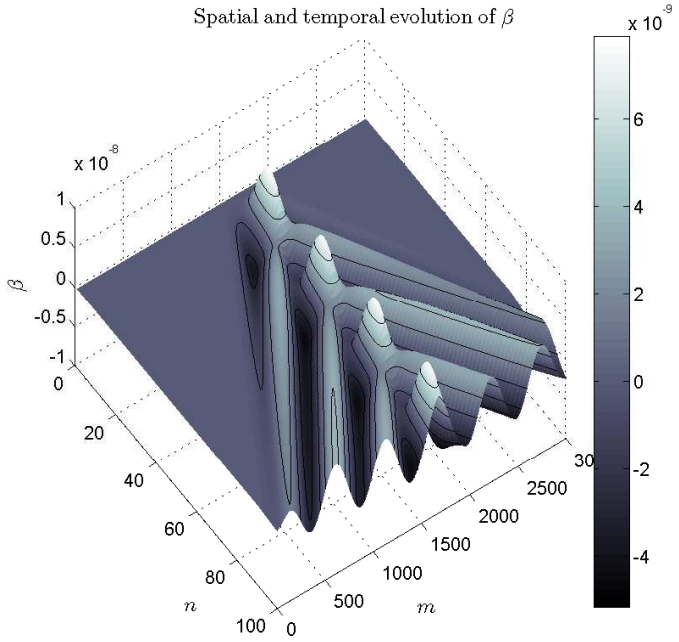

Figure 5.10: Spatial and temporal evolution of the dimensionless axial magnetic field, β, showing clearly the propagation of an electromagnetic signal outwards from the electrostatic oscillation site. During the plasma oscillation the drift velocity, $\mathbf{v}_{\nabla B}$, varies periodically with a frequency $2\omega_H$. The alternating azimuthal current density, Fig. 5.8, triggers propagating axial magnetic field fluctuations. Note that there is no magnetic field fluctuation associated with a purely electrostatic phenomenon.

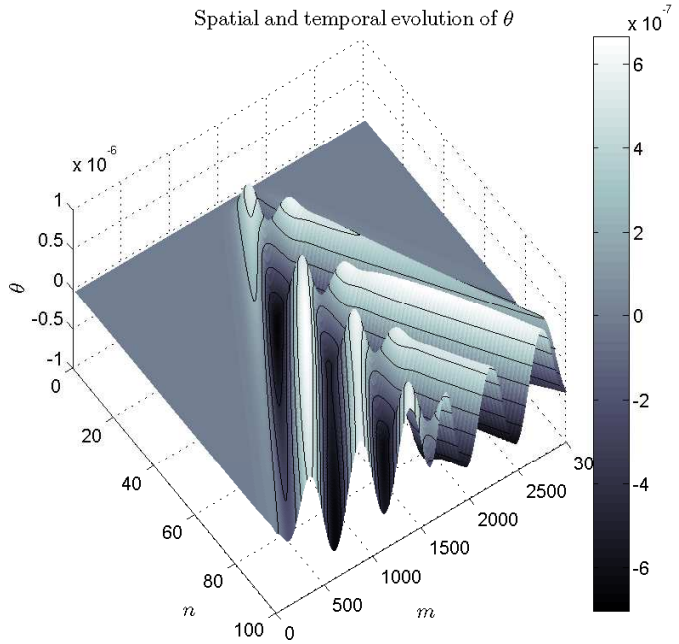

Figure 5.11: Spatial and temporal evolution of the dimensionless azimuthal electric field, θ, of the electromagnetic wave shown in Fig 5.10. The alternating azimuthal current density, Fig. 5.8, triggers axial magnetic field fluctuations, Fig. 5.10, and an accompanying time varying azimuthal electric field that constitutes a radially propagating electromagnetic wave.

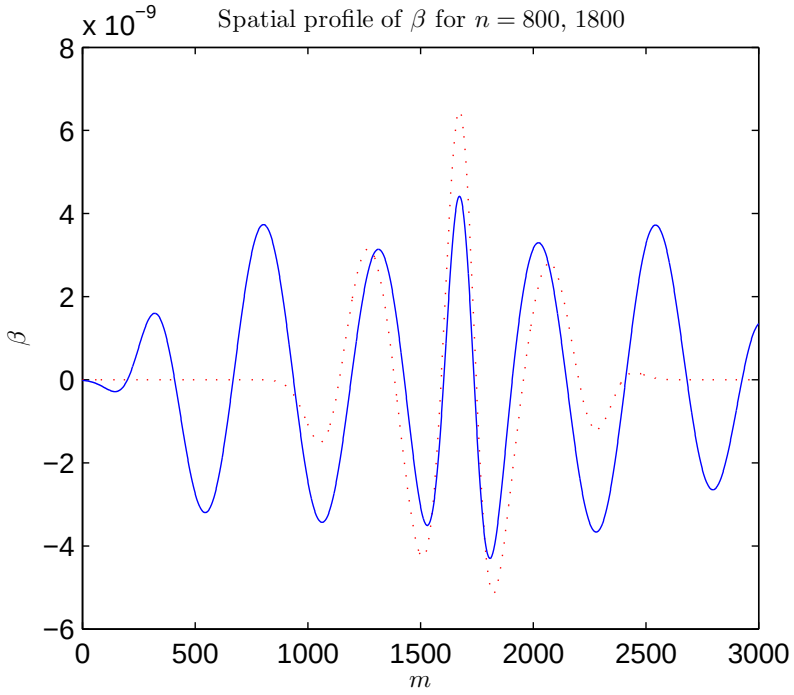

Figure 5.12: Spatial structure of the dimensionless axial magnetic field, β, for time step 800 (dotted line) and 1800 (solid line), corresponding to slices along the ξ-axis in Fig. 5.10, showing that the wave is clearly propagating.

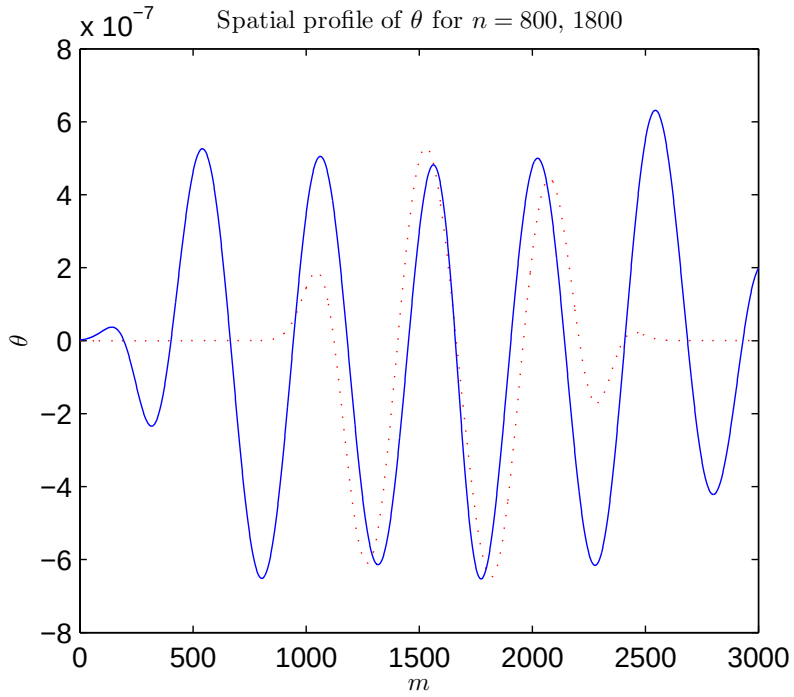

Figure 5.13: Spatial structure of the dimensionless azimuthal electric field, θ, for time step 800 (dotted line) and 1800 (solid line),corresponding to slices along the ξ-axis in Fig. 5.11. Note that the phase of this component, taken with Fig. 5.12, is consistent with an electromagnetic wave.

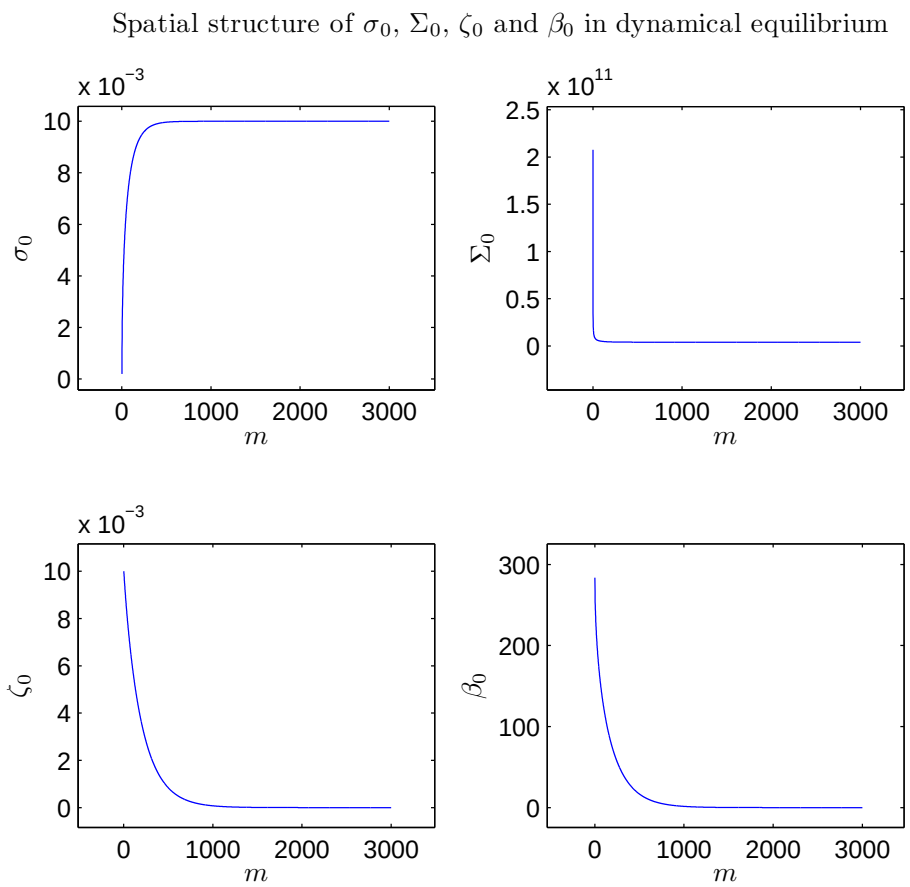

Figure 5.14: Dynamical equilibrium solutions for $\kappa_0 = 4 \times 10^7$, $\kappa_1 = 10^{-2}$ and $\kappa_2 = 4 \times 10^{11}$. Plots show behaviour as function of position for the following quantities: Top left, radial streaming speed σ_0; top right, total number density Σ_0; bottom left, differential azimuthal flow ζ_0; bottom right, magnetic field. Solutions calculated using a bespoke Runge-Kutta routine with the parameters in Table 5.3. The equilibrium calculated here used to produce solutions in Figs. 5.16-5.27

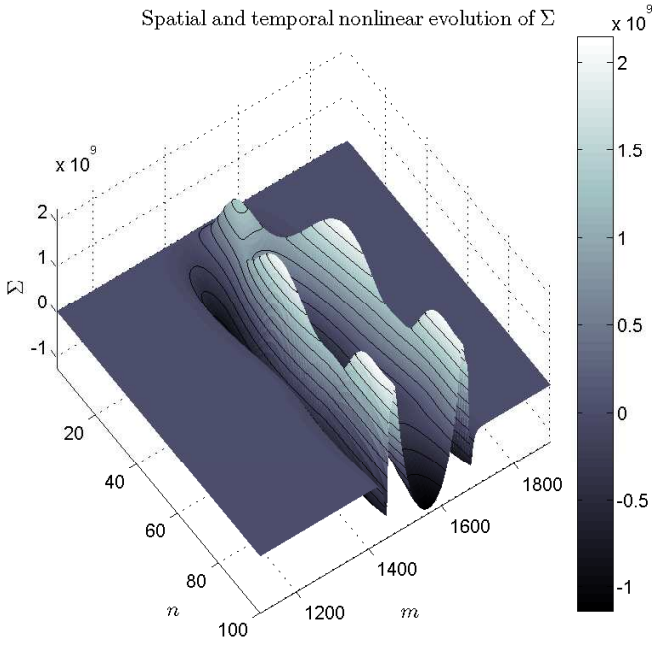

Figure 5.15: Spatial and temporal nonlinear evolution of the average dimensionless plasma density, Σ, for one period of an electrostatic oscillation after an initial 70% charge density perturbation. Note that this plot is of the region of interest between spatial grid points 1150 and 1850. A nonlinear charge density perturbation creates a decrease in the plasma density, hence the plasma frequency, at the centre of the oscillation site. The number density becomes a function of position across the spatial extent of the oscillation, as a result the plasma oscillates over differing timescales. This differential response transports the plasma from slowly varying to rapidly oscillating regions. This results in the growth of density spikes. This plot, and subsequent plots Figs. 5.16-5.27, exhibit the hallmark features of this nonlinearity at an early stage but does not show the ultimate fate of the instability.

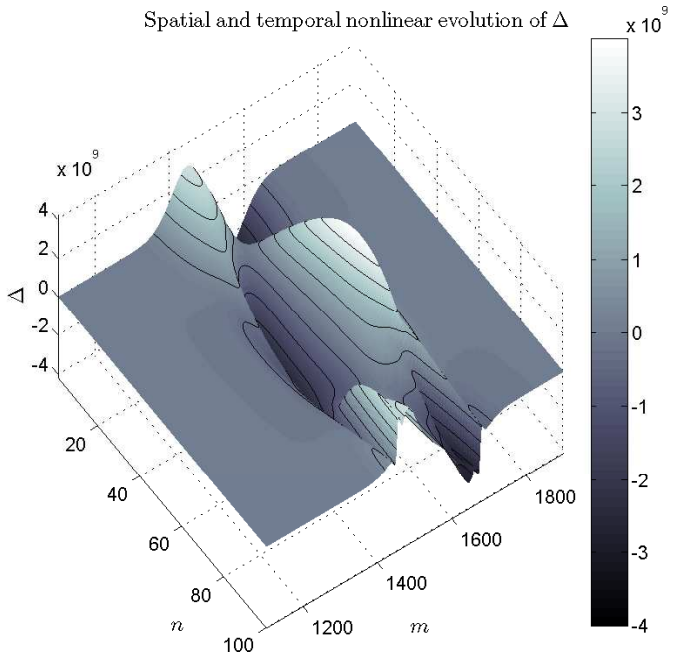

Figure 5.16: Spatial and temporal nonlinear evolution of the difference between the dimensionless e^+-e^- plasma number density, Δ, for one period of an electrostatic oscillation after an initial 70% charge density perturbation. Note the nonlinear evolution of the density and the formation of density spikes in contrast to that exhibited in Fig. 5.4. Note that this plot is of the region of interest between spatial grid points 1150 and 1850.

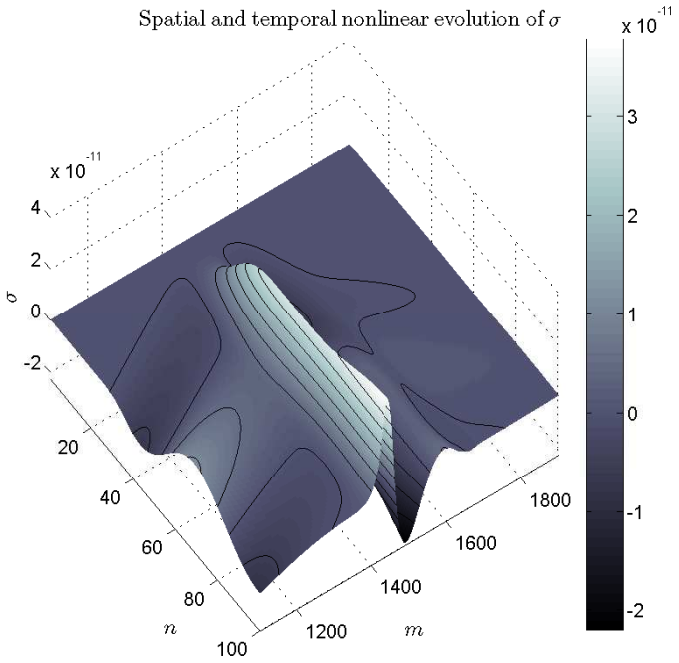

Figure 5.17: Spatial and temporal nonlinear evolution of the average dimensionless radial plasma flow, σ, for one period of an electrostatic oscillation after an initial 70% charge density perturbation. Note that this plot is of the region of interest between spatial grid points 1150 and 1850. In the linear regime, the mode coupling requires that $\sigma = 0$ with deviations from this expressing the nonlinearity of the process. Here $\sigma \sim 10^{-11}$ which is much greater than that in the linear regime shown in Fig. 5.5.

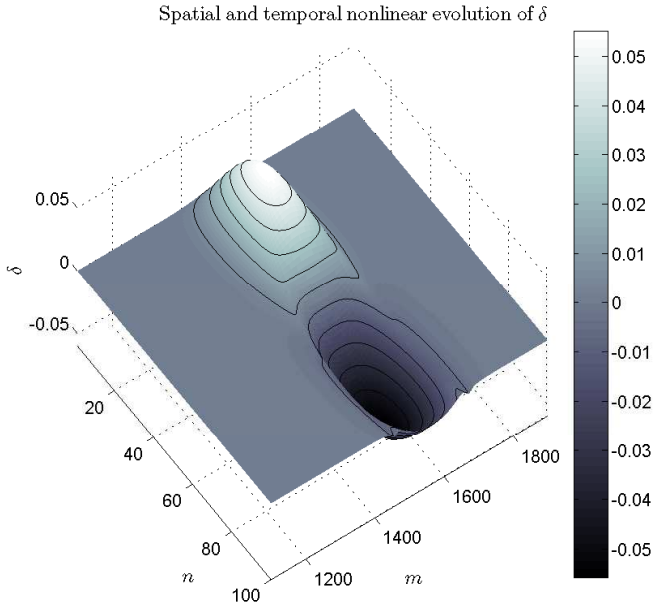

Figure 5.18: Spatial and temporal nonlinear evolution of the difference between the dimensionless e^+-e^- radial velocities, δ, for one period of an electrostatic oscillation after an initial 70% charge density perturbation. Note that this plot is of the region of interest between spatial grid points 1150 and 1850.

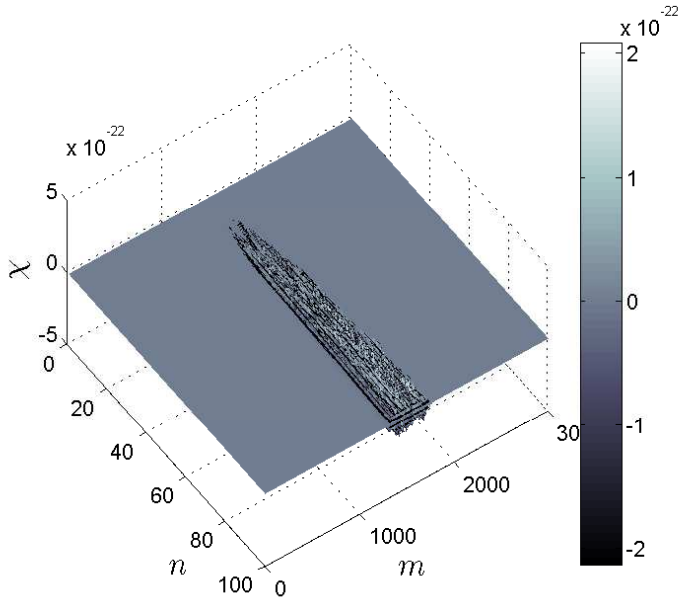

Figure 5.19: Spatial and temporal nonlinear evolution of the average dimensionless azimuthal plasma flow, χ, for one period of an electrostatic oscillation after an initial 70% charge density perturbation. Electrostatic oscillations in the linear, homogeneous regime are characterised by $\chi \neq 0$, the magnetic inhomogeneity has the effect of breaking the azimuthal symmetry of the species fluid velocities due to the charge dependent $\mathbf{B} \times \nabla B$ drift: $\chi = 0$.

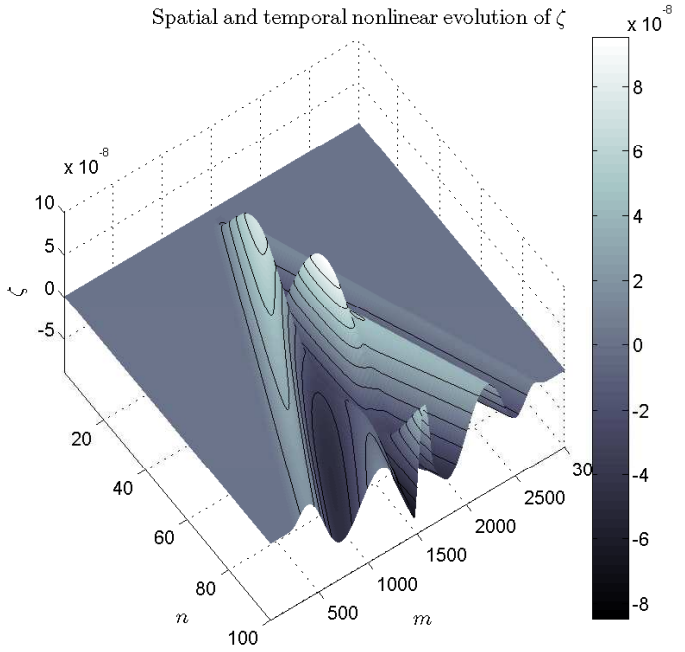

Figure 5.20: Spatial and temporal nonlinear evolution of the difference between the dimensionless e^+-e^- azimuthal velocities, ζ, for one period of an electrostatic oscillation after an initial 70% charge density perturbation.

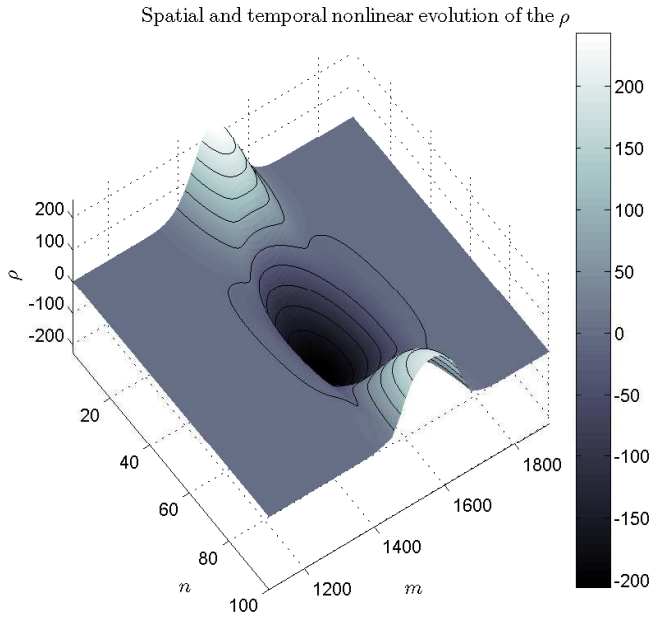

Figure 5.21: Spatial and temporal nonlinear evolution of the dimensionless radial electric field, ρ, of the plasma oscillation consistent with Fig. 5.16. Note that this plot is of the region of interest between spatial grid points 1150 and 1850.

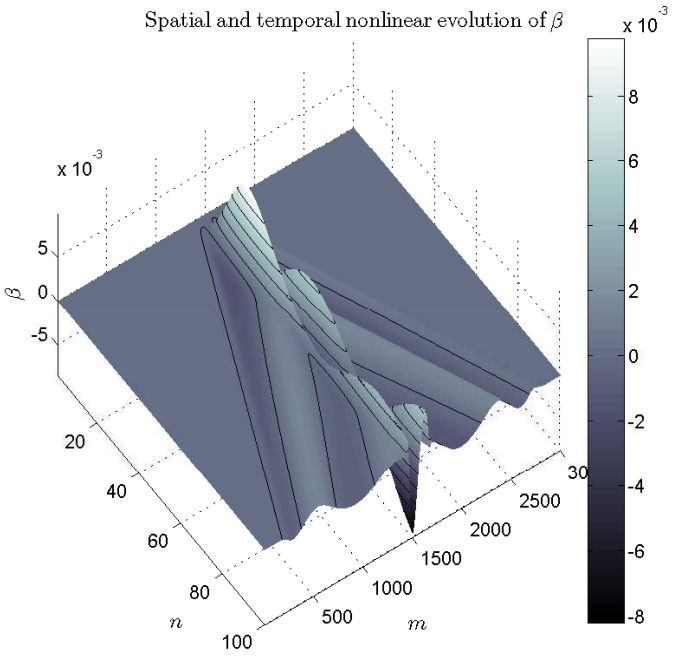

Figure 5.22: Spatial and temporal nonlinear evolution of the dimensionless axial magnetic field, β, showing clearly the propagation of an electromagnetic signal outwards from the electrostatic oscillation site. Note the hallmark features indicative of the nonlinear response of the plasma. This is more clearly exhibited in Fig. 5.27.

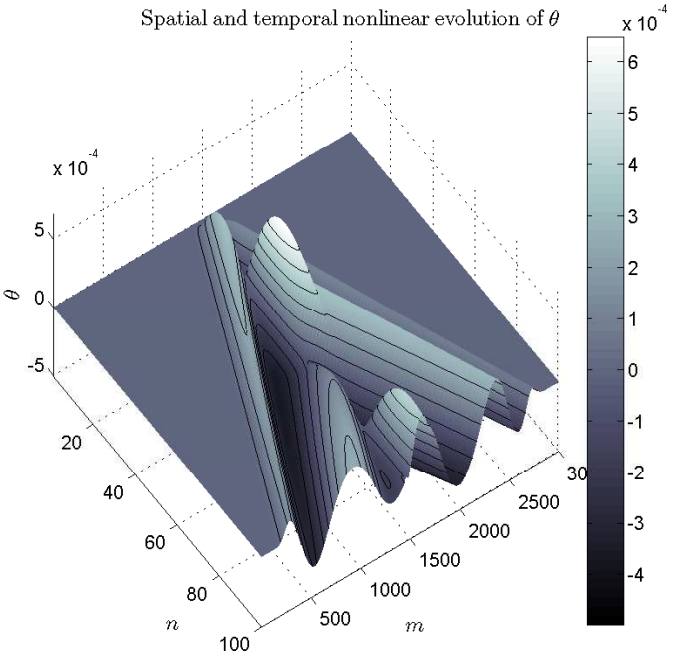

Figure 5.23: Spatial and temporal evolution of the dimensionless azimuthal electric field, θ, of the electromagnetic wave shown in Fig. 5.22. Note the hallmark features indicative of the nonlinear response of the plasma. This is more clearly exhibited in Fig. 5.26.

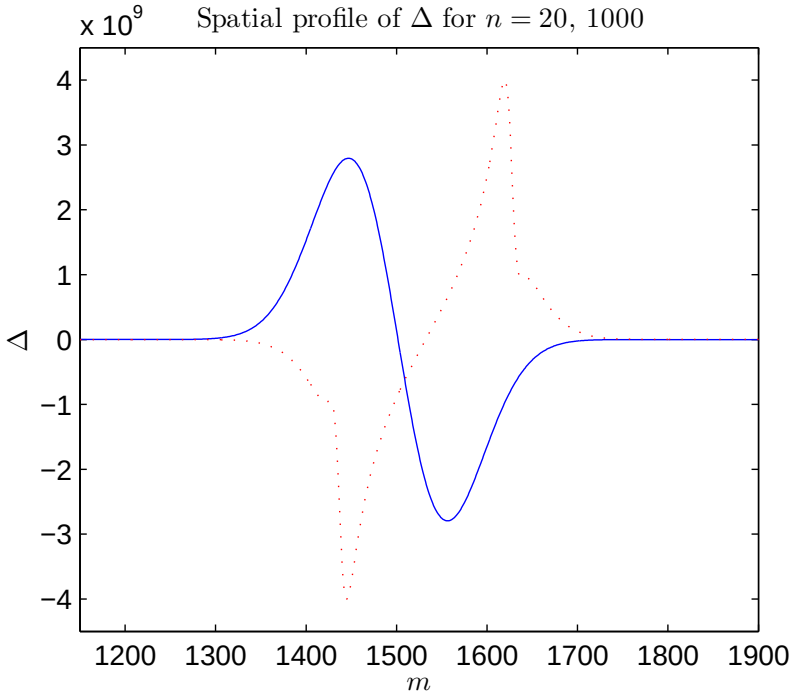

Figure 5.24: Spatial structure of the difference between the dimensionless e^+-e^- plasma number density, Δ, for the time steps 20 (solid line) and 1000 (dotted line). The nonlinear evolution of the plasma oscillation and the onset of the density instability is clearly shown.

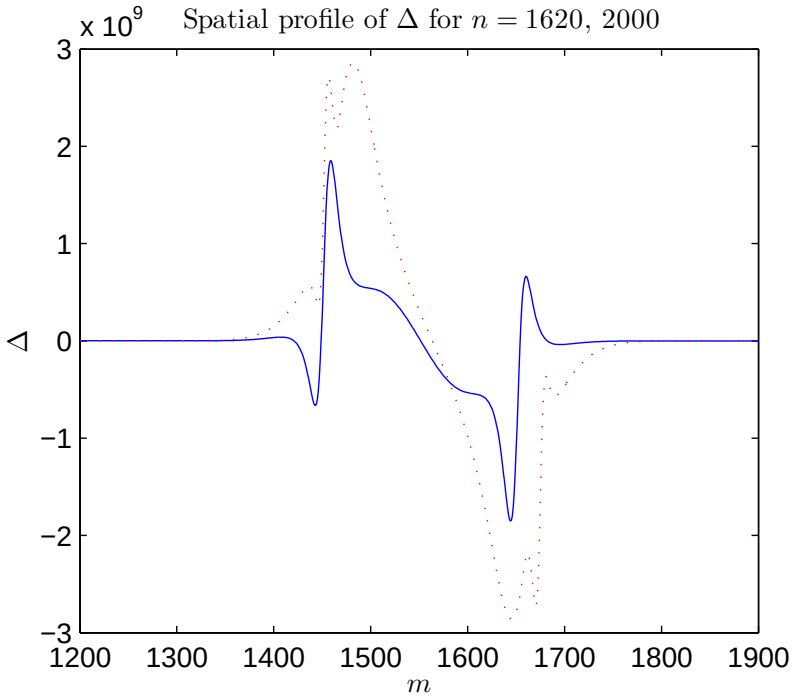

Figure 5.25: Spatial structure of the difference between the dimensionless e^+-e^- plasma number density, Δ, for the time steps 1620 (solid line) and 2000 (dotted line). The nonlinear evolution of the plasma oscillation and the onset of the density instability is clearly shown. Note the gradual flow of the plasma oscillation downstream by the dynamical background plasma.

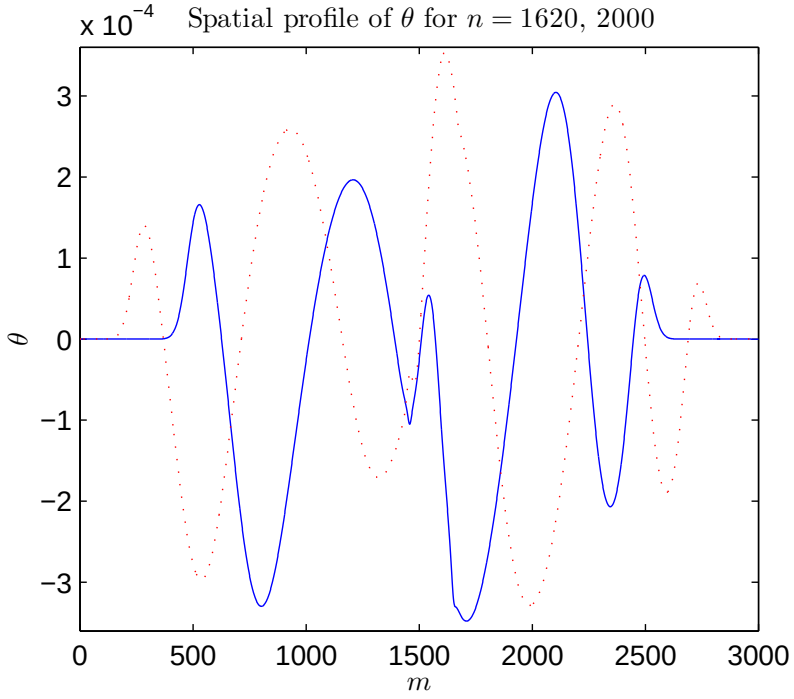

Figure 5.26: Spatial structure of the dimensionless azimuthal electric field, θ, for time step 1620 (solid line) and 2000 (dotted line). Note the nonlinear behaviour consistent with Fig. 5.25.

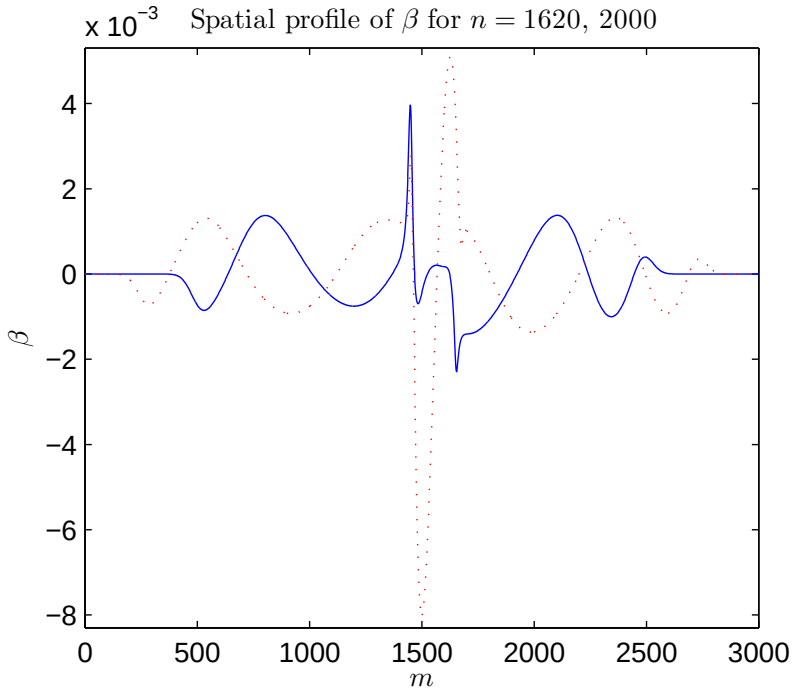

Figure 5.27: Spatial structure of the dimensionless axial magnetic field, β, for time step 1620 (solid line) and 2000 (dotted line). Note the nonlinear behaviour consistent with Fig. 5.25 and 5.26.

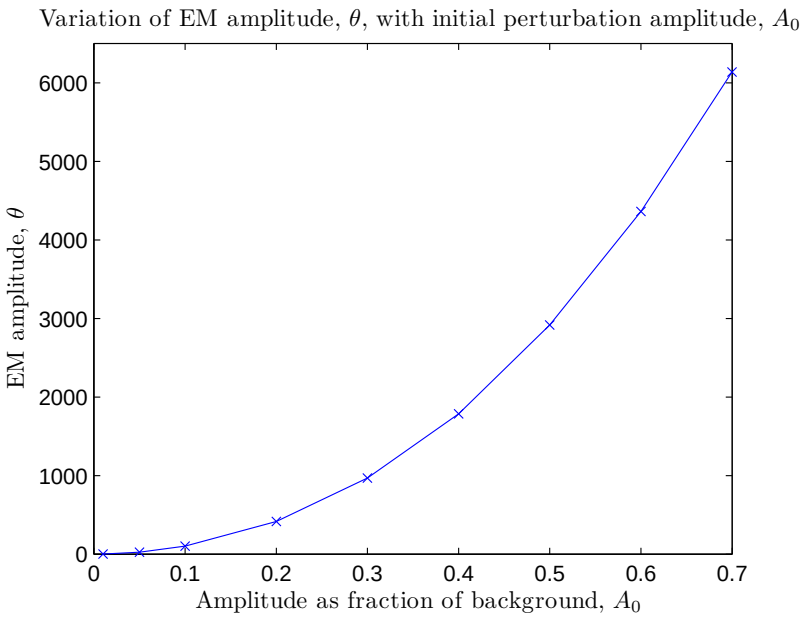

Figure 5.28: Variation of the azimuthal electric field θ of the radiated electromagnetic wave with electrostatic mode amplitude. $|\beta_0'| = 3.5 \times 10^{-7}$ (arbitrary units) at the centre of the oscillation site. Note EM amplitudes have been normalised to the EM amplitude obtained for $A_0 = 0.01$ to aid in the visualisation of the data.

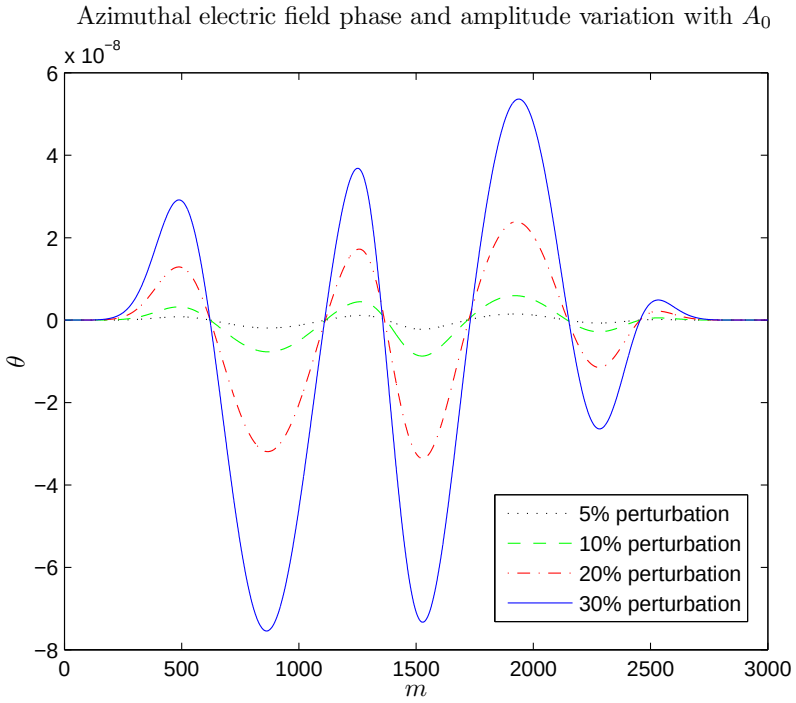

Figure 5.29: Variation of the phase and amplitude of the dimensionless electric field component, θ, of the EM wave with initial perturbation amplitude in the range 5% to 30% of background density.

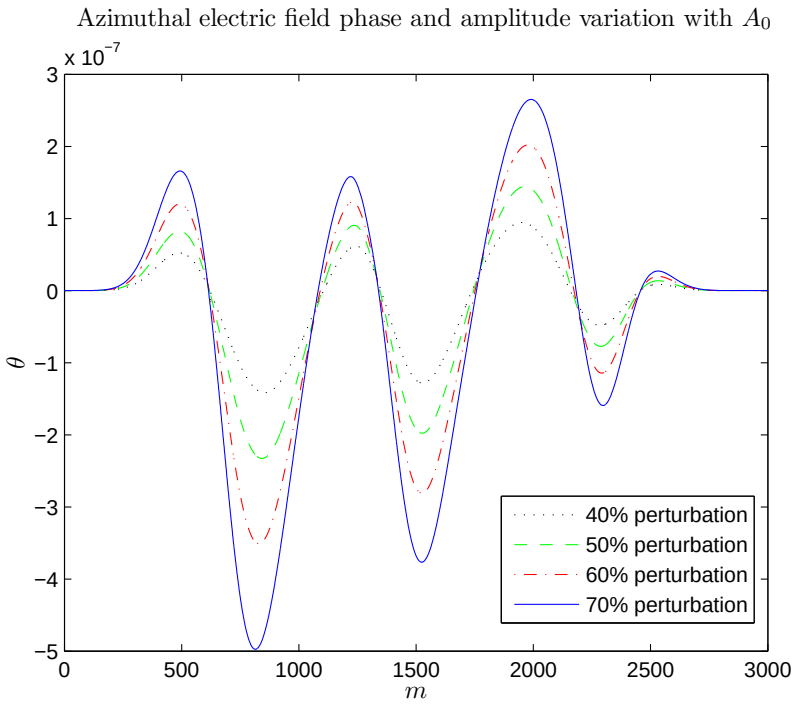

Figure 5.30: Variation of the phase and amplitude of the dimensionless electric field component, θ, of the EM wave with initial perturbation amplitude in the range 40% to 70% of background density.

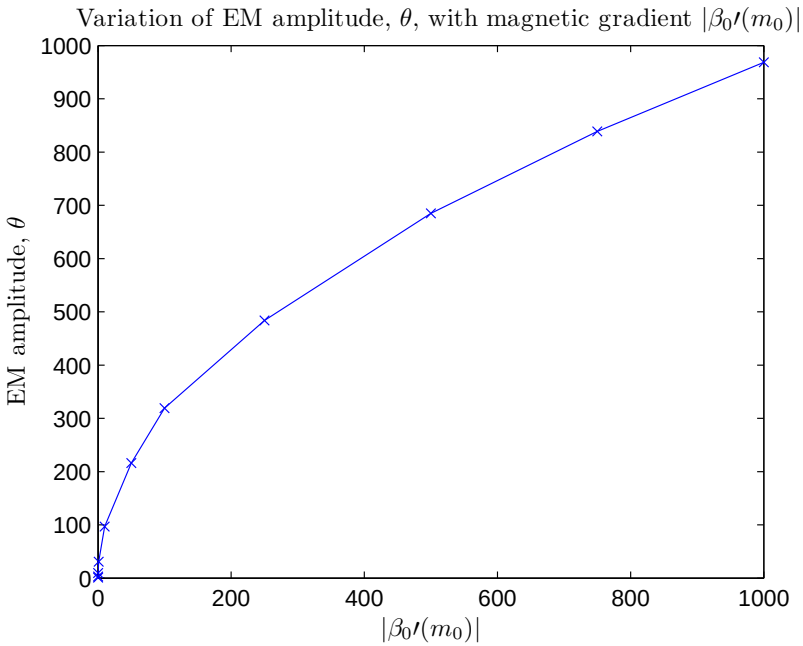

Figure 5.31: Variation of the azimuthal electric field θ of the radiated electromagnetic wave with the dimensionless background magnetic field gradient, β_0', measured at the centre of the oscillation site, after an initial 10% density perturbation. Note the EM wave amplitude has been normalised to the amplitude obtained for $|\beta_0'(m_0)| = 1 \times 10^{-3}$ to aid in the visualisation of the data.

Additional wave mode

In the linear regime, the mode coupling requires that $\sigma = 0$ with deviations from this expressing the nonlinearity of the process: the greater the nonlinearity; the greater the deviation. This is consistent with the nonlinear evolution of large amplitude electrostatic oscillations in a homogeneous magnetic field. In contrast to the expected behaviour, the solution of σ plotted in Fig. 5.5 exhibits a curious, anomalous feature that originates from the edge of the oscillation site and propagates upstream as it grows in magnitude, Fig. 5.32. Fig. 5.33 showcases the residual nonlinear form of σ before the development and evolution of the anomalous feature. When it reaches the edge of the numerical domain its size obscures the other components of the solution, Fig. 5.5. Fig. 5.34 for $m \in [1400, 2000]$ shows the nonlinear residual feature associated with the electrostatic oscillation itself, its relative magnitude is dependent upon the degree of nonlinearity of the oscillation. At $m = 1400$ the hallmark of the anomalous feature is evident. Consistent with the occurrence of the additional feature in σ an equivalent anomalous feature appears in the full nonlinear solution of Σ, its relative magnitude to the solution associated with the electrostatic oscillation is $\sim 10^{-17}$, Fig. 5.35. Note that no other plasma variables exhibit this behaviour. Resolving σ into its constituent components, u_r and v_r, demonstrates that the anomalous feature is very small relative to the oscillation $\sim 10^{-19}$, Figs. 5.36-5.38. This phenomenon is also present in the full nonlinear solutions when the initial 70% charge density perturbation case shown in Figs. 5.15-5.23. Note that in Fig. 5.17 the evolution of σ is shown for one period of an electrostatic oscillation only, therefore the anomalous feature is less pronounced. The absence of peculiarities in the other solutions and the relative size of the features present in the plasma variables, Σ and σ, implies that the anomalous features do not affect the numerical calculations presented here.

The source of the features can be attributed to one of two resolutions, the first being numerical noise. In these simulations the equilibrium is dynamic and streaming, both in the azimuthal and radial directions. When the charge density is perturbed an electrostatic oscillation is triggered that is convected downstream with the plasma radial flow. As this oscillation evolves in time and drifts downstream a discontinuity may develop between the grid points and the edges of the oscillation site. The FDTD method used to solve the governing set of differential equations does not have an inherent diffusion term, unlike the Lax-Wendroff method, so any high frequency signal or discontinuity in the numerical domain will propagate and grow. Numerically this could potentially be the source of the anomalous feature.

The second resolution is that an additional wave mode is being partially stimulated in the simulations. In the linear analysis elucidated in Chapter 3, the two modes required for the mode coupling mechanism were explicitly described, namely the electrostatic and the electromagnetic mode, within the framework of a cylindrical pair plasma. The electromagnetic mode constitutes a radially propagating disturbance with an azimuthal electric field and axial magnetic field - analogous to the extraordinary mode. These will not be the only modes present in the system even though the model presented here is designed to showcase the coupling modes specifically. To get a flavour of the additional modes that could be perturbed in the system one can look to the uniform, homogeneous case for direction.

The normal wave modes of an infinite homogeneous cold pair plasma can be divided into two categories depending on their direction of propagation with respect to the background magnetic field. For parallel propagation the present modes are: an electrostatic oscillation and a transverse electromagnetic mode. In the perpendicular propagation case the modes

are: the hybrid oscillation, the ordinary mode and the extraordinary mode. The ordinary mode has a non-zero electric field in the z-direction and the parallel electromagnetic mode has a non-zero electric field in the r-θ plane. It is possible that a mode similar to these modes is being partially perturbed explaining the anomalous features in the solutions of Σ and σ.

To ascertain what solution resolves and consolidates the numerical results will require further study. One thing is certain that the numerical irregularity does not adversely affect the numerical solutions presented here.

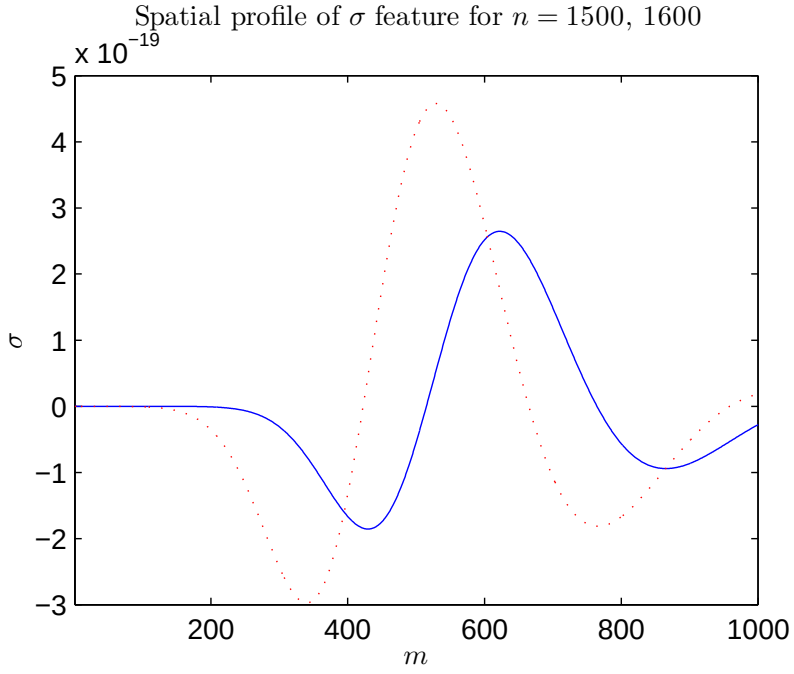

Figure 5.32: Spatial structure of σ in the region $m \in [1, 1000]$ for time steps $n = 1500$ (solid line) and 1600 (dotted line). Plot shows the propagation of the unidentified feature propagating upstream.

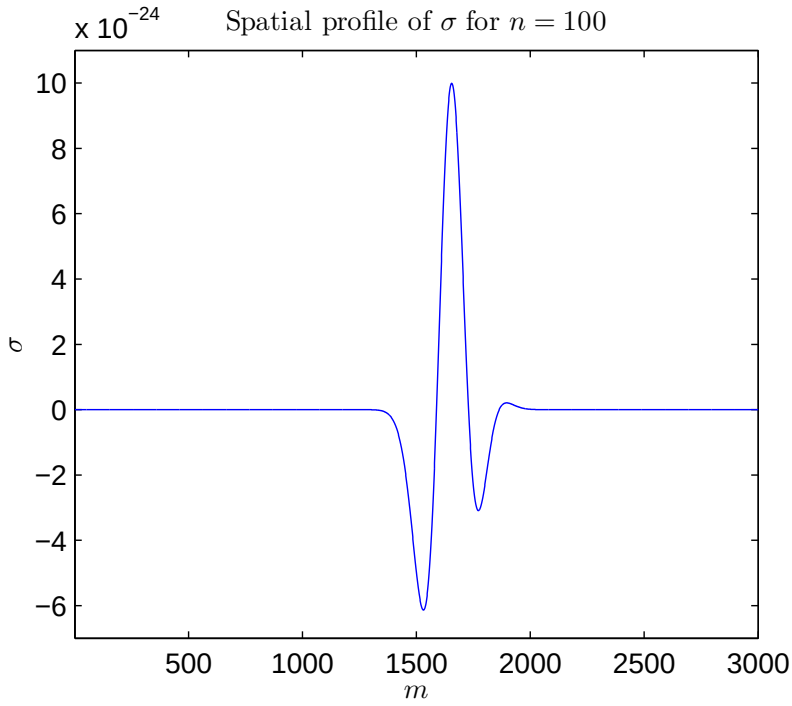

Figure 5.33: Spatial structure of σ for time step $n = 100$. This m-profile for constant n exhibits the σ solution prior to the development and evolution of the unidentified feature.

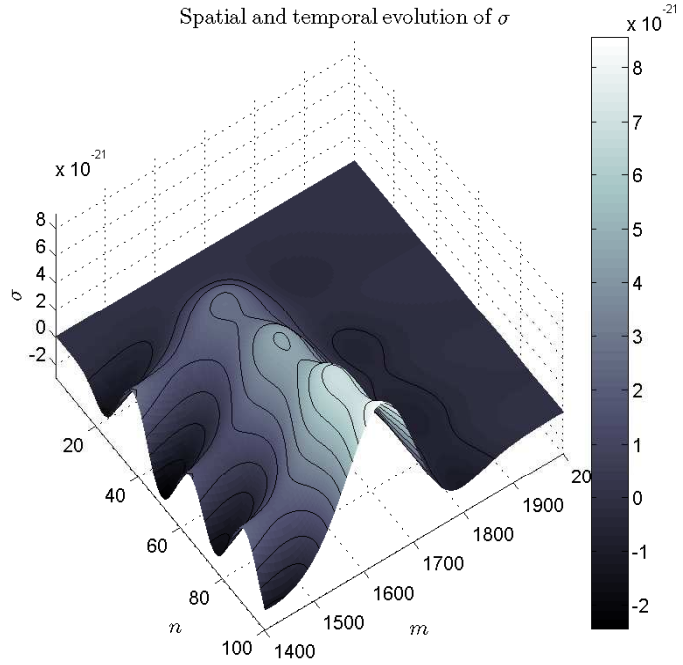

Figure 5.34: Spatial and temporal evolution of σ. This is a re-plot of Fig. 5.5 in the region of interest between $m = 1400$ and 2000, showing the central feature of the σ solution cropping the unidentified feature that propagates upstream.

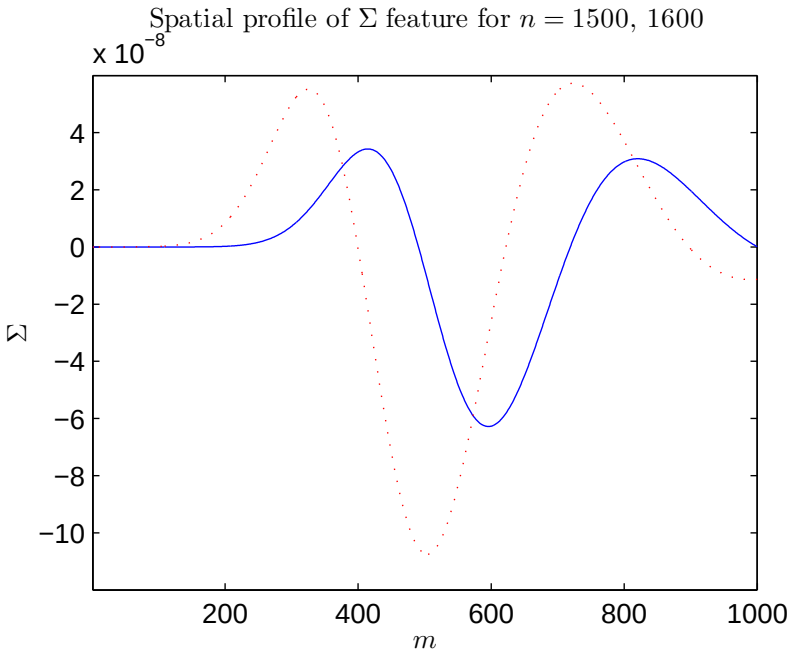

Figure 5.35: Spatial structure of Σ in the region $m \in [1, 1000]$ for time steps $n = 1500$ (solid line) and 1600 (dotted line). Plot shows the propagation of the unidentified feature propagating upstream consistent with the occurrence of the feature in σ.

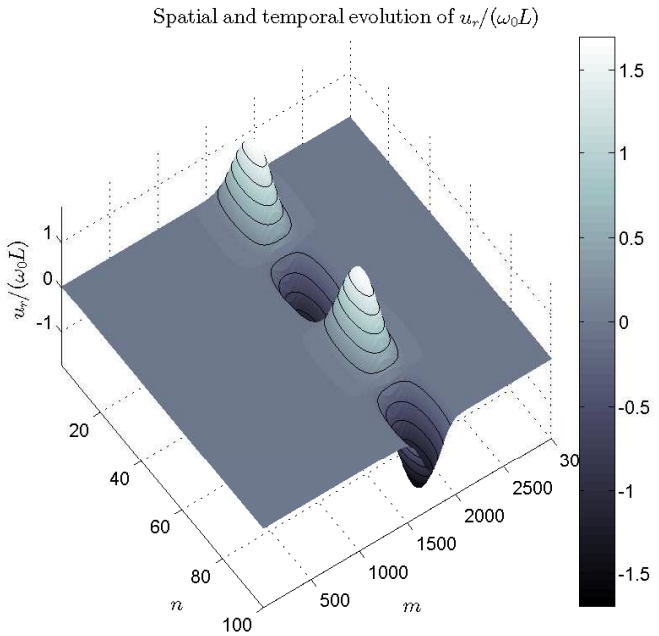

Figure 5.36: Spatial and temporal evolution of $u_r/(\omega_0 L) = \sigma + \delta$. Note the absence a significant unidentified feature that propagates upstream.

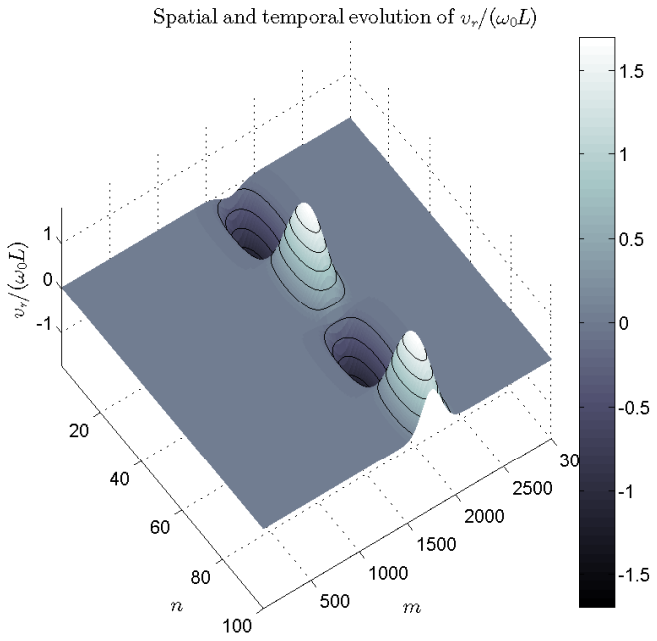

Figure 5.37: Spatial and temporal evolution of $v_r/(\omega_0 L) = \sigma - \delta$. Note the absence a significant unidentified feature that propagates upstream.

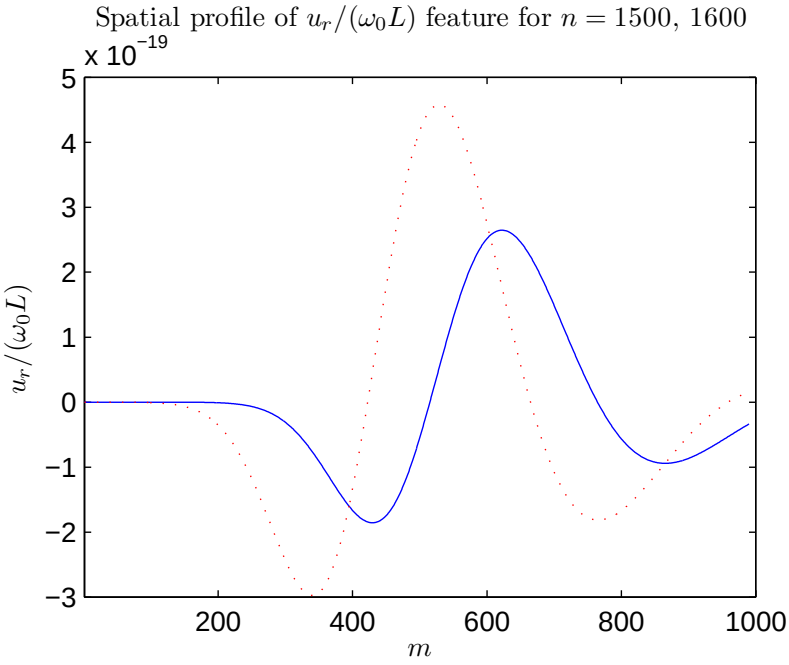

Figure 5.38: Spatial structure of $u_r/(\omega_0 L) = \sigma + \delta$ in the region $m \in [1, 1000]$ for time steps $n = 1500$ (solid line) and 1600 (dotted line). Plot exhibits the corresponding feature in u_r that forms the feature. Note this identical profile is present in the v_r solution.

5.3.2 Multiple wave interactions

Consider the case where there are a number of individual electrostatic oscillations coupling to propagating electromagnetic modes. There will arise the situation where electromagnetic radiation from one oscillation will interact with another oscillation site and its associated radiation field. In this situation the local magnetic field gradient will be altered momentarily, increasing the wave coupling. To investigate this phenomenon an injected electromagnetic pulse propagated towards an established electrostatic oscillation, Fig. 5.40.

Initial conditions

For a given dynamic equilibrium, an electrostatic plasma oscillation is perturbed downstream of an electromagnetic perturbation. The nonlinear mode coupling via an inhomogeneous magnetic field is stimulated as in §5.3.1, by perturbing the charge density:

$$\Delta_m(\tau=0) = \begin{cases} A_0 N_0 \sin\left[\pi\dfrac{(m-m_0-\varsigma)}{\varsigma}\right]\exp\left[-\left(\lambda\dfrac{m-m_0}{\varsigma}\right)^2\right] & m \in [m_0-\varsigma, m_0-\varsigma] \\ 0 & m \notin [m_0-\varsigma, m_0+\varsigma] \end{cases} \tag{5.87}$$

with the accompanying electric field induced by the prescribed charge density perturbation,

$$\rho_m(\tau=0) = \begin{cases} \dfrac{2}{\xi_0 + m\mathrm{d}\Xi}\displaystyle\int_{m_0-\varsigma}^{m} \Delta_{m'}(\tau=0)\mathrm{d}m' & m \in [m_0-\varsigma, m_0+\varsigma] \\ 0 & m \notin [m_0-\varsigma, m_0+\varsigma] \end{cases} \tag{5.88}$$

At $\tau = 0$ the initial conditions for the other plasma variables are $\Sigma_0 = \sigma_1 = \delta = \chi = \zeta_1 = 0$, $\forall\ m$. To stimulate a propagating electromagnetic wave that will interact with the induced plasma oscillation and its associated radiation field the plasma variables θ and β are perturbed such that,

$$\beta_m(\tau=0) = \begin{cases} A_1 N_1 \sin\left[\pi\dfrac{(m-\hat{m}_0-\hat{\varsigma})}{\hat{\varsigma}}\right]\exp\left[-\left(\lambda\dfrac{m-\hat{m}_0}{\hat{\varsigma}}\right)^2\right] & m \in [\hat{m}_0-\hat{\varsigma}, \hat{m}_0+\hat{\varsigma}] \\ 0 & m \notin [\hat{m}_0-\hat{\varsigma}, \hat{m}_0+\hat{\varsigma}] \end{cases} \tag{5.89}$$

$$\theta_m(\tau=0) = \begin{cases} a\beta_m(\tau=0) & m \in [\hat{m}_0-\hat{\varsigma}, \hat{m}_0+\hat{\varsigma}] \\ 0 & m \notin [\hat{m}_0-\hat{\varsigma}, \hat{m}_0+\hat{\varsigma}] \end{cases} \tag{5.90}$$

where N_1 is a constant that normalises the perturbation relative to the background magnetic field gradient at the centre of the charge density perturbation, $\beta'(m_0)$; A_1 is the amplitude of the perturbation expressed as a fraction of $\beta_0'(m_0)$; a is a factor that determines the direction of propagation of the wave; $\hat{\varsigma}$ is the half-width of the perturbation and $\hat{m}_0$ is the centre of the perturbation. Note that the electrostatic oscillation is perturbed downstream of the electromagnetic perturbation such that $m_0 = \hat{m}_0 + l$, where l is the number of grid points separating the centre of the electromagnetic and electrostatic perturbations. Fig. 5.39 shows an example of the initial conditions for the perturbed electromagnetic wave.

Boundary conditions

The numerical simulations are terminated before the generated electromagnetic signal can propagate to and interact with the boundaries of the numerical domain.

Results

Varying the wavelength of the injected wave and its amplitude will alter the local magnetic gradient hence the resultant coupling. Fig. 5.41 shows the results of 3 different wavelengths of injected wave, and their interaction with the electrostatic oscillation: a reflected component moving upstream; a central oscillating feature; and a transmitted feature moving downstream. Note that Fig. 5.41 shows not the waves themselves but the difference between the wave solutions as a result of interaction, and the non-interacting case, to assist in the comparison. The resultant is calculated by subtracting the full nonlinear calculation from the linear superposition of the two non-interacting cases (that is, the electrostatic oscillation alone, and the injected electromagnetic wave on its own).

The physical origin of the reflected feature is due to two main phenomena: (1) the spatially and temporally varying refractive index of the electrostatic oscillation as the wave passes through it; and (2) the increased wave coupling, momentarily stimulated as the injected wave traverses the oscillation site. The structure and shape of the reflected feature depends strongly on these two factors. The central feature represents the increased wave coupling at the oscillation site due to the passage of the injected wave. The transmitted feature represents the influence of the interaction on the injected EM wave as it propagates away from the oscillation site.

The results of wavelength variation of the fixed-amplitude injected EM wave encountering a plasma oscillation of varying amplitude are presented in Figs. 5.42 and 5.43. The plots were obtained from simulations using the numerical parameters listed in Table 5.7. The simulations were executed for a set timescale, T, within which the injected electromagnetic wave had sufficient time to propagate through the electrostatic oscillation site and past it, but not beyond the numerical domain. The magnetic energy of the reflected feature was chosen since it characterises the entire spatial structure of the feature. The magnetic energy is calculated from integrating the magnetic energy density over the scale length of the reflected feature,

$$U_\beta = \int_0^{m_r} \frac{[\beta_{m'}(T)]^2}{2\mu_0} \mathrm{d}m' \tag{5.91}$$

where m_r is the spatial grid point denoting the radial extent of the feature. Note that the electric energy of the feature was not calculated since explicit knowledge is required of the dielectric tensor $U_\theta \propto \epsilon\theta^2/2$. The amplitude of the incoming injected wave was normalised to be the value of the background magnetic field at the centre of the oscillation site, $A_1 = 1.0$; this is kept constant throughout these specific simulations. Figs. 5.42 and 5.43 show that the maximum energy in the reflected feature occurs when the EM wavelength is not less than the width of the oscillation for smaller oscillation amplitudes, but this drifts to larger wavelengths as the oscillation becomes more nonlinear in character.

Fig. 5.44 shows the results for the central feature, under similar conditions as for Figs. 5.42 and 5.43. There does not seem to be a peak in the response here, but instead a monotonic increase. Note that the peak-to-trough amplitude of the central feature after time T is measured.

Increasing the amplitude (but maintaining constant wavelength) of the injected wave also increases the local magnetic gradient at the oscillation site, and so we expect to see similar phenomena as in the variable wavelength case. The wavelength of the injected wave is kept constant and is normalised to the width of the electrostatic oscillation site, $\hat{\varsigma}/\varsigma = 1.0$. The summary of these results is presented in Figs. 5.45 and 5.46, which show broadly similar behaviour to the earlier cases but with one notable difference: the reflected feature shows no maximum amplitude. It is clear that a maximum response is associated only with a resonance in scale-lengths, which is entirely reasonable.

Table 5.7: Table of parameters for multiple wave interaction numerical simulations Figs. 5.40-5.46

Parameter	Value	
κ_0	1.0×10^{1}	a constant parameter
κ_1	1.0×10^{-2}	a constant parameter
κ_2	1.0×10^{3}	a constant parameter
$\hat{\zeta}_0(\xi_i)$	1.0×10^{-6}	initial $\hat{\zeta}_0$ value at ξ_i
$\hat{\beta}_0(\xi_i)$	1.0×10^{-6}	initial $\hat{\beta}_0$ value at ξ_i
ξ_i	500	initial ξ value
m_{max}	3001	number of spatial points
$\mathrm{d}\Xi$	2.75×10^{-3}	spatial mesh increment
ς	100	half-width of initial perturbation
λ	5.0	gaussian coefficient
m_0	1000	centre of perturbation
$\hat{m}_0$	1800	centre of perturbation
$\mathrm{d}\tau$	1.4×10^{-3}	temporal mesh increment
n_{max}	2000	number of time steps

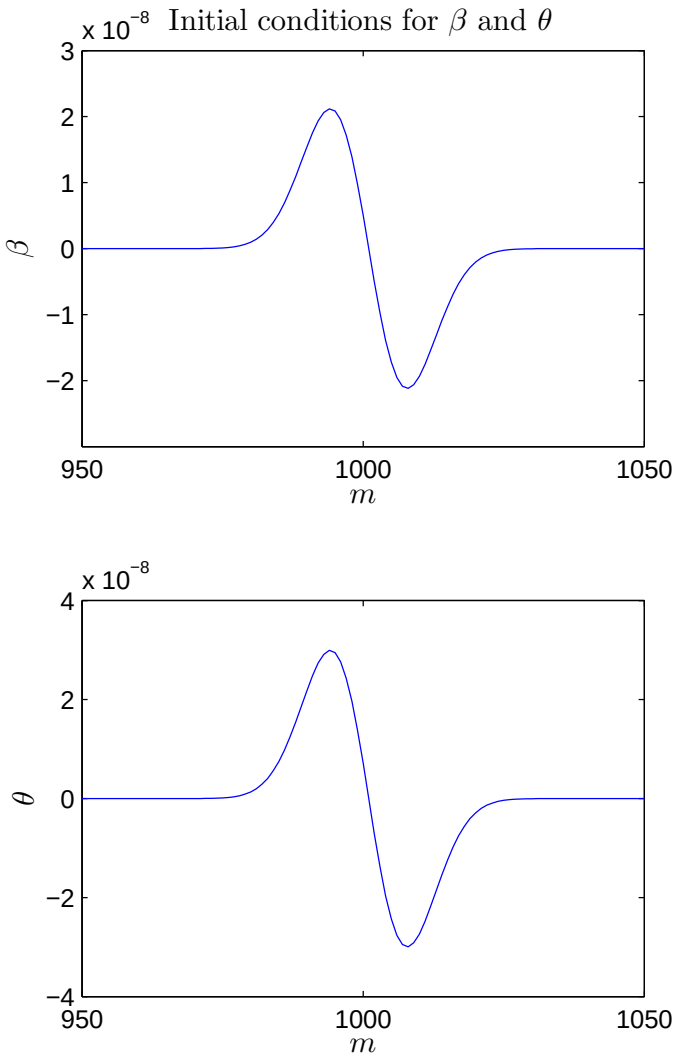

Figure 5.39: Initial conditions for θ and β to stimulate the injected electromagnetic wave. Plots show the magnetic and electric field components of the electromagnetic wave where $\hat{\varsigma} = 50$. The initial conditions are perturbed from an equilibrium defined using the numerical parameters in Table 5.7.

Figure 5.40: Plot of axial magnetic field β showing injected EM wave (left-hand structure) propagating towards EM wave generated by electrostatic coupling.

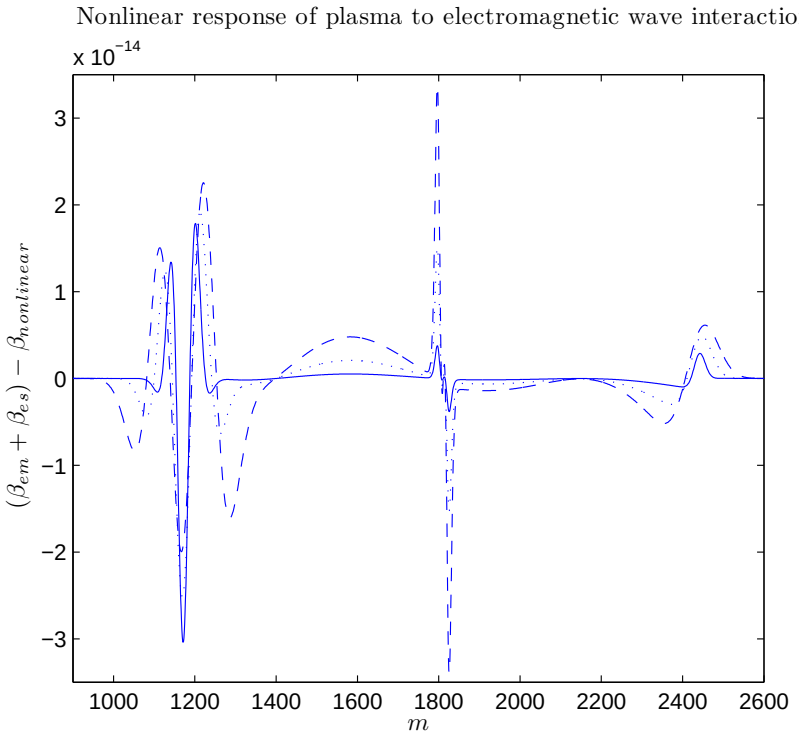

Figure 5.41: Nonlinear response of plasma to EM wave interaction, when the outward directed injected EM wave has passed beyond the edge of the ES oscillation site. Plot shows the difference between the cases where the two EM waves are independently propagating, and when they interact nonlinearly. The solid line is the case where the ratio of the EM wave wavelength to the width of the density perturbation is unity. The dotted and dashed lines correspond to a ratio of 2 and 3 respectively. Note the EM wave amplitude is constant for all ratios. The residual nonlinear response consists of three main features: the reflected feature (left-hand side); the oscillation feature (centre); and a transmitted feature, corresponding to the injected EM wave (right-hand side)

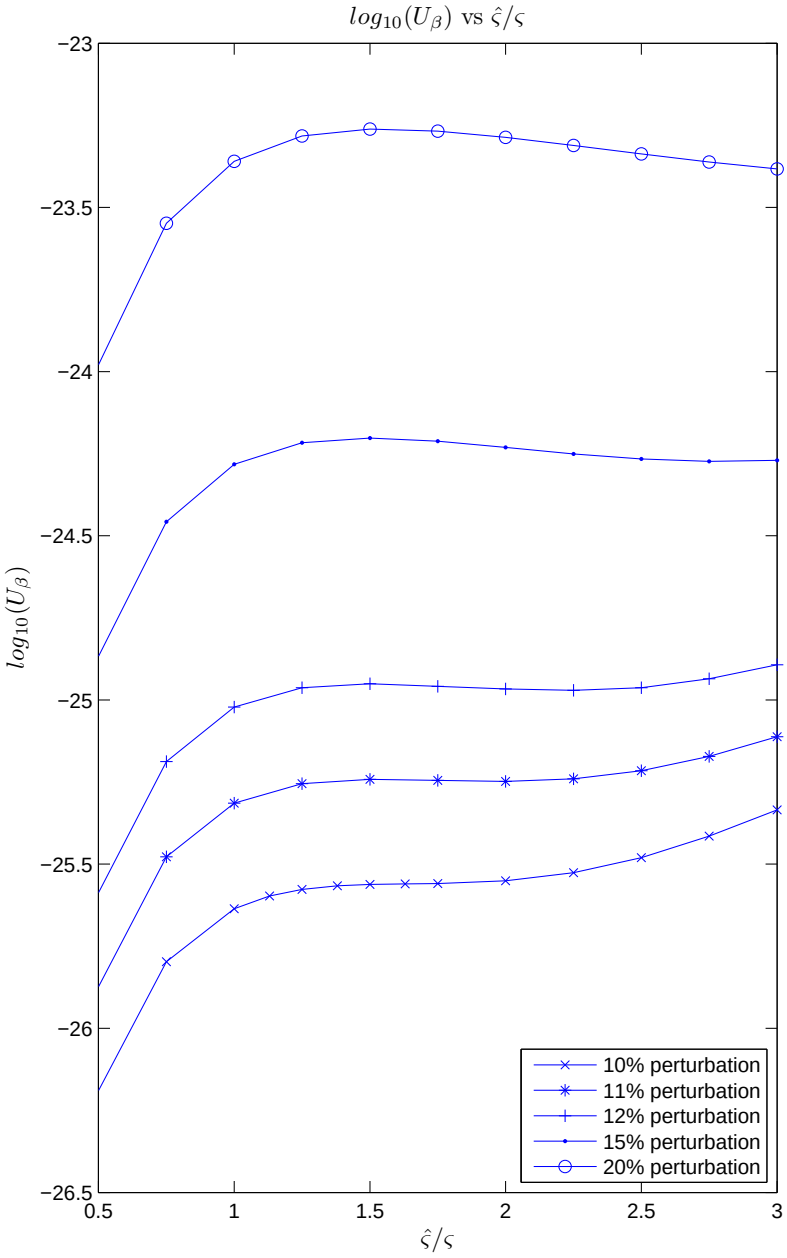

Figure 5.42: Plot of the magnetic energy of the resultant reflected feature as a function of the wavelength of the injected wave normalised to the width of the ES oscillation site. Note that the resultant is calculated by subtracting the full nonlinear calculation from the linear superposition of the two non-interacting cases (that is, the electrostatic oscillation alone, and the injected electromagnetic wave on its own). Notice that for a given density perturbation, the residual reflected feature is a strong function of wavelength of the injected EM wave peaking close to where the wavelength matches the ES site width. However, this peak response drifts with ES amplitude towards longer wavelengths, reflecting the essential nonlinearity of the coupling.

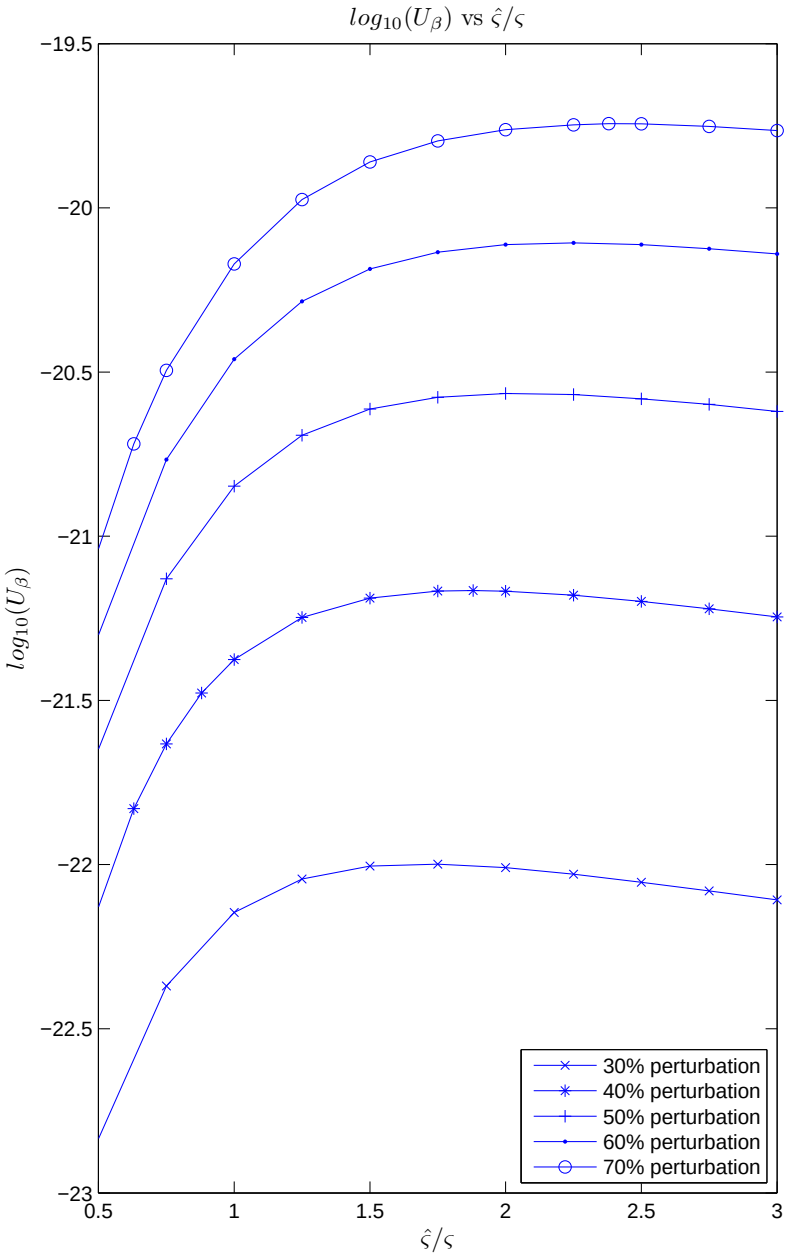

Figure 5.43: Same as for Fig. 5.42.

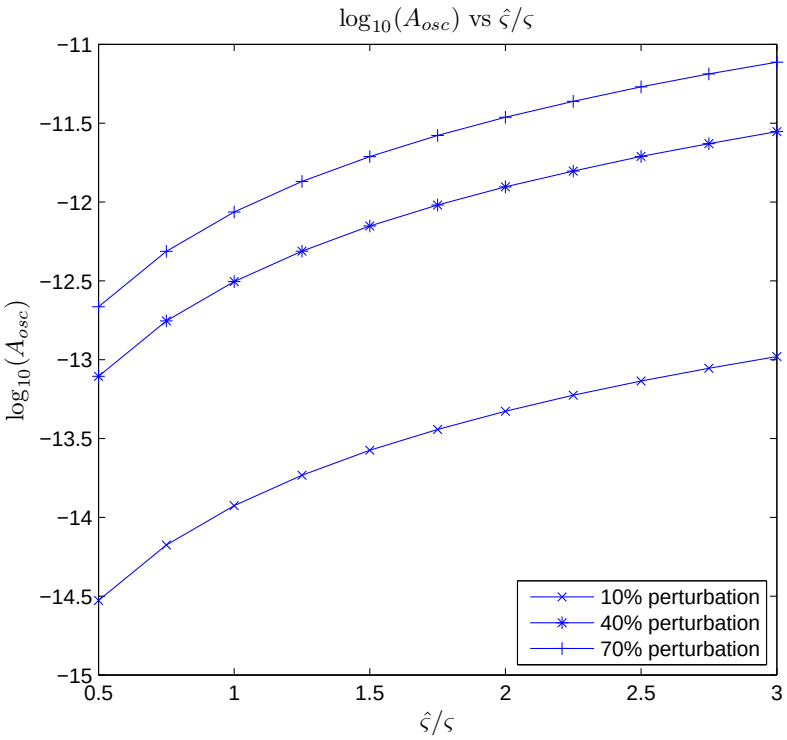

Figure 5.44: Plot of the amplitude of the central oscillating feature as a function of the wavelength of the injected EM wave normalised to the width of the ES oscillation site.

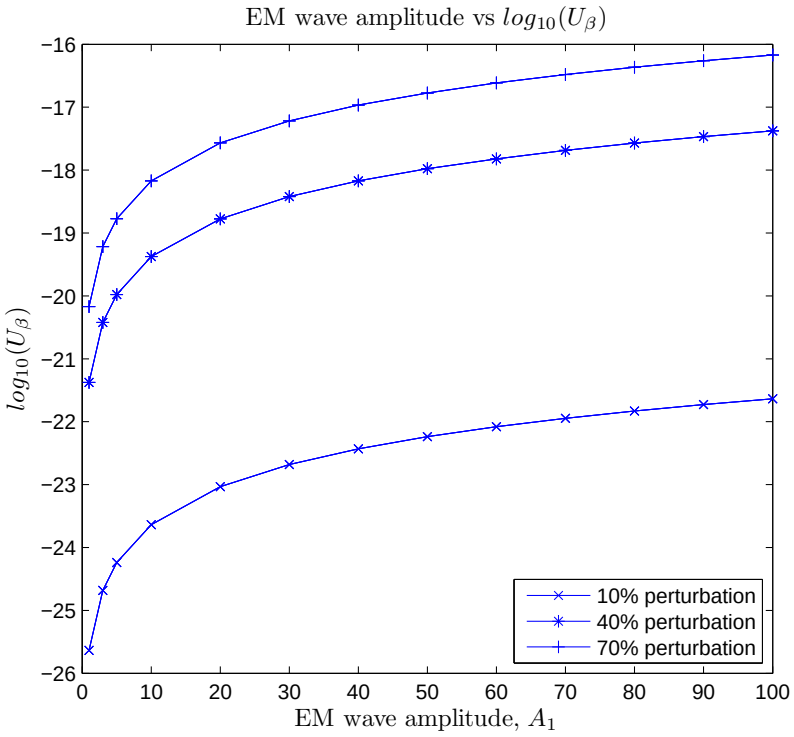

Figure 5.45: Plot of the magnetic energy of the residual reflected feature as a function of the injected EM wave amplitude normalised to the to the value of the background magnetic gradient at the centre of the ES oscillation site.

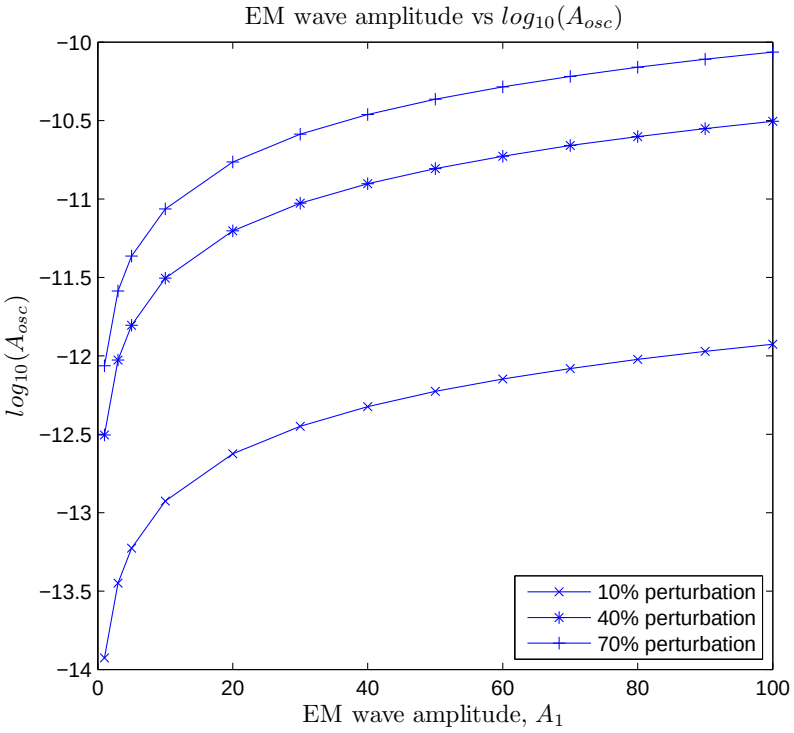

Figure 5.46: Plot of the amplitude of the central oscillating feature as a function of the amplitude of the injected EM wave normalised to the to the value of the background magnetic gradient at the centre of the ES oscillation site.

5.4 Discussion and further developments

The nonlinear system of equations describing a cold pair, cylindrical magnetoplasma does not have a closed form analytical solution and must be ultimately solved numerically. In such a plasma, when the background magnetic field is inhomogeneous, perturbed electrostatic oscillations couple to electromagnetic waves courtesy of a charge dependent $\mathbf{B} \times \nabla B$ drift. The plasma oscillations are perturbed from an equilibrium that self-consistency demands must be non-uniform and dynamic.

The numerical simulations presented here solve the nonlinear set of governing equations describing the equilibrium and the perturbed plasma variables using the Runge-Kutta method and a bespoke FDTD algorithm respectively. The results successfully exhibit the proposed mode coupling in both the linear and nonlinear regime. The nonlinearity of the simulations illustrates the onset of the density instability and its direct effect on the electromagnetic mode. In agreement with the linear analysis described in Chapter 3 the generated electromagnetic mode has no observable Doppler shift since $\sigma_0 \ll p$ which is consistent within the non-relativistic framework adopted. The discrepancy between the expected form of σ and that simulated deserves further investigation to see if new physics is at play.

The nature of the interaction between electromagnetic waves and independent electrostatic oscillations further exemplified the nonlinearity of the simulations. It illustrated the enhanced coupling due to the magnetic gradient of a passing electromagnetic wave-train and its dependence on the waves amplitude and wavelength. The dimensional analysis carried out affirms the feasibility of such a process occurring in a pulsar magnetosphere where assuming $n_- \approx 10^{21}$ m^{-3} yields $E_r \sim 10^9$ Vm^{-1} and $B_z \sim 10^{-3}$ T, which is entirely consistent with the expected values when translated into the rotating pulsar laboratory frame. This confirms the importance of coherent plasma effects and collective plasma processes in the pulsar magnetosphere.

The addition of transparent boundary conditions (also known as Absorbing Boundary Conditions) to the numerical domain would greatly improve the simulations. Transparent boundary conditions are non-reflecting conditions imposed on the boundaries of the bounded numerical domain that mimic the solution of the problem in an unbounded domain. Transparent boundary conditions are a well known numerical technique that allow the extended temporal evolution of wave propagation problems without raising computer memory issues. The simulations here do not allow the generated electromagnetic waves to propagate beyond the numerical domain, simplifying the problem of implementing boundary conditions but limiting the extent and depth of the nonlinear analysis. Implementing transparent boundary conditions unfortunately is non trivial and in this model is further compounded by an equilibrium that is non-uniform such that as $\xi \to 0$ spatial derivatives of the equilibrium variables become very large.

With the transparent boundary conditions the extent to which the coupling mechanism radiatively damps the density instability, apparent in the cold pair plasma model, could be thoroughly studied. For this the plasma oscillation would have to evolve for a large number of oscillations so that the evolution of the instability could be monitored as the mode coupling limited the energy in the oscillation by radiating it away. Without the transparent boundary conditions such an evaluation could not be made as the generated radiation would reach the edge of the numerical domain before a significant number of plasma oscillations would be completed.

Note that the mimicking of an unbounded domain via transparent boundaries would require the reconsideration of boundary conditions in the numerical simulations.

Chapter 6

Elliptical growth of dust grains in astrophysical plasmas

6.1 Introduction

Chapters 2 to 4 have concerned themselves with the discussion of a pulsar radiation source and its propagation in the pair plasma that created it. As discussed earlier in Chapter 1, pulsars are rapidly rotating neutron stars formed from a supernova explosion. In the wake of such an event the newly born pulsar sits at the centre of a supernova remnant, the Crab Pulsar and nebula is the most famous example. The remnant is composed of a hot multi-species, electron-ion plasma and of charged dust, the composition of which is dependent on the elemental abundance of the stellar atmosphere that went before it. The remnant cools and slowly diffuses into the surrounding interstellar medium. In the time frame before it diminishes, radiation produced and emitted by the pulsar must propagate through this complex plasma medium, altering the characteristics of the electromagnetic radiation. The presence of spheroidal dust grains aligned in the ambient magnetic field will result in anisotropic extinction and scattering, polarising the electromagnetic radiation. Upon observation, the unambiguous, true interpretation of the electromagnetic signature can only be made if complete knowledge of the processes involved is understood, opening a diagnostic window on the environment via polarimetric studies. Much research has been carried out on the physical processes behind the formation of dust [85; 86; 64] as well as on the effects spheroidal dust grains have on electromagnetic radiation [87; 88].

Dust growth in gases is initiated via the nucleation of gas atoms and molecules. The dust continues to grow via one of two main processes: via grain-grain coagulation or mantle growth. Coagulation is the process where existing grains collide and stick together forming bigger dust gains. Mantle growth occurs where atoms and molecules in the gas collect on the surface of the dust [40]. In a plasma the growth of dust is fundamentally different since the dust grains and the constituent species of the plasma now possess charge. Instead of growth via nucleation and condensation growth occurs via plasma deposition onto the surface of the dust grain.

6.1.1 Plasma sheaths

To understand the concept of plasma deposition in the context of dust submerged in a plasma it is important to look at the formation of plasma sheaths. Traditionally plasma sheaths were studied in relation to the interaction of a confined plasma with its vessel. With the development of dusty plasmas as an important field the focus has shifted to plasma sheaths around dust particulates.

Consider a neutral electron-ion plasma interacting with a surface. In general ions and electrons striking the surface recombine and are removed from the plasma. The electrons are lost to the surface more frequently due to their greater thermal speed. This leaves the bulk plasma with a net positive charge and the surface with a negative potential with respect to the plasma. The remaining electrons shield the surface from the plasma, creating a sheath region with a width of the order of the Debye length. If an equilibrium state is reached the flux of ions and electrons impinging on the surface is equal. To investigate the form of the potential in the sheath, information is needed regarding the ion and electron distributions.

Following Lieberman and Lichtenberg [89] and using the notation from Chen, one will consider a planar sheath in 1-D [90]. To model the motion of the ions toward the surface they are assumed to have drift velocity, u_0, upon entering the sheath region at $x = 0$. For cold ions, $T_i = 0$, the spatial dependence of the ion velocity in the sheath with a potential $\phi(x)$ is

$$\frac{1}{2}m_i u(x)^2 = \frac{1}{2}m_i u_0^2 - e\phi(x) \tag{6.1}$$

$$u(x) = \left(u_0^2 - \frac{2e\phi}{m_i}\right)^{1/2} \tag{6.2}$$

in order to conserve energy, where m_i is the ion mass. To ensure the conservation of ion flux, the ion distribution in the sheath must obey

$$n_0 u_0 = n_i(x)u(x) \tag{6.3}$$

$$n_i(x) = n_0\left(1 - \frac{2e\phi}{m_i u_0^2}\right)^{-1/2} \tag{6.4}$$

where n_0 is the density of the bulk plasma and n_i is the ion density. The distribution of electrons in the sheath due to the electric potential present is governed by the Boltzmann relation

$$n_e(x) = n_0 \exp\left(\frac{e\phi}{k_B T_e}\right) \tag{6.5}$$

where T_e is the electron temperature; k_B is Boltzmann's constant and n_e is the electron density. With explicit knowledge of the electron and ion distributions, the dependence of the electric potential on x can be found via Poisson's equation:

$$\frac{d^2\phi}{dx^2} = \frac{e}{\epsilon_0}(n_e - n_i) \tag{6.6}$$

$$= \frac{en_0}{\epsilon_0}\left[\exp\left(\frac{e\phi}{k_B T_e}\right) - \left(1 - \frac{2e\phi}{m_i u_0^2}\right)^{-1/2}\right] \tag{6.7}$$

where ϵ_0 is the permittivity of free space. Non-dimensionalising the resulting differential equation using the following variables,

$$\chi = -\frac{e\phi}{k_B T_e} \tag{6.8}$$

$$\xi = \frac{x}{\lambda_D} = x\left(\frac{n_0 e^2}{\epsilon_0 k_B T_e}\right)^{1/2} \tag{6.9}$$

$$\mathcal{M} = \frac{u_0}{(k_B T_e/m_i)^{1/2}} \tag{6.10}$$

yields

$$\frac{d^2\chi}{d\xi^2} = \left(1+\frac{2\chi}{\mathcal{M}^2}\right)^{-1/2} - e^{-\chi} \tag{6.11}$$

where λ_D is the Debye length. This is the nonlinear differential equation describing the electric potential of plane sheath. The order of this differential equation can be reduced by multiplying both sides of the equation by $\mathrm{d}\chi/\mathrm{d}\xi$ and integrating with respect to ξ with the boundary conditions: $\chi = \mathrm{d}\chi/\mathrm{d}\xi = 0$ at $\xi = 0$. Therefore,

$$\frac{1}{2}(\chi')^2 = \mathcal{M}^2\left[\left(1+\frac{2\chi}{\mathcal{M}^2}\right)^{1/2} - 1\right] + e^{-\chi} - 1 \tag{6.12}$$

The right-hand side of the equation must be positive for all values of χ. Expanding the right-hand side in a Taylor series around $\chi = 0$ (including up to second order terms) the following inequality is obtained,

$$\mathcal{M}^2 \geq 1 \tag{6.13}$$

$$u_0 \geq \left(\frac{k_B T_e}{m_i}\right)^{1/2} = u_B \tag{6.14}$$

This is the Bohm sheath criterion and requires that the ions must enter the sheath with a velocity greater or equal to the hybrid term $k_B T_e/m_i$. There must exist a finite electric field in a region called the presheath that accelerates the ions from the bulk plasma into the sheath. These results although derived for a planar sheath still yield great insight into sheath formation in the dust context.

6.1.2 Dust in electron-ion plasmas

Consider a dust grain or seed present in a uniform electron-ion plasma, Fig. 6.1. For a plasma in thermal equilibrium the greater mobility of the electrons ensures the grain becomes negatively charged resulting in an electron depleted sheath region forming around the grain. As the negative charge on the grain builds up, the number of electrons having the appropriate kinetic energy to overcome the grain potential, striking its surface, decreases. Due to the negative charge on the grain there will now exist a flow of ions towards the grain which are deposited on the grain surface altering its size, mass, charge and hence the potential of the grain, Fig. 6.2. As a result the number of electrons reaching the surface increases, further altering the charge. This occurs until the grain reaches the floating potential ϕ_f where the flux of electrons and ions at the surface of the grain are equal,

$$n_0 u_B = \frac{1}{4} n_e \bar{v}_e \tag{6.15}$$

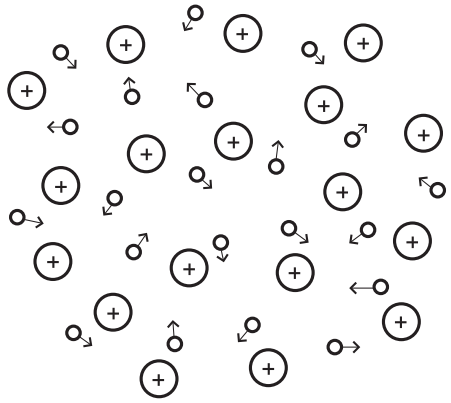

Figure 6.1: A neutral plasma in thermal equilibrium. Note that the greater mobility of the electrons.

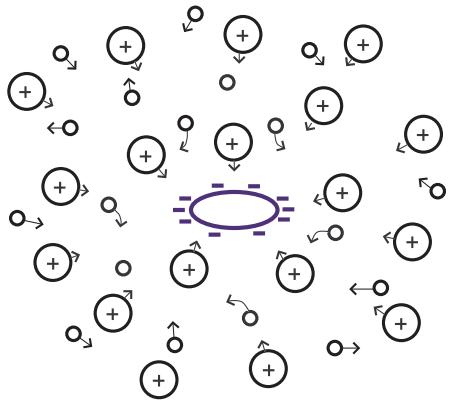

Figure 6.2: A dust grain introduced into the plasma will become negatively charged thanks to the greater mobility of the electrons. The ions see this net charge, are accelerated towards the grain and are deposited on its surface altering the net charge of the grain.

where $\bar{v}_e = (8k_BT_e/\pi m_e)^{1/2}$ is the average electron speed. Substituting from Eqs. (6.5, 6.14) yields the floating potential

$$\phi_f = -\frac{k_BT_e}{2e}\ln\left(\frac{m_i}{2\pi m_e}\right) \tag{6.16}$$

The sheath width is approximately a few electron Debye lengths $\lambda_{De} = (\epsilon_0 k_B T_e/n_e e^2)^{1/2}$, where the potential of the grain is shielded from the plasma [89]. In this steady-state situation ions will be accelerated from the plasma via the presheath into the sheath region at the Bohm Speed, $u_B = (k_BT_e/m_i)^{1/2}$, where they will be deposited ultimately on the grain surface, Fig. 6.3. When λ_{De} is much smaller than the ion mean free path, the Bohm criterion is necessary for the shielding by a stationary sheath [91].

For spherical dust grains the electric field is purely radial around the grain and deposits the ions uniformly on the grain surface. However ellipsoidal dust grains have a non-radial electric field close to the grain and ions could be deposited on the surface in a non-uniform fashion depending on their momentum, leading to growth in a preferred direction. If the momentum of the ions is too large they will not follow the direction of the field lines faithfully and resultant elongated growth may not occur.

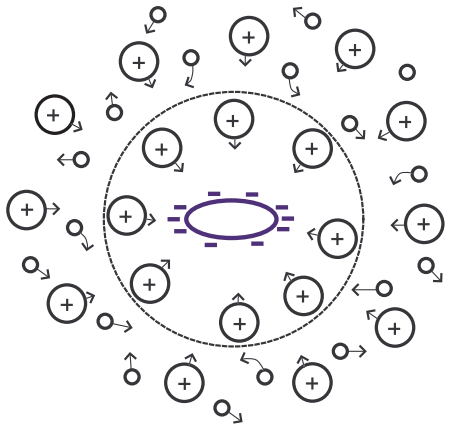

Figure 6.3: Formation of a electron depleted sheath region around a charged dust grain. The dashed line indicates sheath boundary. The grain is at the floating potential, ϕ_f where the ion and electron fluxes are equal.

To see how the growth of elongated dust grains occur, the trajectories of the ions entering the sheath were studied. By considering a uniform distribution of ions at the sheath-plasma interface, each with a velocity equal to the Bohm speed, u_B, the ion trajectories were calculated within the sheath. From these numerical calculations the points on the perimeter of the ellipse where the ions were deposited were calculated.

This chapter addresses the problem of elliptical dust growth in electron-ion plasmas and investigates the applicability of such a mechanism in supernova remnants. In Sect. 6.2 a theoretical model of elliptical grain growth is discussed. Sect. 6.3 formulates the numerical algorithm used to calculate the electric field in the sheath surrounding the grains and hence the trajectories of the ions in the sheath. In Sect. 6.4 the results of the numerical simulations are discussed to see if elliptical growth occurs. Elements of this chapter have been published in a paper written by the author in the journal Astronomy and Astrophysics [92].

6.2 2-D Model: elliptical co-ordinates

To simplify matters the problem will be restricted to 2-D so that the sheath is a circle at the centre of which is an elliptical grain. It is assumed that the semi-major axis of the central elliptical cross-section is small compared to the sheath length in the plasma and that the grain is conducting. It is further assumed that the space between the grain and the sheath-presheath interface is a vacuum, in which there is no distribution of electrons or ions.

The electric potential of the dust grain can be expressed in elliptical co-ordinates as follows. The elliptical cross-section of the grain has cartesian co-ordinates given in parametric form as $(x, y) = (a\cos\theta, b\sin\theta)$, where θ is the angle subtended at the ellipse centre and a and b are the semi-major and minors axes of the ellipse respectively. The pole and equator of the ellipse correspond to $\theta = 0$ and $\theta = \pi/2$ respectively. The family of confocal ellipses

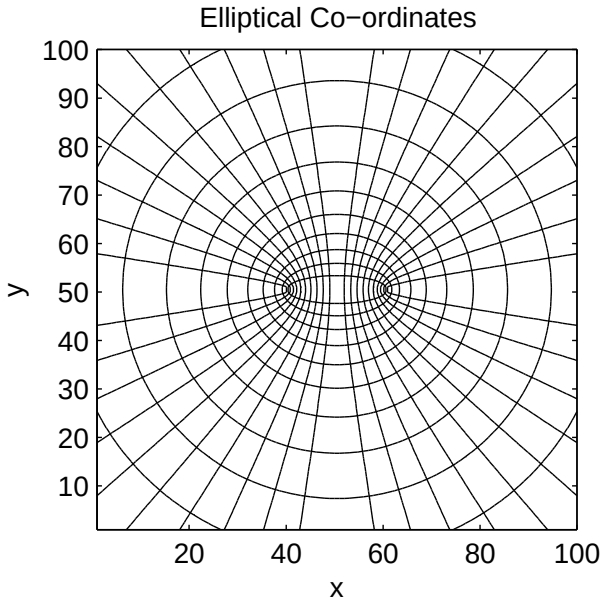

Figure 6.4: Elliptical Co-ordinate system consisting of a system of confocal ellipses and parabolas which represents the electric potential and field respectively.

that describe the contours of the electric potential are given by,

$$\frac{x^2}{\xi^2} + \frac{y^2}{\xi^2 - 1} = 1 \tag{6.17}$$

where $1 < \xi < \infty$, $a = \xi$, $b = \sqrt{\xi^2 - 1}$ and noting that the eccentricity, e, of the ellipse is given by $e = 1/\xi$. The electric field is expressed in the orthogonal co-ordinate system of confocal parabolas, given by

$$\frac{x^2}{\eta^2} - \frac{y^2}{1 - \eta^2} = 1 \tag{6.18}$$

where $-1 < \eta < 1$. In elliptical co-ordinates $\eta = \cos\theta$ where θ is the angle subtended by the asymptote to the parabola generated by the choice of η [81]. The coordinates are shown in figure 6.4.

6.2.1 Anisotropic mass deposition

Consider a uniform circular distribution of ions (and their accompanying electrons) moving into the sheath from the presheath and heading for deposition on the surface of the elliptical grain. The local thickness of the deposited layer depends strongly on the structure of the local electric field. In the case of a circular grain the distribution of ions would be deposited uniformly over the surface of the grain if they were to follow the purely radial electric field lines.

In the case of the elliptical grain, the electric field close to the grain surface is distorted from the purely radial electric field apparent at large distances. This distortion can be quantified by considering the intersection of the parabola that has asymptotes $\theta = \pm\pi/4$ for which $\eta = 1/\sqrt{2}$. This parabola then intersects a quadrant of the ring of ions at the

plasma, and if these ion trajectories were to follow exactly the electric field lines, then this material would be deposited on the section of the elliptic grain perimeter that is intersected by the parabola.

For a specific ellipse and parabola described by ξ and η respectively, equations (6.17) and (6.18) can be solved to obtain the points of intersection of the ellipse and the parabola,

$$x = \pm\eta\xi, \qquad y = \pm\left[\left(\xi^2 - 1\right)\left(1 - \eta^2\right)\right]^{1/2} \tag{6.19}$$

For the case of the parabola $\eta = 1/\sqrt{2}$,

$$x^* = \pm\frac{\xi}{\sqrt{2}}, \qquad y^* = \pm\frac{1}{\sqrt{2}}\left(\xi^2 - 1\right)^{1/2} \tag{6.20}$$

The parabola $\eta = 1/\sqrt{2}$ intersects the circle of matter at the plasma interface at the angles $\pm\pi/4$. If all the charged material were to follow the parabolic electric field lines characterised by $1/\sqrt{2} \leq \eta < 1$ then this quadrant of the circular distribution of material would not intersect one quadrant of the elliptic surface, since the parabola subtends an angle θ^* at the ellipse centre, given by

$$\tan\theta^* = \frac{y^*}{x^*} = \sqrt{\frac{\xi^2 - 1}{\xi^2}} = \sqrt{1 - e^2} \tag{6.21}$$

which is only $\pm\pi/4$ if $\xi = 1/e \gg 1$, that is, if $e \simeq 0$.

The arc length around an ellipse is given by the Incomplete Elliptic Integral of the second kind, denoted $E(\phi, m)$ where ϕ is the angle subtended at the centre of the ellipse by the arc, and $m = e^2$ is the elliptic parameter [81].

Consequently the ratio of the two arc lengths in the first quadrant created by the intersection of the ellipse and the parabola $\eta = 1/\sqrt{2}$ (see Figure 6.5(a)) can be written as

$$R^* = \frac{E(\pi/2, e^2) - E(\theta^*, e^2)}{E(\theta^*, e^2)} \tag{6.22}$$

This function is graphed in figure 6.6, showing R^* as a function of e. As $e \to 1$, the $\pi/4$ segment of the circle at ∞ is mapped to an increasingly smaller fraction of the ellipse surface and $R^* > 1$. As $e \to 0$ material at ∞ is uniformly deposited over the surface since $E(\pi/2, e^2) \to 2E(\theta^*, e^2)$ hence $R^* \to 1$.

Assuming uniform ion flux at the sheath and that charged particle trajectories follow the electric field, the amount of matter deposited on the elliptical surface for $1/\sqrt{2} \leq \eta < 1$ is identical to that deposited for $0 \leq \eta < 1/\sqrt{2}$, since the critical parabola $\eta = 1/\sqrt{2}$ bisects the quadrant at ∞. However, since $E(\pi/2, e^2) > 2E(\theta^*, e^2)$ the mass gain of the polar region of the grain is greater than that of the equatorial regions.

6.3 Numerical simulations

A number of electric potentials were calculated with a range of grain scale size, s, and ratio of semi-major to minor axes, $a : b$. The scale size, s, of an ellipse of semi-major axis, a, is

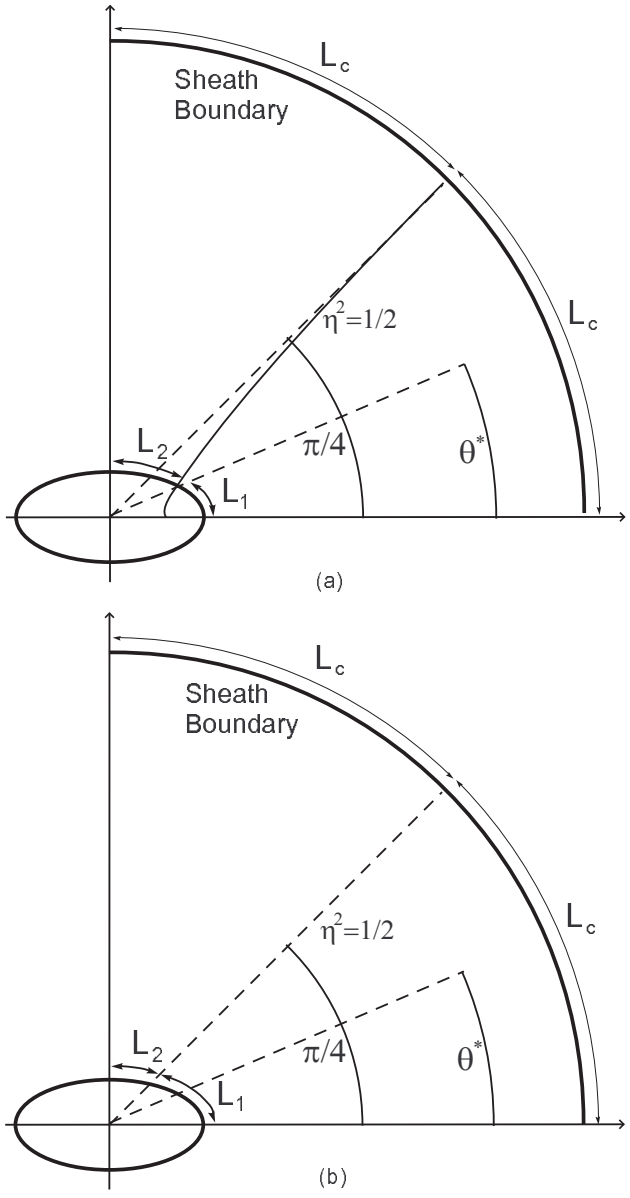

Figure 6.5: Diagram (a) shows the scenario when the ion follows the field lines faithfully giving the results plotted in Fig. 6.6 where $R^* = L_2/L_1$. Diagram (b) shows the scenario when the ion at $\pi/4$ travels undeviated towards the grain surface giving the results plotted in Fig. 6.11 where $R = L_2/L_1$.

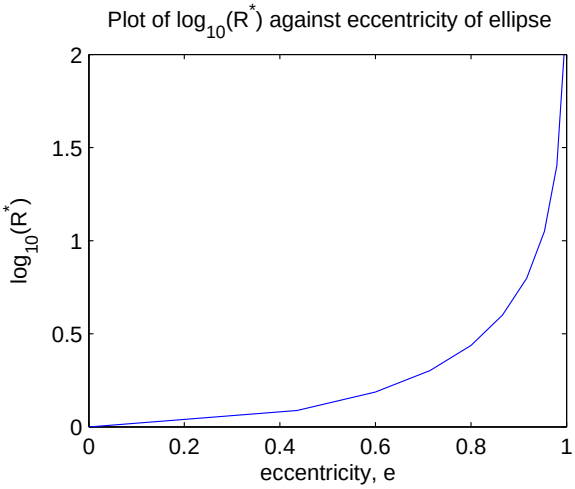

Figure 6.6: Above graph shows that as $e \to 0$, $R^* \to 1$. As $e \to 1$ ellipse becomes more extreme and $R^* \to \infty$.

defined as $s = a/r_s$, where r_s is the sheath length. Using the deposition sites of the ions on the surface of the ellipse, a measure of the grain's elliptical growth was calculated,

$$R = \frac{E(\pi/2, e^2) - E(\theta', e^2)}{E(\theta', e^2)} \tag{6.23}$$

where θ' is the angle subtended at the centre of the ellipse by the deposited ion that initially subtended an angle of $\pi/4$ at the sheath boundary. For anisotropic mass loading leading to elliptical growth $R > 1$. Note that $\theta' \neq \theta^*$ since inertial particles don't follow the field lines.

6.3.1 Electric potential of elliptical grain

In order to obtain the electric potential of an elliptical grain Laplace's equation in two dimensions was solved numerically,

$$\left(\frac{\partial^2}{\partial x^2} + \frac{\partial^2}{\partial y^2}\right)\phi = 0 \tag{6.24}$$

Equivalently an analytical expression for the electrostatic potential can be obtained; however, for ease of implementing boundary conditions and various grain geometries the numerical option was preferred. Grain charging studies (such as Kersten [93]) assume spherical, non-conducting grains preformed from insulating material. In the model presented here we are primarily concerned with grain growth over larger timescales in which inhomogeneous charge deposition is assumed to be averaged out, leaving only the gross geometrical effects controlling the total electrostatic field. Hence we will take the grain boundary to be an equipotential surface (but we note that random perturbations of charge deposition may well be a contributory factor that might merit investigation in a further study). The boundary conditions are therefore,

$$\phi(x, y) = \begin{cases} \phi_s & b^2x^2 + a^2y^2 - (ab)^2 \leqslant 0 \\ 0 & x^2 + y^2 \to \infty \end{cases} \tag{6.25}$$

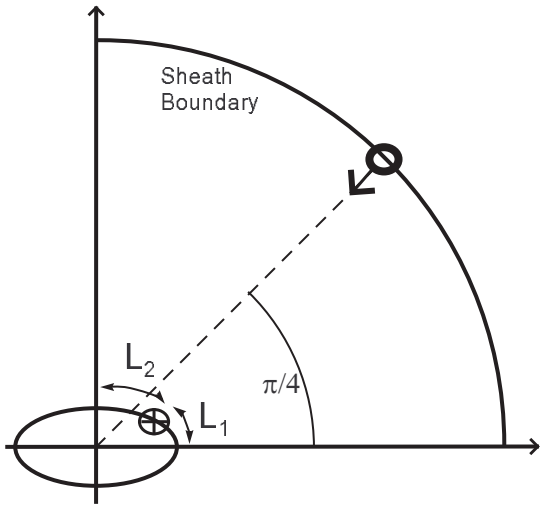

Figure 6.7: For the numerical simulations the ion that initially subtended an angle of $\pi/4$ at the sheath boundary is followed and its position on the elliptical surface calculated. From this a measure of the grains elliptical growth is obtained: $R = L_2/L_1$.

in which a and b are the semi-major and minor axes of the elliptical grain respectively and ϕ_s is the potential on the grain. These conditions state that on the boundary of the ellipse and within the interior the electric potential is ϕ_s, the potential then drops off and tends to zero at the sheath-bulk plasma interface.

The solution of elliptical differential equations using the finite difference method fall into two categories: direct and iterative. Direct methods cast the differential equation into a system of linear algebraic equations of typical form: $A\mathbf{x} = \mathbf{B}$; where A is a coefficient matrix. A solution to which is found in a finite number of prescribed operations. Iterative methods take a guess at the solution and then it is allowed to relax and converge to the exact solution. The number of operations that are carried out to meet this goal is unknown. When the size of the numerical domain is large iterative methods are more favourable. With this in mind instead of solving Eq. (6.24) and the associated boundary conditions directly, one will adopt a relaxation method that allows the numerical solution to converge to that of the exact solution. This can be achieved by solving the Diffusion equation (parabolic equation) with the appropriate boundary conditions and allowing $t \to \infty$,

$$\frac{\partial \phi}{\partial t} - D\left(\frac{\partial^2}{\partial x^2} + \frac{\partial^2}{\partial y^2}\right)\phi = 0 \tag{6.26}$$

where D is the diffusion constant. Casting the problem in non-dimensional form via the relations $\Phi = \phi/\phi_0$, $\tau = t/t_0$, $\hat{\mathbf{r}} = \mathbf{r}/L$ where $\mathbf{r} = (x, y)$ and $\hat{\mathbf{r}} = (\hat{x}, \hat{y})$ yields,

$$\frac{\partial \Phi}{\partial \tau} - \sigma\left(\frac{\partial^2}{\partial \hat{x}^2} + \frac{\partial^2}{\partial \hat{y}^2}\right)\Phi = 0 \tag{6.27}$$

where $\sigma = Dt_0/L$ is a dimensionless parameter; L is the characteristic length scale of the sheath and t_0 is a characteristic time scale of diffusion. D and t_0 have only numerical significance in this context, hence the parameter σ can be set to any desired value.

Numerical technique

To solve Eq. (6.27) an explicit finite difference method for parabolic partial differential equations was used. The continuous domain $(\hat{x}, \hat{y}, \tau)$ was replaced with a discrete cartesian grid with discrete coordinates $\hat{x} = mh$, $\hat{y} = lh$ and $\tau = nk$ such that $m \in [0, m_{max}]$, $l \in [0, l_{max}]$, $n \in [0, n_{max}]$. An arbitrary grid point is given by the coordinate (mh, lh, nk) where m, l, n are integers and h, k are the grid spacings in the $\hat{x}$, $\hat{y}$ and τ coordinates respectively. Writing $\Phi(mh, lh, nk) = \Phi^n_{m,l}$ the finite difference formulae are obtained from the Taylor expansion of u about τ in the neighbourhood of k holding $\hat{x}$ and $\hat{y}$ fixed,

$$\Phi^{n+1}_{m,l} = \exp(k\partial_\tau)\Phi^n_{m,l} \tag{6.28}$$

$$\approx (1 + k\partial_\tau)\Phi^n_{m,l} \tag{6.29}$$

where up to first order terms are retained. Replacing $\partial_\tau \Phi^n_{m,l}$ with $\sigma(\partial^2_{\hat{x}} + \partial^2_{\hat{y}})\Phi^n_{m,l}$ from Eq.(6.27) yields,

$$\Phi^{n+1}_{m,l} = (1 + k\sigma(\partial^2_{\hat{x}} + \partial^2_{\hat{y}}))\Phi^n_{m,l} \tag{6.30}$$

Using second order accuracy finite difference approximations:

$$\partial^2_i \psi_{i,j} = \frac{\psi_{i+1,j} - 2\psi_{i,j} + \psi_{i-1,j}}{h^2} \tag{6.31}$$

where ψ is an arbitrary discrete function. This yields the explicit finite difference algorithm,

$$\Phi^{n+1}_{m,l} = (1 - 4p\sigma)\,\Phi^n_{m,l} + p\sigma\left(\Phi^n_{m+1,l} + \Phi^n_{m-1,l} + \Phi^n_{m,l+1} + \Phi^n_{m,l-1}\right) \tag{6.32}$$

where $p = k/h^2$ is the mesh ratio. This algorithm is stable and convergent if $0 < p\sigma \leqslant 1/4$. The boundary conditions $\forall\ n$ are,

$$\Phi^n_{m,l} = \begin{cases} -1 & b^2(m - m_0)^2 + a^2(l - l_0)^2 - (ab)^2 \leqslant 0 \\ 0 & (m - m_0)^2 + (l - l_0)^2 - r_s^2 \geqslant 0 \end{cases} \tag{6.33}$$

where $m_0 = m_{max}/2$, $l_0 = l_{max}/2$ and r_s is an integer denoting the radius of the plasma sheath and a, b are integers that define the semi-major and minor axes of the ellipse on the discrete cartesian grid (mh, lh).

The parameter n_{max} is chosen to be suitably large to allow the numerical solution to converge to that of the exact solution. The algorithm is executed until

$$\left| \frac{\Phi^{n-1}_{m_1,l_1} - \Phi^n_{m_1,l_1} + \Phi^{n-1}_{m_2,l_2} - \Phi^n_{m_2,l_2}}{\Phi^{n-1}_{m_1,l_1} + \Phi^n_{m_2,l_2}} \right| < 1 \times 10^{-9} \tag{6.34}$$

where $(m_1 h, l_1 h) = ((m_0 + a + 2)h, l_0 h)$ and $(m_2 h, l_2 h) = ((m_0 + r_s - 1)h, l_0 h)$.

Boundary and initial conditions

To ensure that the boundary conditions were applied to the elliptical boundary and not a step-wise approximation to it an accurate field interpolator was used, the explanation of which follows.

The electric potential, Φ, of a source in a vacuum decreases as $\propto 1/d$, where d is the perpendicular distance from the source. Using the perpendicular distance to the immediate

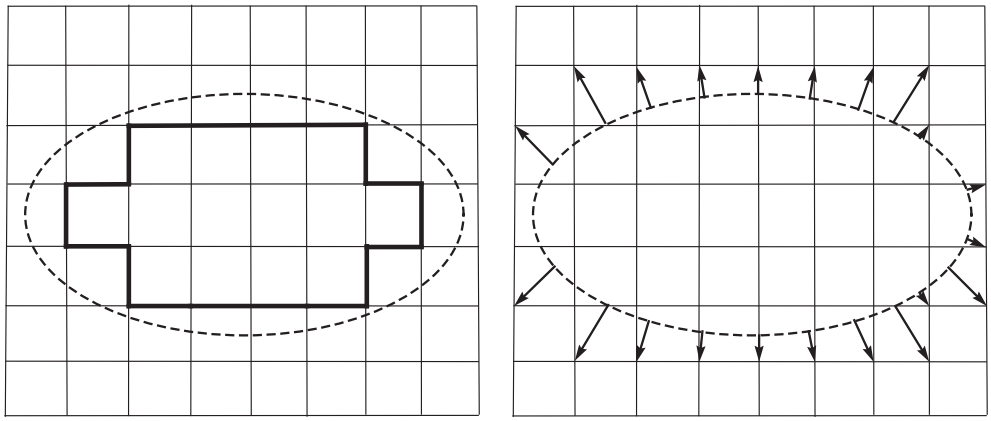

Figure 6.8: Diagram illustrating the implementation of the boundary conditions. The plot on the left-hand side shows the step-wise approximation; the right-hand side plot shows the implementation of the potential interpolator where the electric potential is specified at the immediate mesh points outside of the elliptical boundary. Note that the arrows here do not indicate the geometry of the field solution but indicate the nearest neighbour mesh points where the potential is stipulated by the interpolator method.

mesh points outside the ellipse boundary the corresponding electric potential at these points was calculated using,

$$\Phi\left(\hat{x},\hat{y}\right)=\frac{\gamma\Phi_0}{\gamma+d\left(\hat{x},\hat{y}\right)} \tag{6.35}$$

where $d\left(\hat{x},\hat{y}\right)$ is the perpendicular distance from the ellipse perimeter to the mesh point $(\hat{x},\hat{y})$, and γ is a normalization parameter.

To find the immediate mesh points outside the elliptical boundary the points of intersection between the ellipse and the family of lines $\hat{x}=mh$ for $m\in(m_0-a,m_0+a)$ were found. This would give a family of coordinates on the ellipse perimeter (x_s,y_s). For each of these grid points it was determined for what l satisfied the relation $l<y_s<l-1$ hence giving the nearest grid point $(x_p,y_p)\equiv(mh,lh)$ outside the ellipse in the $\hat{y}$-direction. To make sure all points are accounted for the same was done for the family of lines $\hat{y}=lh$ such that $l\in(l_0-b,l_0+b)$ giving (x_s,y_s). Again, for each of these points it was determined for what m satisfied the relation $m<x_s<m-1$ giving the nearest grid point $(x_p,y_p)\equiv(mh,lh)$ outside the ellipse in the $\hat{y}$-direction.

The perpendicular distance from a point $(\hat{x},\hat{y})$ on the ellipse boundary to an arbitrary mesh point (x_p,y_p) is found by finding the critical points of the Lagrangian function

$$L\left(\hat{x},\hat{y}\right)=f\left(\hat{x},\hat{y}\right)+\lambda g\left(\hat{x},\hat{y}\right) \tag{6.36}$$

where,

$$f\left(\hat{x},\hat{y}\right) = \left[\left(x_p-\hat{x}\right)^2+\left(y_p-\hat{y}\right)^2\right]^{1/2} \tag{6.37}$$

$$g\left(\hat{x},y\right) = \frac{\hat{x}^2}{a^2}+\frac{\hat{y}^2}{b^2}-1 \tag{6.38}$$

where λ is the Lagrangian multiplier. Note that for algebraic convenience an ellipse with its centre located at the origin $(0,0)$ is considered, such that $\hat{x}\mapsto\hat{x}-\hat{x}_0$, $\hat{y}\mapsto\hat{y}-\hat{y}_0$,

$x_p \mapsto x_p - \hat{x}_0$ and $y_p \mapsto y_p - \hat{y}_0$. Any critical point of L must have,

$$\frac{\partial L}{\partial \hat{x}} = -[(x_p-\hat{x})^2+(y_p-\hat{y})^2]^{-1/2}(x_p-\hat{x}) + \frac{2\lambda}{a^2}\hat{x} = 0 \tag{6.39}$$

$$\frac{\partial L}{\partial \hat{y}} = -[(x_p-\hat{x})^2+(y_p-\hat{y})^2]^{-1/2}(y_p-\hat{y}) + \frac{2\lambda}{b^2}\hat{y} = 0 \tag{6.40}$$

$$\frac{\partial L}{\partial \lambda} = \frac{\hat{x}^2}{a^2}+\frac{\hat{y}^2}{b^2}-1 = 0 \tag{6.41}$$

Rearranging Eq. (6.39) for λ and substituting into Eq. (6.40) to eliminate λ yields,

$$a^2\hat{y}(x_p-\hat{x}) = b^2\hat{x}(y_p-\hat{y}) \tag{6.42}$$

Expressing Eq. (6.41) in terms of $\hat{y}$ and substituting into Eq. (6.42) to eliminate $\hat{y}$ yields an 8^{th} order polynomial

$$\sum_{i=0}^{8} A_i \hat{x}^i = 0 \tag{6.43}$$

where

$$A_0 = -2(ab)^4 + b^8 + a^8 \tag{6.44}$$

$$A_1 = 4(ab)^4 x_p - 4a^8 x_p \tag{6.45}$$

$$A_2 = 2(a^3b)^2y_p^2 - 2(ab)^4x_p^2 + 2(ab^3)^2y_p^2 - 2(ab^4)^2 + 4(a^3b^2)^2 + 6a^8x_p^2 - 2a^{10} \tag{6.46}$$

$$A_3 = -4(a^3b)^2x_py_p^2 - 8(a^3b^2)^2x_p + 8a^{10}x_p - 4a^8x_p^3 \tag{6.47}$$

$$A_4 = -2(a^4b)^2y_p^2 + 2(a^3b)^2x_p^2y_p^2 + 4(a^3b^2)^2x_p^2 + (ab^2)^4 - 2(a^2b)^4 - 12a^{10}x_p^2 + a^8x_p^4 + a^{12} - 2(a^2b^3)^2y_p^2 + (ab)^4y_p^4 \tag{6.48}$$

$$A_5 = 4(a^4b)^2x_py_p^2 + 4(a^2b)^4x_p + 8a^{10}x_p^3 - 4a^{12}x_p \tag{6.49}$$

$$A_6 = -2(a^4b)^2x_p^2y_p^2 - 2(a^2b)^4x_p^2 + 6a^{12}x_p^2 - 2a^{10}x_p^4 \tag{6.50}$$

$$A_7 = -4a^{12}x_p^3 \tag{6.51}$$

$$A_8 = a^{12}x_p^4 \tag{6.52}$$

Finding the real roots of this polynomial using a Newton-Raphson method gives the $\hat{x}$ coordinate of the point of the surface of the ellipse that gives the perpendicular distance to the mesh point (x_p, y_p). Newton's method finds a number z such that $f(z) = 0$: it does so by making a series of guesses, based on an initial guess, $x = x_j$ of the root; it then proceeds to construct a tangent line to $y = f(x)$ at $(x_j, f(x_j))$ which has equation

$$f(x_j) = f(x_j) + f'(x_j)(x_{j+1} - x_j) \tag{6.53}$$

Its x-intercept provides a better guess of the root z, this process is repeated until the set of guesses x_j converge to the that of the real root. The point $(x_{j+1}, 0)$ lies on the tangent line, hence

$$x_{j+1} = x_j - \frac{f(x_j)}{f'(x_j)} \tag{6.54}$$

This is Newton's Method formula, given a initial guess at the value of the root it iteratively obtains better approximations of it under certain conditions. For the problem at hand the initial guess for $\hat{x}$ was taken to be x_s. The corresponding $\hat{y}$ coordinate is obtained via

$$\frac{\hat{x}^2}{a^2}+\frac{\hat{y}^2}{b^2}-1 = 0 \tag{6.55}$$

This equation when $\hat{x}$ is known becomes a quadratic for $\hat{y}$ of the form,

$$\sum_{i=0}^{2} B_i \hat{y}_i = 0 \tag{6.56}$$

where

$$B_0 = b^2\hat{x}^2 - (ab)^2 \tag{6.57}$$
$$B_1 = 0 \tag{6.58}$$
$$B_2 = a^2 \tag{6.59}$$

The roots of a general quadratic of the form $p_2x^2 + p_1x + p_0 = 0$ are given by the quadratic formula,

$$x = \frac{-p_1 \pm \sqrt{p_1^2 - 4p_0p_2}}{2p_2} \tag{6.60}$$

One can now calculate the perpendicular distance from the mesh point (x_p, y_p) to the perimeter of the ellipse $(\hat{x}, \hat{y})$, ergo

$$d(x_p, y_p) = \sqrt{(\hat{x} - x_p)^2 + (\hat{y} - y_p)^2} \tag{6.61}$$

Alternatively one can form an 8^{th} order polynomial in $\hat{y}$ instead of $\hat{x}$. Expressing Eq. (6.41) in terms of $\hat{x}$ and substituting into Eq. (6.42) to eliminate $\hat{x}$ yields

$$\sum_{i=0}^{8} C_i \hat{y}^i = 0 \tag{6.62}$$

where

$$C_0 = -2(ab)^4 + b^8 + a^8 \tag{6.63}$$
$$C_1 = 4(ab)^4 y_p - 4b^8 y_p \tag{6.64}$$
$$C_2 = 2(ab^3)^2 x_p^2 - 2(ab)^4 y_p^2 + 2(ab^3)^2 y_p^2 - 2(a^4b)^2 + 4(a^2b^3)^2 + 6b^8 y_p^2 - 2b^{10} \tag{6.65}$$
$$C_3 = -4(ab^3)^2 x_p^2 y_p - 8(a^2b^3)^2 y_p + 8b^{10} y_p - 4b^8 y_p^3 \tag{6.66}$$
$$C_4 = -2(ab^4)^2 x_p^2 + 2(ab^3)^2 x_p^2 y_p^2 + 4(a^2b^3)^2 y_p^2 + (a^2b)^4 - 2(ab^2)^4 - 12b^{10} y_p^2 + b^8 y_p^4 + b^{12} - 2(a^3b^2)^2 x_p^2 + (ab)^4 x_p^4 \tag{6.67}$$
$$C_5 = 4(ab^4)^2 x_p^2 y_p + 4(ab^2)^4 y_p + 8b^{10} y_p^3 - 4b^{12} y_p \tag{6.68}$$
$$C_6 = -2(ab^4)^2 x_p^2 y_p^2 - 2(ab^2)^4 y_p^2 + 6b^{12} y_p^2 - 2b^{10} y_p^4 \tag{6.69}$$
$$C_7 = -4b^{12} y_p^3 \tag{6.70}$$
$$C_8 = b^{12} y_p^4 \tag{6.71}$$

Solving this numerically via a similar Newton-Raphson Method to that described previously gives the $\hat{y}$ coordinate of the point of the surface of the ellipse that gives the perpendicular distance to the point (x_p, y_p). The corresponding $\hat{x}$ coordinate is obtained via Eq. (6.55). This equation when $\hat{y}$ is known becomes a quadratic for $\hat{x}$:

$$\sum_{i=0}^{2} D_i \hat{x}^i = 0 \tag{6.72}$$

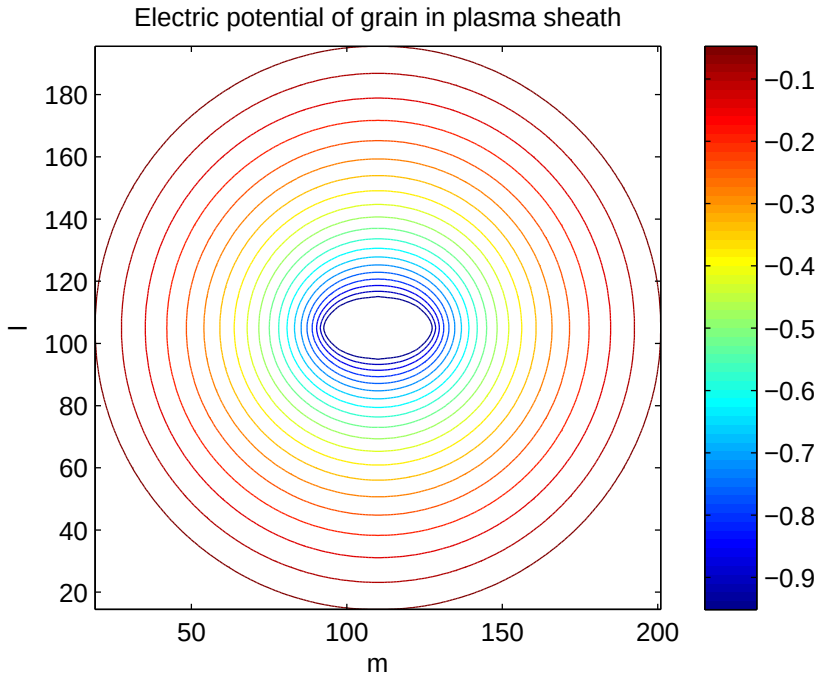

Figure 6.9: Contour plot of an example electric potential, Φ, in the sheath region surrounding the dust grain. Graph illustrates the smooth boundary conditions obtained via the interpolator method explained in the text. The plot is of a dust grain with $a = 16$ and $b = 8$.

where

$$D_0 = a^2\hat{y}^2 - (ab)^2 \tag{6.73}$$
$$D_1 = 0 \tag{6.74}$$
$$D_2 = b^2 \tag{6.75}$$

The roots of which can be obtained via the quadratic formula Eq. (6.60). Fig. 6.9 shows an example of a elliptical grain potential calculated using the bespoke boundary condition interpolator.

Rather than finding the perpendicular distance using the method of Lagrange Multipliers one could have alternatively obtained the same result by finding the minima of d: $\mathrm{d}d/\mathrm{d}\hat{x} = \mathrm{d}d/\mathrm{d}\hat{y} = 0$.

6.3.2 Ion trajectories in sheath region

The model equations governing the dynamics of the ion in the plasma sheath are:

$$\frac{d\mathbf{v}}{dt} = -\frac{q_i}{m_i}\frac{\partial\phi}{\partial\mathbf{r}} \tag{6.76}$$
$$\frac{d\mathbf{r}}{dt} = \mathbf{v} \tag{6.77}$$

Using the predefined non-dimensional quantities, the additional relations $\mathbf{u} = \mathbf{v}/u_0$ and $\hat{t} = t/t_1$, the governing set of non-dimensional equations take the form,

$$\frac{d}{d\hat{t}}\left(u_{\hat{x}}, u_{\hat{y}}\right) = -\alpha\left(\frac{\partial}{\partial\hat{x}}, \frac{\partial}{\partial\hat{y}}\right)\Phi \tag{6.78}$$

$$\frac{d}{d\hat{t}}\left(\hat{x}, \hat{y}\right) = \left(u_{\hat{x}}, u_{\hat{y}}\right) \tag{6.79}$$

where $\alpha = q_i\phi_0/m_i u_0^2$ is a dimensionless parameter in which u_0 is the launch speed of the ion at the sheath-plasma interface and ϕ_0 is the characteristic value of the electric potential. By altering α the ratio of the potential energy to the initial kinetic energy of the incoming ion can be changed. ϕ_0 and u_0 can be taken to be the floating potential, ϕ_f, and the Bohm speed, u_B, respectively. Note that the parameter α will not be constrained by the choice of u_0 or ϕ_0 at this stage.

Numerical technique

The coupled set of equations of motion, Eqs. (6.78) and (6.79), describe the dynamics of the ion in the sheath. This set of ordinary differential equations was solved using a bespoke Runge-Kutta algorithm,

$$\begin{array}{ll}
\mathbf{k}_{\hat{\mathbf{r}}1} = \mathrm{d}\hat{t}\mathbf{u}^n & \mathbf{k}_{\mathbf{u}1} = -\mathrm{d}\hat{t}\alpha\partial_{\hat{\mathbf{r}}}\Phi(\hat{\mathbf{r}}^n) \\
\mathbf{k}_{\hat{\mathbf{r}}2} = \mathrm{d}\hat{t}(\mathbf{u}^n + \mathbf{k}_{\mathbf{u}1}/2) & \mathbf{k}_{\mathbf{u}2} = -\mathrm{d}\hat{t}\alpha\partial_{\hat{\mathbf{r}}}\Phi(\hat{\mathbf{r}}^n + \mathbf{k}_{\hat{\mathbf{r}}1}/2) \\
\mathbf{k}_{\hat{\mathbf{r}}3} = \mathrm{d}\hat{t}(\mathbf{u}^n + \mathbf{k}_{\mathbf{u}2}/2) & \mathbf{k}_{\mathbf{u}3} = -\mathrm{d}\hat{t}\alpha\partial_{\hat{\mathbf{r}}}\Phi(\hat{\mathbf{r}}^n + \mathbf{k}_{\hat{\mathbf{r}}2}/2) \\
\mathbf{k}_{\hat{\mathbf{r}}4} = \mathrm{d}\hat{t}(\mathbf{u}^n + \mathbf{k}_{\mathbf{u}3}) & \mathbf{k}_{\mathbf{u}4} = -\mathrm{d}\hat{t}\alpha\partial_{\hat{\mathbf{r}}}\Phi(\hat{\mathbf{r}}^n + \mathbf{k}_{\hat{\mathbf{r}}3})
\end{array} \tag{6.80}$$

$$\hat{\mathbf{r}}^{n+1} = \hat{\mathbf{r}}^n + \frac{\mathbf{k}_{\hat{\mathbf{r}}1}}{6} + \frac{\mathbf{k}_{\hat{\mathbf{r}}2}}{3} + \frac{\mathbf{k}_{\hat{\mathbf{r}}3}}{3} + \frac{\mathbf{k}_{\hat{\mathbf{r}}4}}{6} \tag{6.81}$$

$$\mathbf{u}^{n+1} = \mathbf{u}^n + \frac{\mathbf{k}_{\mathbf{u}1}}{6} + \frac{\mathbf{k}_{\mathbf{u}2}}{3} + \frac{\mathbf{k}_{\mathbf{u}3}}{3} + \frac{\mathbf{k}_{\mathbf{u}4}}{6} \tag{6.82}$$

where $\mathrm{d}\hat{t} = T/N$ is the temporal step size, T is the integration time and N is the number of time steps.

So that the electric potential in the sheath region would be fully sampled, the time step, $\mathrm{d}\hat{t}$ was chosen such that the final speed of the ion satisfies $u_{\hat{x},\hat{y}}\mathrm{d}\hat{t} \sim h$. The electric potential was only known for each (mh, lh) coordinate, during the numerical iteration of the ion dynamics however the value of the potential at points between these coordinate grid points would have to be known. A bivariate interpolation method was utilized so that the effect of the potential on the ion at any point in the computational region could be evaluated.

Initial conditions

The ion in consideration was initially located at the sheath boundary where it subtends an angle of $\pi/4$ at the centre of the ellipse. At this position the ion was given an initial radial velocity $|\mathbf{u}^0| = 1$. Hence,

$$\mathbf{u}^0 = (u_{\hat{x}}^0, u_{\hat{y}}^0) = (-\cos(\pi/4), -\sin(\pi/4)) \tag{6.83}$$

$$\hat{\mathbf{r}}^0 = (\hat{x}^0, \hat{y}^0) = (\hat{x}_0 + r_s\cos(\pi/4), \hat{y}_0 + r_s\sin(\pi/4)) \tag{6.84}$$

where $(\hat{x}_0, \hat{y}_0)$ is the centre of the ellipse; the superscript 0 denotes initial value.

Ion surface deposition

The Runge-Kutta method gives the position and velocity of the ions in the $\hat{x}$ and $\hat{y}$ directions after each time step. The ion points of deposition $(\hat{x}_d, \hat{y}_d)$ on the ellipse surface can be calculated by calculating the point of intersection between the equation of the ellipse,

$$\frac{(\hat{x} - \hat{x}_0)^2}{a^2} - \frac{(\hat{y} - \hat{y}_0)}{b^2} = 1 \tag{6.85}$$

and the equation of the line joining the points $(\hat{x}_1, \hat{y}_1)$ and $(\hat{x}_2, \hat{y}_2)$,

$$\begin{aligned} \hat{y} &= \mathcal{M}(\hat{x} - \hat{x}_1) + \hat{y}_1 && (6.86)\\ &= \mathcal{M}\hat{x} + c && (6.87) \end{aligned}$$

where $(\hat{x}_0, \hat{y}_0)$ is the centre of the ellipse; $c = \hat{y}_1 - \mathcal{M}\hat{x}_1$; $(\hat{x}_1, \hat{y}_1)$ and $(\hat{x}_2, \hat{y}_2)$ is the last ion position outside of the ellipse and the first ion position inside the ellipse respectively and $\mathcal{M}$ is the gradient of the line:

$$\mathcal{M} = \frac{\hat{y}_2 - \hat{y}_1}{\hat{x}_2 - \hat{x}_1} \tag{6.88}$$

Expanding Eq. (6.85) yields

$$b^2(\hat{x}^2 - 2\hat{x}\hat{x}_0 + \hat{x}_0^2) + a^2(\hat{y}^2 - 2\hat{y}\hat{y}_0 + \hat{y}_0^2) = a^2b^2 \tag{6.89}$$

and substituting Eq. (6.87) to eliminate $\hat{y}$ produces a quadratic equation in $\hat{x}$,

$$\sum_{i=0}^{2} E_i \hat{x}^i = 0 \tag{6.90}$$

where

$$\begin{aligned} E_0 &= b^2 + (a\mathcal{M})^2 && (6.91)\\ E_1 &= 2a^2\mathcal{M}c - 2\hat{x}_0 b^2 - 2\hat{y}_0 \mathcal{M} a^2 && (6.92)\\ E_2 &= (b\hat{x}_0)^2 + (ac)^2 - 2\hat{y}_0 a^2 c + (a\hat{y}_0)^2 - (ab)^2 && (6.93) \end{aligned}$$

The roots of Eq. (6.90) are given by the quadratic formula Eq. (6.60). Once the $\hat{x}$ coordinate of the deposition site has been obtained the corresponding $\hat{y}$ coordinate is obtained from Eq. (6.89) which can be expressed a quadratic in terms of $\hat{y}$:

$$\sum_{i=0}^{2} F_i \hat{y}^i = 0 \tag{6.94}$$

where the coefficients are

$$\begin{aligned} F_0 &= a^2 && (6.95)\\ F_1 &= -2a^2\hat{y}_0 && (6.96)\\ F_2 &= (a\hat{y}_0)^2 - (ab)^2 + b^2(\hat{x} - \hat{x}_0)^2 && (6.97) \end{aligned}$$

The polynomial is solved for $\hat{y}$ given $\hat{x}$ using the quadratic formula, Eq. (6.60). This yields the point of deposition on the elliptical surface $(\hat{x}_d, \hat{y}_d)$.

Parameter	Value	
n_{max}	1×10^6	number of time steps
m_{max}	220	number of spatial points in the $\hat{x}$ direction.
l_{max}	210	number of spatial points in the $\hat{y}$ direction.
σ	1000	dimensionless parameter ($= Dt_0/L$)
p	0.2	mesh ratio
h	1.0	spatial mesh increment
r_s	100	radius of plasma sheath
$\mathrm{d}\hat{t}$	0.5	temporal mesh increment for Runge-Kutta algorithm

Table 6.1: Parameters for numerical simulations involving calculation of grain potentials and the ion dynamics.

The measure of the grains elliptical growth becomes,

$$R = \frac{E(\pi/2, e^2) - E(\theta', e^2)}{E(\theta', e^2)} \tag{6.98}$$

where the Incomplete Elliptic Integral of the second kind is given by

$$E(\theta', e^2) = a \int_0^{\theta'} \sqrt{1 - e^2 \sin^2 \Theta}\, \mathrm{d}\Theta \tag{6.99}$$

and the angle subtended at the centre of the ellipse by the deposited ion is

$$\tan \theta' = \frac{\hat{y}_d}{\hat{x}_d} \tag{6.100}$$

The eccentricity of the ellipse is $e^2 = 1 - b^2/a^2$.

6.4 Results and discussion

The variation of R with α for elliptical grains of varying $a : b$ and differing scale sizes, s, are shown in Fig. 6.10.

When $\alpha \ll 1$ the electric potential energy of the ion is very small in comparison to its initial kinetic energy. In this case the influence of the potential on the ion is minimal and the ion's velocity will not be altered significantly, therefore $\theta' \to \pi/4$, see Fig. 6.5(b). Due to the geometry of the ellipse it follows that $E(\pi/2, e^2) - E(\pi/4, e^2) < E(\pi/4, e^2)$ hence,

$$R \to \frac{E(\pi/2, e^2) - E(\pi/4, e^2)}{E(\pi/4, e^2)} < 1 \tag{6.101}$$

implying that the mass gain of the equatorial region is greater than that of the polar region and elliptical growth doesn't occur. This is evident in Fig. 6.10. The value of R in this situation depends on the eccentricity, e, and decreases in value with increasing e, this is graphed in Fig. 6.11.

When $\alpha \gg 1$ the electric potential energy of the ion is now very large compared to its initial kinetic energy. The influence of the potential is greatly increased and will have a

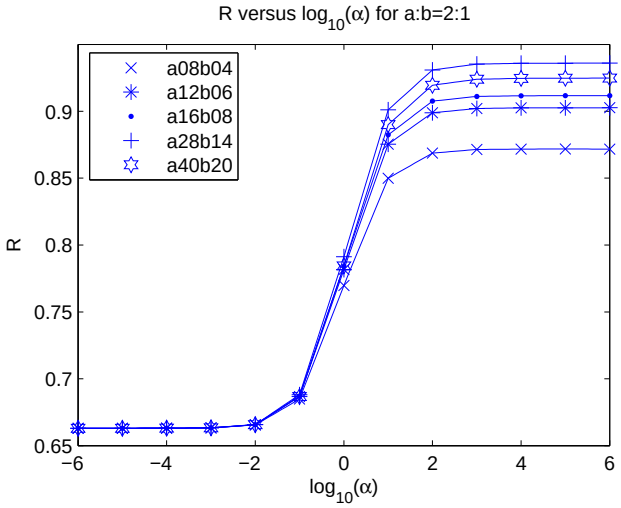

(a) a:b=2:1

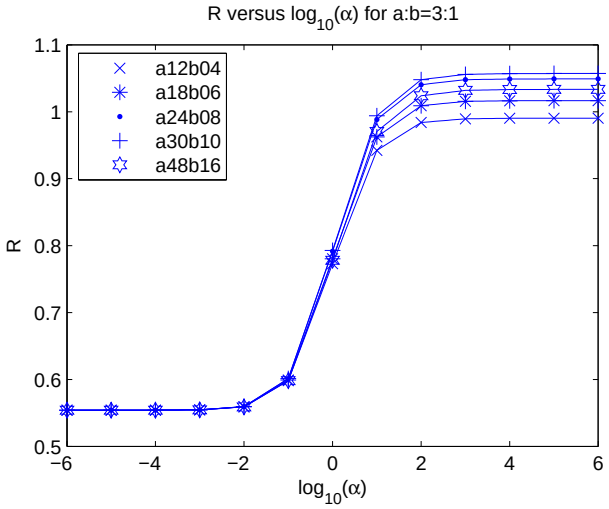

(b) a:b=3:1

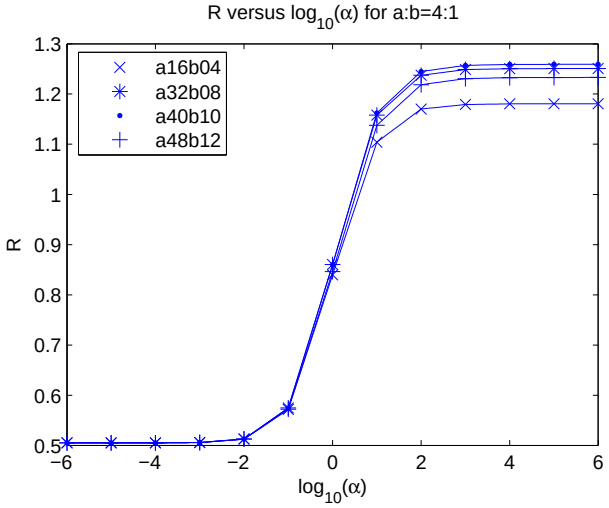

(c) a:b=4:1

Figure 6.10: R against α for varying eccentricities, e, and for several scale sizes, s, where for example the notation $a08b04$ represents an ellipse with a semi-major axis, a, of 8 units and semi-minor axis, b, of 4 units.

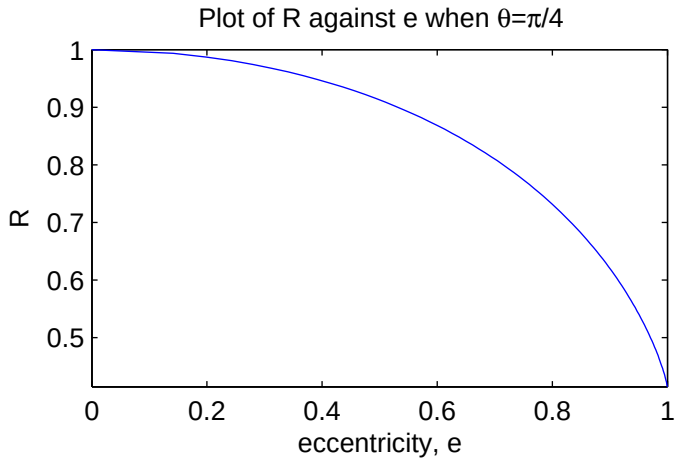

Figure 6.11: As $e \to 1$ the ellipse becomes increasingly elongated and R tends to a minimum.

greater effect on the ions velocity, hence $\theta' \to \theta^*$. Again due to the geometry $E(\pi/2, e^2) - E(\theta^*, e^2) > E(\theta^*, e^2)$ therefore,

$$R \to \frac{E(\pi/2, e^2) - E(\theta^*, e^2)}{E(\theta^*, e^2)} > 1 \tag{6.102}$$

Now the mass gain of the polar region is greater than that of the equatorial and elliptical growth occurs. Assuming the ions follow the field lines exactly, it is expected in this case that since $\alpha \gg 1$ and $\theta' \to \theta^*$ that $R \to R^*$, as graphed in figure 6.6, however as Figs. 6.10(a), 6.10(b) and 6.10(c) show this is not the case. Instead R tends to some value, which is dependent on the eccentricity of the ellipse, that is much smaller than if the ions had followed the electric field lines faithfully. As α is increased and the ions respond to the potential more, there comes a point where the increase in the magnitude of the potential accelerates the ions to such high speeds that the potential close to the grain is not strong enough to alter their trajectories further. Therefore the value of R saturates at some value.

Fig. 6.10(a), shows that elliptical grains of ratio $a : b = 2 : 1$ do not grow elliptically, implying that there is some value of eccentricity below which elongated growth doesn't occur. As $e \to 0$ the field close to the elliptical boundary becomes more radial and tends to that of a field for a circular grain. The field near the grain is therefore not strong enough, nor does it deviate from a radial field significantly to alter notably the trajectories of the ions close to the grain surface.

When $\alpha = 1$ the electrostatic potential energy and the initial kinetic energy of the ions are equal. This signifies a point where the dynamics of the ions in the sheath change from being dictated by the electric potential of the grain to the initial kinetic energy of the ions.

Fig. 6.12 shows R against the scale size, s, when $\alpha = 10^6$ for a number of eccentricities. The graphs show that for each eccentricity there exists a value of s where R is a maximum implying that there exists a size of grain that has optimum elliptical growth. If the scale size of the dust grain is very small compared to the sheath scale length, the ions will be

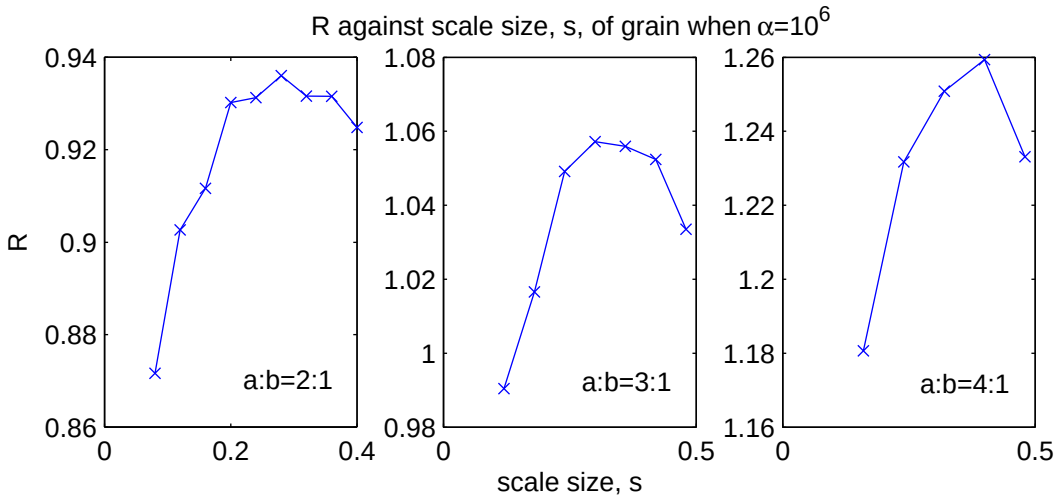

Figure 6.12: The graphs show that for each eccentricity there exists a value of s where R is a maximum implying that there exists a size of grain that has optimum elliptical growth.

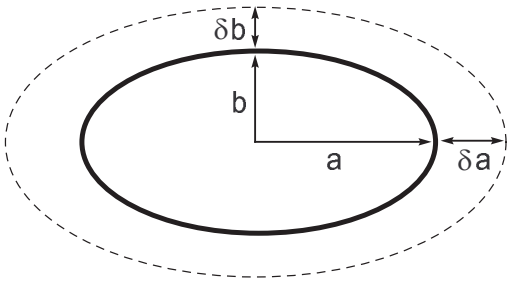

Figure 6.13: As material is deposited on the grain surface $a \to a + \delta a$ and $b \to b + \delta b$ altering the grains scale size and eccentricity.

accelerated by a nearly radial electric field for a large time and will tend to resist the influence of the non-radial field close to the surface of the grain due to its inertia. If the scale size of the dust grain is large compared to the sheath length, then the grain will appear planar at all points. Therefore the growth rate will be similar at all points on the surface.

Fig. 6.12 and 6.10 also imply dust grains, in principle, will grow and pass through a series of evolutionary stages dependent on the eccentricity and scale size of the grain. Consider a dust grain of particular eccentricity, e, and scale size, s. For a certain value of α the grain will have a corresponding value of R and a thin layer of material will be deposited on the grain surface such that $a \to a + \delta a$ and $b \to b + \delta b$. The value of $\delta a/\delta b$ depends on R such that as $R \to 1$, $\delta a/\delta b \to 1$ and as $R \to \infty$, $\delta a/\delta b \to \infty$. The grains eccentricity, scale size and value of R will change accordingly, which will in turn alter the ratio of $\delta a/\delta b$ and hence the way in which material is deposited on the grain surface further changing the eccentricity and scale size of the grain. This process continues until ultimately circular grain growth occurs where $R \to 1$ and $\delta a/\delta b \to 1$, as successive deposited layers wash out the anisotropy in time.

The value of α in the simulations together with the choice of q_i, m_i, ϕ_0 and u_0 define the

physical system to which the results apply. Setting $\phi_0 = \phi_f$ and $u_0 = u_B$ the parameter α becomes

$$\alpha = \frac{Z_i}{2} \ln\left(\frac{m_i}{2\pi m_e}\right) \tag{6.103}$$

where Z_i is the net number of positive charges on an ion. For $a : b = 3 : 1$ elliptical growth occurs for values of α corresponding to plasmas composed of elements no lighter than Lithium, for $a : b = 4 : 1$ there is no such constraint on the elemental composition of the bulk plasma to give elliptical growth. This is providing the elements composing the plasma are fully ionised, however as heavier elements are considered elliptical growth of the grains is less constrained by the degree of ionisation of the plasma. Supernova remnants have very high abundances of heavy elements such as O, Si and Mg suggesting the described growth mechanism may be a process present in remnants.

Given the potential on the grain surface, $\phi_0 = \phi_f$, if one assumes that the capacitance of the dust is that of a conductor of the same size then the net number of negative charges on the grain is given by

$$N = \left(\frac{4\pi\epsilon_0 k_B}{e^2}\right) T_e \sqrt{a^2 - b^2} \ln\left(\frac{m_i}{2\pi m_e}\right) \Big/ \ln\left(\frac{a + \sqrt{a^2 - b^2}}{a - \sqrt{a^2 - b^2}}\right) \tag{6.104}$$

where use has been made of the electrostatic potential ϕ for a charged ellipsoidal conductor,

$$\phi = \frac{Ne}{8\pi\epsilon_0 \sqrt{a^2 - b^2}} \ln\left(\frac{a + \sqrt{a^2 - b^2}}{a - \sqrt{a^2 - b^2}}\right) \tag{6.105}$$

For dust in laboratory and natural plasmas there typically exists a distribution of grain sizes $\sim 10^{-10} - 10^{-6}$ metres and these can carry charges of up to $\sim 10^6 e$. Calculated values of N yield $N \sim 10^{-1} T_e$ for plasmas composed of elements lighter than Iron with grain sizes $\sim 10^{-6}$ where $a = 3b$ (Note smaller grain sizes give $N < 10^{-1} T_e$). Supernova remnants can have an initial temperature of $\sim 10^{10} K$ which falls to lower temperatures as the remnant expands and cools. Elliptical growth as described here should occur in a supernova remnant given T_e is not too large that N becomes inconsistently large, exceeding the maximum number of charges that can be sustained.

6.5 Discussion and further developments

The numerical simulations have shown that within the model presented elliptical growth of dust grains occurs and that there exists an optimum scale size, s, that maximizes this elliptical growth. It was found however that only grains above a certain eccentricity displayed elongated growth when the potential energy of the ions in the sheath was much greater than their initial kinetic energy, $\alpha \gg 1$. This suggests that if collisions between the ions and neutrals in the sheath are incorporated in the model elliptical growth may occur for lower values of α. Collisions between ions and neutrals in a weakly ionised plasma would reduce the velocity of the ions and hence increasing α making them more susceptible to the field close to the grain.

The results here imply that the proposed growth mechanism produces a hierarchy of dust sizes and eccentricities. As they grow, the dust will evolve through this hierarchy depending on the parameters e, s and R until spherical growth is reached. Dust characterised by the

ratio $a : b$ greater than $3 : 1$ will in principle grow in plasmas composed of any element. Since supernova remnants have high abundances of heavy elements it seems feasible that the growth process suggested here is an active one providing the electron temperature in the remnant is not too large.

The numerical simulations here assumed that the sheath region was a vacuum. However in reality, there exists a distribution of electrons and ions whose collective contribution to the field in the sheath may alter the nature of the grain's growth. The electron density in the sheath region would be described by the Boltzmann relation, assuming isothermal electrons, and would be $\propto \exp(e\Phi_0/k_B T_e)$. The ions, assuming that $T_i = 0$ and that they enter the sheath at the Bohm speed, u_B, have a density $\propto (1 - e\Phi_0/2m_i u_B^2)^{-1/2}$ [90]. Due to the greater mobility of the electrons there will be a greater number of ions at all points in the sheath resulting in a positive contribution to the existing negative electric potential of the grain. This would alter the structure of the electric field in the sheath possibly encouraging elliptical growth. In principle the vacuum case reported here encapsulates the relevant physics already, since non-radial field lines yield anisotropic growth depending on the value of α. The extension to the non-vacuum case would be for the benefit of studying further related processes where having a self-consistently calculated sheath would be required.

Incorporating the distribution of ions into the sheath adds a layer of complexity to the system. If the ions, due to thermal fluctuations in the plasma, enter the sheath with a non-zero non-radial component of velocity they will momentarily participate in orbits around the dust grain. The collective effect results in the local field strength being reduced due to partial shielding of the grain field by the orbiting ions. This will affect the field experienced by subsequent ions entering the sheath. A full, self-consistent solution for the plasma sheath would uncover this process.

Chapter 7

Conclusions and further developments

The aim of this thesis was to explore coherent plasma effects and collective plasma processes in pulsar environments. The primary goal was to study a possible emission mechanism in the magnetospheric pair plasma, producing a source of electromagnetic radiation in the pulsar. The observed electromagnetic signature is characterised by the nature of the emission process and by the effects of propagation through the surrounding dust laden supernova remnant. The true, unambiguous interpretation of the electromagnetic signal can only be made with explicit knowledge of the processes involved. Key to this is an understanding of how dust is grown in the supernova remnant. The secondary goal was to study a possible spheroidal growth mechanism via plasma deposition in an electron-ion plasma.

Nonlinear mode coupling in pair plasmas

In a cold pair plasma electrostatic oscillations couple to propagating electromagnetic modes when the ambient background magnetic field is inhomogeneous. Self-consistency demands that in the presence of an inhomogeneous magnetic field, the plasma equilibrium must be non-uniform and dynamic. In Chapter 3, the system of governing equations, in cylindrical geometry, was solved for the equilibrium situation revealing that the magnetic inhomogeneity is related to the equilibrium plasma dynamics. The magnetic field gradient is sustained by a spatially dependent azimuthal current density, which itself is coupled to the equilibrium radial flow to conserve kinetic energy.

The linear analysis in Chapter 3 successfully explored the dynamical responses of the pair magnetoplasma, revealing that the appropriate modes for the coupling were present. The analysis was carried out in an approximate regime where the plasma was perturbed from a uniform, radially streaming plasma, permeated by a constant magnetic field. The electrostatic mode in this regime consisted of a pair plasma oscillation convected downstream with the radially streaming plasma. In the context of the mode coupling this produces a

moving source of radiation in the pulsar magnetosphere. The electromagnetic mode was found to be unaffected by the radial flow of the equilibrium plasma which is a consequence of on the non-relativistic plasma model chosen here. The convective solution presents an additional mode unique to the streaming regime, where certain plasma variables are convected downstream at the flow speed.

The nonlinear system of differential equations describing the cold pair plasma and the mode coupling doesn't have a closed form analytical solution and must be ultimately solved numerically. Chapter 4 assessed the efficacy of the numerical techniques available for the task, namely the LW method and the FDTD method. In comparison to the LW method, FDTD is very easy to implement, particularly when a system of coupled differential equations is considered. For a system of equations the LW algorithm can become hard to obtain as the Jacobian of the system becomes more involved. Although in the empirical stability assessment the LW method exhibits greater stability, it is marginal and cannot solely justify the choice of LW over FDTD. With this in mind it seemed reasonable to opt for FDTD for the solution of the nonlinear set of equations governing the evolution of the inhomogeneous cold pair plasma.

The numerical simulations presented in Chapter 5, solve the set of governing equations describing the equilibrium and the perturbed plasma variables using the Runge-Kutta and a bespoke FDTD algorithm respectively. The results successfully exhibit the nonlinear mode coupling and the nonlinear interaction between electromagnetic waves and independent electrostatic oscillations. The latter illustrating the enhanced coupling due to the magnetic gradient of a passing electromagnetic wave-train and its dependence on the wave amplitude and wavelength. The dimensional analysis carried out affirms the feasibility of such a process occurring in a pulsar magnetosphere where assuming $n_- \approx 10^{21}$ m^{-3} yields $E_r \sim 10^9$ Vm^{-1} and $B_z \sim 10^{-3}$ T, which is entirely consistent with the expected values when translated into the rotating pulsar laboratory frame.

The multiple generation and absorption of electromagnetic radiation by a cascade of electrostatic oscillation sites offers a new and exciting way of diagnosing the magnetospheric environment. Consider the situation in which an oscillation generates a propagating electromagnetic wave with a frequency ω_0 at twice the local hybrid frequency $\omega_H(\xi_0)$: $\omega_0 = 2\omega_H(\xi_0)$. The radiation will propagate away from the source region in radially opposite directions. The inwardly propagating component (ξ decreasing) will encounter regions of increasing plasma density attenuating the wave until the background plasma frequency is comparable to that of the wave, $\omega_H(\xi_1) = \omega_0$. This results in the wave being partially absorbed and also stimulating a new electrostatic oscillation that generates its own electromagnetic signature with a characteristic frequency dependent upon the local plasma conditions $\omega_1 = 2\omega_H(\xi_1) = 2\omega_0$. A component of this new wave will propagate inward and stimulate another electrostatic oscillation and so on. Therefore, the distant observer will see a superposition of waves of frequency ω_0, $2\omega_0$, $4\omega_0$, etc. Such a signature can be described by a Weierstrass function, which has a characteristic power spectrum in frequency space. If this type of structure can be identified in the small scale sub-pulse structure of pulse observations, it offers the opportunity of diagnosing the plasma density.

Extending the cold plasma to a relativistic kinetic one will reveal even richer physics. Electrostatic oscillations in a kinetic magnetoplasma are not stationary but propagate. These propagating oscillations constitute a series of modes called Bernstein modes that propagate perpendicular to the background magnetic field. These modes could act as sources of electromagnetic radiation via the coupling mechanism, providing a rich spec-

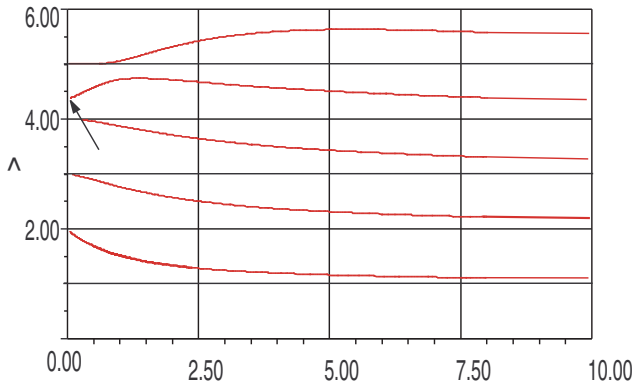

Figure 7.1: Dispersion curves for Bernstein modes in a classical, non-relativistic pair plasma. Plot shows $\hat{\omega}$ versus Λ, where $\hat{\omega} = \omega/\Omega$, Ω is the cyclotron frequency and Λ is the ratio of thermal energy to wave energy. The non-dimensional hybrid frequency is $\sqrt{19}$, for $\hat{\omega}_p = \omega_p/\Omega$, and is shown arrowed in the figure. Bernstein modes are a family of electrostatic waves which occur at frequencies close to the cyclotron harmonics, that propagate perpendicular to the direction of the equilibrium magnetic field.[94]

trum of electromagnetic waves propagating in the magnetosphere. The pair plasma would be governed by the Vlasov-Maxwell system of differential equations, describing the temporal evolution of the plasma distribution function in phase space under the influence of electromagnetic fields governed by Maxwell's equations. Including collisions into the model gives the opportunity of incorporating the annihilation of electrons and positrons in the pair plasma. As the electrostatic oscillations evolve the reaction rate for this process will alter as a function of position and time, affecting the propagating modes resulting in wave damping.

Elliptical dust growth in astrophysical plasmas

A dust grain immersed in a plasma acquires a net negative charge leading to the formation of a plasma sheath surrounding it. Ions are subsequently accelerated from the bulk plasma, through the plasma sheath and are ultimately deposited on the surface of the grain altering its shape and size. For spherical dust grains the electric field geometry is purely radial around the grain and deposits the ions uniformly on the grain surface. However ellipsoidal dust grains have a non-radial electric field close to the grain and ions could be deposited on the surface in a non-uniform fashion depending on their momentum, leading to anisotropic growth.

The degree of anisotropic growth depends strongly on the ratio of the potential energy to the initial kinetic energy of the incoming ion. The numerical simulations reported in Chapter 6 successfully exhibited the growth of elliptical dust grains via plasma deposition. It was found however that only grains above a certain eccentricity displayed elongated growth when the potential energy of the ions in the sheath was much greater than their initial kinetic energy, $\alpha \gg 1$. The results imply that the proposed growth mechanism

produces a hierarchy of dust sizes and eccentricities. As they grow, the dust will evolve through this hierarchy depending on the parameters e, s and R until spherical growth is reached. Dust characterised by the ratio $a : b$ greater than $3 : 1$ will in principle grow in plasmas composed of any element. Since supernova remnants have high abundances of heavy elements it seems feasible that the growth process suggested here is an active one providing the electron temperature in the remnant is not too large.

The model adopted excluded the presence of a background magnetic field, which can be instrumental in aligning the dust grains in the remnant. Since elliptical dust grains grow in an environment where a field is present a more realistic model should incorporate a background magnetic field requiring the problem to be extended to 3 dimensions. In this context the formation of sheaths in the vicinity of a magnetic field would have to be considered; however the following simple argument shows how elongated grain growth may be encouraged when a magnetic field is included. In cylindrical polar coordinates consider a uniform magnetic field directed in the direction of the semi-major axis, $\mathbf{B} = B_0\hat{\mathbf{z}}$, Fig. 7.2. The combination of the electric and magnetic field will produce an $\mathbf{E} \times \mathbf{B}$ drift in the $\hat{\boldsymbol{\theta}}$ direction, as well as particle gyrations around the magnetic field lines. Ions traveling parallel to the magnetic field will move unimpeded towards the grain while ions traveling perpendicular will now participate in orbits around the grain. Providing $|\mathbf{B}| \gg |\mathbf{E}|$ ions will become trapped in these orbits stopping them from reaching the grain surface and thus encouraging growth at the poles.

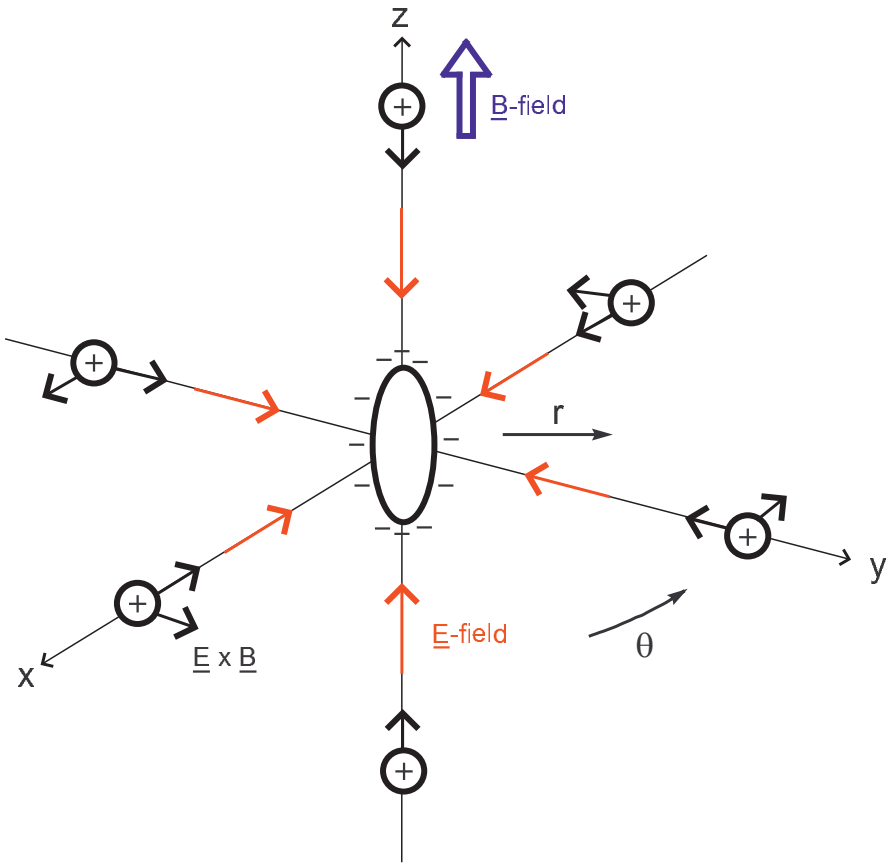

Figure 7.2: Dust growth in presence of background magnetic field. The combination of the electric and magnetic field will produce an $\mathbf{E} \times \mathbf{B}$ drift in the $\hat{\boldsymbol{\theta}}$ direction, as well as particle gyrations around the magnetic field lines. Ions traveling parallel to the magnetic field will move unimpeded towards the grain while ions traveling perpendicular will now participate in orbits around the grain.

Appendix A

Derivation of model equations

A.1 Introduction

The work in this appendix details the construction of the governing set of equations that describe the mode coupling in a pair magnetoplasma. Section A.2 begins by outlining the derivation of the model equations in cylindrical polar coordinates; section A.3 proceeds by casting this set of equations in non-dimensional form; and then concludes in section A.4 with the linearisation of the non-dimensional equations to form the linearised model set of equations. Sections A.2 and A.3 contain work not originally done by the author and were inherited from D. A. Diver and A. A. da Costa.

A.2 Model equations in cylindrical coordinates

The governing equations for a two fluid cold pair magnetoplasma are:

$$\frac{\partial n_s}{\partial t} + \nabla \cdot (n_s \mathbf{u}_s) = 0 \tag{A.1}$$

$$m_s n_s \left[\frac{\partial \mathbf{u}_s}{\partial t} + (\mathbf{u}_s \cdot \nabla)\mathbf{u}_s \right] = n_s q_s (\mathbf{E} + \mathbf{u}_s \times \mathbf{B}) \tag{A.2}$$

$$\mathbf{J} = \sum_s n_s q_s \mathbf{u}_s \tag{A.3}$$

$$\nabla \times \mathbf{B} = \mu_0 \mathbf{J} + \epsilon_0 \mu_0 \frac{\partial \mathbf{E}}{\partial t} \tag{A.4}$$

$$\nabla \times \mathbf{E} = -\frac{\partial \mathbf{B}}{\partial t} \tag{A.5}$$

$$\nabla \cdot \mathbf{E} = \frac{1}{\epsilon_0} \sum_s n_s q_s \tag{A.6}$$

$$\nabla \cdot \mathbf{B} = 0 \tag{A.7}$$

where s denotes the species constituting the plasma; n_s is the species number density; u_s is the species velocity; m_s is the particle mass of the species and q_s is the particle charge of the species. Eqs. (A.1) and (A.2) are the continuity and momentum equations of the plasma fluids describing the conservation of particle number and the dynamics of the fluid under the influence of electromagnetic fields respectively; Eq. (A.3) quantifies the current generated by the motion of the plasma dictated by the electromagnetic fields; Eqs. (A.4) to (A.7) are Maxwell's Equations expressing the temporal and spatial evolution of electromagnetic fields in the plasma. Maxwell's Equations along with Eq. (A.3) couple the two, otherwise non-interacting, fluids together. To cast the equations in cylindrical polar coordinates (r, θ, z) the vector operators appearing in the above equations must be replaced with their cylindrical counterparts given by the following relations:

$$\nabla \cdot \mathbf{F} = \frac{1}{r}\frac{\partial}{\partial r}(rF_r) + \frac{1}{r}\frac{\partial}{\partial \theta}(F_\theta) + \frac{\partial}{\partial z}(F_z) \tag{A.8}$$

$$\begin{aligned} \nabla \times \mathbf{F} &= \frac{1}{r}\begin{vmatrix} \hat{\mathbf{r}} & r\hat{\boldsymbol{\theta}} & \hat{\mathbf{z}} \\ \partial/\partial r & \partial/\partial\theta & \partial/\partial z \\ F_r & rF_\theta & F_z \end{vmatrix} \\ &= \left(\frac{1}{r}\frac{\partial F_z}{\partial \theta} - \frac{\partial F_\theta}{\partial z}\right)\hat{\mathbf{r}} + \left(\frac{\partial F_r}{\partial z} - \frac{\partial F_z}{\partial r}\right)\hat{\theta} \\ &+ \left(\frac{1}{r}\frac{\partial}{\partial r}(rF_\theta) - \frac{1}{r}\frac{\partial F_r}{\partial \theta}\right)\hat{\mathbf{z}} \end{aligned} \tag{A.9}$$

$$\begin{aligned} (\mathbf{G}\cdot\nabla)\mathbf{F} &= \hat{\mathbf{r}}\left(G_r\frac{\partial F_r}{\partial r} + G_\theta\frac{1}{r}\frac{\partial F_r}{\partial \theta} + G_z\frac{\partial F_r}{\partial z} - \frac{1}{r}G_\theta F_\theta\right) \\ &+ \hat{\theta}\left(G_r\frac{\partial F_\theta}{\partial r} + G_\theta\frac{1}{r}\frac{\partial F_\theta}{\partial \theta} + G_z\frac{\partial F_\theta}{\partial z} + \frac{1}{r}G_\theta F_r\right) \\ &+ \hat{\mathbf{z}}\left(G_r\frac{\partial F_z}{\partial r} + G_\theta\frac{1}{r}\frac{\partial F_z}{\partial \theta} + G_z\frac{\partial F_z}{\partial z}\right) \end{aligned} \tag{A.10}$$

Note that the conventional notation for cylindrical coordinates is (ρ, ϕ, z), but here the use of ρ will be reserved to denote the radial electric field so r shall be used instead.

It is assumed that $\mathbf{E} = (E_r(r,t), E_\theta(r,t), 0)$, $\mathbf{B} = (0, 0, B_z(r,t))$, $n_s = n_s(r,t)$, and $\mathbf{u}_s = (u_{s,r}(r,t), u_{s,\theta}(r,t), 0)$. Using the divergence equation (A.8) the continuity equation reduces to:

$$\frac{\partial n_s}{\partial t} + \frac{1}{r}\frac{\partial}{\partial r}(rn_s u_{s,r}) = 0 \tag{A.11}$$

The momentum equation becomes:

$$m_s n_s\left[\frac{\partial \mathbf{u}_s}{\partial t} + (\mathbf{u}_s\cdot\nabla)\mathbf{u}_s\right] = n_s q_s(\mathbf{E} + \mathbf{u}_s\times\mathbf{B}) \tag{A.12}$$

$$= n_s q_s\mathbf{E} + n_s q_s\begin{vmatrix} \hat{\mathbf{r}} & \hat{\boldsymbol{\theta}} & \hat{\mathbf{z}} \\ u_{s,r} & u_{s,\theta} & 0 \\ 0 & 0 & B_z \end{vmatrix} \tag{A.13}$$

$$= n_s q_s(E_r + u_{s,\theta}B_z, E_\theta - u_{s,r}B_z, 0) \tag{A.14}$$

Using Eq. (A.10) this vector equation can be split up into its constituent components; the r component:

$$\frac{\partial u_{s,r}}{\partial t} + u_{s,r}\frac{\partial u_{s,r}}{\partial r} - \frac{u_{s,\theta}^2}{r} = \frac{q_s}{m_s}(E_r + u_{s,\theta}B_z) \tag{A.15}$$

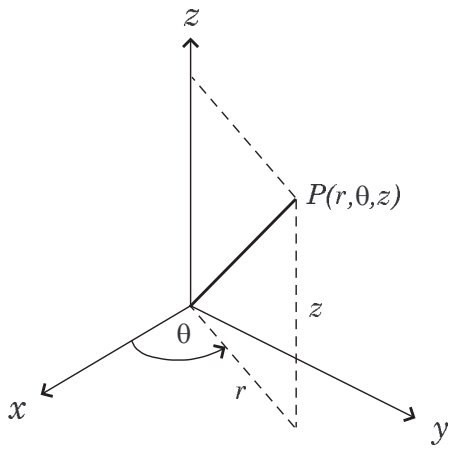

Figure A.1: The point P in cylindrical polar coordinates. Note that the conventional notation for cylindrical coordinates is (ρ, ϕ, z), but here the use of ρ will be reserved to denote the radial electric field so r shall be used instead.

and the θ component:

$$\frac{\partial u_{s,\theta}}{\partial t} + u_{s,r}\frac{\partial u_{s,\theta}}{\partial r} + \frac{u_{s,r}u_{s,\theta}}{r} = \frac{q_s}{m_s}(E_\theta - u_{s,r}B_z) \tag{A.16}$$

Substituting Eq. (A.3) into Eq. (A.4) the Ampère-Maxwell equation becomes

$$\frac{1}{r}\begin{vmatrix} \hat{\mathbf{r}} & r\hat{\boldsymbol{\theta}} & \hat{\mathbf{z}} \\ \partial/\partial r & \partial/\partial\theta & \partial/\partial z \\ 0 & 0 & B_z \end{vmatrix} = \mu_0 \sum_s n_s q_s \mathbf{u}_s + \epsilon_0\mu_0\frac{\partial \mathbf{E}}{\partial t} \tag{A.17}$$

$$\tag{A.18}$$

Resolving into components; the r component:

$$0 = \mu_0 \sum_s n_s q_s u_{s,r} + \epsilon_0\mu_0\frac{\partial E_r}{\partial t} \tag{A.19}$$

and the θ component:

$$-\frac{\partial B_z}{\partial r} = \mu_0 \sum_s n_s q_s u_{s,\theta} + \epsilon_0\mu_0\frac{\partial E_\theta}{\partial t} \tag{A.20}$$

Faraday's law of induction, Eq. (A.5) reads

$$\frac{1}{r}\begin{vmatrix} \hat{\mathbf{r}} & r\hat{\boldsymbol{\theta}} & \hat{\mathbf{z}} \\ \partial/\partial r & \partial/\partial\theta & \partial/\partial z \\ E_r & rE_\theta & 0 \end{vmatrix} = -\frac{\partial \mathbf{B}}{\partial t} \tag{A.21}$$

The only resulting non-zero component is:

$$\frac{1}{r}\frac{\partial}{\partial r}(rE_\theta) = -\frac{\partial B_z}{\partial t} \tag{A.22}$$

Again making use of Eq. (A.8), Poisson's Equation in cylindrical coordinates takes the form

$$\frac{1}{r}\frac{\partial}{\partial r}(rE_r) = \frac{1}{\epsilon_0}\sum_s n_s q_s \tag{A.23}$$

Therefore the model equations in cylindrical polar coordinates are,

$$\begin{aligned}
r\dot{n}_s + (rn_s u_{s,r})' &= 0 && \text{(A.24)}\\
\dot{u}_{s,r} + u_{s,r}u'_{s,r} - u^2_{s,\theta}/r &= (q_s/m_s)(E_r + u_{s,\theta}B_z) && \text{(A.25)}\\
\dot{u}_{s,\theta} + u_{s,r}u'_{s,\theta} + u_{s,r}u_{s,\theta}/r &= (q_s/m_s)(E_\theta - u_{s,r}B_z) && \text{(A.26)}\\
(rE_r)' &= \frac{r}{\epsilon_0}\sum_s n_s q_s && \text{(A.27)}\\
0 &= -\dot{E}_r/c^2 - \mu_0\sum_s n_s q_s u_{s,r} && \text{(A.28)}\\
(rE_\theta)' &= -r\dot{B}_z && \text{(A.29)}\\
B'_z &= -\dot{E}_\theta/c^2 - \mu_0\sum_s n_s q_s u_{s,\theta} && \text{(A.30)}
\end{aligned}$$

where $\dot{}$ denotes $\partial/\partial t$ and $'$ denotes $\partial/\partial r$.

A.3 Non-dimensional equations

Pair, or equal mass, plasmas are composed of two constituent species: both having identical mass and opposite charge. Electron-positron plasmas fall into this category. In contrast to conventional electron-ion plasmas they possess an inherent, natural symmetry. For an electron-positron pair plasma the model equations become:

$$\begin{aligned}
r\dot{n}_+ + (rn_+u_r)' &= 0 && \text{(A.31)}\\
r\dot{n}_- + (rn_-v_r)' &= 0 && \text{(A.32)}\\
\dot{u}_r + u_r u'_r - u^2_\theta/r &= (e/m)(E_r + u_\theta B_z) && \text{(A.33)}\\
\dot{u}_\theta + u_r u'_\theta + u_r u_\theta/r &= (e/m)(E_\theta - u_r B_z) && \text{(A.34)}\\
\dot{v}_r + v_r v'_r - v^2_\theta/r &= -(e/m)(E_r + v_\theta B_z) && \text{(A.35)}\\
\dot{v}_\theta + v_r v'_\theta + v_r v_\theta/r &= -(e/m)(E_\theta - v_r B_z) && \text{(A.36)}\\
(rE_r)' &= (e/\epsilon_0)r(n_+ - n_-) && \text{(A.37)}\\
0 &= -\dot{E}_r/c^2 - \mu_0 e(n_+u_r - n_-v_r) && \text{(A.38)}\\
(rE_\theta)' &= -r\dot{B}_z && \text{(A.39)}\\
B'_z &= -\dot{E}_\theta/c^2 - \mu_0 e(n_+u_\theta - n_-v_\theta) && \text{(A.40)}
\end{aligned}$$

where $\pm$ denotes the sign of the species; u, v are the positron and electron velocities respectively. Non-dimensionalisation is a mathematical technique where a dimensional variable, y, is replaced with a non-dimensional counterpart, $\hat{y}$, such that $\hat{y} = y/y_0$. Where y_0 is a characteristic value of the variable which is specific to the system in question. This simplifies numerical and analytical analysis of the problem and allows it to be paramterised

easily. The model equations were cast in non-dimensional form using the following variables

$$
\begin{aligned}
f &= \xi n_+/n_0 && \text{(A.41)}\\
g &= \xi n_-/n_0 && \text{(A.42)}\\
a &= u_r/(\omega_0 L) && \text{(A.43)}\\
b &= u_\theta/(\omega_0 L) && \text{(A.44)}\\
c &= v_r/(\omega_0 L) && \text{(A.45)}\\
d &= v_\theta/(\omega_0 L) && \text{(A.46)}\\
\rho &= eE_r/(m\omega_0^2 L) && \text{(A.47)}\\
\theta &= eE_\theta/(m\omega_0^2 L) && \text{(A.48)}\\
\beta_0+\beta &= eB_z/(m\omega_0) && \text{(A.49)}\\
\xi &= r/L && \text{(A.50)}\\
\tau &= \omega_0 t && \text{(A.51)}
\end{aligned}
$$

and

$$
\begin{aligned}
\omega_0^2 &= n_0 e^2/(\epsilon_0 m) && \text{(A.52)}\\
p &= c^2/(\omega_0^2 L^2) && \text{(A.53)}
\end{aligned}
$$

where L, $1/\omega_0$ are characteristic length, time scales respectively and n_0 is a characteristic number density. This returns

$$
\begin{aligned}
\dot{f} &= -(af)' && \text{(A.54)}\\
\dot{g} &= -(cg)' && \text{(A.55)}\\
\dot{a} &= -\frac{1}{2}(a^2)' + b^2/\xi + \rho + b(\beta_0+\beta) && \text{(A.56)}\\
\dot{b} &= -ab' - ab/\xi + \theta - a(\beta_0+\beta) && \text{(A.57)}\\
\dot{c} &= -\frac{1}{2}(c^2)' + d^2/\xi - \rho - d(\beta_0+\beta) && \text{(A.58)}\\
\dot{d} &= -cd' - cd/\xi - \theta + c(\beta_0+\beta) && \text{(A.59)}\\
(\xi\rho)' &= f - g && \text{(A.60)}\\
\dot{\rho} &= -\frac{1}{\xi}(af - cg) && \text{(A.61)}\\
\dot{\theta} &= -p(\beta_0+\beta)' - \frac{1}{\xi}(fb - dg) && \text{(A.62)}\\
\dot{\beta} &= -\theta' - \theta/\xi && \text{(A.63)}
\end{aligned}
$$

To highlight the symmetry of the problem it is desirable to form the sum and difference between similar plasma variables of the two species, hence

$$\dot{f}+\dot{g} = -(af+cg)' \tag{A.64}$$
$$\dot{f}-\dot{g} = -(af-cg)' \tag{A.65}$$
$$\dot{a}+\dot{c} = -\frac{1}{2}(a^2+c^2)' + (b^2+d^2)/\xi + (b-d)(\beta_0+\beta) \tag{A.66}$$
$$\dot{a}-\dot{c} = -\frac{1}{2}(a^2-c^2)' + (b^2-d^2)/\xi + 2\rho + (b+d)(\beta_0+\beta) \tag{A.67}$$
$$\dot{b}+\dot{d} = -ab'-cd'-(ab+cd)/\xi - (a-c)(\beta_0+\beta) \tag{A.68}$$
$$\dot{b}-\dot{d} = -ab'+cd'-(ab-cd)/\xi + 2\theta - (a+c)(\beta_0+\beta) \tag{A.69}$$
$$(\xi\rho)' = f-g \tag{A.70}$$
$$\dot{\rho} = -\frac{1}{\xi}(af-cg) \tag{A.71}$$
$$\dot{\theta} = -p(\beta_0+\beta)' - \frac{1}{\xi}(fb-dg) \tag{A.72}$$
$$\dot{\beta} = -\theta' - \theta/\xi \tag{A.73}$$

Substituting the following:

$$a = \sigma+\delta \tag{A.74}$$
$$b = \chi+\zeta \tag{A.75}$$
$$c = \sigma-\delta \tag{A.76}$$
$$d = \chi-\zeta \tag{A.77}$$
$$f = \Sigma+\Delta \tag{A.78}$$
$$g = \Sigma-\Delta \tag{A.79}$$

into Eqs. (A.64-A.73), the following cross terms emerge as

$$af = (\sigma+\delta)(\Sigma+\Delta) = \sigma\Sigma+\sigma\Delta+\delta\Sigma+\delta\Delta \tag{A.80}$$
$$cg = (\sigma-\delta)(\Sigma-\Delta) = \sigma\Sigma-\sigma\Delta-\delta\Sigma+\delta\Delta \tag{A.81}$$
$$a^2 = (\sigma+\delta)^2 = \sigma^2+2\sigma\delta+\delta^2 \tag{A.82}$$
$$c^2 = (\sigma-\delta)^2 = \sigma^2-2\sigma\delta+\delta^2 \tag{A.83}$$
$$b^2 = (\chi+\zeta)^2 = \chi^2+2\chi\zeta+\zeta^2 \tag{A.84}$$
$$d^2 = (\chi-\zeta)^2 = \chi^2-2\chi\zeta+\zeta^2 \tag{A.85}$$
$$bf = (\chi+\zeta)(\Sigma+\Delta) = \chi\Sigma+\chi\Delta+\zeta\Sigma+\zeta\Delta \tag{A.86}$$
$$dg = (\chi-\zeta)(\Sigma-\Delta) = \chi\Sigma-\chi\Delta-\zeta\Sigma+\zeta\Delta \tag{A.87}$$
$$ab = (\sigma+\delta)(\chi+\zeta) = \sigma\chi+\sigma\zeta+\delta\chi+\delta\zeta \tag{A.88}$$
$$cd = (\sigma-\delta)(\chi-\zeta) = \sigma\chi-\sigma\zeta-\delta\chi+\delta\zeta \tag{A.89}$$
$$ab' = (\sigma+\delta)(\chi+\zeta)' = \sigma\chi'+\sigma\zeta'+\delta\chi'+\delta\zeta' \tag{A.90}$$
$$cd' = (\sigma-\delta)(\chi-\zeta)' = \sigma\chi'-\sigma\zeta'-\delta\chi'+\delta\zeta' \tag{A.91}$$

Thence the governing system of equations become:

$$\dot{\Sigma} = -(\Sigma\sigma + \Delta\delta)' \tag{A.92}$$
$$\dot{\Delta} = -(\Delta\sigma + \Sigma\delta)' \tag{A.93}$$
$$\dot{\sigma} = -\frac{1}{2}(\sigma^2 + \delta^2)' + (\chi^2 + \zeta^2)/\xi + \zeta(\beta_0 + \beta) \tag{A.94}$$
$$\dot{\delta} = -(\sigma\delta)' + 2\chi\zeta/\xi + \rho + \chi(\beta_0 + \beta) \tag{A.95}$$
$$\dot{\chi} = -\chi'\sigma - \zeta'\delta - (\chi\sigma + \zeta\delta)/\xi - \delta(\beta_0 + \beta) \tag{A.96}$$
$$\dot{\zeta} = -\sigma\zeta' - \delta\chi' - (\sigma\zeta + \delta\chi)/\xi + \theta - \sigma(\beta_0 + \beta) \tag{A.97}$$
$$(\xi\rho)' = 2\Delta \tag{A.98}$$
$$\dot{\rho} = -\frac{2}{\xi}(\Delta\sigma + \Sigma\delta) \tag{A.99}$$
$$\dot{\theta} = -p(\beta_0 + \beta)' - \frac{2}{\xi}(\Sigma\zeta + \Delta\chi) \tag{A.100}$$
$$\dot{\beta} = -\theta' - \theta/\xi \tag{A.101}$$

A.4 Linearisation of model equations

To linearise the coupled set of equations (A.92-A.93) all variables are perturbed from an equilibrium state, $y = y_0(\xi) + y_1(\xi, \tau)$, such that the perturbation is much smaller than the equilibrium value, $|y_0| \gg |y_1|$. Nonlinear combinations of y can be linearised by disregarding powers of y_1 greater than 1. Hence:

$$\Sigma = \Sigma_0 + \Sigma_1 \tag{A.102}$$
$$\sigma = \sigma_0 + \sigma_1 \tag{A.103}$$
$$\zeta = \zeta_0 + \zeta_1 \tag{A.104}$$

where the other plasma variables have a zero valued equilibrium; $y = y_1$. Beginning with Eq. (A.92):

$$\dot{\Sigma}_1 = -[(\Sigma_0 + \Sigma_1)(\sigma_0 + \sigma_1) + \Delta\delta]' \tag{A.105}$$
$$= -(\Sigma_0\sigma_0 + \Sigma_0\sigma_1 + \Sigma_1\sigma_0)' \tag{A.106}$$

Since $\Sigma_0\sigma_0 = \kappa_0$ its derivative equals zero leaving:

$$\dot{\Sigma}_1 = -(\Sigma_0\sigma_1 + \Sigma_1\sigma_0)' \tag{A.107}$$

Eq. (A.93) simply reduces to:

$$\dot{\Delta} = -(\Delta(\sigma_0 + \sigma_1) + (\Sigma_0 + \sigma_1)\delta)' \tag{A.108}$$
$$= -(\sigma_0\Delta + \Sigma_0\delta)' \tag{A.109}$$

Linearising Eq. (A.94) produces

$$\dot{\sigma}_1 = -\frac{1}{2}(\sigma_0^2 + 2\sigma_0\sigma_1 + \sigma_1^2 + \delta^2)' + (\chi^2 + \zeta_0^2 + 2\zeta_0\zeta_1 + \zeta_1^2)/\xi$$
$$+ (\zeta_0 + \zeta_1)(\beta_0 + \beta_1) \tag{A.110}$$
$$= -\frac{1}{2}(\sigma_0^2 + 2\sigma_0\sigma_1)' + (\zeta_0^2 + 2\zeta_0\zeta_1)/\xi + \zeta_0\beta_0 + \zeta_0\beta_1$$
$$+ \zeta_1\beta_0 \tag{A.111}$$

Recall from the equilibrium situation that $(\sigma_0^2)'/2 + \zeta_0^2/\xi + \zeta_0\beta_0 = 0$ (Eq. (3.58)) yielding

$$\dot{\sigma}_1 = -(\sigma_0\sigma_1)' + 2\zeta_0\zeta_1/\xi + \zeta_0\beta_1 + \zeta_1\beta_0 \tag{A.112}$$

Both Eq. (A.95) and (A.96) linearise trivially as:

$$\begin{aligned} \dot{\delta} &= -[(\sigma_0+\sigma_1)\delta]' + 2\chi(\zeta_0+\zeta_1)/\xi + \rho + \xi(\beta_0+\beta_1) && \text{(A.113)} \\ &= -(\sigma_0\delta)' + 2\chi\zeta_0/\xi + \rho + \chi\beta_0 && \text{(A.114)} \end{aligned}$$

and

$$\begin{aligned} \dot{\chi} &= -\chi'(\sigma_0+\sigma_1) - (\zeta_0+\zeta_1)'\delta - [\chi(\sigma_0+\sigma_1) + (\zeta_0+\zeta_1)\delta]/\xi \\ &- \delta(\beta_0+\beta_1) && \text{(A.115)} \\ &= -\chi'\sigma_0 - \zeta_0'\delta - (\sigma_0\chi + \zeta_0\delta)/\xi - \delta\beta_0 && \text{(A.116)} \end{aligned}$$

respectively. Looking at Eq. (A.97)

$$\begin{aligned} \dot{\zeta}_1 &= -(\sigma_0+\sigma_1)(\zeta_0+\zeta_1)' - \delta\chi' - [(\sigma_0+\sigma_1)(\zeta_0+\zeta_1) + \delta\chi]\xi + \theta \\ &- (\sigma_0+\sigma_1)(\beta_0+\beta_1) && \text{(A.117)} \\ &= -(\sigma_0\zeta_0' + \sigma_0\zeta_1' + \sigma_1\zeta_0') - (\sigma_0\zeta_0 + \sigma_0\zeta + \sigma\zeta_0)/\xi + \theta - \sigma_0\beta_0 - \sigma_0\beta_1 \\ &- \sigma_1\beta_0 && \text{(A.118)} \end{aligned}$$

The equilibrium situation states that $\sigma_0(\zeta_0' + \zeta_0/\xi + \beta_0) = 0$ (Eq. (3.59)), ergo:

$$\dot{\zeta}_1 = -\sigma_0\zeta_1' - \sigma_1\zeta_0' - (\sigma_0\zeta_1 + \sigma_1\zeta_0)/\xi + \theta - \sigma_0\beta_1 - \sigma_1\beta_0 \tag{A.119}$$

Linearising the radial component of the Ampère-Maxwell equation, Eq. (A.99), yields

$$\begin{aligned} \dot{\rho} &= -\frac{2}{\xi}[\Delta(\sigma_0+\sigma_1) + (\Sigma_0+\Sigma_1)\delta] && \text{(A.120)} \\ &= -\frac{2}{\xi}(\Delta\sigma_0 + \Sigma_0\delta) && \text{(A.121)} \end{aligned}$$

The azimuthal component of the Ampère-Maxwell equation yields

$$\begin{aligned} \dot{\theta} &= -p(\beta_0+\beta_1)' - \frac{2}{\xi}[(\Sigma_0+\Sigma_1)(\zeta_0+\zeta_1) + \Delta\chi] && \text{(A.122)} \\ &= -p\beta_1' - \frac{2}{\xi}(\Sigma_0\zeta_1 + \Sigma_1\zeta_0) && \text{(A.123)} \end{aligned}$$

noting that the equilibrium dictates that $-p\beta_0' - 2\Sigma_0\zeta_0/\xi = 0$. Therefore the linearised governing set of equations read:

$$\begin{aligned} \dot{\Sigma} &= -(\Sigma_0\sigma + \Sigma\sigma_0)' && \text{(A.124)} \\ \dot{\Delta} &= -(\sigma_0\Delta + \Sigma_0\delta)' && \text{(A.125)} \\ \dot{\sigma} &= -(\sigma_0\sigma)' + 2\zeta_0\zeta/\xi + \zeta_0\beta + \zeta\beta_0 && \text{(A.126)} \\ \dot{\delta} &= -(\sigma_0\delta)' + 2\zeta_0\chi/\xi + \rho + \chi\beta_0 && \text{(A.127)} \\ \dot{\chi} &= -\sigma_0\chi' - \zeta_0'\delta - (\sigma_0\chi + \zeta_0\delta)/\xi - \delta\beta_0 && \text{(A.128)} \\ \dot{\zeta} &= -\sigma_0\zeta' - \sigma\zeta_0' - (\sigma_0\zeta + \sigma\zeta_0)/\xi + \theta - \sigma_0\beta - \sigma\beta_0 && \text{(A.129)} \\ (\xi\rho)' &= 2\Delta && \text{(A.130)} \\ \dot{\rho} &= -\frac{2}{\xi}(\Delta\sigma_0 + \Sigma_0\delta) && \text{(A.131)} \\ \dot{\theta} &= -p\beta' - \frac{2}{\xi}(\Sigma_0\zeta + \Sigma\zeta_0) && \text{(A.132)} \\ \dot{\beta} &= -\theta' - \theta/\xi && \text{(A.133)} \end{aligned}$$

where the perturbation subscripts have been dropped. Eqs (A.98) and (A.101) linearise trivially and require no explicit exposition.

A.5 Table of important quantities

Table A.1: Physical meaning of non-dimensionalised plasma quantities

Quantity	Description	Ref.
$n_\pm$	particle number density of $e^\pm$	
$\mathbf{u}$, $\mathbf{v}$	fluid velocity of $e^\pm$	
$\mathbf{E}$	electric field	
$\mathbf{B}$	magnetic field	
(r, θ, z)	cylindrical polar coordinates	
Σ	average plasma number density	(3.25)
Δ	difference between e^+-e^- number densities	(3.26)
σ	average radial plasma flow	(3.27)
δ	difference between e^+-e^- radial velocities	(3.28)
χ	average azimuthal plasma flow	(3.29)
ζ	difference between e^+-e^- azimuthal velocities	(3.30)
ρ	radial electric field	(3.31)
θ	azimuthal electric field	(3.32)
β	magnetic field	(3.33)
ξ	non-dimensionalised radial coordinate	(3.34)
τ	non-dimensionalised time coordinate	(3.35)
ω_0	plasma frequency	(3.36)

References

[1] A. Hewish, S. J. Bell, J. D. H. Pilkington, P. F. Scott, and R. A. Collins. Observation of a rapidly rotating pulsating radio source. *Nature*, 217:709–713, 1968.

[2] J. D. H. Pilkington, A. Hewish, S. J. Bell, and T. W. Cole. Observations of some further pulsed radio sources. *Nature*, 218:126–129, 1968.

[3] T. Gold. Rotating neutron stars as the origin of the pulsating radio sources. *Nature*, 218:731–732, 1968.

[4] J. M. Lattimer and M. Prakash. The physics of neutron stars. *Science*, 304:536–542, 2004.

[5] A. Burrows. Supernova explosions in the universe. *Nature*, 403:727–733, 2000.

[6] R. N. Manchester. Observational properties of pulsars. *Science*, 304:542–546, 2004.

[7] D. Lorimer and M. Kramer. *Handbook of Pulsar Astronomy*. Cambridge University Press, Cambridge, UK, 2005.

[8] F. Pacini. Rotating neutron stars, pulsars and supernova remnants. *Nature*, 219:145–146, 1968.

[9] T. Gold. Rotating neutron stars and the nature of pulsars. *Nature*, 221:25–27, 1969.

[10] R. A. Hulse and J. H. Taylor. Discovery of a pulsar in a binary system. *The Astrophysical Journal*, 195:L51–L53, 1975.

[11] A. G. Lyne, M. Burgay, M. Kramer, A. Possenti, R. N. Manchester, et al. A double-pulsar system: A rare laboratory for relativistic gravity and plasma physics. *Science*, 303:1153–1157, 2004.

[12] D. C. Backer, S. R. Kulkarni, C. Heiles, M. M. Davis, and W. M. Goss. A millisecond pulsar. *Nature*, 300:615–618, 1982.

[13] M. A. Alpar, A. F. Cheng, M. A. Ruderman, and J. Shaham. A new class of radio pulsars. *Nature*, 300:728–730, 1982.

[14] D. R. Lorimer. Binary and millisecond pulsars. *Living Reviews in Relativity*, 8:7, 2005.

[15] J. W. T. Hessels, S. M. Ransom, I. H. Stairs, P. C. C. Freire, V. M. Kaspi, et al. A radio pulsar spinning at 716 hz. *Science*, 311:1901–1904, 2006.

[16] M. D. Young, R. N. Manchester, and S. Johnston. A radio pulsar with an 8.5-second perid that challenges emission models. *Nature*, 400:848–849, 1999.

[17] F. Graham-Smith. The radio emission from pulsars. *Reports on Progress in Physics*, 66:173–238, 2003.

[18] A. G. Lyne and F. Graham-Smith. *Pulsar Astronomy.* Cambridge University Press, Cambridge, UK, 2005.

[19] T. H. Hankins, J. S. Kern, J. C. Weatherall, and J. A. Eilek. Nanosecond radio bursts from strong plasma turbulence in the crab pulsar. *Nature*, 422:141–143, 2003.

[20] A. D. Kuzmin. Giant pulses of pulsar radio emission. *Astrophysics and Space Science*, 308:563–567, 2007.

[21] F. D. Drake and H. D. Craft. Second periodic pulsation in pulsars. *Nature*, 220:231–235, 1968.

[22] D. C. Backer. Pulse nullling phenomena. *Nature*, 228:42–43, 1970.

[23] D. C. Backer. Peculiar pulse burst in psr 1237+35. *Nature*, 228:1297–1298, 1970.

[24] M. Kramer, A. G. Lyne, J. T. O'Brien, C. A. Jordan, et al. A periodicaly active pulsar giving insight into magnetospheric physics. *Science*, 312:549–551, 2006.

[25] M. A. McLaughlin, A. G. lyne, D. R. Lorimer, M. Kramer, et al. Transient radio bursts from rotating neutron stars. *Nature*, 439:817–820, 2006.

[26] P. Goldreich and W. H. Julian. Pulsar electrodynamics. *The Astrophysical Journal*, 157:869–880, 1969.

[27] D. B. Melrose. The models for radio emission from pulsars-the outstanding issues. *Journal of Astrophysics and Astronomy*, 16:137–164, 1995.

[28] M. M. Komesaroff. Possible mechanism for the pulsar radio emission. *Nature*, 225:612–614, 1970.

[29] M. A. Ruderman and P. G. Sutherland. Theory of pulsars: Polar gaps, sparks, and coherent microwave radiation. *The Astrophysical Journal*, 196:51–72, 1975.

[30] A. F. Cheng and M. A. Ruderman. Bunching mechanisms for coherent curvature radiation in pulsar magnetospheres. *The Astrophysical Journal*, 212:800–806, 1977.

[31] V. I. Karpman, C. A. Norman, D. ter Haar, and V. N. Tsytovich. Relativistic solitons and pulsars. *Physica Scripta*, 11:271–274, 1975.

[32] J. Gil, Y. Lyubarsky, and G. I. Melikidze. Curvature radiation in pulsar magnetospheric plasma. *The Astrophysical Journal*, 600:872–882, 2004.

[33] P. E. Hardee and W. K. Rose. A mechanism for the production of pulsar radiation. *The Astrophysical Journal*, 210:533–538, 1976.

[34] D. B. Melrose. The status of pulsar emission theory. *Pulsar Astronomy-2000 and Beyond, IAU Colloquim*, 177:721–726, 2000.

[35] J. C. Weatherall. Modulational instability, mode conversion, and radio emission in the magnetised pair plasma of pulsars. *The Astrophysical Journal*, 483:402–413, 1997.

[36] Yu. E. Lyubarskii. Generation of pulsar radio emission. *Astronomy and Astrophysics*, 308:809–820, 1996.

[37] Q. Luo and D. B. Melrose. Coherent curvature emission and radio pulsars. *Monthly Notices of the Astronomical Society*, 258:616–620, 1992.

[38] F. Cernuschi, F. Marsicano, and S. Codina. A contribution to the theory on the formation of cosmic grains. *Annales d'Astrophysique*, 30:1039–1051, 1967.

[39] F. Hoyle and N. C. Wickramasinghe. Dust in supernova explosions. *Nature*, 226:62–63, 1970.

[40] D. C. B. Whittet. *Dust in the Galactic Environment*. IoP, New York, USA, 2002.

[41] B. T. Draine. Interstellar dust grains. *Annual Reviews of Astronomy and Astrophysics*, 41:241–89, 2003.

[42] Eli Dwek. The supernova origin of interstellar dust. *Science*, 313:178–180, 2006.

[43] Ben E. K. Sugerman, Barbara Ercolano, M. J. Barlow, A. G. G. M. Tielens, et al. A contribution to the theory on the formation of cosmic grains. *Science*, 313:196–200, 2006.

[44] Eli Dwek. The detection of cold dust in cassiopeia a: Evidence for the formation of metallic needles in the ejecta. *ApJ*, 607:848–854, 2004.

[45] Jr. Leverett Davis and Jesse L. Greenstein. The polarization of starlight by interstellar dust particles in a galactic magnetic field. *Phys. Rev. Lett.*, 75:1605, 1949.

[46] Hiroki Chihara, Toshihide Okumura, and Chiaki Uyeda. The magnetic ordering of graphite grains and its application to astrophysical problems. *J. Magnetism&Mag. Materials*, 177-181:1455–1456, 1998.

[47] D. A. Diver and D. Clarke. The evolution of cosmic and laboratory plasma dust. *J. Phys. D: Appl. Phys.*, 29:687–690, 1996.

[48] Edward M. Purcell and Carlton R. Pennypacker. Scattering and absorption of light by nonspherical dielectric grains. *ApJ*, 186:705–714, 1973.

[49] D. B. Vaidya and R. Gupta. Extinction by porous silicate and graphite grains. *A&A*, 328:634–640, 1997.

[50] D. B. Vaidya and R. Gupta. Interstellar extinction by porous grains. *A&A*, 348:594–599, 1999.

[51] D. B. Vaidya, R. Gupta, and T. P. Snow. Composite interstellar grains. *Monthly Notices of the Astronomical Society*, 379:791–800, 2007.

[52] D. B. Vaidya, R. Gupta, J. S. Dobbie, and P. Chylek. Interstellar extinction by composite grains. *A&—*, 375:584–590, 2001.

[53] Ranjan Gupta, D. B. Viadya, J. S. Dobbie, and Petr Chylek. Scattering properties and composition of cometary dust. *Ap&SS*, 301:21–31, 2006.

[54] P. Todini and A. Ferrara. Dust formation in primordial type ii supernovae. *Monthly Notices of the Royal Astronomical Society*, 325:726–736, 2001.

[55] E. A. N. Deneault, D. D. Clayton, and B. S. Meyer. Growth of carbon grains in supernova ejecta. *The Astrophysical Journal*, 638:234–240, 2006.

[56] S. Bianchi and R. Schneider. Dust formation and survival in supernova ejecta. *Monthly Notices of the Royal Astronomical Society*, 378:973–982, 2007.

[57] T. Nozawa, T. Kozasa, A. Habe, E. Dwek, H. Umeda, et al. Evolution of dust in primordial supernova remnants: can dust grains formed in the ejecta survive and be injeted into the early interstellar medium? *The Astrophysical Journal*, 666:955–966, 2007.

[58] D. A. Mendis. Progress in the study of dusty plasmas. *Plasma Sources Science and Technology*, 11:A219–A228, 2002.

[59] Y. Watanabe. Formation and behaviour of nano/micro-particles in low pressure plasmas. *Journal of Physics D: Applied Physics*, 39:R329–R361, 2006.

[60] R. Bingham and V. N. Tsytovich. New mechanism of dust growth and gravitational-lik instabilities in astrophysical plasmas. *A&A*, 376:L34–L47, 2001.

[61] Ch. Hollenstein. The physics and chemistry of dusty plasmas. *Plasma Physics and Controlled Fusion*, 42:R93–R104, 2000.

[62] A. Gallagher. Model of particle growth in silane discharges. *Physical Review E*, 62:2690–2706, 2000.

[63] K. De Bleecker, A. Bogaerts, W. Goedheer, and R. Gijbels. Investigation of growth mechanims of clusters in a silane discharge with the use of a fluid model. *IEEE Transaction on Plasma Science*, 32, 2:691–698, 2004.

[64] B. F. Gordiets and E. Bertran. Kinetic model for generation and growth of plasma dust nanoparticles. *Chem. Phys. Lett.*, 414:423–428, 2005.

[65] K. De Bleecker and A. Bogaerts. Detailed modeling of hydrocarbon nanoparticle nulceation in acetylene discharges. *Physical Review E*, 73:026405, 2006.

[66] K. De Bleecker, A. Bogaerts, and W. Goedheer. Modeling of the formation and transport of nanoparticles in silane plasmas. *Physical Review E*, 70:056407, 2004.

[67] K. S. Kim, D. J. Kim, J. Y. Park, Y. Watanabe, and M. Shiratani. The changes in particle charge distribution during rapid growth of particles in the plasma reactor. *Journal of Colloid and Interface Science*, 257:195, 2003.

[68] D. Shi, S. X. Wang, W. J. van Ooij, L. M. Wang, J. Zhao, et al. Unifomr deposition of ultrathin polymer films on the surfaces of al_2o_3 nanoparticles by a plasma treatment. *Applied Physics Letters*, 78, 9:1243–1245, 2001.

[69] J. Cao and T. Matsoukas. Deposition kinetics on particles in a dusty plasma reactor. *Journak of Applied Physics*, 92, 5:2916–2922, 2002.

[70] T. Matsoukas and J. Cao. Film deposition on particles trapped in the sheath of reactive dusty plasma: Effects of size distribution. *IEEE Transactions on Plasma Science*, 32, 2:699–703, 2004.

[71] A. L. Yarin, B. Rovagnati, and F. Mashayek. A reaction model for plasma coating of nanoparticles by amorphous carbon layers. *Journal of Applied Physics*, 99:064310, 2006.

[72] G. A. Stewart. PhD thesis, University of Glasgow, 1993.

[73] N. Shukla and P. K. Shukla. Generation of magnetic field fluctuations in relativistic electron-positron magnetospheres. *Phys. Lett. A*, 362:221–224, 2007.

[74] M. Marklund, B.Eliasson, and P. K. Shukla. Nonlinear propagation of broadband intense electromagnetic waves in an electron-positron plasma. *Phys. Plasmas*, 13:083102, 2006.

[75] F. Verheest and T. Cattaert. Large amplitude solitary electromagnetic waves in electron-positron plasmas. *Phys. Plasmas*, 11,6:3078–3082, 2004.

[76] S. S. Bulanov, A. M. Fedotov, and F. Pegoraro. Damping of electromagnetic waves due to electron-positron pair production. *Phys. Rev. E*, 71:016404, 2005.

[77] A. A. da Costa, D. A. Diver, and G. A. Stewart. Pulsar magnetospheres: Numerical simulations of large amplitude electron-positron oscillations. *A&A*, 366:129–137, 2001.

[78] D. A. Diver, A. A. da Costa, and E. W. Laing. Coupling between electrostatic and electromagnetic behaviour in a cylindrical equal-mass plasma. *A&A*, 387:339–346, 2002.

[79] C. R. Stark, D. A. Diver, A. A. da Costa, and E. W. Laing. Nonlinear mode coupling in pair plasmas. *Astronomy and Astrophysics*, 476:17–30, 2007.

[80] C. R. Stark, D. A. Diver, and A. A. da Costa. Magnetised electron-positron plasmas. *Proceedings of the 363. WE-Heraeus Seminar on "Neutron Stars and Pulsars", eds. W. Becker & H. H. Huang*, MPE Report 291:145–148, 2007.

[81] M. Abramowitz and I. A. Stegun. *Handbook of Mathematical Functions.* Dover Publications, Inc, New York, USA, 1972.

[82] D. Zwillinger. *Handbook of Differential Equations.* Academic Press, San Diego, USA, 1989.

[83] K. S. Yee. Numerical solution of initial boundary value problems involving maxwell's equations in isotropic media. *Antennas and Propagation, IEEE Transanctions*, 14:302–307, 1966.

[84] A. R. Mitchell and D. F. Griffiths. *The Finite Difference Method in Partial Differential Equations.* John Wiley and Sons Ltd, Chichester, UK, 1980.

[85] A. B. C. Patzer, T. M. Köhler, and E. Sedhnayr. Primary astrophysical dust formation: laboratory desiderata. *Planet. Space Sci*, 43:1233–1239, 1995.

[86] Joseph A. Nuth, Frans J. M. Rietmeijer, and Hugh G. M. Hill. Condensation processes in astrophysical environments: The composition and structure of cometary grains. *Meteorites&Planet. Sci.*, 37:1579–1590, 2002.

[87] R. Gupta, T. Mulai, D. B. Vaidya, A. K. Sen, et al. Interstellar extinction by spheroidal dust grains. *A&A*, 441:555–561, 2005.

[88] David Bazell and Eli Dwek. The effects of compositional inhomogeneities and fractal dimension on the optical properties of astrophysical dust. *ApJ*, 360:142–150, 1990.

[89] M. A. Liebermann and A. J. Lichtenberg. *Principles of Plasma Discharges and Materials Processing*. Wiley-Interscience, New Jersey, USA, 2005.

[90] Francis F. Chen. *Introduction to Plasma Physics and Controlled Fusion. Volume 1: Plasma Physics*. Plenum Press, New York, USA, 1984.

[91] K-U Riemann. The bohm criterion and sheath formation. *J. Phys. D: Appl. Phys.*, 24:493–518, 1991.

[92] C. R. Stark, H. E. Potts, and D. A. Diver. Elliptical dust growth in astrophysical plasmas. *Astronomy and Astrophysics*, 457:365–370, 2006.

[93] H. Kersten, H. Deutsch, and G. M. W. Kroesen. Charging of micro-particles in plasma-dust interaction. *Mass. Spect.*, 233:51–60, 2004.

[94] D. A. Keston, E. W. Laing, and D. A. Diver. Bernstein modes in weakly relativistic electron-positron plasma. *Phys. Rev. E*, 67:036403, 2003.